Light-Assisted Collisions and Quantum State Tomography of Single-Atom Motion in Optical Tweezers

by

Mark O. Brown

B.S., Virginia Polytechnic Institute and State University, 2015

M.S., University of Colorado, Boulder, 2017

A thesis submitted to the

Faculty of the Graduate School of the

University of Colorado in partial fulfillment

of the requirements for the degree of

Doctor of Philosophy

Department of Physics

2022

Committee Members:

Cindy Regal, Chair

Jose D'Incao

Ana Maria Rey

Adam Kaufman

Kelvin Wagner

Brown, Mark O. (Ph.D., Physics)

Light-Assisted Collisions and Quantum State Tomography of Single-Atom Motion in Optical Tweezers

Thesis directed by Prof. Cindy Regal

This thesis presents experiments with single ^{87}Rb atoms trapped in arrays of tightly confining optical tweezers. Optical tweezer arrays are a pioneering new platform for studying ultracold atomic physics and quantum computation. I begin by presenting our recent work in the preparation of large atom arrays and the quantum motional control of single atoms. Then, I present a new optical tweezer loading technique and our studies of the processes by which single atoms can be loaded near-deterministically into the microtraps. These processes depend sensitively on the long-range molecular physics of pairs of atoms, so I additionally discuss our theoretical calculations of the molecular potential landscapes relevant for such collisions. Finally, I present our all-mechanical time-of-flight-based quantum tomography of atoms in carefully prepared excited motional states of the optical tweezers.

Acknowledgements

I must begin by thanking my advisor, Cindy. Even as a young graduate student, Cindy placed a great deal of trust in me and gave me a great deal of freedom and responsibility in running the lab in B232. Combining that with the right amount of guidance and mentorship resulted in an experience I do not think I could have gotten anywhere else. I am leaving with more confidence, experience, and knowledge than I could have possibly imagined at the start of my PhD. For that I will be forever grateful.

I must of course also thank those who built the B232 lab for me to work in: Adam and Brian. My first day in the lab was Adam's last day, but I have referenced his thesis more times than I can count. I was lucky enough to work with and learn from Brian for the first year and a half of graduate school. When Brian finished his PhD, the lab postdoc Yiheng Lin carried me from bumbling ignorance to a place where I could really run the lab myself. After Yiheng left, Tobias Thiele would become a great friend, always being up for getting coffee or lunch in just 5 minutes. Tobias was always willing to discuss any problems we encountered and was a great mentor to me throughout the middle of my PhD. Additionally I must thank Ana Maria Rey and her theory group, especially Sean and Robert, for all of the fruitful discussions we have had over the years.

A special thanks go out to the Randall, Max, Daniel, Thanmay, Ting You, Chris, Zhenpu, Ting-Wei, Willa, Steven, and the optomechanics crew. Thanks for your friendship and all of their work and scientific contributions over the years. Willa and Steven will continue to do great work in the B232 I'm sure. I look forward to seeing what new developments come out of the lab!

Contents

Chapter

Tables

Table

Figures

Figure

Chapter 1

Introduction

1.1 Optical Tweezer Arrays: Historical Background

The field of neutral atom atomic physics has undergone a number of evolutions, but it received a particularly great boost with the invention of the laser. Coming soon after the maser, the laser was first publicly conceptualized in the late 1950's and first implemented in 1960 [1, 2]. The optical tweezer would be invented a decade later where it was first used to trap microparticles [3]. After a couple years in 1975, laser cooling was proposed and implemented in 1978 [4, 5, 6]. The magneto optical trap (MOT), capable of trapping a large cloud of neutral atoms, was developed a decade afterwards [7]. Then, single atoms would be isolated and studied in a MOT [8]. There are many useful reviews of the physics and history of these foundational developments to which I would direct the interested reader [9, 10, 11, 12].

In the '90s and early 2000s, the great progress was made in the study of degenerate quantum gases of bosonic atoms [13, 14], fermionic atoms [15], and molecules [16, 17]. These degenerate gases continue to be fruitful areas of study to this day and are the starting points for many new experiments [18, 19, 20]. For example, quantum gas microscope experiments often start by using condensation and related phase transitions to prepare low-entropy states, and follow with leveraging single atom imaging and increasingly fine control over potentials and ultracold dynamics to conduct novel quantum simulation experiments [21, 22, 23, 24, 25, 26, 27].

In parallel, developments in the loading of single atoms and molecules into optical tweezers have enabled a more bottom-up approach to studying atomic systems. Beginning in 2001, this work continued for about ten years at a smaller scale, where research focused on establishing the core functionality and characterizations of such systems [28, 29, 30, 31, 32] and then harnessing strong and long-range Rydberg interactions [33, 34, 35, 36]. In the past ten years or so, there has been a small explosion of optical-tweezer based single-atom experiments and increasing interest in the platform. Now, there exist many more projects utilizing similar systems for studying fermions, molecules, alkali-earth atoms, and even some commercial enterprises hoping to use the platform for quantum computing [37, 38, 39, 40, 41, 42, 43, 44, 45, 46].

1.2 This Thesis

In general, improvements in quantum state readout and state preparation herald progress in the field of atomic physics. New methods for optical trapping predicted a new generation of trapped-atom experiments. Motional ground-state preparation via Raman sideband cooling preceded a wave of quantum information experiments with trapped ions. The preparation of Bose-Einstein condensates anticipated the current plethora of quantum simulation experiments.

With the optical tweezer platform, we push the limits of single neutral atom control into new regimes. Here, we are equipped with single-atom imaging and spin and motional control optical pumping, microwaves, and Raman transitions, and the mechanical manipulation of our tweezers. More uniquely, we also have control over the exact number and position of the atoms we work with.

One of the major scientific themes of this thesis is the use of these tools to study light-assisted multi-atom collisions in new regimes for the development of novel techniques for the loading of single particles into tightly confining optical potentials. Light-assisted collisions are routinely used in the field, but under their technical application lies rich molecular physics waiting to be studied [47, 48, 49, 39]. We apply the tools enabled by our single-atom control and the interplay of laser-cooling techniques to study this problem. In our experiments, we find that because of the combination of the ultracold temperatures of our atoms and the tight but overall low-energy confinement of the optical potential, that tweezer platforms are uniquely situated to study very long-range and low-energy light-assisted molecular collisions.

Another major scientific theme of this thesis is the quantum control of single particles near their motional ground state. While the optical tweezer platform is particularly attractive for Rydberg atom-based experiments and quantum computing, our focus has often been on near-ground-state physics [50, 51, 52]. Quantum motional control, as distinct from control of quantum spins, comes with unique opportunities for unique measurement techniques, such as time-of-flight imaging, and applications in the quantum control of macroscopic objects [43, 53, 54]. Working with ground-state atoms entails its own set of challenges and rewards. Optical tweezers are in many ways more individually controllable than alternative traps such as optical lattices, and so tweezers promise many unique ways to prepare states and dynamics potentials that would be more challenging in other systems. These capabilities include dynamic movement and reconfiguration of the array of atoms, including into structures which are closely-spaced on the order of the wavelength of atomic transitions, capabilities which can be used for whole other category of experiment involving atom-light interactions [55, 56].

One of the core components of this control in our experiments is quantum tunneling from tweezer to tweezer. An optical lattice, achieving its potential structure through the interference of only two beams, it is a very clean and suitable environment for realizing tunneling [57]. In a tweezer system, however, the potential must be constructed piece by piece, which makes it a technically challenging endeavor [51, 58, 42]. In this thesis, I characterize and push our motional control to further limits, enabling the production and tomography of non-classical motional states. We study these states using free-space imaging in the first such measurement of single ground-state bosons. We also apply methods similar to those used in optical homodyne tomography to map out the quantum state of our single particles. Our demonstration will enable future experiments with single atoms or larger particles to explore quantum effects in more complex and macroscopic systems [59, 60, 61, 62].

1.3 Outline

The scientific content of this thesis focuses primarily on the developments we made in enhanced loading, molecular physics, and quantum tomography. While I contributed to experiments in vector magnetometry, metalens optics, and in a more distant sense, Rydberg physics, I would point readers to the future but relatively forthcoming theses from our group of Christopher Kiehl and Ting-Wei Hsu for more information about this work.

Chapter 2 is titled “Apparatus for Ground-State Optical Tweezer Experiments”. Here, I will discuss the experimental apparatus upgrades I made, mostly in the earlier stages of my PhD. This includes upgrades to laser and optics systems, mechanical innovations, our control system, and other important physical developments made during my PhD.

In Chapter 3, I will discuss a number of atom-based experiments, techniques, and upgrades we developed. This includes new, previously unpublished iterations on Raman sideband cooling and quantum tunneling experiments conducted in recent years, as well as novel rearrangement techniques among other new technical developments.

Chapter 4 is all about our new technique for the enhanced loading of single atoms into optical tweezers. It reviews our published work [63] and explores further unpublished experiments we have recently conducted to learn more about this mysterious process, including details on the role of the Λ-enhancement and gray-molasses level structure on the loading process.

In Chapter 5, I will present theoretical calculations of the ultra-long range molecular potentials that we believe are important for the enhanced loading technique discussed in Chapter 4. Previous works have modeled the collisional process but tend to approximate the effect of the excited state molecular potential on the loading dynamics. By calculating the potentials fully, we find that the true nature of these potentials significantly alters our conception of how the loading process works. These calculations pave the way for future experiments and understanding of these complicated dynamics.

Lastly, Chapter 6 will focus on our all-mechanical time-of-flight-based quantum tomography experiment. This experiment makes use of the rapid cycle time of the experimental apparatus, our ground state cooling, quantum tunneling, and new free-space imaging techniques. The measurements give direct access to new observables and unprecendented information about single particle quantum states in our apparatus. We leverage all these tools to do full quantum tomography on motionally excited states of our optical tweezer potentials.

1.4 List of Publications

For reference, I am including here a list of papers which I have contributed to.

1. B. J. Lester, Y. Lin, **M. O. Brown**, A. M. Kaufman, R. J. Ball, E. Knill, A. M. Rey, and C. A. Regal, Measurement-Based Entanglement of Noninteracting Bosonic Atoms, Phys. Rev. Lett. 120, 193602 (2018).

2. T. Thiele, Y. Lin, **M. O. Brown**, and C. A. Regal, Self-Calibrating Vector Atomic Magnetometry through Microwave Polarization Reconstruction, Phys. Rev. Lett. 121, 153202 (2018).

3. **M. O. Brown**, T. Thiele, C. Kiehl, T.-W. Hsu, and C. A. Regal, Gray-Molasses Optical-Tweezer Loading: Controlling Collisions for Scaling Atom-Array Assembly, Phys. Rev. X 9, 011057 (2019).

4. T.-W. Hsu, W. Zhu, T. Thiele, **M. O. Brown**, S. B. Papp, A. Agrawal, and C. A. Regal, Single Atom Trapping in a Metasurface Lens Optical Tweezer, ArXiv:2110.11559 [Physics, Physics:Quant-Ph] (2021).

5. **M. O. Brown**, S. R. Muleady, W. J. Dworschack, R. J. Lewis-Swan, A. M. Rey, O. Romero-Isart, and C. A. Regal, Time-of-Flight Quantum Tomography of Single Atom Motion, arXiv:2203.03053 [quant-ph] (2022).

6. **M. O. Brown**, et al., Molecular Potentials for Ultra-Long Range ^{87}Rb Dimers, (unpublished).

Chapter 2

Apparatus for Ground-State Optical Tweezer Experiments

2.1 Overview

In this section I introduce the physical apparatus used to conduct the experiments discussed elsewhere in this thesis. The experimental apparatus originated through the hard work of Adam Kaufman and Brian Lester among others, and as such, many details about the apparatus at earlier times are best found in Adam's thesis [64] and Brian's thesis [65]. However, here I will provide a brief overview for completeness, while more discussion of new and modified systems will begin in Sec. 2.2.

An experiment for cooling and trapping single atoms must take place in ultra-high vacuum, or else collisions between the atoms of interest and other atoms and molecules will contribute to heating and loss from traps. The vacuum apparatus we use is very simple, consisting of an ion pump, evaporative rubidium getters, and a single glass cell in the shape of an octagonal prism where the cooling and trapping occurs. The vacuum system we use is itself unchanged from the vacuum system developed by Adam Kaufman and described in his thesis [64]. We anticipate changing the vacuum system at some point in the future in order to introduce fresh ^{87}Rb getters, upgrade the glass cell to a version with flatter windows and more specialized optical coatings, and make use of a 2D+ magneto optical trap (MOT) cell we purchased from Cold Quanta. Many other species of atoms require more specialized vacuum apparatus such as Zeeman slowers, source ovens, or make use of multi-chamber systems in other ways. Thanks to the simple electronic structure and favorable physical parameters of ^{87}Rbsuch as having a large mass, such complications are not necessary here (Table 2.1).

Parameter	Value	Units	Source
Mass	$1.44316060(11) \times 10^{-25}$	kg	[66]
Relative Natural Abundance	27.83(2)	%	[66]
$F = 2 \leftrightarrow F = 2$ Scattering lengths	95.44	a_0	[67]
$F = 1 \leftrightarrow F = 1$ Scattering Length	100.4	a_0	[67]
$F = 1 \leftrightarrow F = 2$ Scattering Length	98.006	a_0	[67]
D_2 **Transition** ($5S_{1/2} \rightarrow 5P_{3/2}$)			
Decay Rate	$38.11(6) \times 10^6$	s^{-1}	[66]
Natural Linewidth (Γ)	$2\pi \times 6.065(9)$	MHz	[66]
Recoil Velocity	5.8845	mm/s	[66]
Recoil Temperature	361.96	nK	[66]
Doppler Temperature	146	µK	[66]
I_{sat} D_2 Resonant Isotropic Polarization $2 \rightarrow 3'$	3.576(4)	mw/cm^2	[66]
I_{sat} D_2 Resonant Cycling $\vert 2,2\rangle \rightarrow \vert 3,3\rangle$	1.669(2)	mw/cm^2	[66]
I_{sat} D_2 Far-Detuned	2.503(3)	mw/cm^2	[66]
D_1 **Transition** ($5S_{1/2} \rightarrow 5P_{1/2}$)			
Decay Rate	$36.10(5) \times 10^6$	s^{-1}	[66]
Natural Linewidth (Γ)	$2\pi \times 5.746(8)$	MHz	[66]
Recoil Velocity	5.7754	mm/s	[66]
Recoil Temperature	348.66	nK	[66]
Doppler Temperature	138	µK	[66]
I_{sat} D_1 Far-Detuned	4.484(5)	mw/cm^2	[66]

Table 2.1: **Table of Selected ^{87}Rb Constants.** A table displaying a variety of ^{87}Rb constants that I have found useful over the years. Also see Fig. 2.3.

In order to cool and trap atoms in this cell, we must make use of a plethora of lasers and laser systems. These systems have changed non-trivially and are therefore documented in detail in Sec. 2.2.1. The physical arrangement of the laser systems around the vacuum chamber is viewable in Fig. 2.1 and Fig. 2.2.

At the heart of the electrical control system for our experiment is our digital output (DO) system, which outputs a series of precisely timed digital pulses. These pulses trigger other devices, such as cameras and radio frequency (RF) waveform generators at the appropriate time, they open and close electrical gates such as those for magnetic field coils, and they open and close RF switches which has the effect turning on or off laser beams. This system originated as a DIO-64 event analyzer/control module (long since discontinued) system from Viewpoint Systems, and more

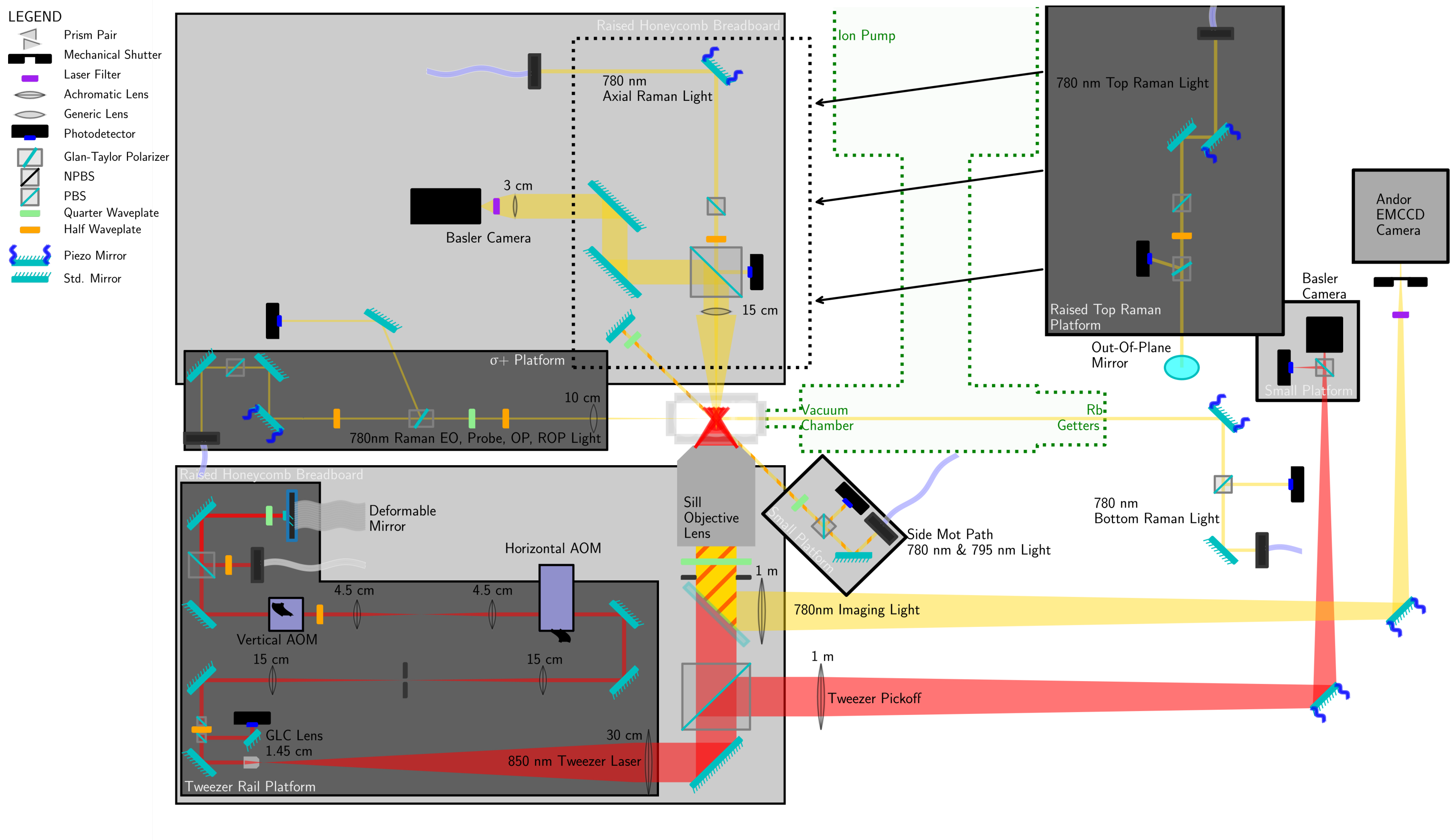

Figure 2.1: **The Main Experiment Apparatus Layout.** This figure is not precisely to scale but care has been taken to make it a relatively accurate representation of the experiment layout. 850 nm light is shown as red light, 795 nm light is orange, and 780 nm light is yellow. Where two beams overlap, the two colors are represented with colored hatches in the beam. Platforms are indicated by shaded boxes, where darker shades indicate higher elevations. Most common optics are identified in the legend in the top left corner. The tweezers diverge after the objective and are not blocked, but this divergence and other similar unused beams are not shown for clarity. The vacuum chamber is roughly outlined in green. The bottom Raman path goes underneath the vacuum chamber, as is more evident by looking at Fig. 2.2 which is a companion to this figure.

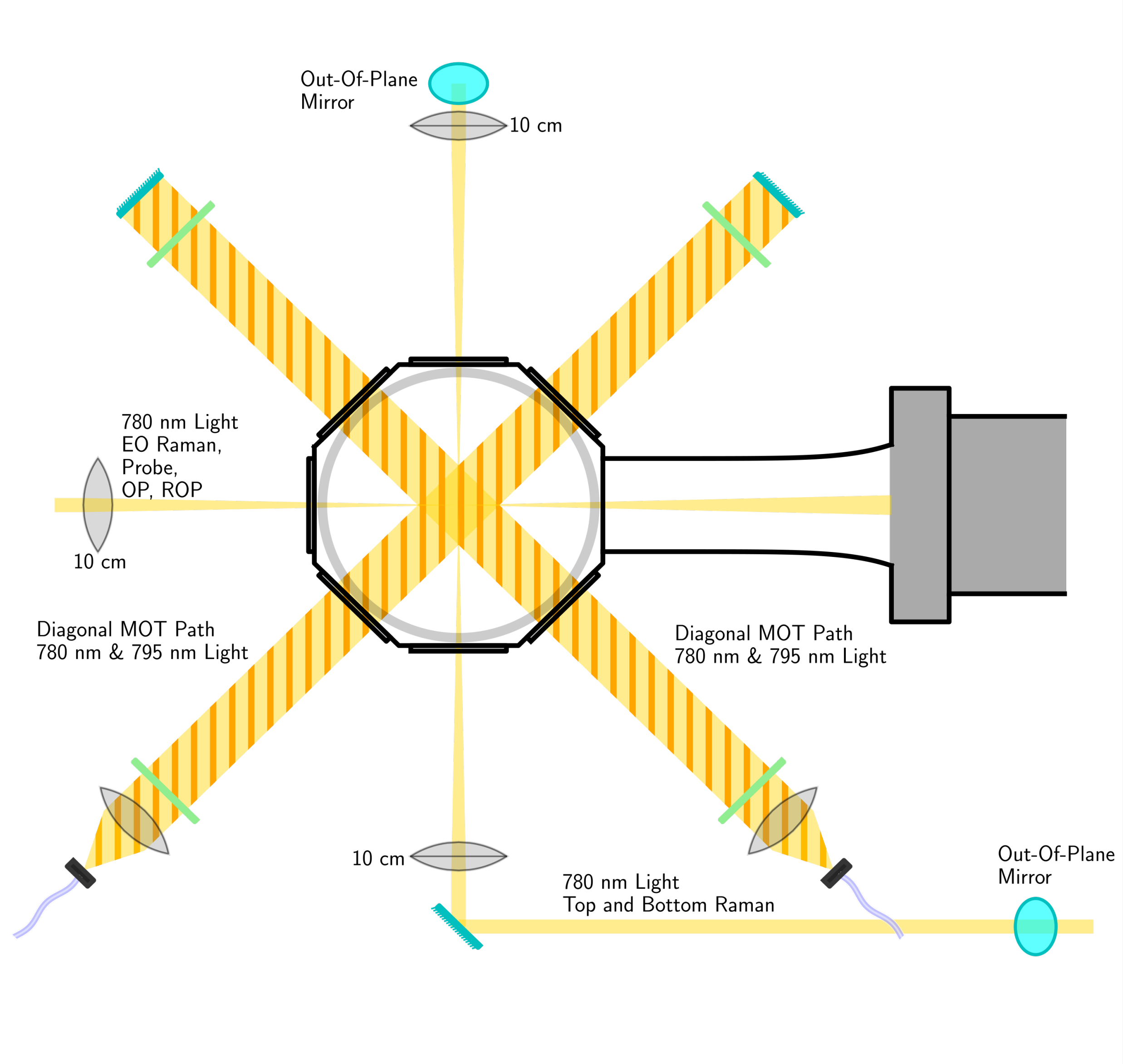

Figure 2.2: **The Main Experiment Apparatus Layout, Viewed from the Side.** This figure is viewed from the side of the objective lens, rather than the side of the axial beam path. It is more evident from this angle that the bottom Raman beam goes under the vacuum chamber. See legend in Fig. 2.1.

recently has been implemented through a custom FPGA system designed to emulate the DIO-64 system.

Also crucial are analog input and output systems. Analog outputs (voltage range -10 V to +10 V) are mostly used for controlling relative laser powers or magnetic field currents. As other systems in the experiment are increasingly digital, we find fewer uses for analog outputs now than we used to. Analog inputs are primarily used for experiment diagnostics and automatic laser power calibrations. The analog inputs and outputs we use are National Instruments cards PCI-6221 and PXI-6722 respectively.

Laser cooling sequences and spin state preparation typically require careful control over magnetic fields in the vicinity of the atoms. To control the magnetic fields, we use 8 electric coils, 2 of which are configured in an anti-Helmholtz configuration for the creation of a MOT, and 6 of which are in a Helmholtz configuration for zeroing background magnetic fields or setting a constant magnetic field. As we only need to drive currents less than 10 amps, these coils are simple copper coils and are driven by custom but simple current servo systems based off of Hall detectors.

We use a number of Keysight (formerly Agilent) arbitrary waveform generators, mostly models 33522A/B for a number of purposes:

- Time-varying intensity servo set points for our tweezer servo system
- Square waves with specific relative phases and duty cycles for flashing imaging techniques
- Calibrated pulses for pulsed Raman sideband cooling techniques.

We currently use voltage-controlled oscillators (VCOs) for a number of purposes, including determining lock offsets and driving acousto-optical deflectors and modulators (AODs and AOMs). However, we are slowly gravitating toward the use of a home-built direct digital synthesis (DDS) RF generator based on Analog Devices AD9959 evaluation boards. These have numerous advantages in that they provide cleaner, programmable outputs, have wider frequency output ranges, and are more stable than VCOs, which are useful features for most of our applications. Our system for driving the optical tweezer deflection AODs is more non-trivial and discussed in Sec. 2.4.2.

Lastly, we require a flexible microwave source for driving electro-optical modulators and a sawed-off microwave horn. In particular, even for a single experiment we generally need to be able to change the microwave frequency during different experiment stages, for example from the settings optimized for Λ-enhanced grey molasses (ΛGM) loading to those optimized for in-trap

ΛGM cooling. This is typically accomplished using a “list”-mode, where the generator switches from one list entry (containing a frequency and power to output) to another on being triggered by the DO system.

In the past, we have used a Rhode-Schwarz microwave generator (RSG) to generate the signals we need for these devices. Recently, especially after a power supply failure in the RSG, we have gravitated toward using devices from Windfreak Technologies. The devices we use are the “SynthHD PRO (10MHz – 24 GHz) Dual Channel Microwave Generator”, and the “SynthHD (54 MHz – 13.6 GHz) Dual Channel Microwave Generator”.

2.2 An Updated Physical Apparatus

In the time since Brian’s departure, there have been a number of changes to our physical setup with important optics and electronics were introduced among other things which I will discuss in detail.

2.2.1 Laser Systems

^{87}Rb is the only atom species we use in the lab. We have numerous laser systems that we use to address the various ^{87}Rb transitions (Fig. 2.3). At the start of my PhD, most of the lasers in the lab were external cavity diode lasers (ECDLs), typically constructed with anti-reflection coated diodes from Eagleyard Photonics and a laser grating in a Littrow configuration. These lasers were not initially very stable and would come unlocked several times a day. I eventually tracked this down to be a fixable electronics issue in the servo systems. Afterwards, these lasers were very functional, however they were still relatively sensitive to vibrations, temperature, and humidity drifts due to the macroscopic cavity that exists outside of the laser diode. As such, it was still difficult to keep them locked for more than a day or so. Meanwhile, the company Photodigm began refining their distributed Bragg reflector (DBR) lasers to have a low enough linewidth to be useable for our ^{87}Rb systems. As a result, we slowly started switching from ECDLs to DBR lasers until at this point we only use DBRs.

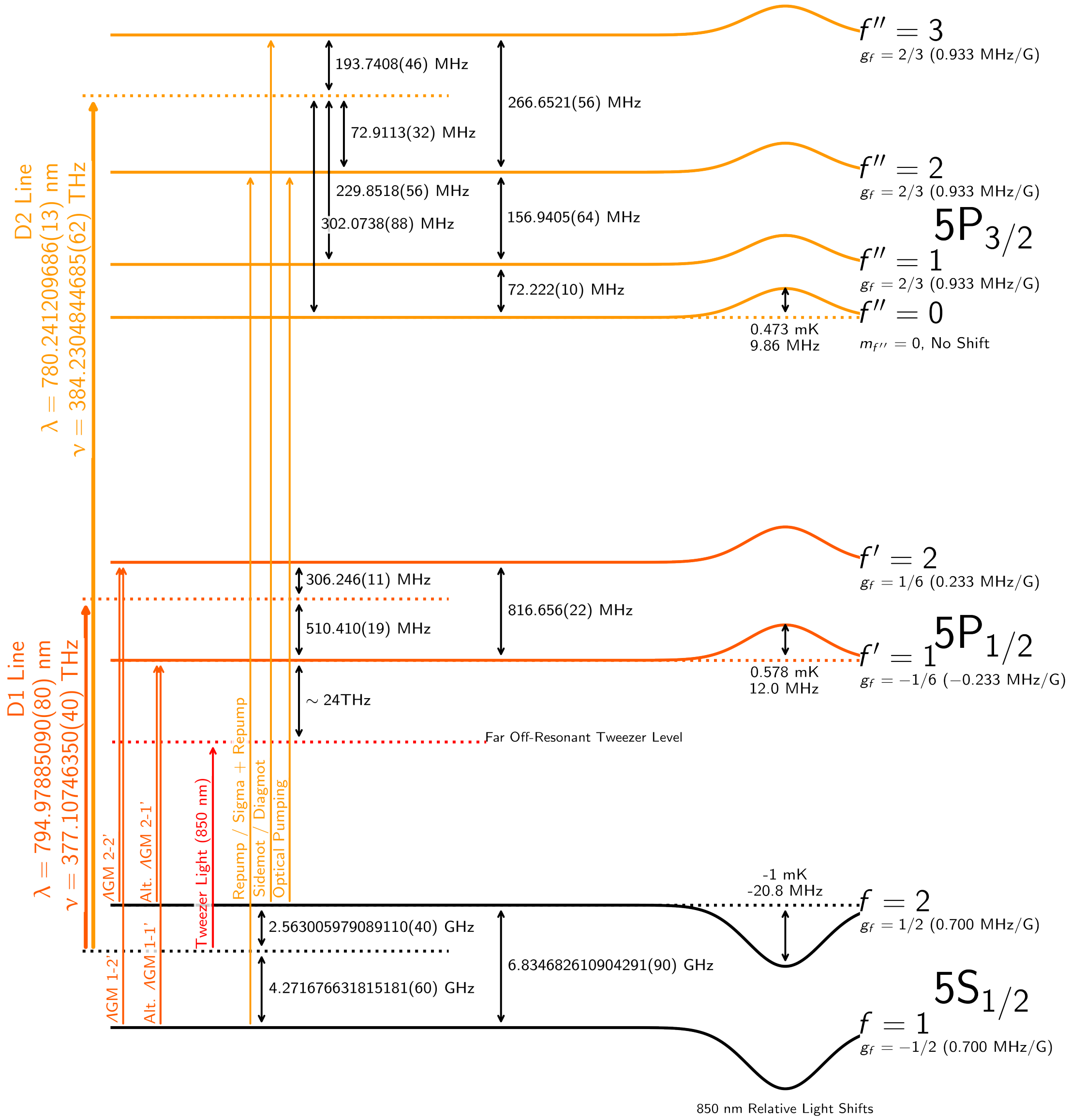

Figure 2.3: **A ^{87}Rb Level Diagram.** Not to scale. Values are primarily from [66]. The dips on the right-hand-side of the levels are reflective of the relative light shifts of the 850 nm optical tweezer traps. Shown on the left hand side are lines indicating the major laser systems we use in our experiment, including the tweezer lasers, 780 nm lasers, and both configurations of 795 nm laser systems that have been used.

The DBR lasers have only a few downsides, including that they are relatively expensive (~$5k per module), and some models, in particular our initial high power 795 nm models, broke faster than expected ($\sim$ 6 months) under normal use. In the past several years, however, we have not had such troubles. None of our 780 nm modules have died, including one that has been in use for $\sim$ 10 years.

One of our strategies, both for dealing with these occasional issues and for characterizing our lasers, is to separate the "head" of the laser system (i.e. the laser module itself followed by any required beam shaping and optical isolation) from the rest of the laser system by an optical fiber connection. This approach has several advantages: if a laser dies, it is easy to immediately replace the laser head with a portable "platform laser" which can substitute for the table-mounted laser until a replacement arrives and is installed without needing to realign the rest of the laser system. As well, the early fiber launcher provides an easy way to test the laser's wavelength with a wavemeter, and the fiber spatially filters the laser for the rest of the system's alignment. This split setup is visible in the 795 laser schematic (Fig. 2.4).

2.2.1.1 780 nm Laser System

We use four main 780 nm lasers in our experiment. One is the Raman laser, which is $\sim$50 GHz red-detuned and typically unlocked. This laser is split into the four Raman beams that go to the experiment.

I will call the other lasers the "D_2 master" laser, the "D_2 $f = 2$" laser, and the "D_2 $f = 1$" laser, where f is the total angular momentum including electronic orbital, electronic spin, and nuclear spin angular momentum. Historically, the D_2 $f = 2$ laser has also been called the "MOT" laser despite it being used for more than just MOT light, and the D_2 $f = 1$ laser has been called the "repump" laser. The term "master" here is for historical continuity purposes. If renaming it today I would call it the "reference" laser, since the laser is not the "master" in either the "mastery", "master/slave" or "master/replica" senses. The D_2 master laser is static throughout all experiments and is locked to the ^{87}Rb D_2 $f = 2 \to f'' = 3$ line (Fig. 2.3) (the f' symbol will be reserved for the ^{87}Rb D_1 line). We use a standard saturation spectroscopy setup in order to create the relevant line structure, and use a frequency modulation spectroscopy setup to convert these transition lines into usable error signals [68, 69, 70]. This is as opposed to modulation transfer spectroscopy setups which are also common in the field [71]. The frequencies of the other two lasers are changed dynamically throughout a single experiment repetition, and they are locked with reference to the master laser via an offset lock system. As the linewidth of ^{87}Rb transitions is relatively large and the level structure forgiving, the locking electronics we use are custom but simple proportional-integration (PI) systems.

The D_2 $f = 1$ laser is split into two separate beams, referred to as the "repump" beam and the "$\sigma+$ repump" beam, both tuned near the $f = 1 \rightarrow f'' = 2$ transition. The repump beam serves to repump the atoms during the standard MOT, red-detuned polarization gradient cooling (RPGC), and imaging phases of a typical experiment. The $\sigma+$ repump is specifically used during any optical pumping procedures to minimize the number of photons needed to optically pump into the $|f, m_f\rangle = |2, 2\rangle$ state. This is especially important for Raman sideband cooling procedures.

The D_2 $f = 2$ laser is split into many more beams. As such, we need slightly more power from this laser, so the DBR laser seeds a 1 W 780 nm tapered amplifier from Eagleyard. The beam then splits into what are typically referred to as the "diag. MOT", "side MOT", "$\sigma+$ optical pumping (OP)", and "probe" beams. Most of these are tuned to the D_2 $f = 2 \rightarrow f'' = 3$ transition, with the exception of the optical pumping beam, which is given a slight shift via AODs to be resonant with the D_2 $f = 2 \rightarrow f'' = 2$ transition.

2.2.1.2 795 nm Laser System

ΛGM Paper Configuration Originally, the 795 nm laser system used for our Λ-enhanced gray molasses (ΛGM) scheme (discussed in Chapter 4) consisted of a single laser. Early in the beam handling, the laser was split along two paths, with one path going into an AOD and then a standard saturation spectroscopy setup which locked the laser frequency on this path to the ^{87}Rb D_1 $f = 2 \rightarrow f' = 2$ transition. Then, when changing the **frequency** that this AOD operated at, the lock would compensate and shift the laser current to maintain the lock, thus shifting the **other** path's frequency relative to that of the locked path. The other path would go through a fiber-based electro-optical modulator (EOM) and then a tapered amplifier. This setup worked well enough for that paper, but pretty significantly limited the effective frequency range that we could scan over during that experiment. It also wasn't that stable.

Modern Configuration Before too long therefore, we upgraded this system to have two separate lasers, which I will refer to as the "D_1 master laser" and the "D_1 $f = 2$" laser. (Note, the D_1 $f = 2$ laser has had a number of informal names in the lab over the years, including the "worker" laser and the "main D_1" laser, before I settled on this more operational name).

The D_1 master laser in this new configuration is locked (with no AOD this time) directly to the ^{85}Rb $f = 2 \to f' = 1$ transition (note the different species!) (Fig. 2.3). The lock is a relatively standard lock, using saturation spectroscopy to get the desired transition line signal, and then again frequency modulation spectroscopy to generate an error signal. This configuration is very similar to that of the 780 nm master lock.

The D_1 $f = 2$ laser is then offset locked by a variable detuning red-shifted from the master laser (Fig. 2.3). Being red-shifted by a small amount from the ^{85}Rb D_1 $f = 2 \to f' = 1$ transition puts you blue-shifted from the ^{87}Rb D_1 $f = 2 \to f' = 2$ transition, as is desired for the Λ-enhanced grey molasses (ΛGM) scheme. Our offset lock configuration is much more widely tunable, with a tuning range of approximately 1 GHz, far superior to our previous tuning range of ~ 40 MHz.

The D_1 $f = 2$ laser then enters a fiber EOM which is driven with an approximately 6.834 GHz signal in order to give a tunable sideband on the D_1 $f = 2$ light that are close to the ^{87}Rb D_1 $f = 1 \to f' = 2$ transition which can act as coherent repumping light, as is desired for ΛGM (Fig. 2.3). The fiber-EOM is not particularly efficient or stable, and so the resulting light is passed through a 3 W Tapered Amplifier (TA) in order to get enough light for conducting ΛGM. We don't need anywhere near 3 W, this was just the only tapered amplifier available at the time.

This arrangement works well, although it has a couple downsides. The EOM coupling is not particularly stable, which mostly only makes it a nuisance to maintaining laser powers. Nowadays these powers are part of an automatic calibration system, so there are no problems as long as the overall power doesn't drop too low. One might also generally worry that the extra sidebands of the EOM could complicate the effect of the ΛGM, although we have seen no direct symptoms of this. An alternative would be adding a separate, 3rd D_1 $f = 1$ laser for repumping, mimicking our 780 nm setup, and upgrading our offset locking system to be capable of a robust phase lock between these two lasers. Quite possibly the resulting light would still need to seed a TA in order to get sufficient power, but this different configuration might help with some of the other issues.

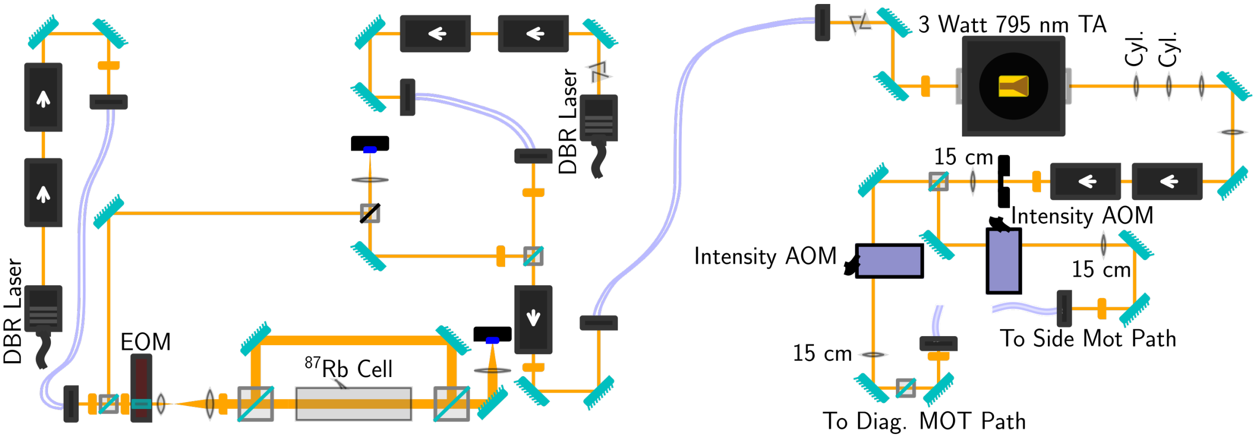

Figure 2.4: **The D_1 Laser Layout.** Visible are the D_1 master laser, D_1 $f = 2$ laser, saturation spectroscopy and offset lock beating setup on the left-hand side. The tapered amplifier and diagonal / side path splitting setup is on the right-hand side. See legend in Fig. 2.1.

2.2.1.3 850 nm Laser System (Tweezers)

The tweezer light source has changed many times over the years, but most recently comes from a temporally incoherent light source. The incoherent light source that we use is a super-luminescent LED (SLED) module from a company called Superlum, with part number BLMS-mini-381-HP3-PM-PD-OI. The module outputs about 25 mW of light with a bandwidth of 15 nm, which we immediately filter down to a full-width half-maximum of 3.2 nm using a band pass filter from Semrock, part number LL01-852-12.5. The resulting light has a fairly short coherence length of ∼80 µm. As a result of this short coherence length, reflections and back reflections of the tweezer light in our tweezer rail system should generally not coherently interfere with the main tweezer beams. This type of interference was generally a concern for us, as we are very sensitive to temporal fluctuations of our tweezer potentials, slow or fast. When we implemented this, we saw some improvement in the relative bias fluctuations of our tweezers, but we did not see any serious improvement of the overall performance of the system as measured by the atom's response to the potentials, in the form of the measured trap shape or tunneling properties. However, we still use this source, mostly as there's little reason to use anything else and this might still help on the margins.

In the past, we have used a number of TA setups, including a single-pass 1 W TA, a double-pass 2 W TA, and currently a 1 W TA followed by a 3 W TA (Fig. 2.5). The double-pass 2 W TA setup worked somewhat well but did not seem very stable and was tricky to align properly. Therefore, when the TA eventually died, we decided to change our setup to the two-TA system we use now.

After filtering down the SLED output, we only have a couple mW of incoherent light, which is not enough to properly seed a TA, as TAs typically require ∼30-50 mW to get their full power output. Therefore, we use the incoherent light to first seed a 1 W TA, which is under seeded but can still easily output 100's of mW of power. The excess light has occasionally been used for additional beams or tests in our system, but usually we just use this to have comfortably enough power to properly seed the 3 W TA with the required amount of power.

In general, we find that these TA modules die rather quickly (with a lifetime of 1-2 years) if driven at their full power consistently, while they last much longer if driven at lower powers. Therefore, while we have in the past operated our 3 W TA at full power (in particular to get enough power to load 100 traps during the ΛGM paper), recently we drive it at about half of it's maximum output power and work more conservatively with smaller arrays of traps, which are all that is necessary for our current work regardless.

2.2.1.4 Ti:Sapphire Laser

We own a Ti:Sapphire laser which has been used for a number of purposes over the course of my PhD. It is a very flexible laser, capable of outputting on the order of 1 W of optical power at all wavelengths that we use in the lab. It is seeded by a 10 W green pump laser from Lighthouse

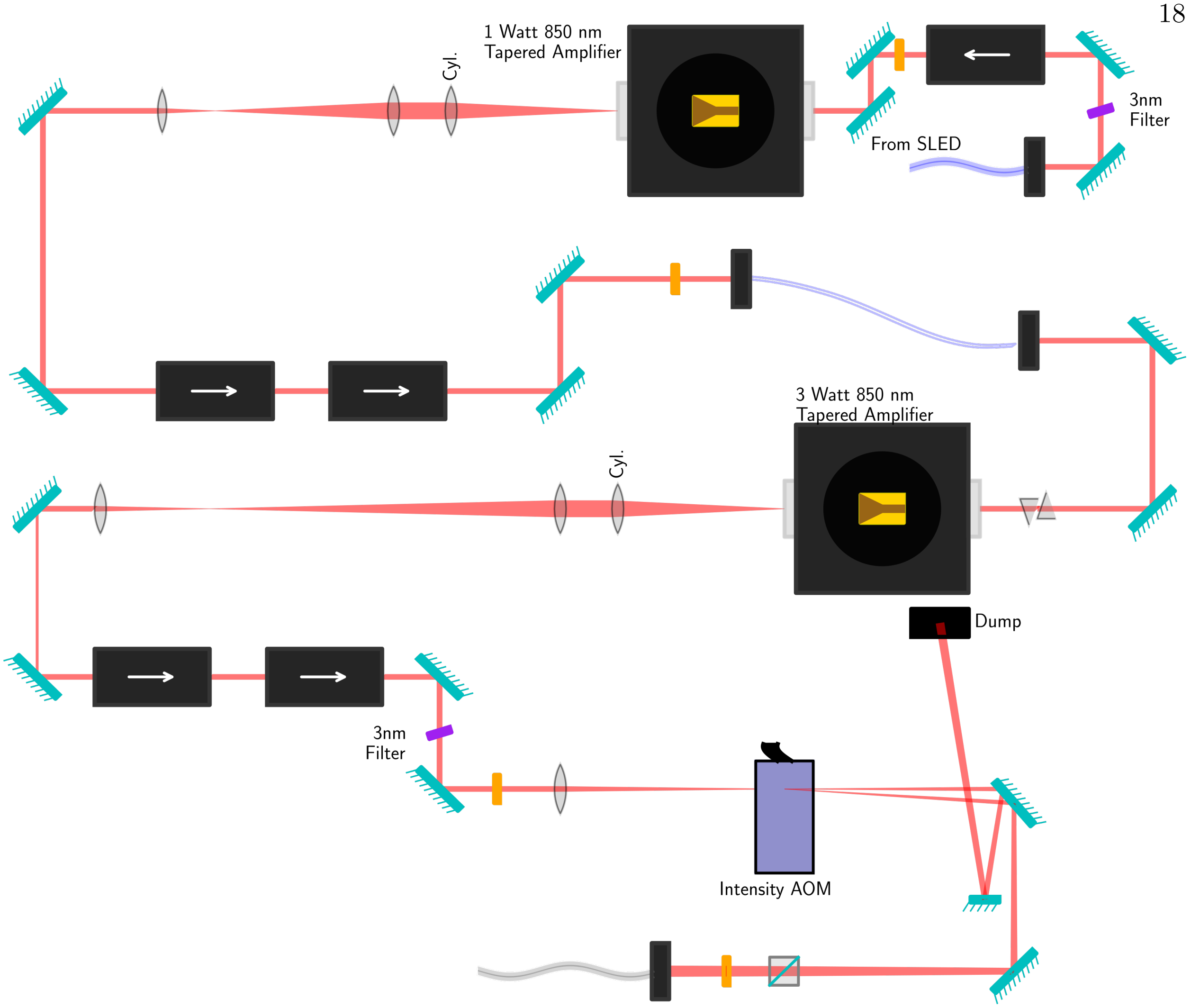

Figure 2.5: **The 850 nm tweezer TA laser layout.** Visible is the 1 W TA setup above, which seeds the 3 W TA setup below. Beam shaping after the TA chips is tricky. Sometimes an extra pickoff would be added after the two isolators in the 1 W section in order to get some extra 850 nm light. The multiple filters may be unnecessary but are attractive in reducing any long tail of amplified spontaneous emission (ASE) that the TA chips may output. See legend in Fig. 2.1.

Photonics, a “Sprout” model. Higher power models are available. As such, it has at various times been used as our Raman laser, tweezer laser, and even for some 795 nm testing purposes. Soon, we plan on using it to create an optical lattice to compliment the tweezer potentials.

2.2.2 Mechanical Shutters

In an experiment such as this it is often required to completely extinguish light entering the experiment apparatus from a given laser path. This is especially true for lasers that are resonant with an atomic transition and which if left unattended, would result in slow heating of the atoms after they have been ground-state cooled. It is also crucial to block the input to our EMCCD camera at various times, especially in the tomography experiment discussed in chapter 6. At the height of data taking for this experiment, because of the large number of images necessary, we were destroying the imaging shutter every couple weeks.

In general, we use acousto-optical deflectors with varying RF input powers to variably attenuate laser beams for dynamic control during an experiment. Even after extinguishing the RF power completely, however, one is still limited by scattering off of the AOD crystal which can scatter into an optical fiber at small but significant rates. It is possible, and possibly optimal, to use chained acoustic optical modulators in order to attenuate by a significant enough amount for our purposes. However this is rather expensive and creates longer and less stable laser paths. It is worth noting as well that double-pass AOD configurations do not generally solve this scattering effect, as one may be limited by backwards-scattering from the first pass through the AOD unless the crystal is large enough to support two physically separated deflection regions for each pass.

We therefore often turn to mechanical shutters which physically obstruct the laser path in order to completely extinguish laser beams when necessary. Originally we primarily used expensive shutters from the company Uniblitz, typically model LS6 6 mm. These shutters are fast and have convenient mounting configurations, especially for connecting to our EMCCD where we need to be able to block the entire opening to the camera sensor. However they are at this moment still relatively expensive. We also experimented with Thorlabs shutters (part number SHB025T), however these have similar drawbacks to the Uniblitz shutters.

Other experiments deal with similar challenges. However, the relatively fast repetition rate of our experiments compared to other cold-neutral-atom experiments, combined with the relatively slow rate of the actual science experiment compared to more strongly interacting systems like ions, create a perfect storm. We really need shutters to get sufficient extinction during the longer science stages of the experiment, but we actuate them frequently enough that they break on relatively short time-scales.

As a result, over the course of my PhD, we have used a number of different designs for custom mechanical shutters. We tried designs based on speaker actuators as outlined by [72], and by rotating flags driven by simple motors as outlined by [73]. Both of these designs are cheaper than commercial options, but in our experiment both can also break frequently and perform irregularly in devious ways. A shutter that occasionally sticks or bounces open is worse than no shutter at all. We had relatively more success with the rotary design [73], and a lucky few shutters have lasted a number of years and are still in use. However, our continued struggles lead us to consider other alternatives.

Our most recent innovation is the use of free-space micro-electromechanical system (MEMS) technology from the company Agiltron, specifically their 700 µm FSVOA devices. As the name suggests these devices can be used as variable optical attenuators, but if carefully configured, these devices can be completely attenuating, and we believe that their reliance on MEMS-technology, as well demonstrated by the telecom industry, will lead to significantly longer lifetimes than other designs which involve mechanical collisions as the shutters close. Indeed, none of the 4 devices we originally made two years ago have failed or had any issues, a much better track record than our other custom solutions. The small aperture size means one must focus through the device. We are currently working on implementing one of these shutters for use in our imaging system as well. This was an original idea and is unpublished. Ideally one might use fiber-based MEMS shutters, but unfortunately we struggled to find fiber-based MEMS shutters which were polarization-maintaining and single-mode at the wavelengths of interest to us (780 nm - 850 nm). Perhaps in the future such devices will be available.

2.2.3 Sill Objective Lens

At the start of my PhD, the lab was using a high numerical aperture (NA) objective lens from the company ASE Optics. The lens performed at around an effective NA of ~ 0.5, and while this was good enough for a wide variety of experiments, it is generally desirable to have as tight and well-behaved optical tweezers as possible. This is especially true for experiments with side-band cooling, where our ground-state fidelity is limited primarily by having relatively low axial trap frequencies, and for experiments with tunneling, which are thought to be sensitive to aberrations in the trap in a number of ways. As such, before my thesis started, the lab purchased two high-NA objectives from the company Sill Optics. The initial motivation for purchasing two lenses was for their potential for double-objective setups with one objective on either side of the vacuum chamber, although we have never attempted this in practice.

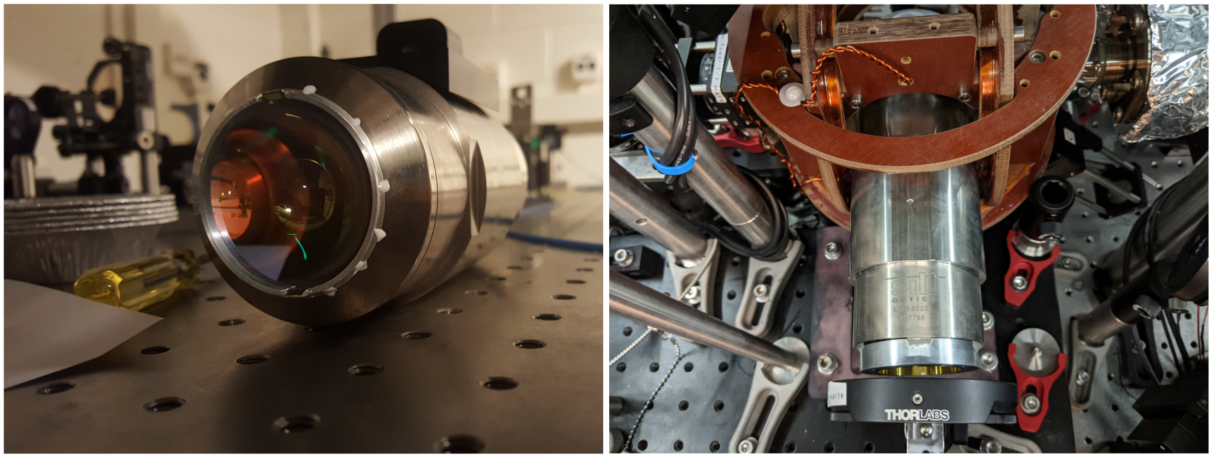

Figure 2.6: **Photos of the Sill Objective Lens.** **(Left)** The Sill lens viewed from the front. Visible is a ring assembly which has been epoxied to the front of the lens using Hysol, which holds two mirrors in place. The mirrors are angled to make it possible to create an axial lattice with a single beam, although this has never been utilized. **(Right)** The sill lens viewed in situ. Visible on the bottom side of the image is the phase plate, which has been attached to the objective via J. B. Weld epoxy.

2.2.3.1 Sill Lens Objective Characterization

It was found after the objective lenses arrived that the two objectives were defective and could not meet their quoted performance. As such, near the beginning of my PhD, we embarked on a long sequence of tests and modifications in order to try to improve the performance of the lenses. This report is a collection of work done by various students in the lab, including myself, Junling Long, and Ludovic Brossard.

The first task was to measure the aberrations of the objective lens. This was done using what was effectively a Michelson interferometer setup. A large input beam was split along two paths, with one path hitting a flat mirror, and the other traveling through the objective and hitting a reference sphere held inside an unevacuated vacuum chamber cell. The reference sphere was held inside the unevacuated vacuum chamber cell primarily in order to best mimic the effect of the cell window on the performance of the objective. The reference sphere was a small silicon-nitride ball bearing.

The primary results of the measurement are listed in Table 2.2.3.1. As can be seen here, the main measured aberration is coma, which has an egregious magnitude above twice the wavelength in phase, a clear explanation of the problems we encountered early on with the lens. The RMS wavefront error of the uncorrected lens was 0.92 λ at 850 nm.

After this measurement, we commissioned a phase plate, a very slightly shaped piece of glass, that was designed in order to correct these aberrations. The piece was ordered from Light Machinery. Although originally spec'd to correct the Sill lens to a very high accuracy, the company also had trouble machining the specific profile we ordered, and the result was imperfect aberration correction. The measured aberrations of the corrected Sill lens are also denoted in table 2.2.3.1. The results, while not as good as hoped, reduced the remaining aberrations to approximately the level which we expect from out "rail" system that we use to generate the tweezer array: an RMS error of approximately $\lambda/5$. We realized that for further improvement, we would have to try something more active.

Name Abberation Coordinates	H. Astig. (2,-2)	V. Astig. (2,2)	H. Coma (3,-1)	V. Coma (3,1)	Spherical (4,0)	RMS
Unmodified	-0.08	0.00	1.44	2.05	0.08	0.92
With Phase Plate	0.10	0.16	0.02	-0.18	-0.01	0.147

Table 2.2: **Sill Objective Lens Aberration Coefficients.** Listed are the coefficients before and after various corrections. Numbers are in units of λ, the wavelength, at 850 nm. Even after adding the phase plate, there were non-trivial aberrations remaining, which we eventually corrected with a deformable mirror.

2.2.3.2 Deformable Mirror

As a result of the limitations of the phase-plate, we purchased a deformable mirror from Boston Micromachines for further objective correction. The deformable mirror is an active optic which uses electrostatic actuators to continuously deform a continuous mirror surface. Options are available with segmented surfaces for less interactuator coupling but high-frequency artifacts from the actuator edges. We purchased a multi-C model, which features 137 actuators capable of 1.5 µm stroke in an approximately circular configuration.

The deformable mirror model has numerous advantages over other adaptive optics. Unlike digital mirror devices commonly used in quantum gas microscope experiments, the mirror is nearly perfectly efficient [74]. Unlike liquid-crystal based spatial light modulators, the device is driven with a static voltage, reducing noise concerns, and it is fast, featuring up to 100 kHz update speeds [75]. It is important to realize, however, that the deformable mirror is in this case primarily to be used for static, or very slowly (over days) changing aberrations, as the aberration calibration process itself is slow.

The deformable mirror is placed before either tweezer AOD in our rail system, so that the same aberration configuration is applied to all tweezers uniformly. The configuration is visible in schematic form in Fig. 2.1 and is visible in Fig. 2.7. The downside of this configuration is that the beam must travel through a long optical path from the Deformable Mirror (DM) before creating the tweezers, and because of limitations imposed by the pre-existing rail setup, the DM is not in a precise 4-f configuration with the tweezers. Therefore, applying coma for example on the DM will not result in exactly coma being applied to the tweezers. A future configuration might place the DM in a 4-f configuration with the tweezers, with the DM being placed in-between the AODs and the large tweezer expansion telescope. This might make the operations of the DM more predictable and result in better optimizations.

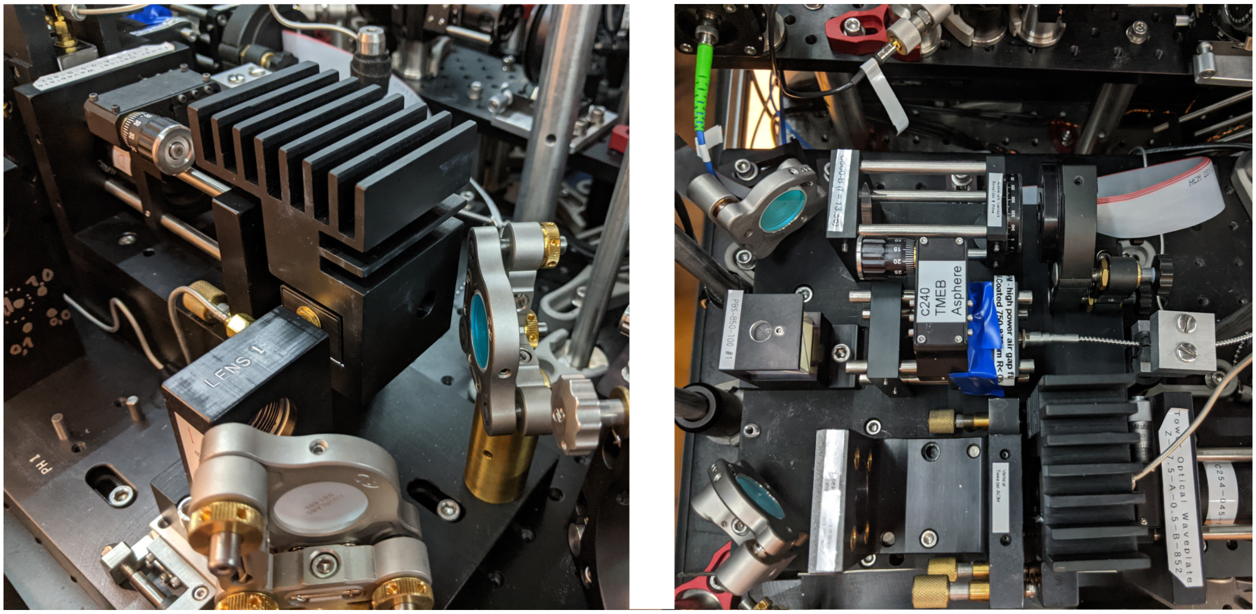

Figure 2.7: **Photos of the Tweezer Rail System.** **(Left)** The horizontal Intraaction AOD, nestled within a rather bulky custom heat sink to help maintain low thermal fluctuations in the AOD. **(Right)** The deformable mirror configuration right out of the launcher into the rail setup. The deformable mirror is visible near the top with a long ribbon cable coming out of it.

Our original calibration of our deformable mirror was slow and churning, as we had to manually change the deformable mirror pattern between each measurement of the trap frequency or depth, which we were attempting to optimize. In the end, we were able to improve the performance of the Sill lens creating a single tweezer potential, achieving a single tweezer NA of approximately 0.64, where the Sill lens with the phase plate but with no DM corrections performed with an NA of approximately 0.55.

Unfortunately, however, we ran into two major problems with this plan. The most important of which is that while a single tweezer experienced this nice optimized NA, when we tested the same DM configuration while producing many tweezers, the result was much poorer, and we did not see significant improvement from the DM. It may be possible to specifically optimize the performance of an array of traps using these mechanisms, but we could no longer expect that there would be one good configuration for all of our tweezer experiments. The most likely culprit for this behavior is that the measured imaging point spread function (Fig. 6.8), suggests that the tweezers may have a somewhat long tail, causing multiple tweezers to distort each other, even when they are different frequencies and far separated.

The second issue was that the DM's aberration correction calibration seemed to drift relatively quickly. As mentioned, the original calibration was somewhat manual and lengthy, which decreased our appetite for recalibrating the DM frequently. Recently, however, control over the deformable mirror has been incorporated into our experiment control system, Chimera, and so automated calibrations should be possible in the future which should greatly alleviate this issue.

Despite its limitations, the deformable mirror remains a powerful optic for use in our lab. Future uses of this may include better trap optimization, or optimization in a different configuration, or of optimization of different optics. As well, the DM can change it's profile very fast ($\sim$100 kHz), and so it is possible that we could use the DM to programmatically modulate the trap shape, which could be useful for creating non-classical superposition states. Similarly, the DM could be used to programmatically change the trap shape to, for example, make a nearly quartic potential rather than a nearly harmonic potential.

2.3 Computer Control Systems

2.3.1 Chimera Control

At the beginning of my PhD, the control system was split between two separate computers. One contained the camera control system, which was a stock program (Andor Solstis) for controlling the camera on its own computer, and the second was a computer running Windows XP that ran the old Visual Basic 6 code, which was responsible for programming the DO system and AO system. Many of the additional systems already discussed did not exist at the time. The setup was functional, and served previous generations well. However, there were a number of limitations that resulted from this setup:

- Communication between the different systems in this configuration is difficult. In particular, we anticipated eventually wanting to do rearrangement of atoms within tweezers. This requires communication between the camera system, which detects atoms, and the NIAWG system, which is capable of moving atoms.
- With three computers, there are more potential points of failure of the system. If any computer crashed or died, the experiment would stop.
- With three control computers, running the experiment is significantly more complicated. Even starting a run required a non-trivial sequence of commands which had to be done in the right order on the different computers.
- Visual Basic 6 is an old language no longer supported by modern operating systems. As such, the computer which ran this needed to run Windows XP, which at the time of my PhD was no longer supported by Microsoft, and so had to exist off of the JILA internet network in order to prevent infection by malware, which is rather inconvenient.
- Being restricted to Visual Basic 6 means that it is difficult to upgrade the control system with new modern graphical user interface (GUI) features.

I could go on, but this short list indicates the drawbacks of the previous configuration, and our motivation for an upgrade. At the start of my PhD, I started developing an independent NIAWG control system, and after that experience, I embarked on a complete overhaul of the rest of the system. As the system was initially mostly a combination of these three independent systems, I called it Chimera, a fitting reference to the mythological animal composed of many different animal parts. To understand the system now at the end of my PhD, it is useful to understand a bit of the history of development.

Initially, I was ignorant of modern GUI design principles and tools. The first implementation of the combined control program was implemented in the "raw" Win32 API in C++. As a result, most of the original implementation was basically C-code with minimal class structure or modern C++ design principles. At some point, I realized that there was a better API to use, called the "Microsoft foundation classes" (MFC) application programming interface (API). This was a step forward, but the MFC API was still Windows-exclusive and quite old, not making good use of modern C++ design or tools. Recently, furthered by having extra remote time during the pandemic, I performed a last upgrade, upgrading the system to using Qt 5 instead of MFC. Qt is a modern, well-maintained, well-documented, cross-platform API for creating GUIs in a variety of languages. It provides many powerful language features which make adding advanced GUI functionalities much easier than with MFC. For example, adding tool-tips to GUI elements is quite complicated in MFC and took me several months to implement properly, while in Qt it is as simple and natural as a one-line call to a built-in function.

In the end, Chimera is mostly similar to any other system that controls experimental apparatus in a lab, although I'd like to think it's a very well-designed and modern such system. Several illustrative screenshots are visible in Fig. 2.8. Chimera has several relatively unique features that are worth emphasizing:

- Real-time data analysis: it is possible to select specific locations on the incoming images, and monitor incoming data for programmable patterns such as loading, survival, tunneling, and more.
- Automated laser calibrations: Most of our laser powers are controlled by sending a variable DC voltage into a mixer, which variably attenuates an RF signal going to an AOD. Chimera can programmatically vary this voltage and measure the resulting laser powers through photodetectors which are connected to Chimera's analog input system. It can thus create a "voltage versus laser power" calibration curve, which can be re-run at regular intervals to accommodate for drifting laser powers.

- Automated experiment calibrations: There are many regular experiments that should be run in order to make sure all systems in the experiment are working correctly. These include MOT loading tests, MOT temperature tests, ΛGM cooling tests, single atom loading tests, single atom imaging tests, Raman frequency calibrations, and Raman sideband cooling tests among others. Chimera is capable of running a set of pre-designated calibrations at times when the experiment is not typically in use, such as the early morning, creating a record of the system's performance as well as keeping systems well tuned.

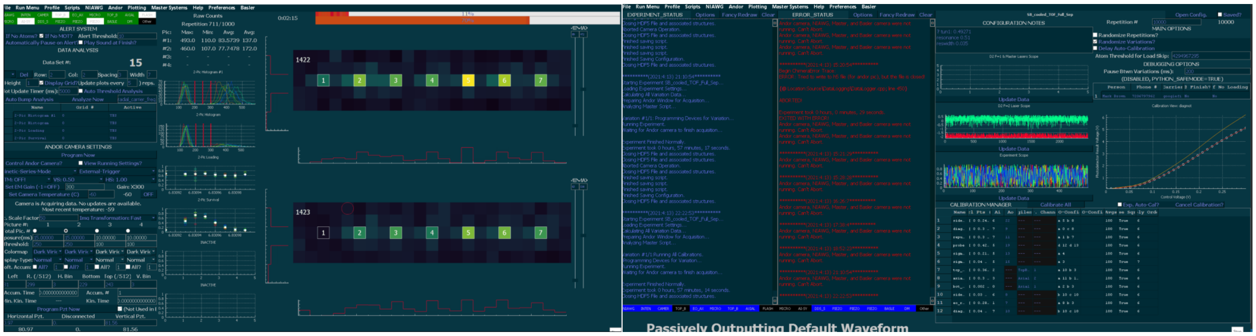

Figure 2.8: **Screenshots of Chimera Control.** **(Left)** The Andor camera window of Chimera. On the right side of this window, one can see the display showing real-time images collected from our camera, and on the left side of this window one can see real-time data analysis plots, among other camera settings. From top to bottom, the real-time analysis plots show the (1) first picture count histograms (different colors correspond to the different atom locations being analyzed), (2) second picture count histograms, (3) The loading fraction as a function of the parameter being scanned (in this case a Raman transition frequency), and (4) the survival as a function of the parameter being scanned. **(Right)** The "main" window of Chimera, which shows the main status logs and the automated laser calibration system. The listview on the bottom right shows settings for different laser calibrations, and the plot above and on the right shows the calibration curve in real-time as the data comes in. There are four other windows for controlling other various other systems in the experiment not shown.

These features reflect the fact that as experiments like this one get more complicated, there is an increased need for automation and streamlining of the data collection process. Chimera is a heavily multithreaded program, as most GUI programs are. While the plotted real-time analysis data above is not time-sensitive, Chimera is also capable of performing fast real-time calculations such as those necessary for doing real-time rearrangement of single atoms in the middle of an experiment. This will be discussed in depth in Sec. 3.6.

2.3.2 Climate Control

We monitor the temperature and humidity in the lab with a home-made temperature monitoring system. The sensors are sensitive to temperatures to about 0.1 degree C, and some thought has been put into attempting to purchase or make more sensitive sensors in the future.

In general, we find that the temperature is stable within the lab to approximately 1 degree C over the course of the day, with the temperature fluctuating less around the somewhat isolated and airflow-controlled main experiment table. The temperature tends to be more stable in the winter, and less stable in the summer, presumably due to differences in the way JILA's central air handling system handles the two cases. Midway through my PhD, we moved the thermostat sensor from being stationed near the door to the room, where there is presumably more noise and fluctuations coming from the hallway and door, to the middle of the lab. We found that this improved the stability to its current level.

2.4 Other Systems

2.4.1 Intraaction AODs

At the beginning of my PhD, we used Gooch and Housego acousto-optic devices in order to generate the tweezers. We use a number of AOMs and AODs in the experiment, mostly from Gooch and Housego, which at various times has labeled their products either as AOMs or AODs. While perfectly serviceable, these devices had a relatively low bandwidth for our tweezer deflection application, which limited the number of tweezers we could make simultaneously. So as we scaled up the capabilities of the platform, we desired more suitable deflectors.

We eventually purchased a pair of AODs from the company Intraaction which designs AODs with a phased-array RF-to-acoustic transducer design which allows deflections over a much wider frequency. Most AODs are driven roughly by carefully attaching a piezo-electric transducer to one side of the AOD crystal which converts the RF wave on the input to a mechanical wave in the crystal. The limiting factor of the bandwidth is that the deflection angle, and therefore the correct matching input angle, changes as a function of the drive frequency. Therefore while the transducer might be able to drive the crystal over a large bandwidth, the laser will only be deflected over a relatively narrow frequency range without realignment.

By using a phased-array transducer design, it is possible for the angle of the acoustic wave to change as a function of frequency in order to compensate this effect. This is the basic operational principle behind the Intraaction AODs, and why they outperform our previous system.

The model number of the AODs we purchased is ATD-1803DA2.850. The center frequency of the AODs is spec'd to be 180 MHz, with a quoted bandwidth of about 90 MHz and a corresponding deflection range of 36 milli-radians. The AODs have an active aperture of 3x4 mm. The laser beam inside the AOD has a $1/e^2$ waist of 0.8 mm. The combination of the active aperture size and the total RF bandwidth in principle limits how many resolved tweezers it would be possible to make, but we are limited by other factors in the experiment first. In practice, we also find that we can use the AODs over a broader bandwidth of approximately 120 MHz. We find the driving performance of the AODs to be slightly irregular, and find that we need between 2 W and 4 W of RF power in order to efficiently drive the AODs. This drive leads to some non-trivial heating of the AOD devices, and so in order to maintain thermal stability as much as possible, throughout the experiment sequence these AODs are driven with a constant total RF power, and the AODs are fitted with some aggressive heat sinks and fins (Fig. 2.7).

Especially when driving the AOD with many tones, intermodulation effects are significant. Compensation for these effects is discussed at length in Sec. 3.2. In general we are able to maintain overall 2-axis deflection efficiencies above 50% even when driving with as many as 11 RF tones, although these efficiencies vary non-trivially with the overall RF power and details of the drive configuration.

2.4.2 NI 5451 Arbitrary Waveform Generator

In 2015 we acquired a National Instruments arbitrary waveform generator (NIAWG colloquially), model 5451. This PXIe card is in principle capable of outputting arbitrary, individually programmed voltage samples at 400 million samples per second (MS/s) on each of two output channels. Designed partially with IQ mixing setups in mind, this device was purchased for the purpose of driving our two tweezer-deflection generating AODs, where we would use the arbitrary functionality to program different relative tone powers, phases, and frequencies, while doing more complicated operations like precise frequency ramps for moving the tweezers and carefully designed flashing patterns, and real time programming for active rearrangement experiments.

Although expensive, the NIAWG can accomplish most of these things efficiently. In particular, our use of it in conducting rearrangement procedures will be discussed in Sec. 3.6. In working with the device we encountered one major flaw, which is that in operating the device in our desired mode, “scripting mode” with frequent triggering, the NIAWG is incapable of operating consistently at its maximum sample rate of 400 MS/s and we therefore we have generally operated the device at 320 MS/s. This means that the maximum frequency and total bandwidth we can output is approximately 160 MHz as limited by the Nyquist limit.

Newer designs in the lab and around JILA make use of custom-programmed FPGA devices to achieve similar functionality. While not-truly arbitrary, most of the functionality described above, with the possible exception of some of the flashing techniques, can be accomplished with an array of DDS cores on a sufficiently fast and large FPGA device.

Because we create tweezers with different AOD deflections, different tweezers within a given row or column will always have slightly different frequencies and therefore not interfere, except on fast time-scales which the atoms are not generally sensitive to. However, in a 2D array, diagonal groupings of tweezers within the array will have the same frequency, and can interfere (Fig. 2.9).

2.4.2.1 Mix-up Setup

An astute reader will have noticed that there is a mismatch between the center frequency of the AODs and the available frequency range of the NIAWG system. This is real, and our solution is to mix up the NIAWG output. In this way, we get all the flexibility of the NIAWG over it’s relatively large 160 MHz bandwidth, but at a higher frequency. We mix up the NIAWG output

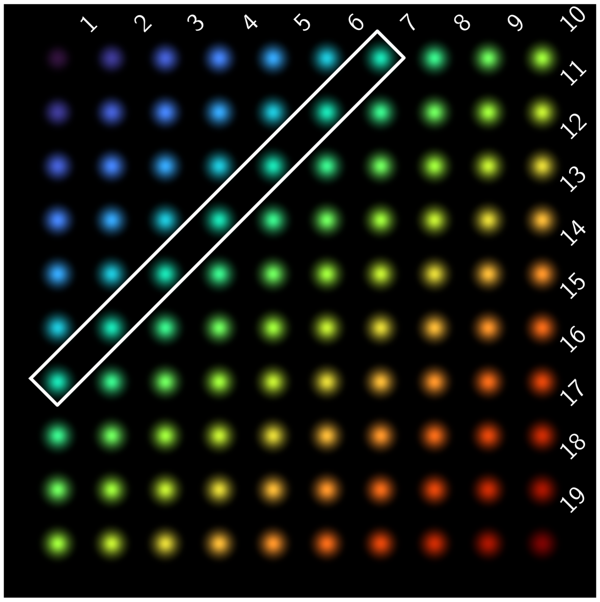

Figure 2.9: **Tweezer Array Frequency Distribution.** A depiction of a 10x10 tweezer array, with the different frequencies of each tweezer represented by the color of the tweezer. Tweezers in diagonal slices of the 2d array have the same frequency, despite shifts from the AODs. A typical spacing for loading, imaging, and cooling is approximately 10 MHz, while a typical spacing for tunneling is accomplished with 4-5 MHz tones.

by combining it with a 255 MHz tone from a Marconi microwave generator in a high quality mixer from Marki Microwave, part number T3-12LQP. The output contains upper and lower sidebands, and we use a nice custom low pass RF filter from the company K&L Microwave in order to filter out the unneeded higher tone and carrier leakage, part number 7L340-229.5/T500-O/O{135}. The output then goes through a pre-amplifier, and then a standard 5 W amplifier from Mini-circuits, part number ZHL-5W-1+. In general, we find that intermodulation in the AODs themselves are the leading contribution to non-linear effects in the RF chain, so we do not concern ourselves with purchasing a higher power or particularly low noise amplifier.

2.4.3 Other Devices of Note

2.4.3.1 Electro-Optical Modulators

We use fiber EOMs from the company EOSpace, part numbers PM-0S5-10-PFA-PFA-780-SUC315-UL and PM-0K5-10-PFA-PFA-800-UL for creating sidebands for Raman transitions and to generate a coherent repumper for the ΛGM schemes. These EOMS work well at the high 6.834 GHz frequencies required for both of these schemes, although their transmission is not very stable. Putting more than a couple mW of optical power through these devices requires heating up the devices in order to avoid photo-bleaching effects.

Chapter 3

Raman Sideband Cooling, Tunneling, Rearrangement, and Other Techniques

In this chapter I describe various refinements of Raman sideband cooling, quantum tunneling, and various other experiments developed over the course of my PhD. As opposed to Chapter 2, which deals with experiment hardware, these are all developments that use single atoms.

3.1 Larger Tweezer Arrays

At the beginning of my PhD, the largest array of atoms that we had loaded was a 2×2 array. Larger arrays of atoms are useful for a variety of our experiments and futures plans, and so early on we decided to embark on a number of projects designed to improve the size of the array we use. These projects were:

- Upgrading our tweezer laser power source to a 2 W and eventually a 3 W tapered amplifier (Sec. 2.2.1.3), in order to have sufficient optical power to generate the tweezer array.

- Switching from the ASE lens to the Sill lens (Sec. 2.2.3), hoping that the Sill lens would have a larger field of view and produce tighter traps than the ASE lens and therefore be able to support more tweezers among other benefits.

- Upgrading from generic waveform generators to the NIAWG 5451 (Sec. 2.4.2), which was required to do intermodulation compensation and generating large numbers of RF tones to create many AOD deflections.

- Upgrading to the IntraAction AODs (Sec. 2.4.1), which have a larger bandwidth and can therefore support more deflections than our original AODs.

As a result of these upgrades, at our peak we were able to produce and load a 10x10 array of atoms with reasonably good performance (Fig. 3.1). Although the array could probably be expanded a little to 11x11 or 12x12, at this size, we are running into a number of hard limitations:

- Needing more laser power. This is probably the easiest problem to fix with sufficient funding, as I believe one could get more power than we have now with better optimized tapered amplifier systems, or because Ti:Saph laser systems with larger seeds than our 10 W seed are commercially available.
- The bandwidth of our AODs. It is hard to get a wider bandwidth of deflections without negatively changing the spacing of our optical tweezers per unit of RF frequency difference between tones. It is important that this ratio remain small in order to perform quantum tunneling. Other technologies, such as liquid crystal spatial light modulators, deformable mirror devices, and microlens arrays, can help address this problem as the array of tweezers these technologies generate. However all of these are either static or relatively slow compared to AOD-based systems and so dynamical tunneling may be challenging using them.
- The finite field of view and spot size of our objective. Improving this would require a new objective system with a large field of view and similar trap performance. These objectives are quite expensive and take a lot of time and resources to design and test.

In the meantime, a number of groups have expanded their atom systems significantly larger, and to my knowledge the largest such system is 361 usable traps [76].

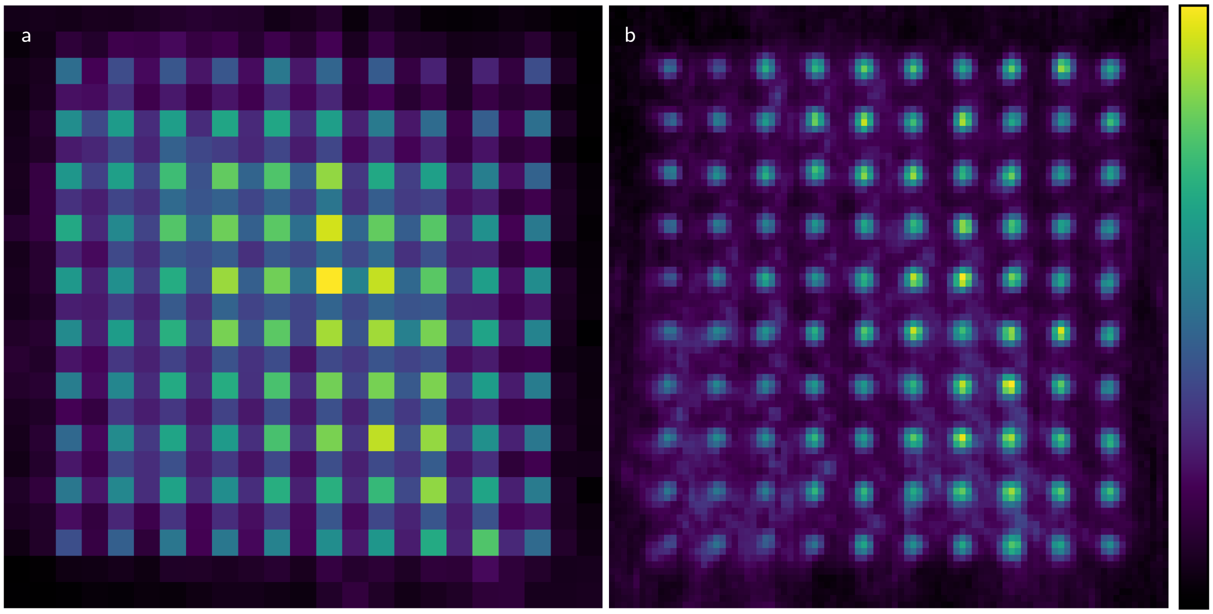

Figure 3.1: **Atom Array Images.** **(a)** A binned, averaged picture of a 10x10 array of atoms. Differences in intensity reflect a combination of field of view effects and background noise. **(b)** An **unbinned**, averaged picture of a 10x10 array of atoms. Notable is a significant “pedestal” of background noise that the atoms sit on, suggesting a long tail of the imaging point spread function, and some aberrations affecting the atom images in the bottom left corner of the image.

3.2 The Evening of Optical Tweezers / Intermodulation Compensation

In order to create an array of tweezers, we drive our tweezer AODs with a sum of up to 10 RF tones simultaneously. In general, the maximum voltages achieved by a sum of 10 RF tones will be much larger than the voltage achieved by a single tone, even if the same amount of total power is in both sets of drive tones. This happens when there is a significant amount of constructive interference between the different tones at a specific time in the waveform. As such, a sum of tones will generally be more sensitive to nonlinearities in the AOD’s response, which will both reduce the overall deflection efficiency, add higher order intermodulation effects outside of the original tones, and cause relative un-evenness between the different deflections. As such, we wish to minimize these negative effects.

To first order, the effects are very predictable by simply examining the total many-tone waveform. After calculating the waveform given a number of RF frequencies, amplitudes, and phases, one can estimate how bad the intermodulation is likely to be based off of metrics such as the peak voltage in the waveform or high order moments of the voltage of the waveform. Typically, we will set up a function which calculates such a metric as a function of the many individual phases, amplitudes, and frequencies of the RF tones, and then plug the function into a minimization algorithm which will find a set of phases which minimizes this metric. These parameter spaces tend have many local minima, so we use a basin-hopping algorithm to find a good global minimum. We then fix the phases of our tones. One could check the resulting intermodulation on an RF spectrum analyzer, but this routine is robust enough that we typically do not bother, and instead turn to optimizing the evenness of the traps.

In general, after the phase-optimization algorithm described above, the traps are even enough to at least load into all traps. However, for larger arrays, it can be helpful at this point to image the tweezer array directly on a camera, where one can quickly see "by eye" how evened the trap is. We can then manually even the powers of the RF tones in order to even the array by eye. In general, due to aberrations in the objective lens, evening an array on such a camera does not result in an evened array inside our vacuum chamber, and so at this point we must turn to optimizing based on tests that probe the potentials that the atoms actually experience. We can measure the evenness of the traps using a couple metrics, such as the trap depth or the trap frequency. Typically these will not be simultaneously optimized due to fluctuating trap shapes across the field of view of the objective. Most commonly we optimize the depth, which we measure by measuring the light-shift of the tweezers on the D_2 $f = 2 \rightarrow f'' = 3$ transition [64].

This depth optimization procedure is an iterative one. We measure the depths by analyzing the light shift they induce on an accessible transition. Then, we assume that the depths are proportional to the powers in each of the RF tones (effectively ignoring intermodulation effects) [64]. With this assumption and a given set of powers and depths, we can predict a new set of powers which will minimize the variation among the depths. This is our next iteration's powers. We again measure the depths using these new RF powers, and repeat the procedure until the depths converge to the desired level of precision. For a 1D array, we are limited by our ability to precisely and quickly measure the trap depth and temporal fluctuations, but typically achieve depths that are even to within approximately 1%. For a 2D array of traps, we are more fundamentally limited by spatially dependent aberrations in our tweezer generation system that make it impossible to create an evened set of traps given our limited set of controls over the tweezers. As such, we can only achieve depths that vary with a standard deviation of approximately 5% of the average depth.

3.3 Flashing Imaging

For large atom arrays, effective imaging can be affected significantly by the uniformity of the tweezer array. In particular, variations in the trap depths result in variable light shifts on the atom, which can dramatically change the scattering rate of the imaging light (Fig. 3.2). Additionally, the optical tweezer is anti-trapping for excited state ^{87}Rb atoms, which may lead to some additional heating in typical configurations.

Inspired by the work done at Harvard, as we ramped up the size of the arrays we were using, we started using what we refer to as a “flashing imaging” technique [77]. The technique consists of rapidly alternating the optical tweezer with the imaging light. The flashing is fast enough that the atom’s motion is primarily influenced by the time averaged tweezer potential, but the configuration is such that the light only scatters off of the atom when the tweezers are off and therefore when the atom experiences no tweezer light shift and no anti-trapping. This avoids the issues with the tweezer uniformity, and so is especially useful in the initial setup and calibration of the tweezer array before the depths are evened.

In our case we typically flash the traps and imaging light with period of 0.5 µs. We can typically gain enough fluorescence to identify an atom after 5-15 ms of imaging time. Notably, the flashing is done with the tweezer’s intensity servo AOD, which is separate from and before either of the tweezer deflection AODs that we flashed for rearranging procedures (Sec. 3.6). The imaging light is in a common $\sigma+$, $\sigma-$ red-detuned PGC configuration with zero’d background fields. The imaging light is typically detuned from the D_2 $f = 2 \rightarrow f'' = 3$ transition by about 30 MHz or about

5Γ, where Γ is the natural linewidth of the transition. This balances the need to scatter photons at a sufficient rate to be detectable above background light with the need to keep atoms cold enough to remain trapped. The imaging light is flashed with a 42% duty cycle, while the trapping light is flashed with a 50% duty cycle. In our system, the waveforms are typically applied with a phase offset of 165 degrees in order place the imaging light to be centered in the time when the tweezers are off, however this is in general sensitive a variety of delays determined by things such as the position of the laser light in the AODs which are used to flash the light. Since these parameters are all programmatically controlled via Chimera, they can easily be optimized by scanning them and simultaneously maximizing the imaging survival and the mean count value seen when an atom is loaded.

Our analog servo is typically active and set to a constant set point during this flashing procedure, but the servo bandwidth, which is typically on the order of 100 kHz, is slow enough that we do not run into significant issues with this. We have experimented with using "sample and hold" servo techniques to mitigate some servo fluctuations that happen during and immediately after the procedure, but we found that keeping this functionality well-tuned in our system was challenging and generally not worth the additional effort.

3.4 Raman Sideband Cooling

Resolved Raman sideband cooling is a crucial technique in preparing ground-state atoms for our experiments [78, 58]. Throughout this thesis, we use a pulsed method, details of which are recorded in Adam's thesis [64]. However, we experimented with a number of small variations while attempting to cool larger arrays of atoms, and techniques that make use of the ΛGM we developed.

3.4.1 Use of In-Trap ΛGM for Better Initial Cooling

One of the most important parameters for Raman sideband cooling is the initial temperature of the atoms. In order to be deep in the Lamb-Dicke regime where sideband cooling is effective, the initial size of the atomic wave packet needs to be small, or all else being equal the atom needs to

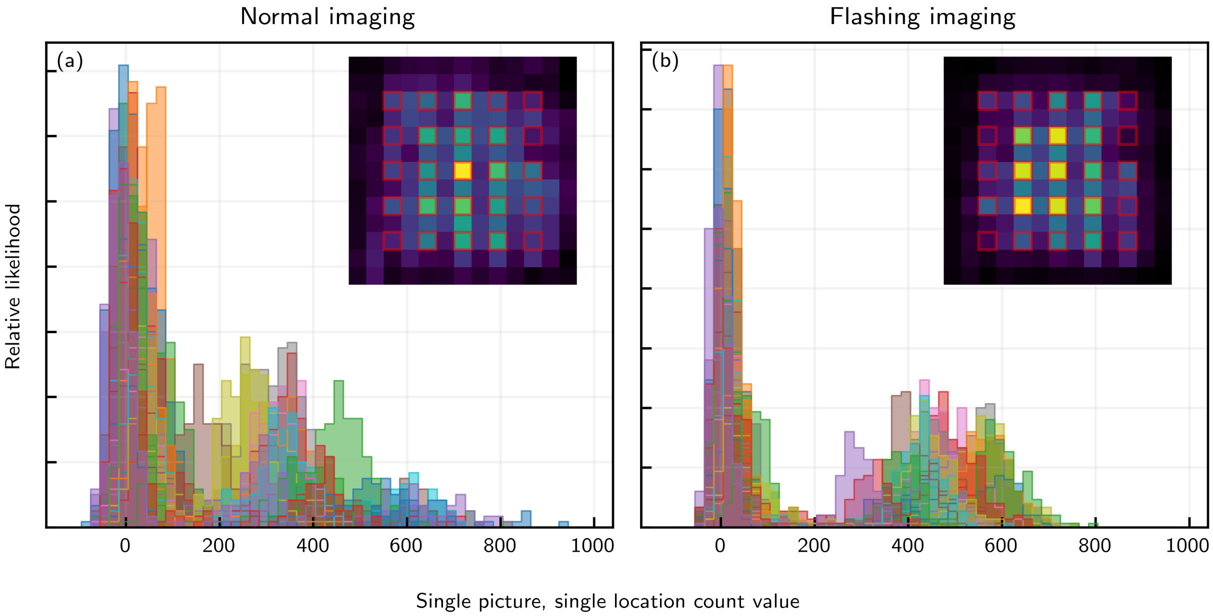

Figure 3.2: **Direct Flashing Imaging Vs. Normal Imaging Comparison.** **(a)** Normal imaging, where some atom locations have dramatically reduced imaging signal compared to the others, and **(b)** flashing imaging, which despite uneven and poor loading in the given data set, can still produce reasonable count histograms. Insets: averages of the images used to produce the histograms. Much of the variation still seen is due to the finite field of view of our objective and other light collection issues. Notably, this data set is not particularly representative of the best imaging signal which is possible, but it is a good direct comparison between flashing imaging and regular imaging. Red outlines in the inset indicate tweezer locations.

already be relatively cold in the trap. We typically accomplish this with an initial stage of cooling in between the initial atom imaging stage and the Raman sideband cooling stage. Traditionally, a stage of in-trap optimized red-detuned polarization gradient cooling (RPGC) was used for this stage. However, with the development of the ΛGM we use for loading techniques (Chapter 4), we had an additional tool at our disposal here.

There are many ways to characterize the temperature of the atoms in a trap, in order to judge how well different cooling techniques work. Near the ground state of the trap, Raman sideband spectroscopy can be used to great effect. However for hotter temperatures such as our pre-Raman sideband cooling temperature, we use another technique. We start by loading and imaging our atoms and then either apply in-trap optimized ΛGM cooling, RPGC cooling, or no cooling at all,

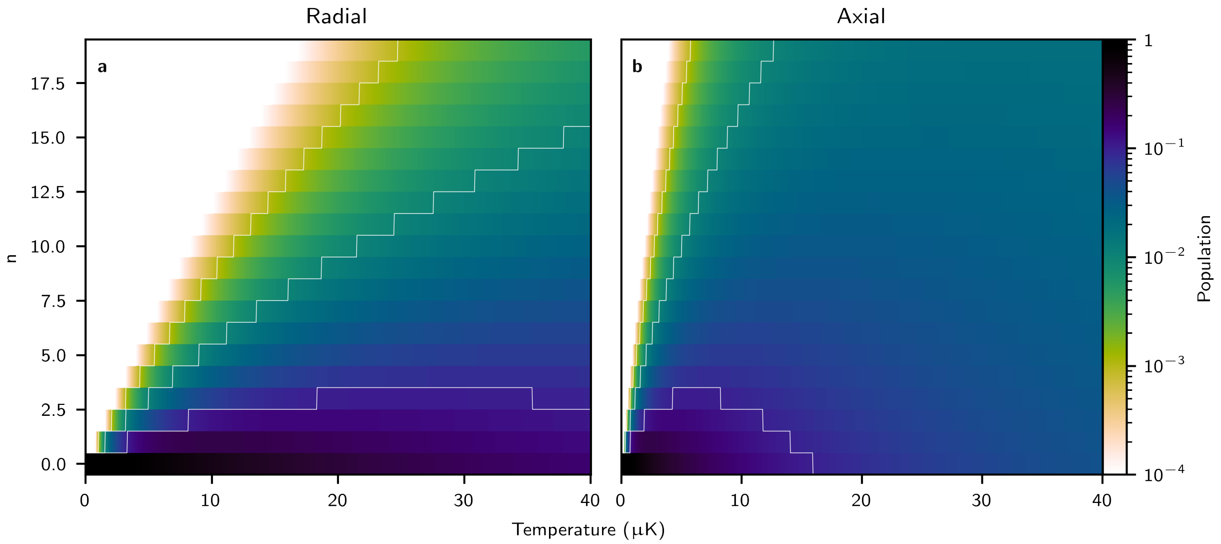

Figure 3.3: **Harmonic Oscillator Excitation Populations.** A visualization of the population of a given quantum state n depending on the temperature of the single atom. At low populations, the atom is increasingly concentrated in the lowest harmonic oscillator level, but as expected at high temperatures states are increasingly evenly populated. Contours are placed at populations of 0.1, 0.01, 0.001, and 0.0001. **(a)** Plot for typical radial frequency of 150 kHz, and **(b)** plot for typical axial trap frequency of 35 kHz.

leaving the atom at its relatively hot post-imaging temperature. We then reduce the trap depth to the scale of 1 µK before raising the trap back to its relatively deep imaging depth and conducting a final image. We then analyze the pair of images to determine how likely the atom is to survive this lowering process as a function of the reduced depth. This data can be analyzed to determine the atom's temperature, but it also immediately indicates that the ΛGM cooling works marginally better than the RPGC cooling (Fig. 3.5) [31]. As a result, we have used the in-trap optimized ΛGM cooling before Raman sideband cooling ever since. The main difference of the optimization of the ΛGM for in-trap cooling rather than loading is the detuning. While the detuning for the loading process may be on the order of 20 MHz from the free-space resonance, the detuning of the in-trap optimized ΛGM may be as much as 100 MHz in order to cool most effectively. Otherwise, the procedures are identical.

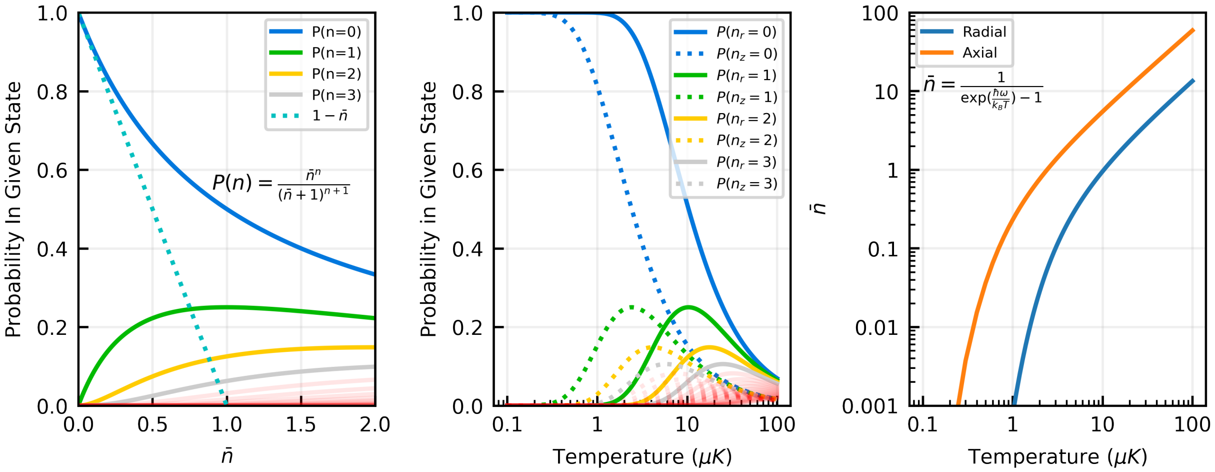

Figure 3.4: **Harmonic Oscillator Statistics.** A variety of useful plots showing the conversion between various useful measures of an atom's temperature in a harmonic potential. **(a)** Probability of being in a given harmonic oscillator n level as a function of the mean occupation number $\bar{n}$ which is the metric typically reported based on sideband spectroscopy. **(b)** Probability of being in a given harmonic oscillator n level as a function of the atom's temperature, using a typical radial trap frequency of 150 kHz and a typical axial trap frequency of 35 kHz. **(c)** Mean occupation level $\bar{n}$ as a function of the atom's temperature, using the same trap frequencies as (b).

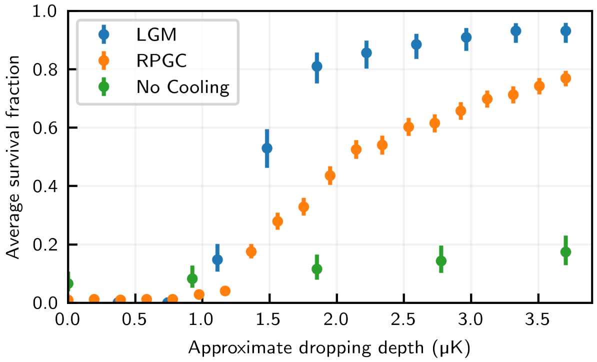

Figure 3.5: **The Relative Performance of In-Trap ΛGM.** After applying in-trap optimized ΛGM (blue data), a larger fraction of atoms survive at a given dropping depth than either using RPGC (orange data) or using no additional cooling (green data). Note that the system at this time was calibrated for large traps, and there may be a non-trivial offset to our calibration of the trap depth here. Cooling is done at a typical trap depth of 1.0 μK

3.4.2 Raman Sideband Cooling of Larger Arrays

One topic that is of perennial interest to the group is the construction of many-atom degenerate gases starting from individually cooled single atoms. While we did not publish any work on this front during my PhD, we did do various exploratory experiments in this direction (Sec. 3.5). The pre-requisite for this work however is starting with a larger array of ground-state cooled atoms, which is challenging in a number of ways.

The main challenge we experienced with sideband cooling of larger arrays is that of trap uniformity. Our evening procedure (Sec. 3.2) is not capable of creating a perfectly even set of traps, but in fact the bigger issue we faced was differences in the trap shapes that became noticeable near the edges of a 10-by-10 array. This manifested itself most noticeably in the splitting of Raman transitions into multiple frequencies. Similar splitting has been noticed in other experiments [79], and is presumably due to high order aberrations in the optical tweezer potentials, making them relatively anharmonic. In particular, simple astigmatism effects should not cause such splittings, as the atom should always sit in the circle of least confusion of an astigmatic potential.

Still, relatively efficient cooling could be achieved of the large array of traps, at least in the radial direction of the traps. The radial $\bar{n}$ value of the data in Fig. 3.6 is 0.10(22), where the number in parenthesis is the standard deviation of the results, obtained by fitting individual data sets with a sum of three Gaussian distributions. This result was achieved also by modulating the Raman cooling frequency at 10 kHz in order to effectively broaden the cooling drive. Many types of experiments would still be sensitive to the remaining thermal population in the tweezers, but these results are still promising for a number of types of experiments that we dream of. We believe that the best approach for improving these results is improving the traps themselves, which could be done with a combination of new objective systems and lattice systems.

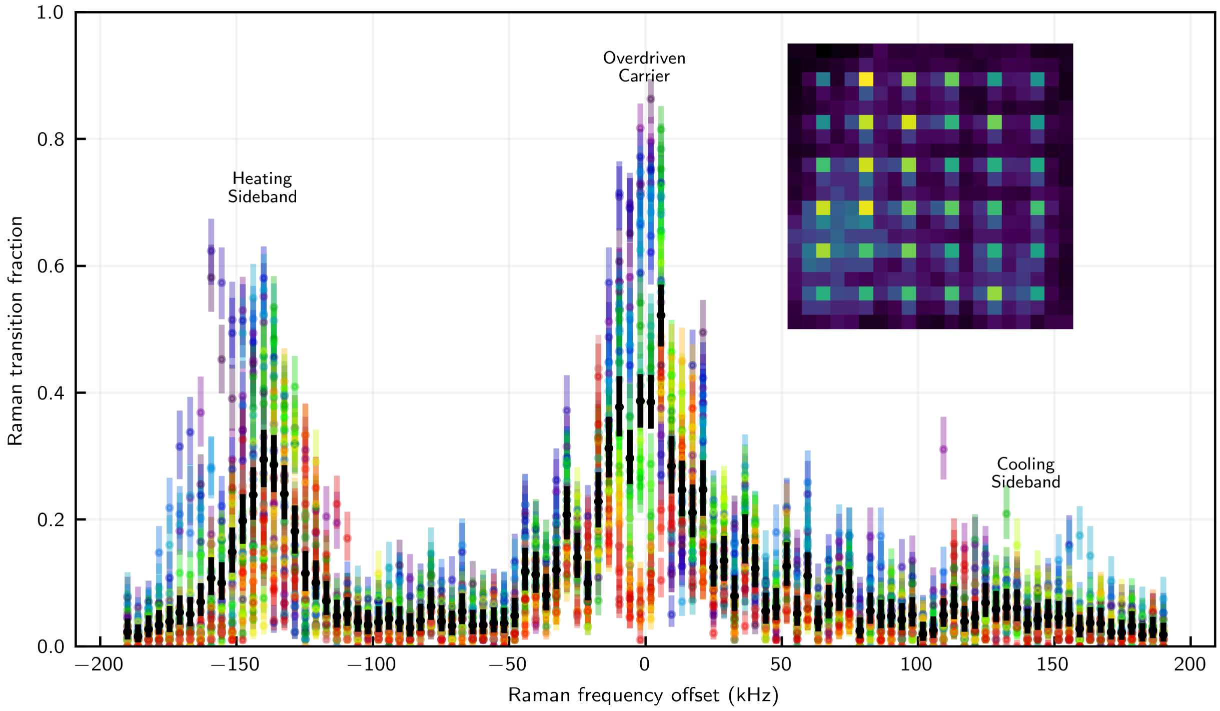

Figure 3.6: **Simultaneous Raman Spectroscopy of 36 Atoms.** Different colors represent different atom locations, the black dataset is the average of all individual atoms and the black error bars represent the standard deviation of the single atom values.

3.5 Tunneling

3.5.1 Dumping Techniques

A general problem in early tunneling experiments was getting the tweezers to be shallow enough in order to have strong tunneling at large tweezer spacings. Our typical approach in the past was to simply change the set point of our servo system in order to servo at low powers. However, this means that for low power servoing the photodetector is detecting small optical signals which are susceptible to noise, and that the servo system is working on very low voltage signals which are difficult to get working properly in our analog servo. The main tweezer light at the point of servoing typically has maximum powers ranging from 3 mW to 200 mW depending on the number of tweezers used in a given experiment, (although only a small fraction is used to servo) which is attenuated to give a readout of approximately 10 V on our photodetector, which is a Thorlabs

PDA10A photodetector which has been modified with some extra filtering in order to have improved noise performance. Without extra techniques, the minimum voltage during a tunneling experiment might then be approximately 1 mV.

Other attempts included using a digital servo which had been utilized by some ion trapping groups at NIST [80], and using a logarithmic photodetector which had been in use by some groups at Harvard. These both basically worked but were not much improvement over our original system, and came with their own technical problems.

Eventually, I found a better solution: instead of lowering the set point, we dumped extra power in “auxiliary tweezers” that would be placed far away from the tweezers of interest. Thus, the servo would be servoing the same overall power (counting the power in the auxiliary tweezers in addition to the tweezers of interest), but there would be less power in the tweezers of interest reducing the overall depth that is relevant for the atoms. This works very effectively, but requires the ability to dump extra power into tweezers. In our system this is done by having an extra set of tweezers a large distance (and RF frequencies) away from the main tweezes, and similar approaches might be difficult for doing similar techniques with larger arrays where it’s difficult to put extra tweezers far away from the tweezers of interest.

This technique allowed us to get to extra small depths spaced extra wide in order to attempt tunneling in this regime. However, it is also generally useful in other circumstances, as in various configurations it allows the intensity servo to be run at the same set point settings while having the absolute depth of the tweezers change. This is particularly important for configurations that use different numbers of atoms, as it may be desirable to, in multiple configurations, have similarly large ranges of servoing while having very different total powers. Without this technique, one would either have to manually alter the servo parameters between configurations or attempt to operate the servo over an even larger range than an individual experiment requires. The latter is undesirable because the intensity servo can be somewhat finnicky to keep working well at a variety of different depth parameters for many experiments. It is easy for the servo to drift and start ringing at extreme parameters.

This trick works well enough that we can make our traps shallow enough such that even after sideband cooling, the traps are so shallow that they only support ground-state atoms. This can be a useful technique as it allows us to release any excited state atoms from the trap before conducting an interesting experiment. This allows us to make cooling or temperature issues manifest as loss, which it is generally possible to post-select away, rather than have these thermal atoms contaminate other signals. Notably, one expects rather discretized loss from our optical tweezers as individual levels, including eventually the ground-state, should be either supported or not supported at various depths. We measure however that the atoms are lost gradually as we reduce the trap depth. This is suggestive that at these extremely low depths, the traps may be affected by fluctuations in depth or shape during the ramp process which cause some variable fraction of the atoms to be lost during the ramp. There are no indications that atoms are gradually lost at the shallow depth as a function of time, which might be the expected manifestation of consistent noise **at** the final depth or gravitationally assisted tunneling out of the trap.

Notably, we find that we must put the dump tweezers unexpectedly far away from the main tweezers. For example, for tunneling experiments we will typically set the NIAWG to output 75 MHz and 87 MHz tones to the horizontal AOD, creating a 12 MHz spacing which will shrink to a 5 MHz spacing during the tunneling portion of the experiment. We find however that we must use vertical frequencies of 81 MHz and 117 MHz, a spacing of 36 MHz (24 MHz being insufficient), where the 81 MHz tone creates the “main” tweezers which we optimize and analyze for tunneling, while extra power is dumped into the 117 MHz tweezers. We find that if we put the dump tweezers closer, that there is a large amount of loss in the main tweezers when they move closer together to initialize the tunnel coupling. This is surprising. The nature of intermodulation, which is normally the culprit for effects like this, is such that each axis should independently effectively have extra (usually weak) tweezers that are offset from the main tweezers by multiples of the frequency differences in the driving RF tones, which should not allow for any sort of cross-coupling effects. Therefore the nature of this issue is suggestive of a combination of cross-coupling between the two RF systems and intermodulation. Another possibility is a combination of frequency-reducing very-high-order intermodulation and a second-order AOD deflection, which could conspire to produce very weak extra light near the moving traps which could cause heating. This is one of several possibly related indications of strange couplings within our tweezer generation system, the other main one including issues we face with the "stiff" rearrangement scheme 3.6.3.

3.5.2 Considerations on Tunneling Fidelity

In general, we expect that quantum tunneling procedures are particularly sensitive to the shape of our optical traps (Fig. 3.7). In order to understand this and other parts of this section, I will briefly overview the idea behind quantum tunneling in a double-well potential.

We start by assuming that the tweezer potential is symmetric and the tweezers are far separated from each other, in which case the ground state of the system has a degeneracy of 2, and can be constructed as any two orthogonal superpositions of the ground states of the two individual tweezers. The natural two states of the system when the tweezers never come close are $|L\rangle$ and $|R\rangle$, the two single-tweezer ground states. In the case that the tweezers couple, the ground state degeneracy is broken, but the potential is still symmetric under the parity operator along the two-trap axis. As a result, the parity eigenstates $|\psi^+\rangle = |L\rangle + |R\rangle$ and $|\psi^-\rangle = |L\rangle - |R\rangle$ with parity eigenvalues $+1$ and -1 respectively will still be good eigensolutions of the problem. Our initial state preparation is of atoms in the first basis, which can be represented in the second basis, for example as $|\psi\rangle(0) = |L\rangle = |\psi^+\rangle + |\psi^-\rangle$. Then, when the tunnel coupling breaks the degeneracy, the state will evolve as $|\psi\rangle(t) = |\psi^+\rangle + |\psi^-\rangle e^{-iJt}$, resulting in the state at a later evolution time $t = \pi/J$ being $|\psi\rangle(\pi/J) = |\psi^+\rangle - |\psi^-\rangle = |R\rangle$, and hence we have quantum tunneling. Hong-Ou-Mandel (HOM) interference occurs when two bosonic atoms tunnel and interfere with each other in coupled tweezers, and is an important demonstration of the type of physics we can explore with our system [64, 81, 51, 82, 57, 52].

With this foundation established, it is not too difficult to see in concrete ways how the detailed nature of the tweezer potential can affect these dynamics. If the tweezer potential is not symmetric, then the sum of single tweezer ground states is no longer an eigenstate of the parity operator, and the state will not transfer perfectly. The tweezer potential can be asymmetric for a number of reasons, including that the bias or relative depth of the two tweezers can be different. Asymmetric aberrations from our objective system may make each tweezer individually asymmetric, which would also make the sum asymmetric. Spatially dependent aberrations may make each tweezer different from each other, which would break this asymmetry as well.

The above analysis treats the problem in one-dimension, but the impact of the other dimensions can be significant as well. In general, the different coordinates of a gaussian potential are separable nearest to the bottom of the trap, and thus we hope that since the tunnel coupling should ideally be a perturbation only in the radial direction, that the tunnel coupling can not couple states with different axial excitations. However, considering that the axial excited states are energetically close, if there is a small axial coupling, it might be easy for either off-resonant couplings or bias fluctuations to result in transfer to excited states which would negatively affect our tunneling.

All of these issues are difficult to probe directly but guide our attempts to improve the tunneling performance of our system.

3.5.3 Recent Two-Tweezer Tunneling

The above considerations (Sec. 3.5.2) were a major motivating factor for our work in developing the Sill lens as a replacement for our previous objective. If the tunneling is very sensitive to the nature of the traps, then we'd like the traps to be as tight and well-behaved as possible, which might be achievable with a new custom objective lens. It should not come as too large of a surprise however, considering the struggles we had with the Sill lens (Sec. 2.2.3), that at this point the tunneling with the new objective is no better than before. Key metrics, such as the single particle tunneling contrast and the Hong-Ou-Mandel (HOM) dip were not improved by the introduction of the new objective.

In particular, other than simply having the different objective, our improvements to our control over the trap depth (Sec. 3.5.1) allowed us to test tunneling at even further spacings and shallower depths, which had seemed to work well previously. Unfortunately, we did not find

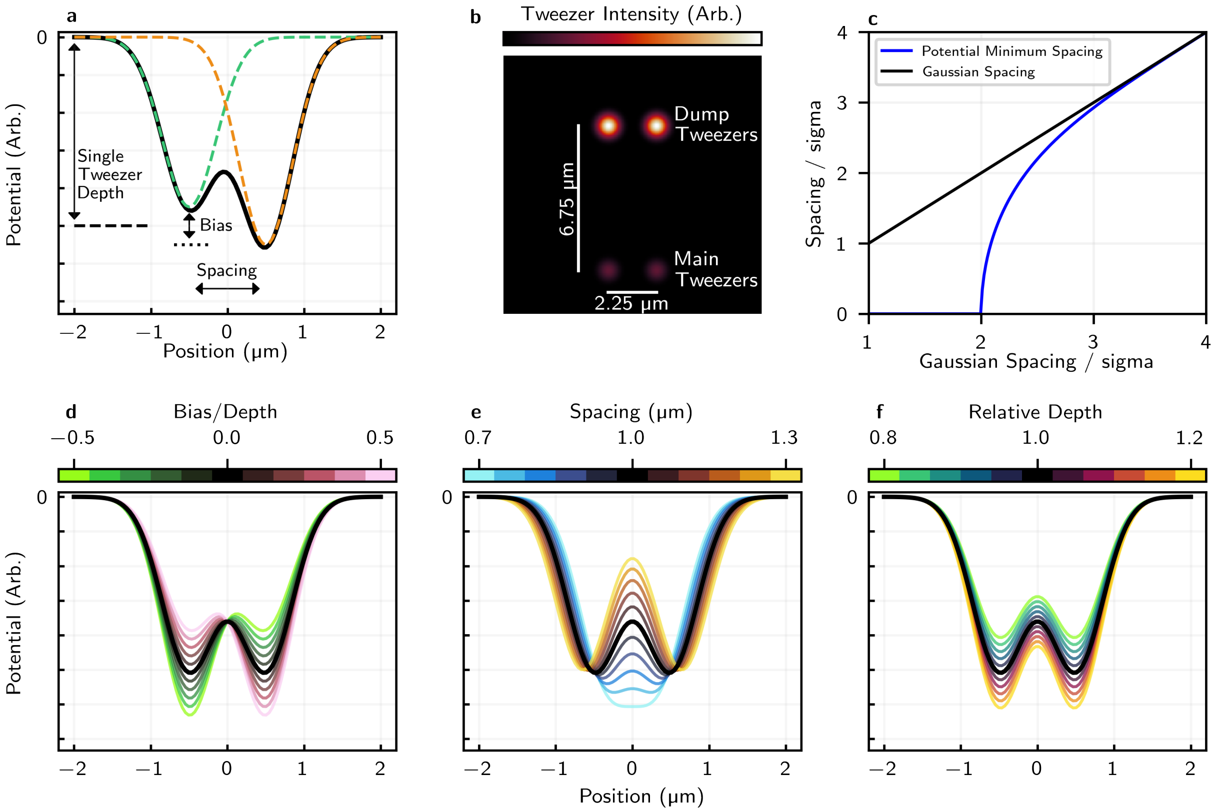

Figure 3.7: **Visualizations of Tunnel-Coupled Optical Tweezers.** All Gaussians have a typical waist of 700 nm, although these plots could be also be displayed in a dimensionless fashion as a function of the trap spacing over the trap waist. **(a)** Definitions of various parameters for tunnel-coupled optical tweezers. **(b)** Simulated image depicting typical spacing and relative powers of main tweezers, which hold atoms, and dump tweezers, which generally don't and are never analyzed or optimized, for a two main tweezer configuration during, for example, the loading stage. With only two main tweezers, most of the power is in the dump tweezers, as the configuration with zero dumping is typically set to support for a larger array. **(c)** Numerical calculation of the spacing between the two minima of a double-gaussian potential as a function of the gaussian spacing. **(d)** Visualization of variations of the bias between tweezers. **(e)** Visualizations of variations of the spacing of the tweezers. When the spacing is reduced to a single trap waist, the bump between the two potentials disappears. **(f)** Visualizations of variations of the single tweezer depth.

improved performance here, but rather we believe we run into more fundamental limitations of shallow tweezer tunneling. At typical depths, the tunnel coupling between the ground and the nearby excited $n_x = 1$ motional state is expected to be larger than the ground-to-ground coupling due to the tweezer geometry, but should still be finite and small enough to not significantly affect ground-to-ground tunneling. At particularly shallow depths and larger spacings, as one approaches the regime where there is only one bound state per tweezer, we expect that the ground-to-excited coupling increases dramatically before eventually becoming ill-defined as the bound-states are lost. In this regime, the ground-to-excited state coupling can become quite large and potentially interfere with the ground-to-ground tunnelling on the relevant side of the tunneling resonance. This is highly visible in Fig. 3.8(d), where the tunneling resonance in bias-space is highly asymmetric. Eventually, we additionally suffer significant single-particle loss when working with shallower and further spaced traps. We may also be increasingly affected by issues with the trap shape as at reduced depths the wavefunction is larger and samples more of the flawed potential. Additionally, it is possible that we suffer issues in coupling to axial excited states as the axial trap frequency approaches the tunneling frequency. There are some hints of asymmetry and extra resonances in bias scans such as Fig. 3.8(d), however it is in general difficult to tell whether these issues come from issues with state preparation, tunneling initialization, or such extra resonances.

The tunnel coupling is generally increased by working at a closer spacing, and decreased by working in deeper tweezers. We can therefore achieve similar tunneling coupling strengths by both decreasing the spacing and increasing the tunneling depth, and by doing this we can attempt to avoid the issues discussed above. In general we find that tunneling works best at tunnel rates greater than 100 Hz, and presumably at weaker couplings we are sensitive to other types of noise such as intensity noise in our traps. At short distances and deep traps, however, we suspect that we are increasingly sensitive to shot-to-shot bias fluctuations. This is supported by the fact that at deep depths, it is difficult to get coherent tunneling, where we have to consistently sit on-resonance, but that adiabatic rapid passage works pretty well (Chapter 6, Fig. 6.7).

Even at large depths, we still see hints of unexpected, non-trivial structure in our tunnel couplings. These are visible in scans of the bias over large ranges, which were completed in order to find ground-to-$n = 1$ and ground-to-$n = 2$ states as was required for our quantum tomography work (Fig. 3.8(c)). In these scans, we can see significant unexpected structure in the tunneling transfer, which may indicate couplings to unexpected states, and is worth future investigation. This structure may result from aberrations and structure in the tweezer potential, couplings to axial or orthogonal radial excitations, or combinations thereof. One should also not completely rule out more mundane issues with state preparation and tunneling initialization, as it can be non-trivial to cleanly create the desired initial state at the beginning of the tunneling procedure, and we have less experience doing this in the highly asymmetric traps required for excited state transfer.

Many of these comments regarding possible explanations for tunneling issues are at some level speculative. The direct things that we can measure while tunneling are the tunneling contrast, HOM contrast, and tunneling decay rates, which are all relatively indirectly related to these potential causes, making it in general difficult to precisely identify the causes of reductions in the tunneling performance.

An example set of coherent tunneling data with HOM interference is shown in Fig. 3.8(b). The HOM dip is seen in data where an atom was loaded in each tweezer and manifests as a reduction in the probability of measuring one atom in each tweezer (P_{11}) at times when each atom has had a chance to delocalize over the tweezer pair and interfere with the other. HOM interference causes the bosons to bunch up and prefer to lie in the same tweezer at these times, in which case our imaging system will tend to kick out the pair of atoms and we will observe no signal, i.e. a reduction in P_{11}. Ideally, after loading two atoms, we measure either one atom in each tweezer or zero atoms at all. However, we occasionally observe a single atom in the final image, which we refer to as a $2 \rightarrow 1$ event (referring to two atoms in the initial image, and a single atom in the final image). This can occur because a single atom was lost due to finite temperature effects or background collisions, cases which should be discarded in the HOM data, or cases where at the end of the experiment, two atoms were in the same tweezer but the imaging only kicked out one of the pair of atoms. In this latter case, the single atom remaining is a sign of HOM bunching, and this should be included in the data set and contribute to the P_{11} drop.

The data in Fig. 3.8(b) is conservative, and throws away all such single atom measurements, resulting in a minimum HOM P_{11} signal of approximately 0.30. This can be viewed as a upper bound estimate of the HOM dip, which is significantly lower than classical expectations already.

Aggressively including all such single atom measurements in the analysis, as if they all resulted from imperfect imaging instead of single particle loss, yields an optimistic minimum P_{11} signal of approximately 0.19, which can be viewed as a lower bound. Both of these limits are discussed in Adam Kaufman's thesis [64], and the latter is typically plotted. Independent imaging measurements, conducted well after the tunneling measurements, indicate that at typical imaging parameters, when attempting to image two atoms loaded into one tweezer, a single atom remains after the image approximately 25% of the time, and the rest of the time zero atoms remain. This imaging imperfection is consistent with numbers reported by Adam. There are then several simple ways of estimating the true P_{11} fraction before the imaging takes place.

(1) Knowing the expected number of single-particle loss-based $2 \rightarrow 1$ events based on independent single particle loss measurements, one can attribute the remaining $2 \rightarrow 1$ events to imperfect-imaging.

(2) Knowing the imaging imperfection rate (approximately 25%) and knowing the number of $2 \rightarrow 0$ events observed, one can calculate the number of imaging-based $2 \rightarrow 1$ events we expect to have occured and include this many in the calculation of the P_{11} dip. This analysis was completed and suggests a true P_{11} minimum of approximately 0.24, which sits nicely in between these bounds. Confidence in this estimate could be reasonably improved by conducting such imaging tests at the exact same parameters as were used in tunneling measurements, and in more reasonable temporal proximity.

(3) Lastly, one can look at fluctuations in the observed $2 \rightarrow 1$ fraction as a function of tunneling time, and therefore effectively the true pre-imaging P_{11} fraction, in order to estimate how many of the $2 \rightarrow 1$ events are due to this imaging issue. This was effectively done in Adam's thesis [64].

This area in general is fruitful ground for interesting tests of our system, and in general we think that there are many ways to continue to create and study interesting non-classical motional states. However, such testing is very time-consuming, especially considering the need to keep the

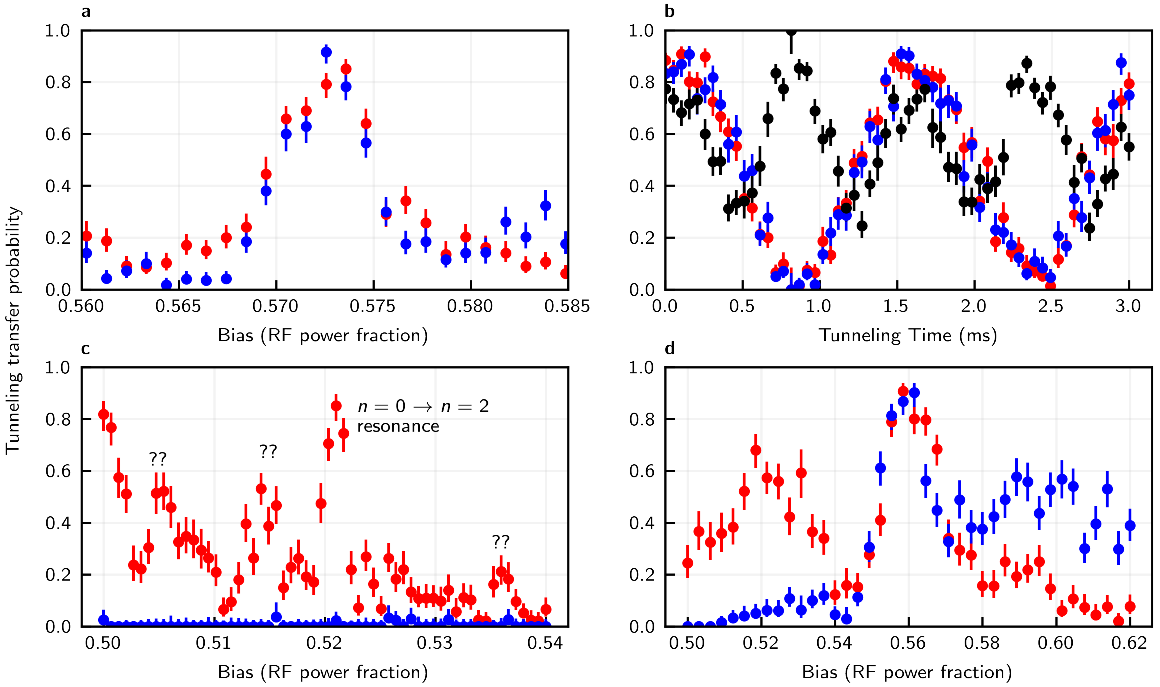

Figure 3.8: **Tunneling of Single Atoms Between Two Tweezers.** Shown in all plots are the probabilities of an atom tunneling from the left tweezer to the right tweezer (red data), and the probability of tunneling from the right tweezer to the left tweezer (blue data). **(a)** A typical tunneling bias scan taken at a single-tweezer depth of 1.23 µK and a spacing of 0.84 µm. One can refer to Fig. 3.7 for illustration of the bias parameter. Notably, the tunneling does not perfectly go to zero outside of the bias resonance here, and the tunneling resonance does not rise all the way to 1, which are a consistent problems in optimizing the tunneling. **(b)** A reasonably good time tunneling scan taken at the shallow depth of 0.25 µK and a gaussian spacing of 0.84 µm. Shown are the tunneling probabilities as a function of the amount of time during which the tunnel coupling is on. Also shown are the probabilities of measuring one particle in each tweezer post-selected on either zero or two atoms surviving, typically referred to as P_{11} (black data). Some typical problems are seen here in that the tunneling atom does not transfer all the way to the opposing tweezer, but returns to the original tweezer nicely. Typically, at these shallow depths, the tunneling time traces remain well-behaved longer than the bias scans do. **(c)** A wide bias scan at the relatively deep depth of 1.89 µK and relatively wide spacing of 0.94 µm which was close to what was used for preparation of 1st and 2nd excited states for the tomography work discussed in Chapter 6. Shown are many unexpected resonances surrounding the expected $n = 0 \to n = 2$ resonance. Notably, the reverse transfer is very small, a signal which is useful for diagnosing temperature issues in the state preparation. On the far left side of the resonance, we expect increasingly incoherent dumping of the atom from one tweezer into the other. **(d)** A tunneling bias scan at a relatively wide spacing of 0.94 µm and shallow depth of 0.32 µK. In this regime, on the relevant side of the bias resonance, the transfer population does not nicely go towards zero, but rather it seems that the atom is almost immediately delocalized between the tweezers on the relevant side of the resonance.

Raman sideband cooling highly optimized throughout testing. As a result, as it became clear that our tunneling performance was not significantly improved over previous results, we did not delay too much in sustained tests at this point in my PhD, and instead moved on to new experiments in various attempts to circumvent these issues.

3.5.4 Three-Tweezer Tunneling

One of the categories of things that we were interested in was expanding the tunneling experiments to more tweezers, and potentially involving more atoms. To that end, we wished to analyze a single atom tunneling between 3 optical tweezer potentials. This problem can be approximated as an implementation of the following simple Hamiltonian:

$$\begin{bmatrix} 0 & J_3 & 0 \\ J_3 & 0 & J_3 \\ 0 & J_3 & 0 \end{bmatrix} \tag{3.1}$$

Where each atom is directly coupled to the motional eigenstates of its nearest neighbors. We neglect couplings to tweezers further away or any relative biases between tweezers, although this could be easily added. Diagonalizing this Hamiltonian gives three non-degenerate eigenstates:

$$\psi_1 = \frac{|L\rangle - |R\rangle}{\sqrt{2}} \tag{3.2}$$

$$\psi_2 = \frac{|L\rangle + \sqrt{2}|C\rangle + |R\rangle}{2} e^{i\sqrt{2}J_3 t} \tag{3.3}$$

$$\psi_3 = \frac{|L\rangle - \sqrt{2}|C\rangle + |R\rangle}{2} e^{-i\sqrt{2}J_3 t} \tag{3.4}$$

$$\tag{3.5}$$

For single-tweezer eigenstates centered on the left, center, or right tweezer being labeled $|L\rangle, |C\rangle$, and $|R\rangle$ respectively. Then, given that you start in the leftmost tweezer (similar to starting in the right), the probability of being in any tweezer evolves in time as:

$$|\langle L|\psi\rangle|^2 = \left(\frac{\cos(\sqrt{2}J_3 t) + 1}{2}\right)^2 \tag{3.6}$$

$$|\langle R|\psi\rangle|^2 = \left(\frac{\cos(\sqrt{2}J_3 t) - 1}{2}\right)^2 \tag{3.7}$$

$$|\langle C|\psi\rangle|^2 = \frac{1 - \cos(2\sqrt{2}J_3 t)}{4} \tag{3.8}$$

While if you start in the center tweezer, the probabilities evolve with:

$$|\langle R|\psi\rangle|^2 = |\langle L|\psi\rangle|^2 = \frac{1 - \cos(2\sqrt{2}J_3 t)}{4} \tag{3.9}$$

$$|\langle C|\psi\rangle|^2 = \frac{1 + \cos(2\sqrt{2}J_3 t)}{4} \tag{3.10}$$

These calculations form the basis of our expectations for a single particle tunneling between three wells. In adding more wells, it becomes somewhat more tedious to set the biases of the three tweezers to enable resonant tunneling, but I believe it is not particularly complicated. After aligning this bias, we experimentally measure the probability of an atom being in a given tweezer as a function of the tunneling time during which the tunnel coupling is active (Fig. 3.9).

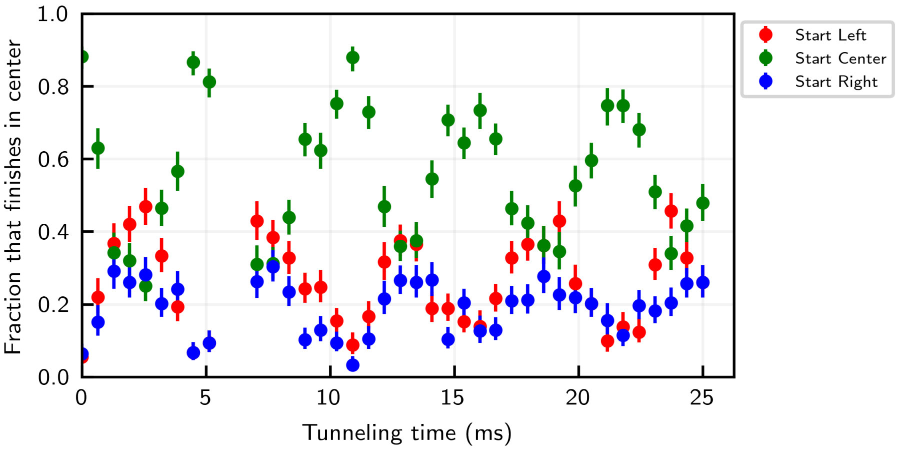

Figure 3.9: **Tunneling of a Single Atom Between Three Tweezers.** Shown are the probability of an atom finishing in the center tweezer given that it starts in the left tweezer (red), the center tweezer (green) or the right tweezer (blue). Ideally the red and blue should be identical, and the green curve should drop completely to zero and rise completely to one.

These results show nice, relatively coherent tunneling of a single atom between three optical tweezers, and suggest that our system could likely be expanded to support tunneling in more tweezers. We did not seriously examine multiparticle dynamics in three tweezers, as we expected it to be difficult to see appreciable interference affects without significant work. However, since our goal was to examine the interactions between many particles, we soon proceeded to other experiments in order to explore these dynamics, and did not return to single particle tunneling dynamics afterwards given the challenges we encountered there.

3.5.5 Predicting Two-Particle Tunneling with Interactions

In general calculating the eigenstates of double-well Gaussian tweezers is done using relatively involved discrete variable representation (DVR) techniques. This has been done in the past in specific circumstances with the help of theorist Michael Wall [83]. Additionally, Sean Muleady has also assisted us in understanding how various factors such as additional couplings and thermal population could be affecting our tunneling performance.

A simpler approach is to assume that the ground states will be approximately a sum of Gaussians, and to use the variational principle in order to create an estimate for the parameters of the sum of Gaussians as a function of the spacing of the two tweezers (Fig. 3.7). The variational principle is specifically used to calculate the parameters of a single particle in a symmetric sum of two gaussian wavefunctions, and does not involve interactions. This variational calculation could be expanded to include two particles or asymmetric sums of the wavefunctions for more accuracy (Fig. 3.10).

With this solution, we can then estimate the interaction strengths, kinetic energy, potential energy and total energies as a function of the tweezer spacing. For gaussian wavefunctions with a given spacing, these energies can be determined analytically and calculated quickly. To facilitate understanding of the ground-state dynamics, we calculate these parameters for four potential combinations of the ground state, which we refer to as the “Mott-insulator”-like state, Ψ_{MI}, the “double-filled” state Ψ_D, the “superfluid-like” state Ψ_{sup}, and the “anti-superfluid”-like state, or what would extend to a superfluid with a single excitation, Ψ_{asup}. The states, interaction energies, and kinetic energies are recorded for the x-dimension of the problem in Table 3.1, and the actual values as a function of distance, using the variationally calculated parameters for two 3D gaussian potentials, are plotted in Fig. 3.11. These parameters were mostly analyzed as a function of the spacing of the two tweezers. Typically, we initialize the tunneling with either an intensity ramp or a bias ramp, so these solutions might be better calculated as a function of either of those parameters.

State Definition	Interaction Energy	Kinetic Energy
$\Psi_{\mathrm{D}} = N_D \psi_g(x_1 + \frac{\Delta}{2})\psi_g(x_2 + \frac{\Delta}{2})$	$I_D = \sqrt{\frac{2}{\pi}}\frac{a}{w_0}$	$K_D = \frac{2\hbar^2}{m w_0^2}$
$\Psi_{\mathrm{MI}} = N_{\mathrm{MI}}\Big(\psi_g(x_1 - \frac{\Delta}{2})\psi_g(x_2 + \frac{\Delta}{2})$ $+\psi_g(x_1 + \frac{\Delta}{2})\psi_g(x_2 - \frac{\Delta}{2})\Big)$	$I_D \frac{2}{\exp(2\chi^2)+1}$	$K_D \times$ $\Big(1 - \frac{2\chi^2}{\exp(2\chi^2)+1}\Big)$
$\Psi_{\mathrm{sup}} = N_{\mathrm{sup}}\Bigg(\Big(\psi_g(x_1 - \frac{\Delta}{2}) + \psi_g(x_1 + \frac{\Delta}{2})\Big)$ $\times\Big(\psi_g(x_2 - \frac{\Delta}{2}) + \psi_g(x_2 + \frac{\Delta}{2})\Big)\Bigg)$	$I_D \times$ $\frac{\exp(2\chi^2)+4\exp(\chi^2/2)+3}{\exp(2\chi^2)+2\exp(\chi^2)+1}$	$K_D \times$ $\Big(1 - \frac{2\chi^2}{\exp(\chi^2)+1}\Big)$
$\Psi_{\mathrm{asup}} = N_{\mathrm{asup}}\Bigg(\Big(\psi_g(x_1 - \frac{\Delta}{2}) - \psi_g(x_1 + \frac{\Delta}{2})\Big)$ $\times\Big(\psi_g(x_2 - \frac{\Delta}{2}) - \psi_g(x_2 + \frac{\Delta}{2})\Big)\Bigg)$	$I_D \times$ $\frac{\exp(2\chi^2)-4\exp(\chi^2/2)+3}{\exp(2\chi^2)-2\exp(\chi^2)+1}$	$K_D \times$ $\Big(1 + \frac{2\chi^2}{\exp(\chi^2)+1}\Big)$

Table 3.1: **Tunnel-Coupled Tweezers Analytic Calculations.** Various energies of interest of four two-particle one-dimensional wavefunctions involving various sums of Gaussians. $\chi = \Delta/w_0$, where Δ is the spacing of the two wavefunction centers and w_0 is the wavefunction waist (not the probability distribution waist, which is used elsewhere). $\psi_g = \exp(-2x^2/w_0^2)$. The parameters of the Gaussian are to be determined using the variational method as shown in Fig. 3.10. Adding the energy contributions of the other dimensions is straightforward (if tedious) if one assumes that the potential is separable and that the solutions in those dimensions are simple Gaussians.

3.5.6 Adiabatic Ramsey Experiments

In general, we have had relatively good success with adiabatic tunneling procedures, where an adiabatic transfer between the ground-state of one tweezer and the first excited state of another tweezer can be done with fidelities as high as $92.4^{+1.9}_{-2.5}\%$. These procedures also leverage that the coherence time of our tunneling procedure is relatively long. Although, there may be more nuance

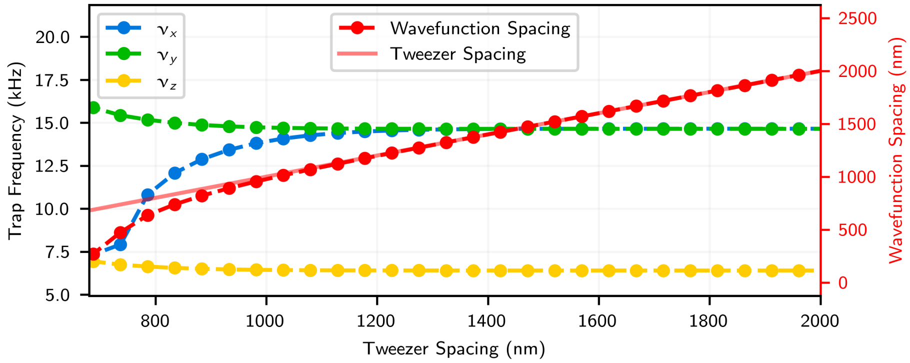

Figure 3.10: **Two-Tweezer Variational Solutions.** Variational Calculation of various ground state solutions to the double-well problem. The axial and y (perpendicular to the multiple tweezer axis) trap frequencies monotonically increase as the separation decreases and the tweezer overlap increases, increasing the effective trap depth. The frequency along the multiple tweezer axis decreases as the tweezers approach each other and the barrier between the two tweezers lowers and reduces the effective trap frequency. Lastly, the location of the wavefunctions more or less follows the bimodal minimums of the potential rather than the actual locations of the gaussians, which diverge at close spacings. At spacings closer than the waist of the tweezer ($2\sigma \approx 700$ nm), data for which is not shown, there is no barrier between the tweezers. The variational solution in this region initially suggests a finite spacing between the multiple gaussians to effectively make a lower-trap-frequency solution, before eventually collapsing to having no spacing.

to the state we prepare using these procedures, as is explored in Chapter 6. While the HOM contrast with diabatically initialized tunneling was always limited, we hoped to be able to circumvent some of these issues with an adiabatically prepared state.

Adiabatic state preparation naturally occurs very slowly, and as such it makes itself a natural method to explore the detailed influence of atom-atom interactions on tunneling procedures. By adiabatically preparing a multi-particle state in regimes where the interactions are significantly stronger or weaker than the tunneling, we would hope to be able to see different tunneling behavior. This would be an important stepping stone to observing similar regimes with more particles, and with enough atoms we might see the transition between these regimes manifest as a quantum phase transition between a mott insulator and a super-fluid.

The main method we used to explore this is effectively an adiabatic prepared Ramsey experiment. First, we attempt to adiabatically bring a pair of traps to be resonant with each other. We experimented in doing this either by lowering the trap depth, which slowly increases the tunnel cou-

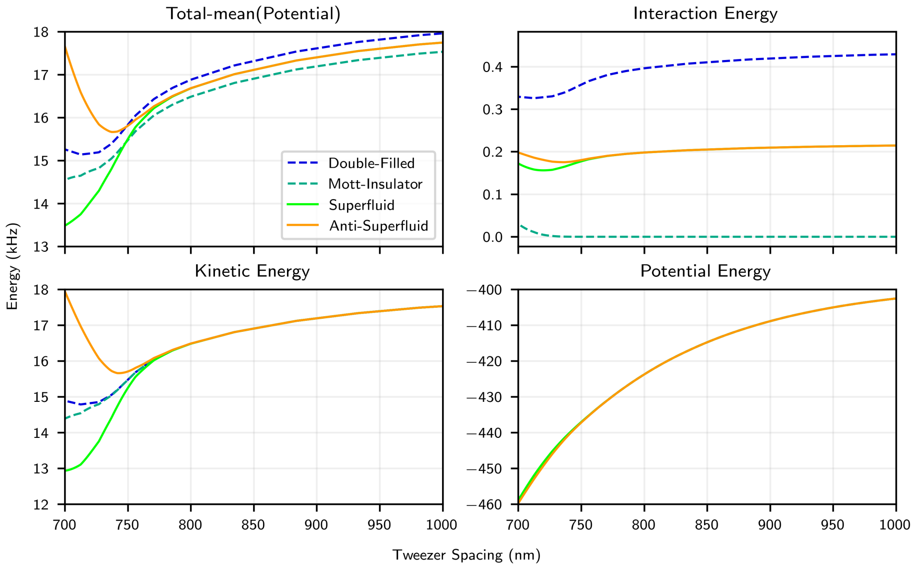

Figure 3.11: **Two-Atom Tunneling Simulation Energies.** Calculation of the various energies in the 3D double well problem as a function of the tweezer spacing at a fixed tweezer depth. States are defined and 1D energies are calculated in Table 3.5.5, parameters of the solutions there are taken from the variational calculations (Fig. 3.10). **(a)** The total energy minus the mean potential energy averaged between the different states. The purpose of the subtraction is simply to make the difference between states more visible, as the potential energy is significantly larger than the other energy scales of the problem. At large distances, the Mott-insulator-like state, which is what we create when we do standard ground-state preparation of two atoms on the same tweezer which contributes a positive interaction energy. **(b)** The interaction energy. The interaction energies decrease slightly as the tweezers start to approach each other as the x-axis trap frequency decreases, but eventually increases due to the increased confinement from the other axes. Superfluid and anti-superfluid states have nonzero interactions throughout which gives them higher energy than the ground state at large tweezer distances. **(c)** The kinetic energy. All kinetic energies are identical at large distances but split as wavefunction overlap between the two tweezers becomes non-negligible. The superfluid state minimizes the kinetic energy. **(d)** The potential energy of the system, which monotonically decreases at smaller spacings as the tweezer overlap, and the effective overall depth, increases.

pling, or by slowly changing the bias between tweezers. In the case of a single atom, this procedure should coherently delocalize the atom between the pair of tweezer potentials. We then abruptly change the bias of the tweezers, causing the two parts of the wavefunction to evolve depending on how large a bias is applied. The bias is then abruptly returned to zero, and the tunnel coupling is adiabatically reduced. Mapping out the final location of the atom as a function of the time the wavefunction evolves in uneven traps results in measurement of characteristic Ramsey oscillations between the two traps. In configurations with strong interactions, we expect no delocalization and no Ramsey oscillations, whereas with weak interactions and relatively strong tunneling, we expect delocalization during the adiabatic passage followed by full Ramsey oscillations.

In the end, however, we were not able to observe the regime where the interactions were stronger than the tunneling and see the effect of the interactions in an unambiguous way on the tunneling. This may be due to a number of factors. The interaction strength in our system may have been smaller than we expected for traps of this relatively shallow depth. Also, noise issues may have prevented us from being adiabatic with respect to the interaction strength anyways. In general, the interaction strength can be relatively large in deep traps. However, we need to be adiabatic in shallower traps to still be able to tunnel effectively.

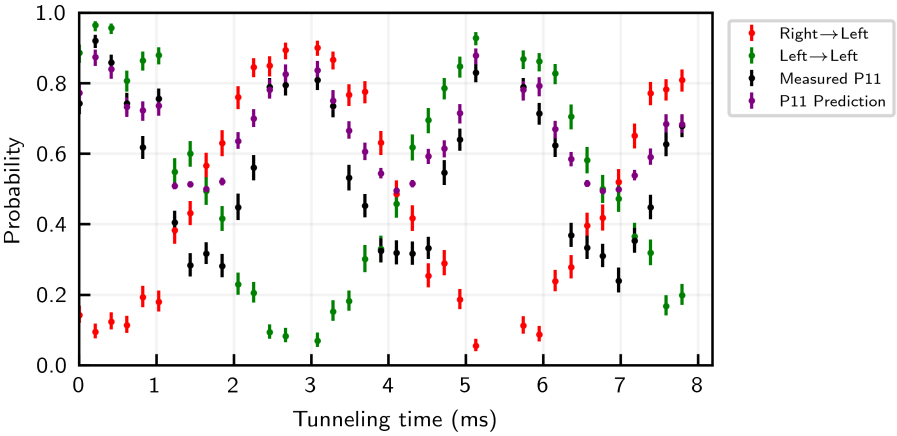

Figure 3.12: **Adiabatic Ramsey Oscillations.** Included are the probabilities for single particles to be in the left well, whether they started in the left (green data) or in the right (red data). Additionally included is the probability to measure a particle in each tweezer (black data), given that two particles were loaded and that either two or zero survived, post-selecting out cases where only one particle survived as this is possibly a result of single particle loss.

3.6 Rearrangement Techniques

As long as it is not possible to deterministically load an optical tweezer, rearrangement of already loaded atoms is the best way to reduce the positional entropy associated with unloaded tweezers, and thus is crucial for quantum simulation and quantum computation experiments with larger arrays of atoms. Rearrangement techniques have proven to provide fruitful ground for many publications, starting with the first demonstrations simultaneously published [84, 85], followed by a series of various expansions, optimizations, and implementations in different systems, including our own. Rearrangement has been demonstrated in a number of groups working with either optical lattices or optical tweezer arrays [86, 87, 88, 89, 90, 76, 91, 92].

The tweezer-generating system we use, which uses two orthogonal acousto-optical deflectors, can only create grids of traps, although the grid can potentially be unevenly spaced. Additionally, tweezers within the grid generally have different frequencies. In particular, if we attempted to use our ordinary tweezer system to create an extra row of traps which traveled between nearby rows in order to transport traps from one row to another, intermodulation effects within the unevenly spaced array of tweezers would cause additional, unwanted tweezers to appear with unpredictable amplitudes throughout the array, which would perturb other trap locations and cause loss. Practically speaking then, it is not possible to do rearrangement in this configuration and we are limited to producing only a regularly spaced array of traps.

Unlike many groups that use slow, shear-wave acousto-optical deflectors to create tweezer arrays, in our group we use fast longitudinal-wave devices. This opens up several possibilities which we were eager to try to take advantage of, and which I describe below. All of these methods worked at a reasonable level, and were sufficient to allow us to generate some nice pictures and results that we included in the ΛGM paper. However, in order to be competitive in large arrays, rearrangement techniques need to be able to move a particle from site to site with $> 90\%$ fidelity, with many applications requiring $> 99\%$ in order to consistently assemble perfect large arrays. As such, we determined that the methods we developed here were insufficient at the best fidelities we could achieve, and that pardon any breakthroughs, in our system it would be best to simply implement a second tweezer system which could be moved independently with respect to the array, similar to the techniques that other groups use. However, I record the results of the techniques we tried here in order to illustrate some of the challenges and pitfalls that others should watch out for.

3.6.1 Flashing Rearrangement

In this first technique, we attempted to move tweezers by rapidly alternating our RF generation system between two RF configurations. One configuration would be the RF to generate a static grid of traps, in which most atoms would sit in. The second configuration would be a single moving trap, or occasionally several moving traps when we were feeling ambitious. If this alternating is done rapid enough, atoms should only see the average of the two optical potentials. However, since the optical potentials are separated in time from each other, there is no interference of the two, avoiding problem (1) above, and additionally it is possible to break the rectangular symmetry posed in problem (2) above. So this method seems promising in principle. We use a Hungarian minimum cost-matching algorithm to calculate the sequence of moves required to rearrange the atoms into a given configuration.

Timing Details In these experiments, since the procedure to rearrange atoms must be done in real time after getting information from the camera, a number of things must happen for rearrangement to occur.

- The first image is completed and received by Chimera from the camera, which involves low level processing by the computer which I have no control over.
- The image must be processed in order to determine where atoms have been loaded.
- The sequence of desired moves, in abstract form (this location to that location) must be calculated
- The RF voltages (each sample must be individually calculated, as this is how the NIAWG is programmed) corresponding to the sequence of moves must be calculated or assembled into the total waveform if precalculated
- The total rearrangement RF waveform must be streamed to the NIAWG. In general, when the NIAWG is in scripting mode and looping on a waveform while waiting for a trigger, it loads only the immediate next waveform into its output buffers. During this looping

however we are free to actively write and overwrite waveforms that are to be outputted later in the experiment, such as a large waveform set aside for rearrangement.

Notably, the each individual move's RF can be pre-calculated and held in memory for reasonable array sizes, and so this step which might otherwise be somewhat taxing for this form of arbitrary waveform generator is circumvented, and the stage of combining the RF for the individual moves only takes ∼3 ms. The image processing and sequence of move calculations are both quite fast on these time-scales and take only ∼1 ms. The time-limiting steps are the time it takes for the image to be received by the Andor camera, which takes about 25 ms for typical image sizes, and the time it takes to stream the waveform to the NIAWG, which is about 50 ms for waveforms that contain about 100 individual moves, or 6 ms worth of moving time. It is likely possible to increase the streaming speed by using a faster PCIe MXI card, which is the card used to communicate with the NIAWG's PXIe crate. We are currently using the slowest such card.

Various Rearrangement Parameters In general the depth of the tweezers being moved is much larger than that of the static array, and the optimal depth varies depending on how fast the move is being conducted. We found that it worked best to use relatively fast movement times of 60 µs. In particular, we found that moving slower made various issues worse rather than better. This seems likely because there is a period of time at the start and end of a rearrangement move where the atom sees both the static tweezer and the moving tweezer, and that this back and forth pattern is a large perturbation that is probably capable of causing heating at frequencies that a single move is not capable of. Generally, intensity fluctuations are symmetric and only couple states of the same parity, causing them to drive transitions when they are near multiples of **twice** the trap frequency, while pointing fluctuations such as this referenced issue are capable of driving transitions at all multiples of the trap frequency.

Flashing Speed The biggest limitation of this technique is the speed at which tweezers can be effectively flashed. While the AOD responds at very high frequencies, it takes a non-trivial amount of time for an acoustic wave to travel across the body of the AOD crystal. Our AOD crystals are telerium-dioxide, which has a acoustic wave velocity of 4.2 mm µs^{-1}, meaning that for our 3 mm wide crystals, it takes 700 ns for the acoustic wave to travel across the crystal (the beam size inside the crystal however only has a waist of 0.8 mm). If we naively switch the RF configurations abruptly, inside the devices the tweezer light will hit both acoustic wave fronts at the same time. Specifically, if switching the horizontal (vertical) AODs between RF patterns f_{ha} and f_{hb} (f_{va} and f_{vb}), while we will get the desired deflections of $f_{ha} \times f_{va}$ and $f_{hb} \times f_{vb}$, we also get undesired tones at $f_{ha} \times f_{vb}$ and $f_{hb} \times f_{va}$. As a result, we typically operated near a flashing rate of 1 MHz, and with a dead time of ∼100 ns, considering that our tweezers do not entirely fill the AOD devices.

Unfortunately, these speed-based limitations are hard to improve on for AOD-generated tweezers. In general, it is desirable to make AOD crystals and the inputted laser size large, as this increases the number of resolvable deflections that the AOD can generate. This downside is addressable by using a smaller wavelength trap light which can, at the same size, make more spots, but we are limited in how short of a wavelength we can use without causing significant scattering off of the ^{87}Rb atoms. We are therefore not able to simply focus into the AOD or use a smaller crystal without sacrificing the size of the array. We are also limited in what materials it is feasible to make an AOD crystal out of. Some materials, such as fused silica, have higher speeds, up to about 6 mm µs^{-1}, but it is unclear to what extent an increase of only 50% solves this problem, and considering the significant time investment in testing a new AOD system compared to the effort of implementing a second independent tweezer system, and we decided the former was not worth the potential upside. However a combination of improvements along these lines along with better-performing objective optics might improve the performance of this method of rearrangement.

Fidelities We found that for a single, deterministic transfer between two tweezers, it was possible to optimize the rearrangement to be highly efficient, near 100% fidelity and not easily distinguishable from background loss in our system. However, for a system of 3×6 tweezers, which is the size we were using at the time, there are 54 possible moves between neighbors that need to work very efficiently. We found that it was quite challenging if not impossible to optimize our system to be efficient for so many different patterns at the same time. We found that our best results, after a large amount of individual move optimization, we could prepare a single loaded optical tweezer in a single experimental cycle with only about 90% fidelity (note that some groups report fidelities after many repeated cycles of rearranging and re-imaging to improve results). This was significantly higher than the loading efficiency of about 50% that we had at the time, but not significantly better than previous results we had obtained with enhanced loading [93] (the ΛGM procedure had not been developed yet). With an efficiency of 90%, it would be difficult to prepare any macroscopic arrangement of atoms with a reasonable repetition rate. However, it was still possible at these rates to create pictures of letters and spell out words (Fig. 3.14).

Flashing Rearrangement Conclusions In the end, after many optimizations, we were faced with a number of confounding issues in the flashing rearrangement that made the technique as a whole seem undesirable.

- Unexpected loss resonances requiring traps to be at very specific depths during the movement.
- Some movements would cause loss in nearby tweezers which in principle should be unaffected.
- Some unexplained issues prevented some moves from ever reaching a high move fidelity at any parameters
- Many of the optimized parameters did not seem very stable and required re-optimization on a weekly scale.

Many of these affects may be explained by a combination of factors:

- Nontrivial variations in trap shape across the field of view of our objective
- Our tweezers, like our PSF, may have a long tail which might be able to non-trivially affect tweezers which we would ordinarily think are far enough away.

It should be emphasized that it is still possible that these issues could be addressed and that the method could work. Indeed, future systems that have more well-behaved objectives may wish to test these ideas, as there are significant advantages in having a self-contained rearrangement system, including the need for consistently registering the two sets of potentials. However, it is important to remember that there is already a well-tested system for doing rearrangement, namely the introduction of a completely separate tweezer system in order to do the rearrangement.

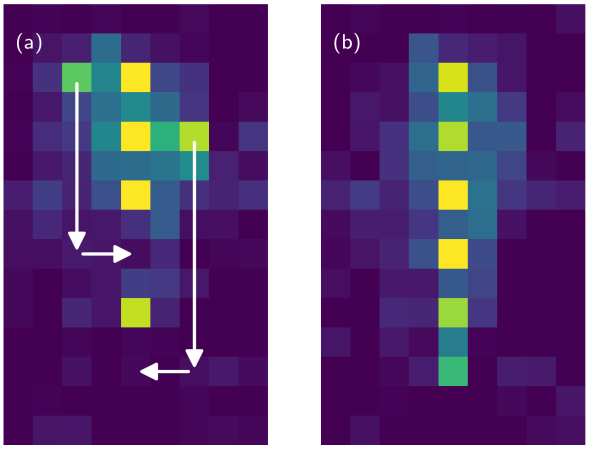

Figure 3.13: **Rearrangement into a Line.** **(a)** The initial loading pattern of a 3x6 array of tweezers. Lines show an example of how atoms could be rearranged to make a one-dimensional line of atoms. **(b)** A line of atoms, after being rearranged.

3.6.2 Jerk Rearrangement

Another idea which avoids some of the issues of flashing rearrangement, but introduces others, is what I call "Jerk" rearrangement. In this method, we turn off the main array, then use a single very deep tweezer to move the target atom from one site to another **very fast** (on the order of 1 µs per move), and then turn the original array back on, before the original atoms had time to fly away. This idea is essentially flashing rearrangement in the speed limit of a single flash. Somewhat surprisingly, it worked with a similar fidelity as the original flashing rearrangement. It suffered from similar issues in that the exact depth (which was generally much deeper) required careful, site-selective calibration, and the movement of the particularly deep tweezer tended to cause loss

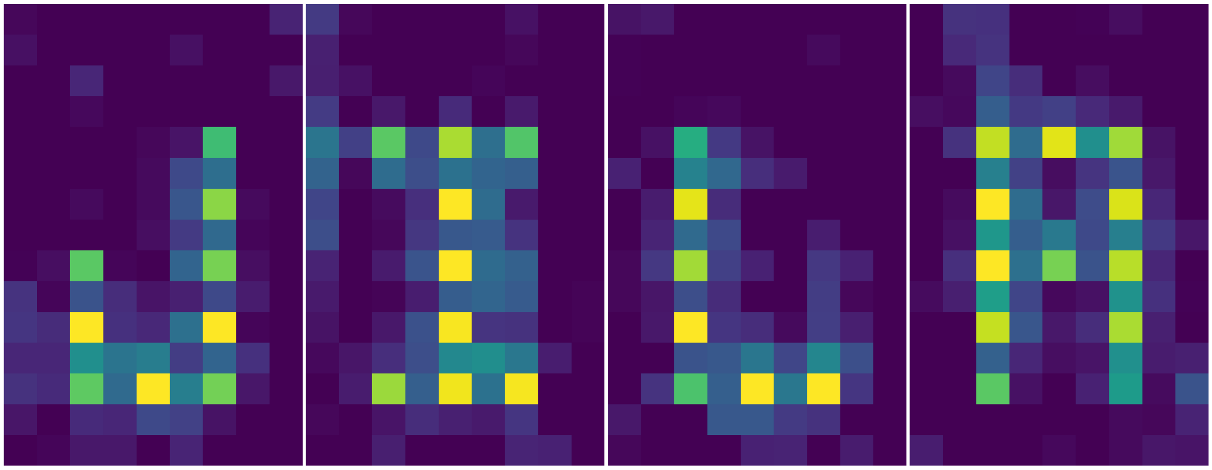

Figure 3.14: **Atoms Spelling Out JILA.** Four separate images of atoms after being arranged into letters to spell out "JILA".

in nearby tweezers.

3.6.3 Stiff Rearrangement

Another technique which seems simpler to implement than the others, but that is less powerful, is what I call the stiff rearrangement technique. This is the technique which went into the enhanced loading paper discussed in Chapter 4 [63]. In this technique, the initial loading configuration is analyzed to determine if one can make a target final array by **removing** entire rows and columns of the initial array, and the shrinking the rest (Fig. 3.15). Although all rearrangement techniques benefit from enhanced loading techniques, this is especially true with stiff rearrangement.

After densely loading an array, we first obtain the location of each atom using a single image (left panel Fig. 3.15(a)). Even with dense loading, the probability of loading a specific set of 6×6 traps is exponentially small (dashed lines in Fig. 3.15(b)). However, there are many potential sets of (sometimes disjoint) 6×6 traps embedded in the 10×10 array. We then search for such a configuration of completely loaded 6×6 traps. If successful, we turn off the extra traps to remove the excess atoms, and then contract and shift the identified disjoint array in a **single** move (right panel) [84]. At the time of this work, successful rearrangement to a square $n = 36$ (6 by 6) array

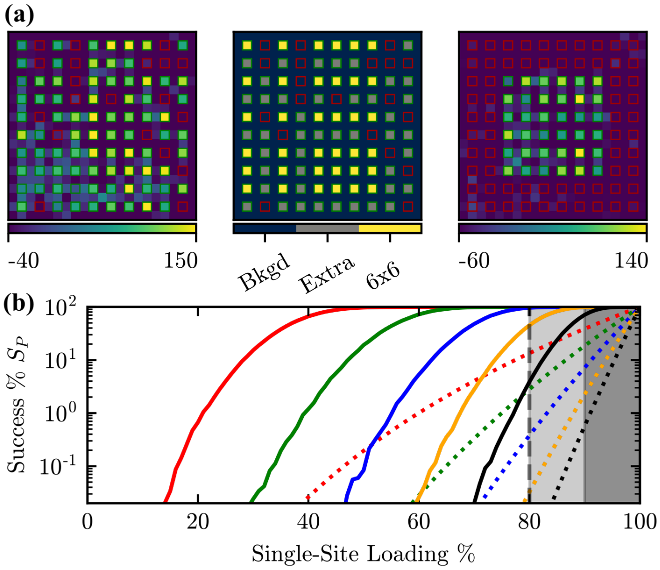

Figure 3.15: **Stiff Rearrangement in 2D. (a)** Single image of 80 atoms in an array of 100 traps with separation 2 μm (left). Binarized loading (center) indicating empty traps (red squares), occupied traps (gray pixels), and loaded traps selected for parallel rearranging (yellow pixels) to a defect-free 6×6 array. For the single-shot images, in each trap pixel (background pixel) the atom count threshold (average threshold of nearest neighbors) is subtracted for clarity from the count number recorded by the camera (see Appendix). **(b)** Monte-Carlo-simulated success probabilities (S_P) of finding a filled disjoint array of atoms within 10×10 traps as a function of loading efficiencies (solid lines), and corresponding loading probability of a specific array without rearrangement (dashed lines). Colors indicate target array sizes: 3×3 (red), 4×4 (green), 5×5 (blue), 6×6 (orange), and 7×7 (black). The light gray area is only accessible with average loading greater than 80%, and the dark gray area for greater than 90%.

only worked in 0.1% of cases due to unexpected loss observed when turning off rows and columns, in which an atom is effectively lost with a 17%-chance. This loss is technical in nature, and potential causes include intermodulation in the tweezer-generating RF tones or collisions between the trapped and dropped atoms. It is potentially related to other issues seen in the dumping of extra power into distant optical tweezers (Sec. 3.5.1) and the non-trivial imaging point-spread function of our system (Fig. 6.8).

However, as illustrated in Fig. 3.15(b), observing this array with this parallel technique would have been impossible without enhanced loading. In increasing the loading probability P from 60% to 80%, the percentage of experiment runs in which one could possibly extract a defect-free 6×6

array goes from 0.02% to 37%. Notably, this entire procedure is completed using only a pair of acousto-optic deflectors to control the optical tweezers.

Chapter 4

Gray-Molasses Based Optical-Tweezer Loading: Controlling Collisions for Scaling Atom-Array Assembly

In this chapter, I discuss our work on developing a new optical tweezer technique using Λ-enhanced gray molasses. It contains a mix of work that was done for our published result, and a variety of updated work that was done in recent months of 2021 after we could utilize a variety of recent experimental upgrades [63].

To isolate individual neutral atoms in microtraps, experimenters have long harnessed molecular photoassociation to make atom loading distributions sub-Poissonian. While a variety of approaches have used a combination of attractive (red-detuned) and repulsive (blue-detuned) molecular states, to-date all loading experiments have been predicated on red-detuned cooling. In our work, we present a shifted perspective – namely, the efficient way to capture single atoms is to eliminate red-detuned light in the loading stage, and use blue-detuned light that both cools the atoms and precisely controls trap loss through the amount of energy released during atom-atom collisions in the photoassociation process. Subsequent application of red-detuned light then assures the preparation of maximally one atom in the trap. Using Λ-enhanced gray molasses for loading, we study and model the molecular processes and find we can trap single atoms with 90% probability even in a very shallow optical tweezer. Using 100 traps loaded with 80% probability, we demonstrate one example of the power of enhanced loading by assembling a grid of 36 atoms using only a single move of rows and columns in 2D. Our insight will be key in scaling the number of particles in bottom-up quantum simulation and computation with atoms, or even molecules.

4.1 Introduction

In quantum simulation and computing, the assembly of large arrays of individually controllable particles is a frontier challenge. Ultracold gases of neutral atoms have long simulated quantum physics on a macroscopic scale, and quantum gas microscopes are now a window to microscopic dynamics [22, 94]. However, the desire for control of individual atoms, in particular for quantum computing, motivates pursuing bottom-up engineering of neutral atom arrays [36, 35, 51, 58]. In a Maxwell's demon approach, experimenters image single atoms and subsequently rearrange them into a desired pattern. The resulting ordered arrays have presented new opportunities in studies of multi-particle quantum dynamics [95, 96, 84, 97, 98, 99, 91, 86, 87]. Yet, compared to trapped ions, single neutral atoms are still difficult to trap and assemble.

In our work, we form ordered atom arrays by combining dense loading of large optical tweezer arrays with atom imaging and rearrangement [Fig. 4.1]. Using Λ-enhanced gray molasses (ΛGM) on the D_1 line of ^{87}Rb [100, 101], we can load single atoms with high efficiency in a trap shallower than required for standard sub-Poissonian loading [28] and nearly an order of magnitude shallower than required for previous enhanced loading [48]. While we demonstrate the idea with an array of optical tweezers in 2D, dense loading could also be used in optical lattices or in microtraps in 3D [86, 87]. We predict our technique will scale-up neutral-atom array assembly by expanding rearrangement algorithms and by enabling considerably larger ordered arrays.

To isolate single atoms in optical tweezers or lattices, one typically drives light-assisted collisions in the collisional blockade regime using red-detuned light [28, 29]. In this case, atoms are photoassociated to attractive molecular states in which they accelerate towards each other and gain kinetic energy that predominantly expels both from the trap [Fig. 4.1(a)]. If the collisions occur quickly enough to dominate the dynamics, as is the case in microtraps, a single atom is left about half the time. In the pioneering work of Ref. [48], after adding a blue-detuned laser to drive atoms into repulsive molecular states, the energy gained in the collision was tuned to induce single atom loss [48, 102, 93, 103]. Loading efficiency was enhanced to 90%, but at the cost of requiring large

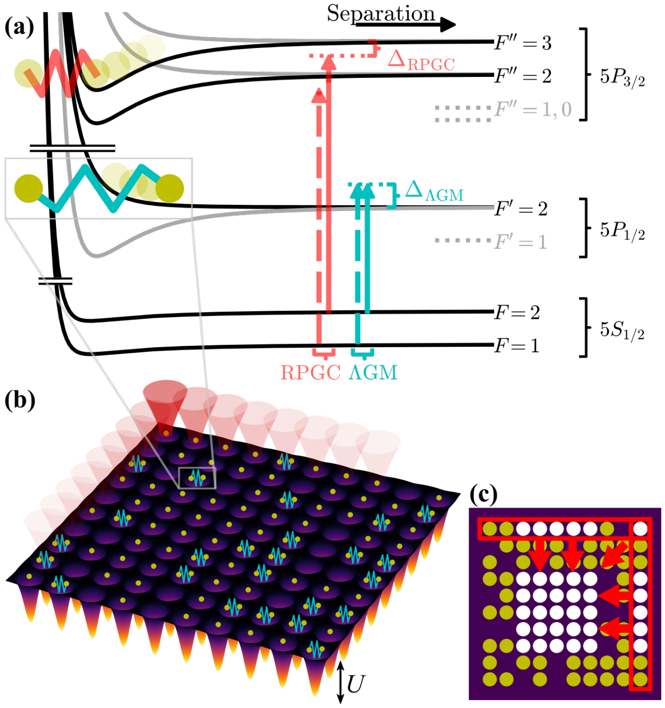

Figure 4.1: **Enhanced Loading and Rearrangement in Large Arrays.** **(a)** Sketch of laser configuration, and molecular energies versus interatomic separation. Solid (dashed) arrows show cooling (repump) lasers with indicated detunings. **(b)** Atoms loaded into an array of 100 traps with depth U formed by optical tweezers undergo blue-detuned light-assisted collisions. **(c)** Schematic of parallel rearrangement to form defect-free array with target atoms (white) after removing a subset of loaded atoms (yellow).

trap depths ($U/k_B \sim 3$ mK compared to 1 mK for red-detuned loading) and hence making use of the technique untenable in large arrays.

Here we resolve the conflict that has existed in previous work with enhanced loading – namely that red-detuned cooling drives lossy collisions and competes with desired blue-detuned collisions. By using ΛGM, we have the ability to cool into the trap and photoassociate with the same blue-detuned laser [Fig. 4.1(a)], and we can control the energy atoms are given in the collision by varying the laser's detuning. Further, we can make use of red-detuned and blue-detuned molecular photoassociation processes at will. In particular, we first modify the atom number distribution in the microtrap with blue-detuned cooling (ΛGM). We then apply red-detuned light, which both assures that not more than a single atom remains and, if it remains, images it. The loading behavior studied in a single trap agrees with a model of consecutive light-assisted collisions to repulsive molecular states. Our model further allows us to identify paths to even more efficient single-atom loading.

We find we can load a single optical tweezer with a trap depth of $U/k_B = 0.63(6)$ mK with 89(1)% efficiency, and a 10 × 10 array with 80.49(6)% efficiency [Fig. 4.1(b)]. We also demonstrate a proof-of-principle rearrangement technique that relies on the enhanced loading to create a 6 × 6 defect-free array using a simplified sequence of parallel moves of entire rows and columns [Fig. 4.1(c)] [84]. Lastly, we discuss how the efficiency of both this simplified rearrangement, as well as atom-by-atom assembly, scale exponentially with initial filling of the array.

4.2 Loading Studies and Modeling

4.2.1 Loading Experiments

Generally, in Λ-enhanced gray molasses (ΛGM) [101, 100] the cooling laser is set blue-detuned of a type-II ($F' \leq F$) transition and in a Λ configuration with a coherent repump laser [Fig. 4.1(a)]. Because of its greater isolation from nearby hyperfine manifolds, we chose to operate the ΛGM detuned from the $5\mathrm{P}_{1/2}|F' = 2\rangle$ state [in contrast to, e.g. $5\mathrm{P}_{3/2}|F'' = 2\rangle$]. Note, we were motivated to use ΛGM mainly as a natural way to blue-detune both cooling and repump lasers, which is a somewhat different motivation than in recent quantum degenerate gas experiments with light atoms and molecules – namely that gray molasses works on open transitions, and Λ-enhancement results in lower temperatures [104, 105, 106, 107, 101, 100, 108, 109, 110, 111, 112, 113, 114].

We first present results from loading a single optical tweezer using ΛGM, and compare to standard loading using red-detuned polarization gradient cooling (RPGC) [Fig. 4.2(b,c)]. We capture ^{87}Rb atoms in a magneto-optical trap (MOT) and then cool them into a spatially-overlapped optical tweezer with depth U with either ΛGM or RPGC. After the cooling and loading stage, we apply RPGC with parameters optimized for fluorescence imaging of the atoms. Initially, this quickly removes remaining atom pairs, and then images whether a single atom or no atom remains

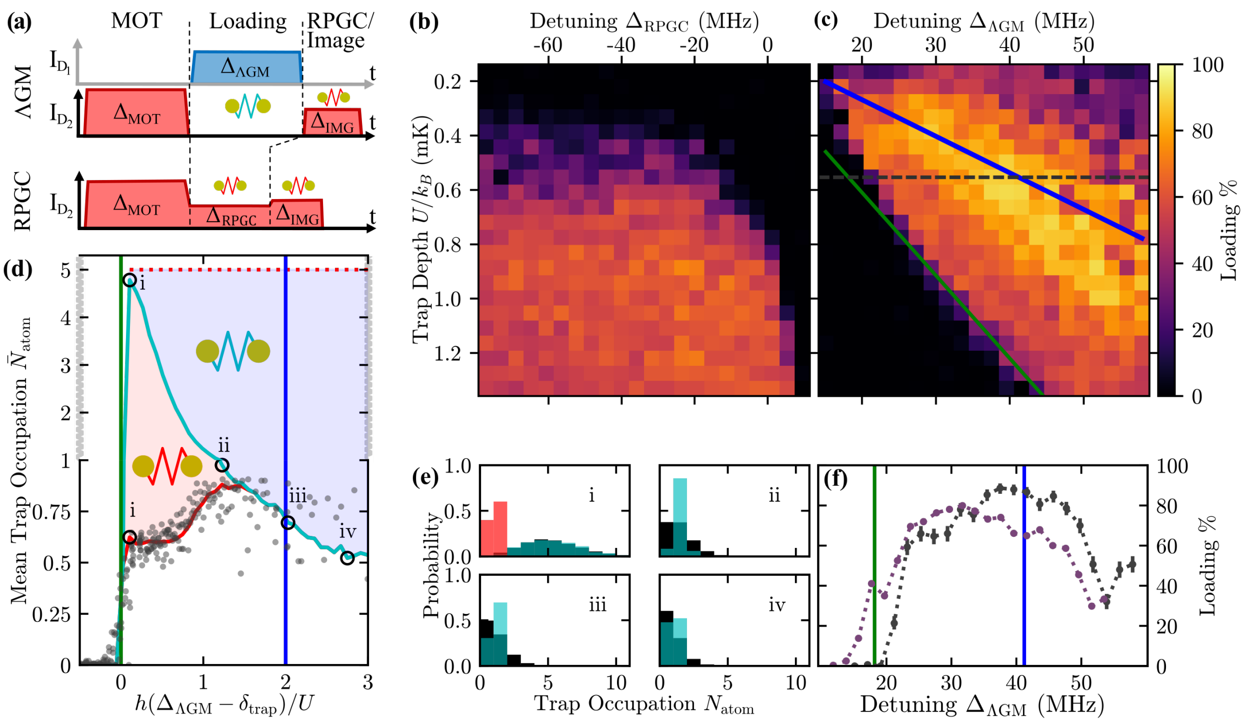

Figure 4.2: **ΛGM Comparative Loading Studies.** **(a)** Flow-diagram of experiments. **(b,c)** Average loading efficiency in to a single optical tweezer from 150 experiment repetitions as a function of bare laser detuning from the free-space resonance and trap-depth, for RPGC (b) and ΛGM (c). **(d)** Monte-Carlo simulated mean trap occupation with bi-linear vertical scale (black and gray axes). In the ΛGM-step, the initial trap occupation (dashed, red line) is reduced (cyan line) by blue-detuned collisions (blue area). In the RPGC imaging step, red collisions (red area) further reduce the trap occupation (red line). The resultant is compared with data (gray points) from (c) averaged for $U/k_B > 0.65$ mK (see text). **(e)** Histograms (cyan) of trap occupancy from the Monte-Carlo after the ΛGM-step for detunings indicated by the black circles in (d), compared to a Poisson-distribution (black) with the same mean trap occupation, and atom distribution after the RPGC-step (red in i). **(f)** Loading efficiency as a function of ΛGM-laser detuning Δ_{LGM} for a single tweezer (black) [see also cut along the black dashed line in (c)] and a regular array of 100 tweezers (purple) at $U/k_B \approx 0.55(5)$ mK. Error bars indicate statistical 1σ-confidence interval (see Sec. 4.7.3). Throughout panels, green lines are AC-Stark-shifted $|F=2\rangle - |F''=3\rangle$ transition (for RPGC) and AC-Stark-shifted $|F=2\rangle - |F'=2\rangle$ transition δ_{trap} (for ΛGM), and blue lines are $\delta_{\mathrm{trap}} + 2U/h$.

in the trap [Fig. 4.2(a)]. The procedure is repeated to determine average single-atom loading efficiencies, i.e., the fraction with which a single atom is found after both the loading and imaging stages. See Fig. 4.2(a) and Sec.4.7.3 for experimental-sequence timing and details of the imaging analysis. Also, see Fig. 4.1(a) and Sec. 4.7.2 for detailed laser configurations.

Fig. 4.2(b,c) shows the loading probability P as a function of both laser detuning from the closest atomic free-space resonance and trap depth, for both RPGC and ΛGM. With ΛGM we observe 89(1)% loading efficiency at $(\Delta_{\Lambda\mathrm{GM}},\ U/k_B) = (45\text{ MHz},\ 0.55(5)\text{ mK})$, and we can still load with $\sim 80\%$ efficiency at trap depths of $U/k_B \approx 0.27(3)$ mK. These findings are remarkable as with the same optical power we can load tweezer arrays that are more densely filled **and** two to three times larger compared to RPGC loading. The maximum RPGC loading of 64(1)% for $(\Delta_{\mathrm{RPGC}},\ U/k_B) \approx (-14\text{ MHz},\ 1.1(1)\text{ mK})$ is among the highest reported for RPGC [93, 103, 97, 84]. In the simplest picture of RPGC, one expects 50% loading, but, in agreement with other studies [103], additional processes result in $\sim 35\%$ of the collisions causing only one atom to leave the trap.

A physically rich picture can be gained from studying the detuning dependence of ΛGM loading [Fig. 4.2(c)]. First, note that the trap light results in an AC Stark shift $\delta_{\mathrm{trap}} = 32.8\frac{\mathrm{MHz}}{\mathrm{mK}}\frac{U}{k_B}$ of the atomic transition in the center of the trap [green lines in Fig. 4.2(c,d,f)]. The blue line in Fig. 4.2(c,d,f), which marks a shift of $2U/h$ from the trap-shifted resonance, is a key energy scale for the physics of the enhanced loading. At shifts smaller than $2U/h$, the collision does not give a pair of zero-temperature atoms sitting at the bottom of the trap enough energy for either to escape, while at larger detunings both atoms will be expelled. A finite temperature, and hence an initial center of mass motion, will blur the transition, and indeed is necessary for inducing the desired single-atom loss. Although our data are roughly consistent with this picture, we look more closely by plotting the data of Fig. 4.2(c) against a dimensionless detuning $h(\Delta_{\Lambda\mathrm{GM}} - \delta_{\mathrm{trap}})/U$. We do this for all data traces $U/k_B \geq 0.65$ mK [Fig. 4.2(d)], and observe a number of interesting features. For example, we observe a $\sim 60\%$ loading probability for small detunings and that the maximum loading peaks below the $2U/h$ shift (blue line).

4.2.2 Loading in Large Arrays

We have also performed a loading study for an array of 10×10 optical tweezers spaced by 2 μm. We display the measurement at $U/k_B = 0.55(5)$ mK as the purple line in Fig. 4.2(f). Compared to the single-trap data at similar U (black), the data are shifted to smaller detunings, and we observe a maximum loading of 80.49(6)% in a single run averaged over the 10×10 array. These effects could be due to a variety of consequences of the larger array: variations in trap shape and depth or overall degradation of the optical spot sizes (see Sec. 4.7.1). Note that our experimental apparatus was designed and optimized to entangle closely-spaced atoms in ground states, in contrast to systems that interface (farther-spaced) Rydberg atoms. This places constraints on the tweezer array, such as acousto-optic device mode, trap-light detuning, optical power, and high-NA field-of-view, that mean with typical loading we are limited to working with array sizes less than 10×10. However, ΛGM-loading allows us to scale up both the size of our arrays as well as the total number of atoms we can trap, and is a unique realization for enhanced loading in optical tweezers.

4.2.3 Loading Model

To elucidate trends in Fig. 4.2(c), we have carried out a Monte-Carlo calculation of the collision dynamics. At the time of the original experiment, we had not yet dived deep into the molecular physics of the two-atom systems, as is done in Chapter 5. Therefore, our original model did not take into account the detailed nature of these potentials and the effect that they may have on the loading process. Those considerations will be discussed in chapter 5. Here, I discuss our original model.

Generally, we expect loading to be affected by both collisions and the ΛGM cooling performance, and both may be influenced by the non-trivial light shifts and polarization gradients in the tweezer traps. Modeling the interplay of these effects is beyond the scope of this work, but we can understand the collisional process quantitatively if we assume the continuous ΛGM cooling can load at least a few atoms per trap, and re-thermalizes any atoms remaining after a collision. The simulation starts by preparing a Poisson-distributed number of atoms N_{atom} with a mean number $\bar{N}_{\text{atom}} = 5$ and temperature T, where $\bar{N}_{\text{atom}}$ was chosen > 2.5 to avoid loading zero atoms initially. To simulate the finite experiment cooling time, we calculate a finite number of 5000 time steps each having two atoms collide once if they are closer than 100 nm. A collision might eject none, one, or both atoms out of the trap depending on the final energy of each atom, which is determined by their pre-collision energy and the collisional energy gain $E = h\,[\Delta_{\Lambda\mathrm{GM}} - \delta_{\mathrm{trap}}]$. This simple assumption makes this simulation easier, but future more accurate simulations could take as inputs results from the molecular physics calculations in Chapter 5. This process continually reduces N_{atom} in each time step. At the end, the RPGC imaging is simulated by assuming that it entails a fast collisional process at the start of the image where red-detuned collisions reduce atom numbers in a manner consistent with our red loading - namely we reduce any remaining $N_{\mathrm{atom}} > 1$ by 2 with a chance of 65% and by 1 with a chance of 35% until $N_{\mathrm{atom}} \leq 1$.

Fig. 4.2(d) shows the result of the Monte-Carlo simulation by indicating the mean trap occupation $\bar{N}_{\mathrm{atom}}$ as a function of the normalized collisional energy gain. During ΛGM-loading, the initial atom number (red dashed line) is reduced (cyan line). During RPGC imaging $\bar{N}_{\mathrm{atom}}$ is further reduced [red line in Fig. 4.2(d)]. Fig. 4.2(e) shows the simulated atom-number distribution (N_{atom}) in the trap and how atom loss in the ΛGM and RPGC-phase modifies the Poisson distribution.

We observe three physical regimes: For $E \ll 2U$ [see panel (i) in Fig. 2(e)], the ΛGM-phase has little effect as almost no atom loss occurs, hence the initial Poisson-distribution (black distribution) is not modified (blue distribution). The initial phase of the RPGC-imaging step, however, reduces the number of atoms to 0 or 1, yielding a RPGC-like 65% mean trap occupation (red distribution). In contrast, for $E \gg 2U$ (panel iv), two-body losses dominate in the ΛGM-phase as every collision expels both atoms from the trap resulting in $N_{\mathrm{atom}} = 0$ ($N_{\mathrm{atom}} = 1$) in $\sim$ 50% of the cases if the loaded N_{atom} was even (odd). Hence after ΛGM, $N_{\mathrm{atom}} < 2$ and the red-detuned imaging phase does not modify the atom-number distribution anymore. At the transition $E \approx 2U$ (panel iii), both single atom and two-body losses occur in the ΛGM-phase with roughly equal probability because of the finite temperature. Since two-body losses tend toward an equal distribution of $N_{\mathrm{atom}} = 0$ and 1, and single-atom loss toward $N_{\mathrm{atom}} = 1$, we load a single atom ($N_{\mathrm{atom}} = 1$) in 75% of the cases. Again, RPGC-imaging does not modify the distribution as $N_{\mathrm{atom}} < 2$ after ΛGM. Maximal loading probability is found at $E < 2U$ (panel ii) where only single-atom loss occurs. Here, any occurrence of $N_{\mathrm{atom}} = 0$ is a result of either no atoms having been loaded initially, or the ΛGM-step has not finished (finite $N_{\mathrm{atom}} > 1$ after ΛGM), and RPGC-imaging then ejects pairs atoms.

This simple model indicates no fundamental limitations to the loading efficiency and that by optimizing the trap size, atom temperature, and related parameters, it may be possible to reach higher loading fractions. Note that the only free parameter that affects the prediction of the simulation is the atom temperature T in the trap. The simulation describes our data well for T =120(10) µK, which needs to be understood as an average value for the different trap-depths U that were investigated. This value is close to the free-space ΛGM temperature we measure of T ≈50 µK, which is higher than typical values, likely due to non-ideal beam geometries (see Sec. 4.7.2).

This model could be refined with a more detailed understanding of the molecular physics involved, which we investigate in Chapter 5.

4.3 Recent Further Explorations

4.4 Role of Λ-enhancement

In gray molasses, the atom is at in general in a coherent superposition of states in a given manifold that experiences coherent population trapping and are therefore somewhat dark ("gray") to the cooling light. In ΛGM configurations, the coherent superposition is extended to involve states in multiple ground-state manifolds, which generally has the effect of improving the cooling limit. The ΛGM configuration was originally chosen simply because it is a convenient cooling configuration which used entirely blue-detuned light. It was not initially clear if the loading would benefit specifically from the Λ-enhancement, and as Λ-enhancement can be technically more challenging than regular gray molasses, we thought it would be useful to explore more thoroughly.

Unenhanced gray-molasses-like cooling is easily available for us by detuning our repump frequency to be near-resonant with the atomic transition instead of with the Raman resonance where there is strong Λ-enhancement. Notably, here the repump is operating on the type-I $F = 1 \to F' = 2$

transition ($F' > F$). There exist cycling transitions here, and we therefore do not expect that any population in this manifold can be dark to the repumping light. Rather, the dark state is entirely in the $F = 2$ manifold, and the repumper only serves to pump into this state. This contrasts with the behavior on the Raman resonance, where the dark state is in general expected to coherently include population in both ground-state manifolds, with the $F = 1$ population prevented from rotating through Raman transition into the $F = 2$ manifold via interference with the $F = 2$ state populations. It should be noted however that, in general, predicting the dark state itself is non-trivial as it depends carefully on the polarizations of the light fields being applied, and in the presence of the tweezer potential would spatially vary.

Recently, we've taken more data indicating that we can get some enhancement with this "regular" gray-molasses, but that we get much better enhancement with the Λ configuration (Fig. 4.3). In Fig. 4.3(a) we scan the frequency around this free-space resonance, and we see that on the blue-detuned side of it we get some enhancement, with a maximum loading efficiency of $0.717^{(+27)}_{(-25)}$. However, there is significantly higher loading efficiency on the Raman resonance, where in this configuration with 7 atoms, we get a maximum loading efficiency of $0.810^{(+15)}_{(-17)}$.

It is as of yet not entirely clear why the loading works better with the Λ-enhancement. Several theories exist, including that with the Raman resonance it is possible to get significant repumping action with the repumper far blue-detuned without unnecessarily broadening the transition. Acting on a broadened transition might prevent us from selecting specifically repulsive potentials. It is also true that we expect the ΛGM configuration to result in a different equilibrium population distribution among the single atom F and m_F levels. This might also have impacts on the symmetry of the colliding atoms, which could affect which transitions are excited to. More research is required to further inform the mechanism at play here.

In addition, we note in passing that in the scan we can see the broadening of the transition with increasing repump power, and that we strangely see the loading suddenly drop at high power. It is not yet clear why this is and may be an uninteresting technical issue with our setup. We create the repump light using a fiber-based EOM, and it is possible we are simply running into technical

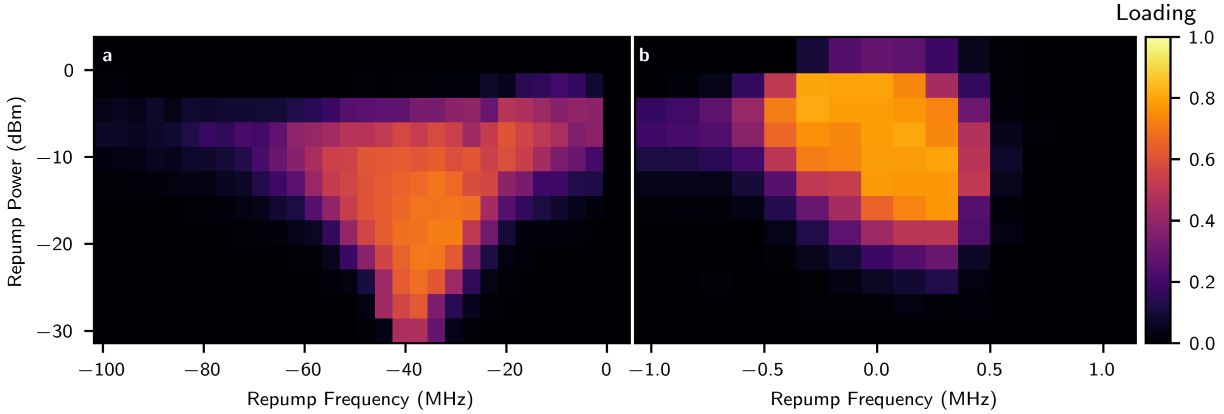

Figure 4.3: **Scan of Repump Power and Frequency Parameters.** **a** A wide scan, where we see loading where the repump light is near-resonant with the atomic transition. Slight loading enhancement without coherent *Lambda*-enhanced cooling is visible on the blue side of the transition. The Raman resonance is not visible because of it's narrowness, but exists on the right-hand side of this data. The zero is the approximate location of the free-space resonance. **b** A zoom in on the Raman resonance, where we benifit from *Lambda*-enhanced cooling. Note the different x-axis scale.

issues when we drive it sufficiently hard.

4.5 Wider ^{87}Rb D_1 $F' = 2$ Parameter Scans

With a new laser system and a new laser locking configuration as discussed in Sec. 2.2.1.2, it was later possible to take larger frequency scans than in our original work. This resut is shown in Fig. 4.4. The broadened scan shows a number of interesting features.

We see poor loading at high detunings and low trap depth, possibly due to inefficient free-space cooling in this regime. The loading reverts to $\leq 50\%$, at larger depths. Perhaps in the larger depth the trapping volume is effectively bigger so that collisions are rarer, leading to poor loading in this region. Perhaps the variations in the light shifts that the atom sees creates a situation where it is difficult to tune the detuning of the loading to be relevant for all shifts. It is not yet clear.

Finally, notably the loading is non-zero at large depths and shallow detunings, where the LGM light is red-detuned (and heating) in the deepest part of the trap. This may be due to a mechanism like that the ΛGM is still cooling at the edges of the trap, where the light shift is

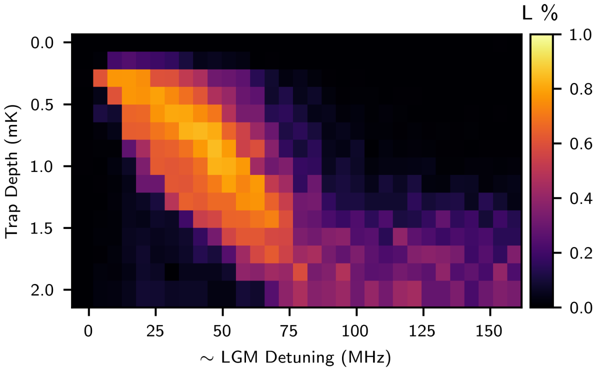

Figure 4.4: **A Wider $F' = 2$ ΛGM Scan.** A scan of the loading on the $F' = 2$ ΛGM system that is wider than original scans could be. We see a number of new interesting additional features here at large depths and larger detunings, which are discussed in the main text.

smaller, and that it's possible to retain an atom in this region.

4.6 Loading on the ^{87}Rb D_1 $F' = 1$ Transition

An interesting further test case that was readily available to us was attempting to load in a different loading configuration, where the main (repump) laser is tuned to the D_1 $F = 2 \rightarrow F' = 1$ ($F = 1 \rightarrow F' = 1$) transition instead of the D_1 $F = 2 \rightarrow F' = 2$ ($F = 1 \rightarrow F' = 2$) D_1 transition (Fig. 2.3). The transition is such that it should support dark states similar to our traditional loading configuration, so we can expect that it is possible to do ΛGM on this transition similarly. In the new configuration, the lasers are all red-detuned of the $F' = 2$ transitions, but it is a-priori not clear that this is important since these transitions are 800 MHz away from the transition of interest.

Practically, we do this by locking the D_1 Master to the ^{87}Rb D_1 $F = 2 \rightarrow F' = 2$ transition and offsetting by ~ -1000 MHz (with an extra 230 MHz included to account for an AOD shift), whereas normally we lock to the ^{85}Rb $F = 2 \rightarrow F' = 1$ transition and offset by ~ -900 MHz. Future laser locking configurations may be able to scan smoothly between these transitions without relocking the laser.

We begin the test by checking the free-space temperature of this different ΛGM configuration, and find a temperature of 12 µK, which is consistent with the temperatures we get from the $F' = 2$ ΛGM configuration in our system, so we can conclude that the free-space single-atom ΛGM performance is similar to that in the $F' = 2$ configuration and should not cause significant issues.

We then examine loading in this configuration in Fig. 4.5. Qualitatively, the dependence of the loading on the laser frequency and trap depth follows the exact same patterns as that on the $F' = 2$ transition, with the exception that the peak loading efficiency is significantly lower, maximizing at $0.601^{(+35)}_{(-34)}$. This is similar to the RPGC configuration, which was also capable of loading slightly greater than 50%.

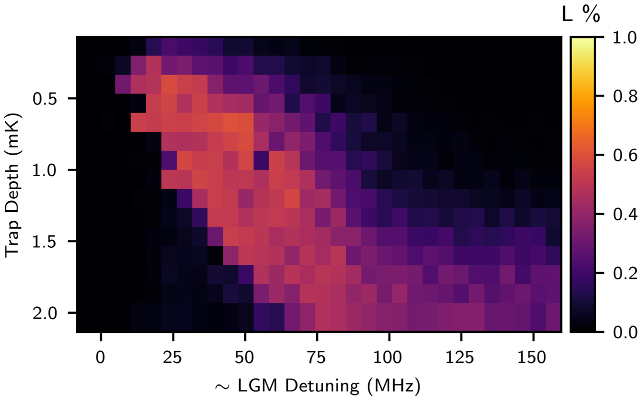

Figure 4.5: **A D_1 $F' = 1$ ΛGM Scan.** Scan of the loading performance as a function of trap depth and loading frequency with the $f = 2 \rightarrow F' = 1$, $f = 1 \rightarrow F' = 1$ ΛGM loading configuration. Features of the loading are almost identical to the $F' = 2$-based configuration, except that the maximum loading efficiency here is significantly lower, and the loading feature is generally more flat-topped than before.

This is a very valuable result, as it is illustrative of the complexities of the ΛGM loading mechanism. With traditional pictures of the loading, it is not at all obvious why the new configuration does not enhance the loading efficiency. Our best explanation for this behavior is actually the nature of the molecular states is significantly different on these transitions than on the $F' = 2$ based ones. In particular, in Chapter 5 we show that many of the blue-detuned molecular potentials that are relevant for this transition do not have significant repulsive barriers and are actually mostly attractive in nature (Sec. 5.7). This would be difficult to predict without the full calculation discussed there and goes a long way towards an explanation of this behavior.

4.7 Technical Details for Grey Molasses Optical Tweezer Loading and Rearranging

4.7.1 Optical Tweezers

We generate an array of optical-tweezer traps spaced by $2\,\mu\mathrm{m}$ in the xy-plane by passing a single 850 nm laser beam through two orthogonal longitudinal-wave $\mathrm{TeO_2}$ acousto-optical deflectors (AODs) with center frequencies (bandwidths) of 180 MHz (90 MHz). Each modulator is driven with a sum of radio-frequency (RF) tones with frequency (amplitude) that can be individually and dynamically adjusted to control the position (intensity) of different tweezer-rows and columns. The relative phases of the tones are set to minimize intermodulation in the RF setup. The array of deflections created by the AODs is then imaged by a 0.6-NA-objective lens into a glass cell. This creates a trap with a $0.68\,\mu\mathrm{m}$ waist for a single tweezer, and traps with an average waist of $0.75\,\mu\mathrm{m}$ for a 10×10 array. The standard deviation of the trap depths was minimized to 8% by optimizing the RF amplitudes. Trap depths are calibrated by measuring light-shifts of in-trap atomic transitions as a function of trap power and applying a linear fit; the slope gives a calibration of the intensity of trap light the atom experiences, which can be used to directly calculate the trap depth [115]. Errors on trap depths are 1-σ errors extrapolated from the errors on the slope of the linear fit. The lifetime of atoms in the traps is limited to 5 sec by the background pressure.

4.7.2 Laser Cooling and Loading

In all experiments, three beam paths are used to address the atoms. Two (diagonal) paths are along the diagonals of the xy-plane, and a third (acute) path in the xz-plane is at an angle of 55° from the z-axis to avoid the objective [64]. All lasers along these paths are retro-reflected and in a $\sigma^+\sigma^-$ polarization configuration.

Our magneto-optical trap (MOT) is spatially overlapped with the trap array and cools atoms for 500 ms to a temperature of $\sim 100\,\mu\mathrm{K}$, measured by imaging its ballistic expansion. The cooling (repump) laser is red-detuned from the D_2 $|F = 2\rangle \to |F'' = 3\rangle$ ($|F = 1\rangle \to |F'' = 2\rangle$) transition, and applied on all three beam paths (on only the diagonal paths). In the case of the 20-ms-long RPGC stage we cool the atoms to 10 µK. For this, we detune the cooling (repump) laser by Δ_{RPGC} (20 MHz), set the intensities at 1.3 I_{sat} (0.1 I_{sat}) on the diagonal paths and 4.5 I_{sat} (0 I_{sat}) on the acute path, and zero the magnetic fields.

In the case of the 200-ms-long Λ-enhanced gray molasses (ΛGM) stage, we apply a cooling laser that is detuned by $\Delta_{\Lambda\mathrm{GM}}$ from the D_1 $|F = 2\rangle \to |F' = 2\rangle$ transition at 2.5 I_{sat} (0.4 I_{sat}) on the acute (diagonal) paths. We create the coherent repump beam from the cooling laser on the acute path using an electro-optic modulator. The repump beam is detuned by $\Delta_{\Lambda\mathrm{GM}} + 0.14$ MHz from the D_1 $|F = 1\rangle \to |F' = 2\rangle$ transition and at 1.5 I_{sat}. Note that the optimal ΛGM free-space temperature of 50 µK is reached for $\Delta_{\Lambda\mathrm{GM}} \approx 15$ MHz and is likely limited by the beam path geometry and repump light configuration.

4.7.3 Imaging, Data, and Statistics

Regardless of the loading configuration, we image the atoms using another RPGC stage with the cooling beam ($\Delta_{\mathrm{RPGC}} = -19$ MHz at 3 I_{sat}) only on the acute path. We alternate the tweezer-light with the imaging light at 2 MHz to scatter light when atoms are experiencing no light shifts. This configuration is maintained for 20 ms during which we collect scattered photons on an EMCCD camera, super binned to 4×4 pixels to reduce readout noise. As we now discuss experimental evidence for, this red-detuned imaging process quickly kicks out any pairs of atoms that might exist, for example, in the case of a gray molasses loading stage with a small detuning [Fig. 4.2(d) and (e)]. Accordingly, it does not resolve a tweezer's occupation number following the gray molasses stage [illustrated by the cyan line in Fig. 4.2(d)], but rather maps the atom number onto 0 or 1. If this loss did not occur quickly compared to the imaging time, we would sometimes collect numbers of photons significantly larger than our calibrated single-atom scattering rate. We do not observe this signature despite high experimental statistics, suggesting a sub-percent impact of these effects on the imaging.

At every atom location individually, to determine a count threshold that indicates the presence of an atom in the trap, we create a histogram of all counts during an experiment and fit it with a sum of two Gaussians. The threshold with maximal fidelity $\mathcal{F}$ is found, where $\mathcal{F} = 1-(E_{fp}+E_{fn})$, with E_{fp} (E_{fn}) being the expected rate of false positives (false negatives) from the fits. This converts a sequence of counts to a sequence of Booleans which is averaged to determine the loading probability. By finding thresholds for each trap individually and subtracting them from the images in Fig. 3.15(a), we compensate for a spatially varying background noise and, due to the limited field of view of our high-NA lens, the different numbers of photons we collect for each trap.

All errors reported indicate 1-σ equal-tailed Jeffrey's prior confidence intervals [116]. The loading efficiencies reported in the main text for RPGC (64(1)%), ΛGM (89(1)%), and 10×10-ΛGM (80.49(6)%) were obtained by analyzing 2000, 1000, and 5000-per-atom repetitions with threshold fidelities 0.987, 0.998, and 0.993 respectively.

4.7.4 Scaling Arguments

The full potential of dense loading using ΛGM will come when combined with the most advanced atom-by-atom rearrangement algorithms in 2D or 3D [97, 86, 87]. In principle, if the Maxwell's demon atom rearrangement operation is perfect, and if a large number of traps are used, one would expect very large arrays could be created through a bottom-up approach regardless of the loading. Practically, however, there are many factors that steeply limit creating large-scale systems with optical tweezer assembly. In particular, a finite atom lifetime compared to the time required for rearrangement, and also simply the number of traps that can be created and loaded.

Our approach addresses these problems because it is efficient in shallow traps. Hence, with ΛGM more loadable traps can be created with the same amount of optical power. Additionally, 2D algorithms fill defects in a target array of size n with a sequence of $m \propto (1-P)n^{1.4}$ single moves, which we verified with Monte-Carlo simulations [97]. In scaling up array sizes, the time and number of moves required become lengthy, lowering the probability of successful rearrangement (S_P) as errors ϵ due to finite move fidelities and background collisions suppress this success rate as

$e^{-m\epsilon}$ [97]. Increasing the loading probability P from $P = 60\%$ to $P = 90\%$ would decrease m by a factor of 4, making larger array sizes more obtainable and exponentially improving the success probability S_P.

4.8 Conclusion

In conclusion, by gaining control over photoassociation to molecular states we have demonstrated enhanced loading of arrays of shallow optical tweezers. As described in Secs III A and B, we achieved a strong relative improvement on our trapped atom-numbers, but experimental platforms designed to host more optical traps than our system will stand to benefit even more. For example, Ref. [97] loads approximately 50 atoms with a 2D-array of 100 traps of 1 mK depth. With the same optical power and ΛGM, one would expect to utilize 370 traps of 0.27 mK depth and, based on the shallow-depth loading of single atoms at $P = 80\%$ of Fig. 2(c), load approximately 300 atoms – a six-fold increase. Further, the density of the filling will affect the number of moves required in rearrangement [84]. Using a technique that moves atoms individually [97], our Monte-Carlo simulations indicate that rearranging 300 atoms at $P = 50\%$ requires approximately 900 moves on average, whereas at $P = 80\%$ it requires 320 moves. As a result, the probability to retain all 300 atoms in the rearrangement protocol increases roughly from 0.1% to 10% when going from $P = 50\%$ to $P = 80\%$, assuming a 420 second atom lifetime [117], 1 ms per move, and a 99.3% move fidelity [97].

We have now more thoroughly studied ΛGM on the ^{87}Rb D_1 $5S_{1/2} - 5P_{1/2}$ transition. It will be interesting to continue to explore a variety of other related cooling techniques in future experiments. This could include transitions with narrower linewidths, such as the $5\mathrm{S}_{1/2} \rightarrow 6\mathrm{P}_{1/2}$ transition. It is also known that gray molasses is effective on the $5S_{1/2} - 5P_{3/2}$ transition [113], and future studies could compare the salient molecular physics in each manifold [118], especially considering details of the molecular potentials which we explore in Chapter 5. Further, there is much room for explorations of the interplay of collisions and cooling in microtraps for a host of blue-detuned cooling mechanisms with alkali atoms, other atomic species, and even molecules [119, 110].

In general we find that these loading studies are full of rich dynamics and unexplained behavior. It is both interesting from a physical perspective and important for practical applications, so we anticipate conducting future research on this topic in order to more fully understand the complicated multi-particle dynamics of these loading configurations.

Chapter 5

Molecular Potentials for Ultra-Long Range ^{87}Rb Dimers

5.1 Introduction

In this chapter, we present early work on the calculation of long-range molecular potentials for a pair of ^{87}Rb atoms in the regime of interest for our recent recent work involving light-assisted collisions between atoms in optical tweezers which are used, among other purposes, to load single atoms into optical tweezers. Compared to common photo-association experiments, these collisions are uniquely very long range ($\gtrsim$ 10 nm), and sensitive to low-energy scales on the scale of the trap depth ($\sim$ 20 MHz) and ultracold collisional energies ($\sim$ 200 kHz). As such, while in general the theory of ultracold photoassociation is well established, especially in the context of photoassociation experiments, feschbach resonances, and Rydberg interactions, there remain many questions about our unique regime that are yet to be studied [120, 121, 122, 123, 124, 118].

The potentials calculated include asymptotic Born-Oppenheimer (BO) interactions, fine structure (FS) and hyperfine structure (HFS) interactions. While related potentials and calculations appear in the literature, there is relatively little explicit discussion of how to properly symmetrize all the interactions and calculate in these potentials [125, 126]. Doing this requires assimilating literature over a very broad range of historical times and notational standards. Speaking personally, as a humble experimentalist this was a uniquely challenging endeavor. It should be understood that developing thorough understanding of these calculations is a very subtle task. This chapter of my thesis should be understood as my best effort to explain these calculations but that there are numerous aspects of the molecular physics here which still elude me, and there is still much work that to expand upon. However, we still think it is useful to summarize my notes here for future work and for others who may find potentials such as these useful. We find that having explicit calculations of the potentials has significantly refined our picture of how the collisions result in loading processes, and yields plausible explanations for many phenomena observed experimentally.

Most of the work in our lab is with individual ^{87}Rb atoms, or with many weakly-interacting ^{87}Rb atoms in their electronic ground-states. Ground state atom-atom interactions can be approximated as S-wave collisions that are parameterized by a single constant: the scattering length [127]. For ^{87}Rb this is $a_{sc} \approx 97a_0$ where a_0 is the Bohr radius, although the value varies by 1% depending on the hyperfine states of the interacting atoms [127].

In the case of loading single atoms into a tweezer using light-assisted collisions, collisions are additionally complicated as a result of the interaction of the atoms with the collisional light. Several other groups have previously made progress with relevant characterizations of single-atom loading and light-assisted collisions [29, 128, 47]. To first order, this technique, which utilizes molecular potentials which are blue-detuned from the separated-atom resonances, can be understood as involving optical shielding effects which have been observed and studied in a number of other contexts [129, 130, 131]. In this case, atoms are excited by the loading light into an “S+P” molecular potential, where the valence electron of one atom is in the ground state $l = 0$ “S” potential, where l is the orbital angular momentum quantum number, and the other is in the excited $l = 1$ “P” potential. This generally results in a significant amount of heating of pairs of atoms, causing pairs of atoms to be lost from the tweezer. The actual dynamics of the loading procedure are presumably then very dependent on the details of the molecular structure of the atoms. We became especially interested in this subject matter upon discovering our gray-molasses-based loading technique, and subsequently began to study these structures in greater detail in order to elucidate the exact mechanisms of the loading technique and hopefully to be able to predict and improve loading rates [63]. Starting in the spring of 2020, I began constructing these calculations with the help of regular discussions with Jose D’Incao and some helpful notes from Paul Julienne [132].

While ^{87}Rb is a "simple" alkali atom, accurately calculating the molecular potentials experienced by two such atoms is technically rather challenging. Despite the prevalance of ^{87}Rb studies in the literature, these calculations are not generally available in the region of interest for the experiment. Most previous studies originate from photoassociation spectroscopy work and deal with energy scales many orders of magnitude larger than those of interest to us. As a result, most of the calculations in the field don't go so far as to include the hyperfine interactions, for instance. However, several photoassociation review articles[120, 118] are still especially useful here. Several books are also useful references, especially for some of the theory regarding the symmetries in molecules [133, 134].

5.2 Problem Statement

It is easy to get lost in the results of these calculations, and lose track of exactly what purpose they serve and how they should be interpreted. As such, we start with a pedagogical explanation of our problem, the BO approximation which is essential to our approach, our methods, and how the results should be interpreted.

In general we are interested in characterizing the way in which two atoms collide with each other. In particular, for single-atom loading processes, we are interested in characterizing the amount of energy that the pair of atoms might gain in a collision, and what influences these energies. As such, the approach is to write down the full Hamiltonian of the system and use it to derive eigenstates, eigenenergies, and analyze scattering processes. This is challenging, however, since the Hamiltonian representing the interaction of two neutral atoms consists of the interactions between two nuclei and two electrons, and generally more considering the complicated electron-electron interactions between heavy atoms that are very relevant at short distances. As such, a simplification should be made, and the standard approach is the use of the BO approximation.

Anticipating this, in the center-of-mass frame, we can write down our Hamiltonian in a suggestive manner:

$$H = T_R + H_{EE}(R, \vec{e}) \tag{5.1}$$

Where R is the internuclear distance, $T_R = -(\hbar^2/2\mu)\partial^2/\partial R^2$ is the relevant kinetic energy operator with μ the reduced nuclear mass, and $H_{EE}(R, \vec{e})$ includes "everything else" in the Hamiltonian, including electron kinetic energy operators, electron-electron interactions, electron-nucleus interactions, and any other corrections one wishes to include. $\vec{e}$ represents all other coordinates, such as electron coordinates, that would be needed to describe the Hamiltonian.

The Hamiltonian has no explicit time-dependence, so we are quickly dealing with the time-independent Schrodinger's equation. What we'd **like** to do, is to use the separability ansatz that $\psi(R, \vec{e}) = \psi_R(R)\psi_{*e}(\vec{e})$, but one quickly arrives at a problem: $E - T_R\psi_R(R)/\psi_R(R) = H_{EE}(R, \vec{e})\psi_{*e}(\vec{e})/\psi_{*e}(\vec{e})$. At this point, continuing with standard separation of variables strategies, we would normally declare that each side is a function of different variables and therefore that in order to be equal, they must both be constant. This strategy however pales in face of the R-dependence of the $\hat{H}_{EE}$. Therefore, we now introduce the BO approximation, that R and the center of mass kinetic energy are effectively constant, and that the problem is effectively separable and can be stated as solving the pair of equations:

$$H_{EE}(R, \vec{E})\psi_e(R, \vec{e}) = V_{EE}(R)\psi_e(R, \vec{e}) \tag{5.2}$$

$$E\psi_R(R) = [T_R + V_{EE}(R)]\psi_R(R) \tag{5.3}$$

Where we have reluctantly re-introduced the R-dependence back into ψ_e (and removed the asterisk). This approximation greatly simplifies the analysis. This assumption can also be stated as the assumption that the nuclear motion is very slow compared to all other dynamics in the system. This should generally be true, as any nucleus is many orders of magnitude heavier than it's electrons. This assumption might not hold for sufficiently high energy collisions, but the collisions we are interested in are especially cold, so we can make the assumption with some comfort.

Our problem then, can be stated as calculating $V_{EE}(R)$, the eigenvalues of $H_{EE}(R)$. Since each eigenvalue can be expected to have a dependence on R, the result which we will show are then a set of R dependent potential energy curves. For a given curve, we would then get a standard one-dimensional Schrodinger's equation for the nuclear separation wavefunction, which could be solved or analyzed to determine the positions of bound-states, scattering amplitudes, and other metrics of interest.

In this paper, we will primarily work with the Hamiltonian

$$H_{EE}(R) = H_{BO}(R) + H_{FS} + H_{HFS} \tag{5.4}$$

where H_{BO} is the long internuclear distance asymptotic order Born-Oppenheimer Hamiltonian, H_{FS} is the fine structure Hamiltonian, and H_{HFS} is the hyperfine structure (HFS) Hamiltonian. The rotational Hamiltonian $H_R = \hat{L}_R^2/2m_\mu R^2$ where m_μ is the reduced mass, could be included as well, but as discussed in Sec. 5.8, we believe a great amount of insight can be gained without including the rotational couplings. We still cover some of the considerations for including rotation in Sec. 5.9 and Sec. 5.10. In general, the Born-Oppenheimer Hamiltonian includes all of the Coulomb interactions between particles in the system among other terms, and are a function of all of the other coordinates in the system as well. In this case, since we are only interested in the long-range behavior of S+P molecules, we take only the asymptotic longest-range terms from it which are dipole-dipole interactions for these molecules and which are only a function of R.

The different sub-Hamiltonians in H_{EE} are easily stated in the bases in which they are diagonal. However, the challenge here is that these are different bases, and none of these individual bases will have good symmetry properties for the total Hamiltonian. We must therefore carefully study the symmetry properties of each Hamiltonian in order to construct a final basis which has good symmetry, and then relate the bases relevant for the above Hamiltonian to our final basis.

5.3 Definitions, Notation, and Key Relations

Now, we must introduce some complicated notation for describing the molecular states. In general, for work such as this, it's a good idea to reference textbooks dedicated to angular momentum algebra. There are many options, several that I've used are cited here [135, 136].

In the single-atom case we had 5 important angular momenta that are generally considered: $\hat{l}_a, \hat{s}_a, \hat{i}_a, \hat{j}_a$, and $\hat{f}_a$. Now, we have at least all of these angular momenta for both atoms, plus the molecule's rotational angular momentum, and many more combinations thereof. I report all the angular momenta in Table 5.1.

I am following several patterns in the definitions of angular momentum in this chapter, which will hopefully make it easier to follow. Single particle angular momentum, such as l_a and f_b, are referred to with lower case labels and a subscript of "a" or "b". Multi-particle angular momentum such as $J = j_a + j_b$ are referred to using upper case labels. In the previous chapters we refer to the total single atom angular momenta as F in order to remain consistent with our previous work and

Angular momentum projections of angular momentum along a space-fixed axis are referred to using the common m_X notation, where X can be replaced with any angular momentum operator. Projections along specifically the internuclear axis are referred to using Greek letters $(\Lambda, \lambda_\alpha, \Sigma, \sigma_\alpha, \Omega, \omega_\alpha, \Phi, \phi_\alpha, \mathcal{I}, \iota_\alpha)$ that still follow the capitalization scheme used for operators. The rotational angular momentum and total angular momentum including rotation are referred to using special symbols N, and L_{JR} or L_{FR} depending on whether HFS is included. Note that in some references, J and F are used for the total angular momentum including rotation, while j and f are the total angular momentums excluding rotation. Hopefully the Table 5.1 helps clarify any confusion on this.

There are a couple pattern breakings, including the fact that capital "Iota" is typically identical to the letter "I", and so instead we use $\mathcal{I}$ in place of the capital "Iota" symbol. Note as well that the symbols for the projections of various on the angular momentum $(\Lambda, \Sigma, \Omega)$ are not to be confused with the labels of different values of Λ ($\Lambda = 0$ gets labeled Σ, $\Lambda = 1$ gets labeled Π, etc. when referring to specific BO potentials later in this chapter).

When a combined angular momentum, such as $j_a = l_a + s_a$, is a good quantum number for a state, the constituent quantum numbers are also good. The question then arises as to which quantum numbers are included in the state descriptions. When included, they will be included in parentheses near the relevant quantum number such as $|L\Lambda(l_a l_b)\rangle$. There are many cases in which there is only one reasonable way to combine angular momentum, and in these cases the extra angular momentum are omitted. As such, I will simply declare here:

$$\begin{aligned} |L\Lambda(l_a l_b)\rangle &\equiv |L\Lambda\rangle \\ |S\Sigma(s_a s_b)\rangle &\equiv |S\Sigma\rangle \\ |I\mathcal{I}(i_a i_b)\rangle &\equiv |I\mathcal{I}\rangle \\ |j_\alpha \omega_\alpha(l_\alpha s_\alpha)\rangle &\equiv |j_\alpha \omega_\alpha\rangle \\ |f_\alpha \phi_\alpha(j_\alpha(l_\alpha s_\alpha) i_\alpha)\rangle &\equiv |f_\alpha \phi_\alpha\rangle \end{aligned} \tag{5.5}$$

There are notable cases with two molecules where there is at least the potential for ambiguity. These include J which can be and will be constructed either as $|J\Omega(j_a j_b)\rangle$ or $|J\Omega(LS)\rangle$. Notably, these are very different states, and in general $\langle J\Omega(j_a j_b)|J\Omega(LS)\rangle \neq 1$. Similarly, for F, one will need to construct states either through $|F\Phi(f_a f_b)\rangle$ or $|F\Phi(JI)\rangle$ states. For these cases, the constituent quantum numbers will always be included.

5.3.1 Angular Momentum Symbols

Clebsch-Gordon Symbols: While the Clebsch-Gordon symbols are typically taught at the undergraduate physics level, a firm understanding of them is key for later discussions and there are even some unique nuances to their use here. We consider for example that you have a system with any two arbitrary angular momentum, j_1 and j_2. You might define a basis with well-defined such angular momentum and projections, $|j_1 m_{j_1}\rangle|j_2 m_{j_2}\rangle$. However, suppose you have an interaction that couples the two angular momentum, an interaction with significant $j_1 \cdot j_2$ content. Then, states of the form $|j_1 m_{j_1}\rangle|j_2 m_{j_2}\rangle$ are not eigenstates fo this interaction, and so these generally stop being good quantum numbers. However, the eigenstates of the total momentum operator, $j := j_1 + j_2$, are eigenvalues of the above interaction, and so we can expect all of $|j m_j(j_1 j_2)\rangle$ to be good quantum numbers. Here, as elsewhere, I use the parenthesis to group together j_1 and j_2 in order to indicate that j is composed of these two angular momentum. In other words, while the individual projections of individual spins are no longer conserved, the projection of the total spin is still conserved, as is the total angular momentum. It is important to note that the individual spins j_1 and j_2 are still conserved for every hamiltonian we deal with in this chapter, although these extra quantum numbers are often dropped as it is typically obvious from the context what they should be (e.g. for two electrons with total spin S, these sub-momenta would be the individual electron spins). However I will tend to be very explicit here as there are so many to keep track of and occasionally these details are important. As a result, depending on the presence of interaction terms, we will need to perform basis transformations between these two bases, and to do those we need the matrix elements $\langle jm_j(j_1j_2)|j_1m_{j_1}j_2m_{j_2}\rangle := C^{jm_jj_1j_2}_{j_1m_{j_1}j_2m_{j_2}}$. These constants are known as the Clebsch-Gordon symbols. Note again that while this 'C' symbol is common, the extra angular momentum in the superscript are often omitted for brevity. It is useful to note that one can consider symbols where the values of j_1 and j_2 don't match, but they are zero: $\langle jm_jj_3j_4|j_1m_{j_1}j_2m_{j_2}\rangle = \delta_{j_1,j_3}\delta_{j_2,j_4}C^{jm_jj_1j_2}_{j_1m_{j_1}j_2m_{j_2}}$ for some extra potentially independent momentum j_3 and j_4. We can then write the decomposition:

$$|jm_j(j_1j_2)\rangle = \sum_{m_{j_1},m_{j_2}} C^{jm_j(j_1j_2)}_{j_1m_{j_1}j_2m_{j_2}}|j_1m_{j_1}\rangle|j_2m_{j_2}\rangle \tag{5.6}$$

9j Symbols There exist in general what are called “3j” and “6j” symbols, which are used to describe the coupling of 2 and 3 angular momentum, but most useful in this chapter are the “9j” symbols [135, 136]. In general, suppose you have 4 angular momentum j_i for $i \in (1,2,3,4)$. Then, denote $\hat{j}_{ij} = \hat{j}_i + \hat{j}_j$, and $j_{1234} \equiv j_*$ for brevity. There is a common matrix element to consider between the coupling of these four angular momentum:

$$\langle j_*m_{j_*}(j_{12}j_{34})|j_*m_{j_*}(j_{13}j_{24})\rangle \equiv \sqrt{\breve{j}_{12}\breve{j}_{34}\breve{j}_{13}\breve{j}_{24}} \begin{Bmatrix} j_1 & j_2 & j_{12} \\ j_3 & j_4 & j_{34} \\ j_{13} & j_{24} & j_* \end{Bmatrix} \tag{5.7}$$

The matrix element **almost** looks like a Clebsch-Gordon symbol, but is dramatically more complex. We use here a common abbreviation $\breve{x} = 2x + 1$ for any angular momentum quantum number x. The symbol is called a “breve” symbol, and this is only to shorten long equations we will see later. The big matrix-looking term in curly brackets is **not** a matrix, but rather the 9j symbol. The 9j symbol should be thought of as a function of 9 arguments which is only defined non-zero for physically sensible angular momentum numbers. The matrix element $\langle j_* m_{j_*}(j_{12}j_{34})|j_* m_{j_*}(j_{13}j_{24})\rangle$ can also be written as an appropriate sum of Clebsch-Gordon coefficients.

5.4 Born-Oppenheimer Interactions

5.4.1 Introduction

In general, the problem of finding eigenenergies and eigenstates of a neutral dimer molecule involves at least four particles, two electrons and two nuclei, each of which generally has both a motional wavefunction and a spin wavefunction. The BO approximation (Sec. 5.2), the most common approximation in molecular physics, is the approximation that the relative nuclear spatial wavefunctions are separable from the rest of the system’s wavefunction. In this approximation, the rest of the Hamiltonian is diagonalized with a constant value of R in order to get the potential energies of the different possible collisional states at the internuclear distances R. This procedure can be done at a variety of values of R in order to turn these eigenenergies into energy curves $V(R)$ which tell you what the potential energy of the system is at a particular internuclear distance R. Then, these potential energy curves could be plugged back into Schrodinger’s equation with the nuclear kinetic energy operator in order to find vibrational and rotational eigenstates of the molecule, do scattering analysis, and other procedures. In this chapter, we focus only on calculating the asymptotic potential energy curves and understanding the associated symmetries and other physics behind them.

In order to start our analysis, it is essential to identify the relevant quantum numbers of the states we are dealing with. Just as the relevant quantum numbers determine, for example, FS interaction energy offsets, the quantum numbers for BO states will determine BO energies. Here, we will start by identifying the symmetries and quantum numbers relevant when considering only the Born Oppenheimer potentials, and disregarding FS, HFS, and rotation. In the coming sections, we will carefully discuss how the new interactions break previous symmetries and introduce new symmetries. A thorough understanding of these symmetries is both key for calculating the results as well as interpreting the resulting curves. Although these symmetries have been discussed at length over many years, it is difficult to find text with the symmetries of all of the interactions we will consider all discussed in the context of each other, so here we will do a thorough review.

Consider two alkali atoms that are very far separated, such that they are without any BO interactions at all. For a hydrogen-like single atom, the potential is spherically symmetric, leading to the nice spherical harmonics as solutions to the angular part of the equation. As such, there is a good basis to describe the electronic states of this system, namely the separated atom basis:

$$|n_a l_a m_{l_a}; n_b l_b m_{l_b}\rangle = |n_a l_a m_{l_a}\rangle |n_b l_b m_{l_b}\rangle \tag{5.8}$$

n, l, and m_l are the principle quantum number, orbital angular momentum quantum number, and orbital angular momentum projection quantum number respectively. The subscripts a and b here refer to which nuclear center the quantum numbers belong to, as they will for the rest of this paper. When we wish to refer to an arbitrary single nuclear center, we will use α. Here, the quantum number m_{l_α} points along an arbitrary (so called "space-fixed") axis. As we build up our set of quantum numbers and notation for these problems, we refer the reader to Table 5.1 where we have compiled all the quantum numbers for reference.

When the atoms are close enough to experience the non-radially symmetric BO interactions, the spherical symmetry is broken. In general, as we get closer, eigenfunctions of the new interacting Hamiltonian will be complex superpositions of states different of different n, l, and m_l, making these no longer good quantum numbers. We can consider a total angular momentum $\hat{L} = \hat{l}_a + \hat{l}_b$, but for the same reason this too is not a good quantum number. It is important to realize an important nuance here though. While the B.O. solutions themselves do not have good values of l_a and l_b, they asymptotically connect to the separated atom states which do. Because we are only working with the asymptotic order B.O. interactions, the states we are working with oftentimes will be assumed to have good l_a and l_b quantum numbers, and it takes care to realize when it is appropriate to introduce these.

5.4.2 Λ Symmetry

While the molecular system is not spherically symmetric, it is instead cylindrically symmetric about the internuclear axis. Therefore, if we pick our angular momentum's quantization axis along the internuclear axis, the BO interactions will not mix states of different total angular momentum projections along this axis. We call the projection of $\hat{L} = \hat{l}_a + \hat{l}_b$, the total orbital angular momentum, on the internuclear axis "Λ". We can refer to the projections of the single angular momentum l_α (when relevant) along this specific axis λ_α, although these individual projections are not good quantum numbers of BO eigenstates. It turns out as well, that unlike in the single atom case where states of different m_{l_a} were all degenerate without an external electric or magnetic field, Born Oppenheimer states with different **magnitudes** of Λ, i.e. different values of $|\Lambda|$, are **not** degenerate. Therefore, states are typically represented by their value of $|\Lambda|$, and indeed sometimes in the literature the absolute value is dropped and understood to be implicit. We will discuss the labels used for these states below.

5.4.3 Spin Symmetry

The BO potential includes primarily electrostatic interactions and does not include electronic spin-dependent interactions. Therefore the total spin states $\hat{S} = \hat{s}_1 + \hat{s}_2$ of the molecule are not mixed, and S is a second good quantum number for B.O. states. Furthermore, different spin states (singlet vs triplet) will have different energies due to the impact the spin state has on the symmetrization of the electronic wavefunction. The spin S's projection along the internuclear axis, called Σ, is also unbroken by BO interactions, but states with the same S and different Σ are degenerate until we introduce fine structure interactions in the next section.

5.4.4 $\hat{\mathbb{I}}_{\mathbf{BO}}$ Inversion Symmetry

For homonuclear molecules, the system is also symmetric on the inversion of all electron coordinates through the center of charge of the molecule. For homonuclear systems this is also the center of mass of the molecule. We label the operator which does this inversion $\hat{\mathbb{I}}_{\mathrm{BO}}$, and give its eigenvalues the symbol $\mathbb{I}_{\mathrm{BO}} = \pm 1$. The states of positive parity with $\mathbb{I}_{\mathrm{BO}} = 1$ are typically called "gerade" states (g), and states with negative parity "ungerade" (u). Oftentimes in the literature the symbol used for its eigenvalues is given as $\sigma = 0, 1$, and then when this symmetry impacts a phase somewhere terms are multiplied by $(-1)^{\sigma}$ instead of just $\mathbb{I}_{\mathrm{BO}}$. This notation could be confused with the spin projection quantum numbers, so we instead insist on using $\mathbb{I}_{\mathrm{BO}}$.

5.4.5 $\hat{\kappa}_{\mathbf{BO}}$ Kronig Symmetry

Lastly, states can also be eigenstates of the operator that flips the wavefunction about a plane **containing** the internuclear axis. This is sometimes called a "Kronig" symmetry. We therefore call the operator that does this flip $\hat{\kappa}_{\mathrm{BO}}$, and since it is a parity operator it has eigenvalues again $\kappa_{\mathrm{BO}} = \pm 1$. In general, I recommend carefully considering the states at hand before considering the operation of this Kronig symmetry, as there are numerous subtleties in the action of κ_{BO} on a given state. For example, in the long-distance limit discussed here, the result can be derived by analyzing the single-atom basis states that the B.O. molecular states dissociate to. For a longer discussion, we reference [134]. For the work in this paper, the following rule suffices:

$$\hat{\kappa}_{\mathrm{BO}}|L\Lambda\rangle = (-1)^{-\Lambda}|L, -\Lambda\rangle \tag{5.9}$$

Thus states of $\Lambda = 0$ (which are called Σ states, not to be confused with Σ as the projection of S on the internuclear axis) have positive parity. Note that states with $|\Lambda| = 1$ (which are called Π states) at the BO level **do not** have well defined parity as they are usually defined, but one can construct states of good $\hat{\kappa}_{\mathrm{BO}}$ parity using various Π states, for example $|L\Lambda\rangle \pm (-1)^{-\Lambda}|L, -\Lambda\rangle$ [120]. As the B.O. hamiltonian does not contain spin-dependent interactions, we need not consider the action of operators like this on the spin of the state yet.

This symmetry is slightly surprising from an atomic physics perspective since states from our normal hydrogen atom basis $|n_a l_a m_{l_a}\rangle$ are not eigenstates of this operator. However, if one wished, one could easily use a different basis for the Hydogen atom which respected this symmetry, as e.g. the superpositions (using $|n_a l_a m_{l_a}\rangle$ notation) $|111\rangle \pm |11,-1\rangle$ are eigenstates of this operator.

It is not hard to see from this discussion that there is some ambiguity in the definition of $\hat{\kappa}_{\mathrm{BO}}$, in particular by choosing a different plane to invert through one can reverse the phase of these states [133]. We use the typical phase standard which was set by Condon and Shortley [137].

5.4.6 Born-Oppenheimer Symmetry Labels

With these three main good quantum numbers, BO eigenstates typically get labeled by the following symbols: ${}^{2S+1}\Lambda^{\kappa_{\mathrm{BO}}}_{g/u}$. For example, for alkali atoms the ground $S+S$ states split into only two states: ${}^3\Sigma^+_g$ and ${}^1\Sigma^+_u$. In fact, it is a common exercise to do a simple BO calculation for the H_2 molecule. It is much more complicated to do excited state calculations as the excited $S+P$ states split into ${}^3\Sigma^+_g$, ${}^3\Sigma^+_u$, ${}^1\Sigma^+_g$, ${}^1\Sigma^+_u$, ${}^3\Pi_g$, ${}^3\Pi_u$, ${}^1\Pi_g$, and ${}^1\Pi_u$. Note that as mentioned prior the Π states are not simultaneous eigenfunctions of $\hat{\kappa}_{\mathrm{BO}}$ and thus have no $\pm$ superscript. For more on these calculations, see e.g. [138]. These states can also be labeled in ket form with a more full set of quantum numbers $|L\Lambda\mathbb{I}_{\mathrm{BO}}\kappa_{\mathrm{BO}}S\rangle$ (with l_a, l_b, s_a, and s_b implicitly good quantum numbers as well). We will introduce the nuclear spin later. In the asymptotic limit one could add l_a and l_b to this ket. More quantum numbers which are degenerate at this level but important later could also be added, such as the single-atom electron and nuclear spins s_α, i_α, and the various projections of these and their combined angular momenta on the internuclear axis. The correct way to construct the bases for future calculations which require identifying these quantum numbers will be discussed in Sec. 5.5.5.

5.4.7 Resonant Dipole Born-Oppenheimer Interactions

BO states always have good values of $S, |\Lambda|, \mathbb{I}_{\mathrm{BO}}, \kappa_{\mathrm{BO}}$. At close distances, they do not have good L values. In order to evaluate fine structure corrections at all distances it is necessary to properly relate the BO eigenstates to the separated atom basis, which would require e.g. being able to identify BO states in terms of a superposition of atomic states with different orbital angular momentum. However, all BO states dissociate to states with good L at long distances. Since we are only interested in the long-distance limit of the BO states, our BO bases will always have good L, and more specifically $L = 1$, simplifying this calculation greatly. Since for homonuclear atoms the asymptotic order BO interaction is the resonant dipole-dipole interaction, BO eigenstates are superpositions of single-atom excitation states of the form:

$$\begin{aligned} |\Lambda \mathbb{I}_{\mathrm{BO}} \kappa_{\mathrm{BO}} S\rangle &\to |L = l_a, \Lambda = \lambda_a, \mathbb{I}_{\mathrm{BO}} \kappa_{\mathrm{BO}}\rangle |S\Sigma\rangle \\ &= (|00 l_a \lambda_a\rangle + p|l_a \lambda_a 00\rangle)|S\Sigma\rangle/\sqrt{2} \end{aligned} \tag{5.10}$$

where the kets in the latter equality are of the form $|l_a \lambda_a l_b \lambda_b\rangle = |l_a \lambda_a 00\rangle$ for example. p should be chosen to make the **entire** wavefunction of the two electrons antisymmetric with respect to particle exchange. In the case that $l_a = l_b$ for potentials which are not "S+P" in nature, or for heteronuclear molecules, we can take $p = 0$. The other parts of the wavefunction that factor into this are the spin part and the spatial part, so we can therefore relate p to the total spin and spatial inversion quantum number of the state:

$$p = (-1)^S \mathbb{I}_{\mathrm{BO}} \tag{5.11}$$

This relation ensures that the wavefunction of the two electrons antisymmetric with respect to particle exchange. This parity quantum number is an alternative representation of the other quantum numbers used. It is evidently convenient here, but in general we will continue using $\mathbb{I}_{\mathrm{BO}}$ and S for stylistic continuity with other resources.

With the symmetries of the BO potentials established, we can move on to considering the magnitudes of these potentials and how to include them in our eventual calculation. The BO potentials are extremely deep compared to the energy scales we are interested in. The magnitudes of these potentials are on the order of the energy spacing between different angular momentum quantum numbers, so e.g. on the order of the D_1 and D_2 lines for alkali earths, or hundreds of THz. As well, the length scale at which these full calculations are important is the length at which the overlap of the atomic electron wavefunctions about the two nuclei is significant, or typically < 1 nm.

In general, calculating these curves exactly is quite complex. For our purposes, however, we are interested in low-energy, very long range interactions, and so it suffices to take only the asymptotic terms from the BO potentials, which can be approximated as being of the form C_x/R^x for various values of x. The coefficients C_x are known as "dispersion coefficients". For the case of a homonuclear $S + P$ dipole, the asymptotic order interactions are well-known to be $1/R^3$ resonant dipole-dipole interactions. These can be thought of as arising from a combination of exchange symmetrization requirements and the resonant exchange of the single excitation between the two atoms. The exact values can be calculated through relatively involved perturbation theory calculations where the perturbation is the Coulomb interactions between atoms far apart from each other [139]. The result to first order in perturbation theory is

$$\begin{aligned} V = -\frac{1}{R^{2l_e+1}}\frac{(-1)^{l_e+m_{l_e}+1}[(-1)^{l_e+S}\mathbb{I}_{\mathrm{BO}}]}{2l_e+1}\binom{2l_e}{l_e+m_{l_e}} \\ \times\langle n_e l_e|r^{l_e}|n_g 0\rangle^2 \end{aligned} \tag{5.12}$$

For excited states with quantum numbers n_e, l_e, m_{l_e} and ground state quantum numbers $n_g, l_g = 0, m_g = 0$, and excited state electron cooredinate r. The term in parenthesis is a binomial coefficient. The equation is valid for states with $l_e \geq 1$. The first order perturbation theory to $S + S$ atoms with $l_e = 0$ is zero, and one must go to second order perturbation theory to get the leading contribution, which turns out to be $1/R^6$ as one might have guessed.

Note that these calculations are independent of which nuclear center is excited and so we use the "e" subscript to reflect the excited quantum number, deviating from our "a/b" notation.

One can see in Eqn. 5.12 that for $S+P$ molecules the asymptotically go as $1/R^3$, and that because of the dipole matrix element $\langle n_e l_e | r^{l_e} | n_g 0 \rangle$ the coefficient will only be non-zero for states that are connected by electric dipole transitions. This calculation does not include fine or HFS in the states involved, but a straightforward generalization would presumably show the same thing, which will become important later. Similarly, the asymptotic potentials for $S+D$ molecules with $l_e = 2$ are driven by electric quadrupole $1/R^5$ interactions.

The fact that the form of the dispersion coefficients for S+P potentials is relatively simple leads it to commonly be described in terms of only a few parameters for the different BO states:

$$\begin{aligned}
V_{^3\Sigma_g^+, ^1\Sigma_g^+} &= -\frac{2C_3}{R^3} + \frac{C_6}{R^6} + \mathcal{O}(R^{-8}) \\
V_{^1\Sigma_g^+, ^3\Sigma_u^+} &= \frac{2C_3}{R^3} + \frac{C_6}{R^6} + \mathcal{O}(R^{-8}) \\
V_{^3\Pi_g, ^1\Pi_u} &= \frac{C_3}{R^3} + \frac{C_6}{R^6} + \mathcal{O}(R^{-8}) \\
V_{^1\Pi_g, ^3\Pi_u} &= -\frac{C_3}{R^3} + \frac{C_6}{R^6} + \mathcal{O}(R^{-8})
\end{aligned} \tag{5.13}$$

In general these constants, C_3 and others, and those higher order corrections have been measured or calculated (especially for common atoms like alkali metals) and can be looked up (for example, [139] is a great reference here). These are the energies which I will plug into H_{BO}.

5.5 Fine Structure Interactions

The inclusion of FS interactions was originally done by Movre and Pischler [140], and so the resulting potentials are sometimes called Movre-Pischler potentials. The FS interactions turned out to be quite important historically as they predicted the presence of the relatively long-range 0_g^- and 1_u bound states in alkali atoms. These states which are relatively long range and loosely bound compared to BO molecules, but still experimentally detectable [141]. [142] is a useful good reference for this calculation.

The atomic fine structure interaction for atom a is given by $A_{\mathrm{FS}}(\hat{l}_a \cdot \hat{s}_a)$ where A_{FS} is a typically experimentally determined constant. This energy tends to become important at large distances where the electron wavefunction overlap becomes small. This is the regime where the two atom's wavefunctions overlap very little and therefore need not consider corrections such $s_a \cdot l_b$ or $l_a \cdot l_b$. Therefore, here we consider the total FS Hamiltonian is

$$H_{\mathrm{FS}} = A_{\mathrm{FS}}(\hat{l}_a \cdot \hat{s}_a + \hat{l}_b \cdot \hat{s}_b) \tag{5.14}$$

Generally the fine structure interaction will result in a spatially varying mixing of the BO states, with the mixing being relatively weaker at short distances where the terms from the BO interactions dominate, then becoming stronger and eventually becoming the normal single-atom mixed states in the long distance limit. The basis in which this Hamiltonian is diagonal is the separated atom basis with coupled l_α and s_α:

$$|j_a\omega_a; j_b\omega_b\rangle = |j_a\omega_a\rangle|j_a\omega_a\rangle \tag{5.15}$$

with $\hat{j}_\alpha = \hat{l}_\alpha + \hat{s}_\alpha$ and $\omega_\alpha = \lambda_\alpha + \sigma_\alpha$, which satisfies

$$\begin{split} H_{\mathrm{FS}}|j_a\omega_a; j_b\omega_b\rangle = \\ A_{\mathrm{FS}} \sum_{\alpha\in(a,b)} \Big(j_\alpha(j_\alpha+1) - l_\alpha(l_\alpha+1) - s_\alpha(s_\alpha+1)\Big)|j_a\omega_a j_b\omega_b\rangle \end{split} \tag{5.16}$$

Where we recall that states with good j_α also have good l_α and s_α, but that we need not consider the nuclear spin i_α yet. To calculate the fine structure interaction matrix elements, one must convert each two-atom BO state to the appropriate sum of single-atom fine structure states.

5.5.1 Ω Symmetry

Similar to L and l_α, J and j_α, (with $\hat{J} = \hat{j}_a + \hat{j}_b$) will not be good quantum numbers due to the H_{BO} interactions, but the projection of J on the internuclear axis, which is called "Ω" will be. The FS operator won't mix states of different Ω. Thus the total matrix will be block-diagonal in these states. Specifically, similar to $|\Lambda|$, with only FS interactions, states of different Ω but the same $|\Omega|$ are degenerate, and so typically only positive values are reported.

5.5.2 $\hat{\mathbb{I}}_{\mathbf{FS}}$ Inversion Symmetry

Despite adding the electron spin into the total Hamiltonian, the problem's two nuclei are still identical at this stage, and so the Hamiltonian and therefore the eigenfunctions still respect the $\mathbb{I}_{\mathrm{BO}}$ symmetry. In other words, $\mathbb{I}_{\mathrm{BO}}$ is still a good quantum number, g and u are still good symmetry labels, and $\hat{\mathbb{I}}_{\mathrm{BO}} = \hat{\mathbb{I}}_{\mathrm{FS}}$.

5.5.3 $\hat{\kappa}_{\mathbf{FS}}$ Kronig Symmetry

It is not hard to see that the Kronig symmetry $\hat{\kappa}_{\mathrm{BO}}$ as defined in Eqn. 5.9 does not commute with $\hat{l}_\alpha \cdot \hat{s}_\alpha$ terms in H_{FS}, but that we can define a similar operator $\hat{\kappa}_{\mathrm{FS}}$ which flips the spin operator as well which **does** commute with this term. In this case:y

$$\kappa_{\mathrm{FS}}|L\Lambda S\Sigma;\Omega\rangle = (-1)^{L-\Lambda+S-\Sigma}|L,-\Lambda,S,-\Sigma,-\Omega\rangle \tag{5.17}$$

Similar to before, the phase here is tricky and has some amount of arbitrariness to it. Note that κ_{FS} is not explicitly related to κ_{BO}. As well only states with $\Omega = 0$ have well-defined non-degenerate $\hat{\kappa}_{\mathrm{FS}}$ symmetries, but the $\hat{\kappa}_{\mathrm{FS}}$ symmetries will be important for constructing states of $\hat{\kappa}_{\mathrm{HFS}}$ symmetry in the next sections [120].

5.5.4 Fine Structure Symmetry Labels

As such, these states are typically labeled by symbols of the form $\Omega^{\kappa_{\mathrm{FS}}}_{\mathbb{I}_{\mathrm{FS}}}$, where $\mathbb{I}_{\mathrm{FS}}$ values are usually replaced by "g/u" for $\mathbb{I}_{\mathrm{FS}} = \pm 1$ respectively, although I will typically still use ± 1 inside bra/ket symbols. For example, ^{87}Rb S+P molecules support 8 different state symmetries at this level: $0_g^+, 0_u^+, 0_g^-, 0_u^-, 1_g, 1_u, 2_g$, and 2_u.

5.5.5 Fine Structure Basis

We aim to construct states with good Ω, $\mathbb{I}_{\mathrm{FS}}$, and κ_{FS} quantum numbers. The first task here is to determine how to compose states of these good quantum numbers out of BO states, which don't have a well defined Σ or Ω. If you recall, the BO eigenstates have good $\Lambda S \mathbb{I}_{\mathrm{BO}}$ and κ_{BO} quantum numbers, and have good L, l_a, and l_b only in the long-distance limit. Only by correctly constructing the new basis can we successfully add the BO energies to the FS energies. The degeneracy responsible for this disconnect is the Σ quantum number. By enumerating the states of different Σ, we can expand our BO basis and construct states of good BO and FS symmetry out of the expanded basis. However, it is not enough to merely add the different Σ states to the BO basis, as states of good Σ do not generally have good κ_{FS}. Instead we can iterate through the new values of Σ, but construct the new states with good κ_{FS} instead. This can be achieved with something like the following lines of pseudo-code:

```
for state in BO_Basis:
  for Sigma in [-state['S'], ..., state['S']]:
    state['Omega'] = Sigma+state['|Lambda|']
    if state['|Lambda|'] != 0 and state['Omega']==0:
      for kappa_FS in [-1,1]:
        newState['K_FS'] = kappa_FS
        expandedBasis.append(newState)
    else if Sigma>=0:
      state['k_FS']=(-1)^(state['L']-state['|Lambda|']+state['S']-Sigma)
      if newState not in BoFsBasis:
        BoFsBasis.append(newState)
```

The $\hat{\mathbb{I}}_{\mathrm{FS}}$ symmetry does not need to be handled explicitly here because this quantum number is contained in the original BO basis states. After constructing this basis, we can construct sub-bases by simply separating out states of particular $|\Omega|, \kappa_{\mathrm{FS}}$, and $\mathbb{I}_{\mathrm{FS}}$. Each of the above states as constructed is already an eigenstate of the BO Hamiltonian, so the only remaining step is the conversion of FS eigenstates to this basis. The states here can then be separated into the relevant sub-bases based on their $|\Omega|$, κ_{FS}, and $\mathbb{I}_{\mathrm{FS}}$ quantum numbers and handled separately.

5.5.6 H_{FS} Transformation

The FS Hamiltonian is diagonal in the two-atom separated j_α basis

$$|j_a\omega_a; j_b\omega_b\rangle \tag{5.18}$$

Therefore in order to add this asymptotic BO Hamiltonian, we must do a frame transformation based on the following matrix elements:

$$\langle|\Omega|, L|\Lambda|; S|\Sigma|\mathbb{I}_{\mathrm{BO}}\mathbb{I}_{\mathrm{FS}}\kappa_{\mathrm{BO}}\kappa_{\mathrm{FS}}|j_a\omega_a; j_b\omega_b\rangle \tag{5.19}$$

We will do the frame transformation in three steps. This can be viewed as first transforming from the good FS basis to the uncoupled two-atom *l*-*s* basis, followed by transforming into the BO basis with good Σ values, followed by transforming into the BO basis with good $|\Omega|$ and κ_{FS}:

$$\begin{aligned} \langle|\Omega|, L|\Lambda|; S|\Sigma|; \mathbb{I}_{\mathrm{BO}}\kappa_{\mathrm{BO}}\kappa_{\mathrm{FS}}|j_a\omega_a; j_b\omega_b\rangle &= \\ \langle|\Omega|, L|\Lambda|; S|\Sigma|\mathbb{I}_{\mathrm{BO}}\kappa_{\mathrm{BO}}\kappa_{\mathrm{FS}}|\Omega L\Lambda; S\Sigma\rangle& \\ \times\langle\Omega L\Lambda; S\Sigma|l_a\lambda_a s_a\sigma_a; l_b\lambda_b s_b\sigma_b\rangle& \\ \times\langle l_a\lambda_a s_a\sigma_a; l_b\lambda_b s_b\sigma_b|j_a\omega_a; j_b\omega_b\rangle& \end{aligned} \tag{5.20}$$

Or more specifically one will want to do this transformation for each of the sub-bases discussed in the Sec. 5.5.4. The first element deals with complications from the κ_{FS} symmetry.

$$\langle|\Omega|, L|\Lambda|; S|\Sigma|; \mathbb{I}_{\mathrm{BO}}\kappa_{\mathrm{BO}}\kappa_{\mathrm{FS}}|\Omega L\Lambda; S\Sigma\rangle = \kappa_{\mathrm{FS}} \tag{5.21}$$

for states with negative Ω and 1 for states with positive Ω, by convention. To be clear, it is also required that the absolute values and signed angular momentum values on both sides are consistent, this is not an accident of notation. For example the matrix element with $|\Lambda| = 2$ on the left hand side and $\Lambda = -1$ on the right hand side would be zero. I could also express this with a lot of delta functions, but this would be tedious. This relationship can be understood by application of the statement above about how κ_{FS} acts on states with the given quantum numbers.

Here is the second element:

$$\langle \Omega L\Lambda; S\Sigma; | l_a\lambda_a s_a\sigma_a; l_b\lambda_b s_b\sigma_b\rangle = p^{l_a} C^{L\Lambda l_a l_b}_{l_a\lambda_a l_b\lambda_b} C^{S\Sigma s_a s_b}_{s_a\sigma_a s_b\sigma_b} \tag{5.22}$$

The last one is the easiest to deal with as it is only based on normal angular momentum combination rules:

$$\langle l_a\lambda_a s_a\sigma_a; l_b\lambda_b s_b\sigma_b | j_a\omega_a; j_b\omega_b\rangle = C^{j_a\omega_a}_{l_a\lambda_a s_a\sigma_a} C^{j_b\omega_b}_{l_b\lambda_b s_b\sigma_b} \tag{5.23}$$

I list the resulting total Hamiltonians $H_{BO} + H_{FS}$ below. These can be viewed as the block-diagonal components of the total Hamiltonian. The symbols to the left of the matrices indicate the quantum numbers corresponding to the state. For example, it should be understood that the first element of the first matrix is, in terms of the basis $|0, 10; 10; 1, -11\rangle$, $\langle|(H_{BO}+H_{FS})|0, 10; 10; 1, -11\rangle$. While there are still a fair number of states here, before adding hyperfine structure it is still reasonable to write this all down.

$$
\begin{array}{cc}
 & {}^{2S+1}|\Lambda|^{\kappa_{\mathrm{BO}}}_{\mathbb{I}_{\mathrm{BO}}} \\
0_g^- : & \begin{array}{c} {}^3\Sigma_g^+ \\ {}^3\Pi_g \end{array}
\end{array}
\begin{bmatrix} \frac{C_3}{R^3} - \frac{2\Delta}{3} & \frac{\sqrt{2}\Delta}{3} \\ \frac{\sqrt{2}\Delta}{3} & -\frac{2C_3}{R^3} - \frac{\Delta}{3} \end{bmatrix}
\quad
\begin{array}{cc}
 & {}^{2S+1}|\Lambda|^{\kappa_{\mathrm{BO}}}_{\mathbb{I}_{\mathrm{BO}}} \\
0_g^+ : & \begin{array}{c} {}^1\Sigma_g^+ \\ {}^3\Pi_g \end{array}
\end{array}
\begin{bmatrix} \frac{C_3}{R^3} - \frac{2\Delta}{3} & \frac{\sqrt{2}\Delta}{3} \\ \frac{\sqrt{2}\Delta}{3} & \frac{2C_3}{R^3} - \frac{\Delta}{3} \end{bmatrix}
$$

$$
0_u^- : \begin{array}{c} {}^3\Sigma_u^+ \\ {}^3\Pi_u \end{array}
\begin{bmatrix} -\frac{C_3}{R^3} - \frac{2\Delta}{3} & -\frac{\sqrt{2}\Delta}{3} \\ -\frac{\sqrt{2}\Delta}{3} & -\frac{2C_3}{R^3} - \frac{\Delta}{3} \end{bmatrix}
\quad
0_u^+ : \begin{array}{c} {}^1\Sigma_u^+ \\ {}^3\Pi_u \end{array}
\begin{bmatrix} -\frac{C_3}{R^3} - \frac{2\Delta}{3} & \frac{\sqrt{2}\Delta}{3} \\ \frac{\sqrt{2}\Delta}{3} & -\frac{2C_3}{R^3} - \frac{\Delta}{3} \end{bmatrix}
$$

$$
1_g : \begin{array}{c} {}^3\Sigma_g^+ \\ {}^1\Pi_g^+ \\ {}^3\Pi_g \end{array}
\begin{bmatrix} \frac{C_3}{R^3} - \frac{\Delta}{3} & -\frac{\Delta}{3} & \frac{\Delta}{3} \\ -\frac{\Delta}{3} & -\frac{C_3}{R^3} - \frac{\Delta}{3} & \frac{\Delta}{3} \\ \frac{\Delta}{3} & \frac{\Delta}{3} & -\frac{2C_3}{R^3} - \frac{\Delta}{3} \end{bmatrix}
\quad
1_u : \begin{array}{c} {}^3\Sigma_u^+ \\ {}^1\Pi_u^+ \\ {}^3\Pi_u \end{array}
\begin{bmatrix} -\frac{C_3}{R^3} - \frac{\Delta}{3} & -\frac{\Delta}{3} & \frac{\Delta}{3} \\ -\frac{\Delta}{3} & \frac{C_3}{R^3} - \frac{\Delta}{3} & \frac{\Delta}{3} \\ \frac{\Delta}{3} & \frac{\Delta}{3} & \frac{2C_3}{R^3} - \frac{\Delta}{3} \end{bmatrix}
$$

$$
2_g : \; {}^3\Pi_g^+ \begin{bmatrix} \frac{C_3}{R^3} \end{bmatrix} \quad 2_u : \; {}^3\Pi_u^+ \begin{bmatrix} -\frac{C_3}{R^3} \end{bmatrix} \tag{5.24}
$$

Diagonalizing all of these matrices realizes at every position R yields the curves in Fig. 5.1.

This discussion may seem heavy-handed for the fine structure interactions where in the end there are only 16 different states in 8 different symmetry classes, making the problem possible to tackle “by hand” and without need for heavy systemization or rigor. However, the problem will suddenly become much more complex when we add the HFS interactions, after which we will have to keep track of 384 states.

5.6 Hyperfine Structure Interactions

Adding hyperfine coupling now breaks the $\hat{\mathbb{I}}_{\mathrm{BO}}$ symmetry because the molecule is generally not symmetric about the internuclear plane when the two nuclei can have different spins (an exception are the $\Phi = 5$ states which both involve nuclear spins that are perfectly aligned with each other and the electronic spins no matter which nuclear center holds the excitation). This leaves only the total parity, the total angular momentum projection on the internuclear axis Φ, and the symmetry about a plane that contains the internuclear axis for $\Phi = 0$ states [125]. Notably, even at

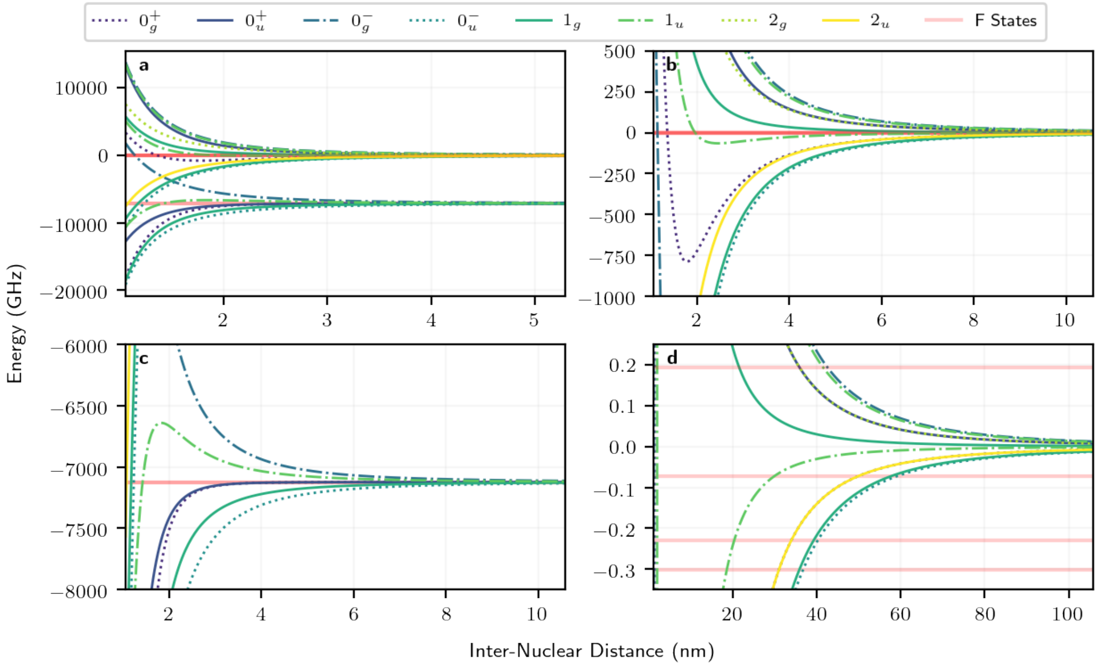

Figure 5.1: **Molecular Potentials with Only Fine Structure Interactions.** Note carefully the different vertical an horizontal scales. Potentials are given different colors and line styles according to their symmetry properties. **a** All molecular potentials at large energy scales and relatively short distance scales. **b** Molecular states dissociating to the $5P_{3/2} + 5S_{1/2}$ atomic states, at smaller energy scales and longer distance scales. Clearly visible are the 1u and 0_g^+ long range bound-state-supporting potentials predicted by this calculation. **c** Molecular states dissociating to the $5P_{1/2} + 5S_{1/2}$ atomic states, at smaller energy scales and longer distance scales. **d** Molecular states dissociating to the $5P_{3/2} + 5S_{1/2}$ atomic states at very small energies and distances relevant for loading processes. The red lines, indicating the free-space hyperfine energies, are displayed in order to give a visual indication of at what energy and distance scale we expect the hyperfine potentials to start to become significant at.

these smaller energy scales, the asymptotic Born-Oppenheimer interactions are still the only thing which is mixing the various single-atom eigenstates and making this problem interesting.

Evaluating the coupling constant is slightly more tricky than the fine structure constant because there are more manifolds for the hyperfine constant whose splittings are generally very different from one another. For example, in ^{87}Rb, the ground state splitting is approximately 6.834 GHz, while the splitting of the D_1 line is about 800 MHz. As such, to evaluate the hyperfine coupling, I simply forced the diagonal elements of the hyperfine coupling matrix in the F basis to match the experimental values. This includes explicitly plugging in the values for the 4 different hyperfine manifolds on the D_2 transition.

5.6.1 $|\Phi|$ Symmetry

Similar to previous interactions, we now must consider that the total angular momentum is $\hat{F} = \hat{f}_a + \hat{f}_b$, which is not conserved due to the lack of spherical symmetry. However, that again because of the cylindrical symmetry of the problem, the projection of F on the internuclear axis, called Φ, is still conserved by all interactions in the problem. Again, until we add rotation, magnetic fields, or other hamiltonians, the states with different-signed Φ values but the same $|\Phi|$ are degenerate.

5.6.2 $\hat{\mathbb{I}}_{\mathbf{HFS}}$ Inversion Symmetry

With the inclusion of the HFS interactions, the inversion symmetry becomes much more complicated. Because the spins of the two nuclear centers in general have different states, the problem is in general no longer symmetric under the exchange of only electron coordinates. We can however define a new total inversion symmetry operator $\hat{\mathbb{I}}_{\text{HFS}}$ which exchanges the coordinates of both of the electrons and both of the nuclear spins. As this is a parity operator, it again has eigenvalues $\mathbb{I}_{\text{HFS}} = \pm 1$. Note that the inclusion of this symmetry is expected to make the eventual calculation of selection rules more non-trivial, as the electromagnetic field primarily interacts with the light electrons rather than the nucleus, and so is easier to define selection rules for states that have good $\hat{\mathbb{I}}_{\text{BO}}$ or $\hat{\mathbb{I}}_{\text{FS}}$ symmetry.

5.6.3 $\hat{\kappa}_{\mathbf{HFS}}$ Kronig Symmetry

The HFS interaction has the character of a spatially-dependent $\hat{\imath}_\alpha \cdot \hat{\jmath}_\alpha$ interaction. Our previous Kronig symmetry operator $\hat{\kappa}_{\text{FS}}$ does not commute with these interaction because it only flips the electron spin and not the nuclear spin, and so we must again revise the operator to include both a flip of the electrons spatial wavefunction about a plane, flipping the electron spin state, as well as the nuclear spin state. This is defined as $\hat{\kappa}_{\mathrm{HFS}}$, and it more or less replaces $\hat{\kappa}_{\mathrm{FS}}$.

5.6.4 Hyperfine Structure Symmetry Labels

As a result of the above considerations we label these stats of good symmetry with symbols of the form $|\Phi|^{\kappa_{\mathrm{HFS}}}_{\mathbb{I}_{\mathrm{HFS}}}$, where $\mathbb{I}_{\mathrm{HFS}}$ values are now "+/-" for $\mathbb{I}_{\mathrm{HFS}} = \pm 1$ (no longer "g/u"). There are 14 different non-degenerate ^{87}Rb S+P molecular state symmetries at this level:

$$|\Phi|^{\kappa_{\mathrm{HFS}}}_{\mathbb{I}_{\mathrm{HFS}}} \in \{0^+_+, 0^+_-, 0^-_+, 0^-_-, 1_+, 1_-, 2_+, 2_-, 3_+, 3_-, 4_+, 4_-, 5_+, 5_-\} \tag{5.25}$$

5.6.5 Hyperfine Structure Basis

With the symmetry properties of the different Hamiltonians established, we can now identify a basis of good symmetry for the total Hamiltonian and begin the process of transforming our individual Hamiltonians into this basis. In this section we will do this as discussed above without yet including rotation. Notably, this basis reduces to the FS basis described above if one sets $i_a = i_b = 0$. Adding rotation is rather significantly more complicated and will be discussed in Sec. 5.10. Eigenstates of the new total Hamiltonian again fall into two categories. All states have a good quantum number Φ, the projection of $\hat{F} = \hat{f}_a + \hat{f}_b$ on the intermolecular axis. States with $\Phi = 0$ also have good $\mathbb{I}_{\mathrm{HFS}}$ and κ_{HFS} quantum numbers, while states with $\Phi \neq 0$ only have a good $\mathbb{I}_{\mathrm{HFS}}$ quantum number. In principle one could construct states of good κ_{HFS} with $\Phi \neq 0$ as well but they are degenerate until we add rotation.

There are 384 total states but states with opposite sign Φ and identical other quantum numbers are degenerate. So there are 230 states remaining to keep track of. We can expand the Born-Oppenheimer with fine structure to include hyperfine structure with something like the following pseudo code:

```
for state in boFsBasis:
  for I_ in [|i_a-i_b|, ..., i_a + i_b]:
    for Iota in [-I_,..., I_]:
      for Omega in [-state['|Omega|'], state['|Omega|']]:
        state['Phi'] = Iota+Omega
        if Omega != 0 and Phi == 0:
          for k_HFS in [-1,1]:
            state['k_HFS'] = k_HFS
            if newState not in boHfsBasis:
              boHfsBasis.append(newState)
        else:
          state['k_HFS'] = state['k_FS']*(-1)^(I_-Iota)
          if newState not in boHfsBasis:
            boHfsBasis.append(newState)
```

One can then construct the basis of good total symmetries out of these states after identifying the total inversion symmetry of each state.

5.6.6 H_{FS} Transformation

The FS basis is often referred to with only the quantum numbers relevant for the FS interaction, i.e. $|j_a\omega_a\rangle$.

Here we are interested in the transformation

$$\langle|\Phi||\Omega|;L|\Lambda|;S|\Sigma|;I|\mathcal{I}|\mathbb{I}_{\mathrm{BO}}\mathbb{I}_{\mathrm{HFS}}\kappa_{\mathrm{BO}}\kappa_{\mathrm{FS}}\kappa_{\mathrm{HFS}}|j_a\omega_a i_a\iota_a;j_b\omega_b i_b\iota_b\rangle$$

This is more or less the same as the transformation given in Sec. 5.5.5 just with the extra nuclear spin quantum numbers which must match, so I omit any further discussion of this here.

5.6.7 H_{HFS} Transformation

The HFS Hamiltonian is diagonal in the two-atom separated basis $|f_a\phi_a; f_b\phi_b\rangle$. And therefore we must form the basis transformation between this and the expanded BO basis out of the following matrix elements:

$$\langle|\Phi||\Omega|; L|\Lambda|; S|\Sigma|; I|\mathcal{I}|\mathbb{I}_{\text{BO}}\mathbb{I}_{\text{HFS}}\kappa_{\text{BO}}\kappa_{\text{FS}}\kappa_{\text{HFS}}|f_a\phi_a; f_b\phi_b\rangle \tag{5.26}$$

We will do this frame transformation in three steps again. This can be viewed as first transforming from the good HFS basis to the uncoupled two-atom l-s-i basis, followed by transforming the l-s-i states into the BO basis with good Σ and $\mathcal{I}$ values, followed by finally transforming into the BO basis with good $|\Sigma|, |\mathcal{I}|$ and κ_{HFS}:

$$\begin{aligned}
\langle|\Phi||\Omega|; L|\Lambda|; S|\Sigma|; I|\mathcal{I}|\mathbb{I}_{\text{BO}}\mathbb{I}_{\text{HFS}}\kappa_{\text{BO}}\kappa_{\text{FS}}\kappa_{\text{HFS}}|f_a\phi_a; f_b\phi_b\rangle = \\
\sum\langle|\Phi|, |\Omega|, L|\Lambda|; S|\Sigma|; I|\mathcal{I}|\mathbb{I}_{\text{BO}}\mathbb{I}_{\text{HFS}}\kappa_{\text{BO}}\kappa_{\text{FS}}\kappa_{\text{HFS}}|\Phi\Omega; L\Lambda; S\Sigma; I\mathcal{I}\rangle \\
\times\langle\Phi\Omega L\Lambda; S\Sigma; I\mathcal{I}|l_a\lambda_a s_a\sigma_a i_a\iota_a; l_b\lambda_b s_b\sigma_b i_b\iota_b\rangle \\
\times\langle l_a\lambda_a s_a\sigma_a i_a\iota_a; l_b\lambda_b s_b\sigma_b i_b\iota_b|f_a\phi_a; f_b\phi_b\rangle
\end{aligned} \tag{5.27}$$

The first element deals with complications from the κ_{HFS} symmetry. It turns out that with the way I have constructed my bases, this is a little more complicated than before. In general, a state with good $|\Phi|$ and κ_{HFS} is composed of the two states with equal and opposite Φ with a phase determined by κ_{HFS}:

$$\begin{aligned}
\langle|\Omega|, L|\Lambda|; S|\Sigma|; I|\mathcal{I}|\mathbb{I}_{\text{BO}}\kappa_{\text{BO}}\kappa_{\text{FS}}|\Omega L\Lambda S\Sigma; I\mathcal{I}\rangle \\
= \kappa_{\text{FS}}\kappa_{\text{HFS}}(-1)^{I-|\mathcal{I}|}
\end{aligned} \tag{5.28}$$

For elements with negative Φ and 1 for elements with positive Φ. To be clear, it is also required that the absolute values and angular momentum values on both sides match, this is not an accident of notation. For example the matrix element with $|\Lambda| = 2$ on the left hand side and

$\Lambda = -1$ on the right hand side would be zero. I could also express this with a lot of delta functions, but this would be tedious. Note that both κ symbols are ±1 so overall this is just a phase. My bases could likely be defined in such a way to make this a little bit more sensible, but this is the way it works in my calculations.

The second element is relatively straightforward:

$$\langle \Phi\Omega L\Lambda; S\Sigma; I\mathcal{I} | l_a\lambda_a s_a\sigma_a; l_b\lambda_b s_b\sigma_b\rangle = \sum p^{l_a+S}\mathbb{I}_{\mathrm{BO}} C^{L\Lambda l_a l_b}_{l_a\lambda_a l_b\lambda_b} C^{S\Sigma s_a s_b}_{s_a\sigma_a s_b\sigma_b} C^{I\mathcal{I} i_a i_b}_{i_a\iota_a i_b\iota_b} \tag{5.29}$$

The last one is the easiest to deal with as it is only based on normal angular momentum combination rules:

$$\begin{gathered}\langle l_a\lambda_a s_a\sigma_a i_a\iota_a; l_b\lambda_b s_b\sigma_b i_b\iota_b | f_a\phi_a; f_b\phi_b\rangle = \\ \sum C^{j_a\omega_a}_{l_a\lambda_a s_a\sigma_a} C^{j_b\omega_b}_{l_b\lambda_b s_b\sigma_b} C^{f_a\phi_a}_{j_a\omega_a i_a\iota_a} C^{f_b\phi_b}_{j_b\omega_b i_b\iota_b}\end{gathered} \tag{5.30}$$

Then, to evaluate the hyperfine coupling, we simply force the eigenvalues of the hyperfine coupling matrix to match the experimental values.

It is notable especially in this case that completely calculating the above transformation matrices may not be the most efficient way of doing the calculation, as even after subdividing the basis into the block-diagonal symmetry classes, we are still working with relatively large bases which makes calculating the full transformation matrices rather numerically taxing, especially considering that one generally has to transform into the complete l-s-i basis for part of this transformation which is large even for ^{87}Rb. As a result, practically speaking I generally find that it is faster to simply transform individual good symmetry states into the relevant basis for calculating energies one at a time rather than constructing the entire matrix above.

5.7 Hyperfine Potentials Results and Discussion

The potentials including hyperfine interactions at a zoomed out level are visible in Fig. 5.2. A number of potentials at a more zoomed in range are visible in Fig. 5.3. Note that all the states with $\Phi \neq 0$ are doubly degenerate corresponding to the positive and negative phi states. The legends of the figures here report the value of Φ and the number of non-degenerate states in parentheses. These potentials reveal a number of interesting features which are worth taking note of. In order to analyze these in the context of the loading, we note that historically it has expected that specifically the repulsive nature of blue-detuned molecular potentials has been thought to be important for enhanced loading processes. Additionally, beyond the linewidth of the transition which is approximately 6 MHz, the most important energy scale of the loading problem is the trap depth. This is up to approximately 20 MHz, which is quite small on the scale of these potentials.

On the D_1 $f = 1, f' = 2$ and D_1 $f = 2, f' = 2$ transitions (Fig. 5.3(c,d)), which are the set of excitations used for the loading which works well, there is a nice repulsive potential for nearly every symmetry which is accessible on each transition. There are only a few exceptions such as the highest Φ symmetry states available on each transition, which only have one attractive and one repulsive potential available to split between the two inversion symmetry classes. Specifically, the 3_+ and 4_- states on the $f = 1$ and $f = 2$ transitions respectively only have a single attractive potential. But the relative plethora of repulsive states otherwise should make it relatively easy to primarily excite to repulsive states.

On the D_1 $f = 1, f' = 1$ and D_1 $f = 2, f' = 1$ transitions (Fig. 5.3(e,f)), where Λ-enhanced gray molasses is still possible but the loading of single atoms does not work as well, we see quite different behavior. For many available symmetry classes, especially on the $f = 1$ transition, there are no available repulsive transitions, or the repulsive transitions have only very shallow repulsive bumps. As a result, we expect it to be relatively difficult to selectively excite to repulsive potentials and control the amount of energy gained in a collision.

Lastly, on the D_2 $f = 1, f'' = 2$ and D_2 $f = 2, f'' = 2$ transitions where again Λ-enhanced gray molasses is possible, (Fig. 5.3(a,b)), we see in general a less clear picture, especially on the $f = 2$ transition. However, there are a number of avoided crossings at relatively large distances which cause many repulsive potentials to again only have relatively shallow barriers, which we expect to be important in the loading dynamics. It is therefore not so surprising that minimal enhanced loading is achieved in this configuration.

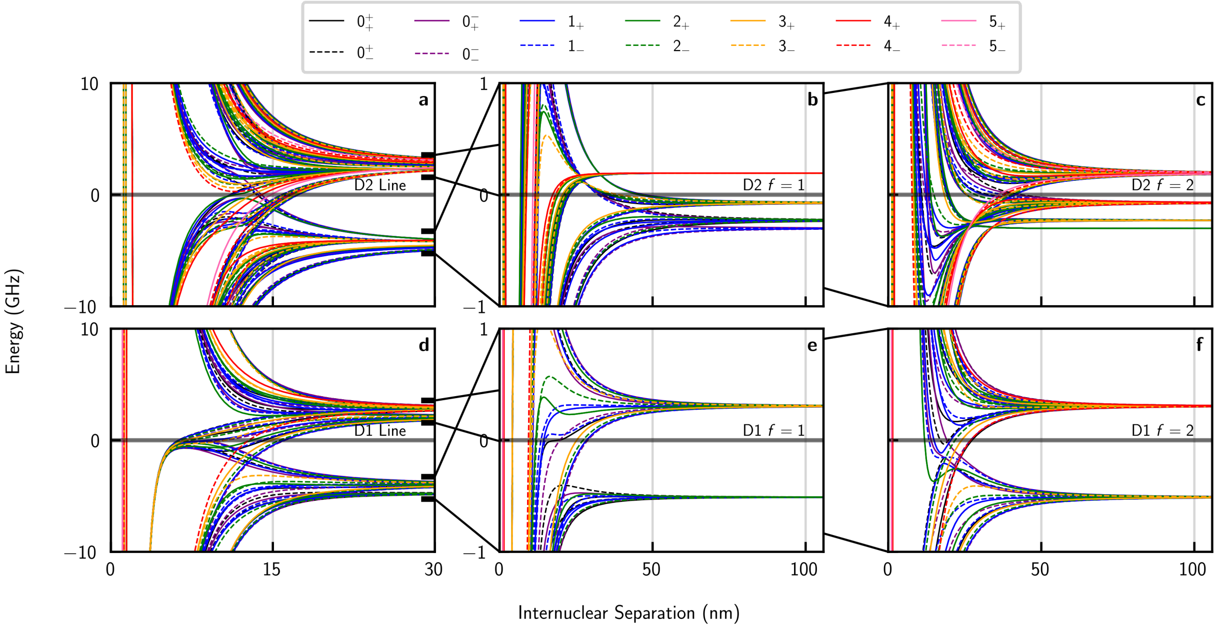

Figure 5.2: **Molecular Potential curves calculated with hyperfine structure included.** Different line styles and colors indicate the different symmetries of the states. Legend symbols are of the form $|\Phi|^{\kappa_{\mathrm{HFS}}}_{\mathbb{I}_{\mathrm{HFS}}}$. Zoomed out figures at the scale of Fig. 5.1 are omitted as at those large energy scales the HFS is not visible. **(a)** A relatively high-energy, short distance view of potentials that dissociate to the free space D_2 line. **(b)** A relatively low-energy, long-distance view of potentials that dissociate to the free space D_2 ground state $f = 1$ states. **(c)** Similar, but dissociating to the free space D_2 ground state $f = 2$ states. **(d)** A relatively high-energy view of potentials that dissociate to the free space D_1 line. **(e)** A relatively low-energy, long-distance view of potentials that dissociate to the free space D_1 ground state $f = 1$ states. **(f)** Similar, but dissociating to the free space D_1 ground state $f = 2$ states.

5.8 Discussion of Rotation Effects

The Hamiltonians above are diagonal in bases of non-rotating states, such that all nuclear motion is along the inter-nuclear axis. These rotating states are eigenstates of the Hamiltonian $\hat{L}_R^2/2m_\mu R^2$ with eigenvalues $\hbar^2\ell(\ell+1)/(2m_\mu R)$, for inter-nuclear angular momentum $\hat{L}_R$ and reduced mass m_μ. Relating the eigenbasis of this rotation Hamiltonian to the stationary bases of the other Hamiltonians is possible but non-trivial and beyond the scope of our present analysis, which we believe captures most of the dynamics that we are interested in.

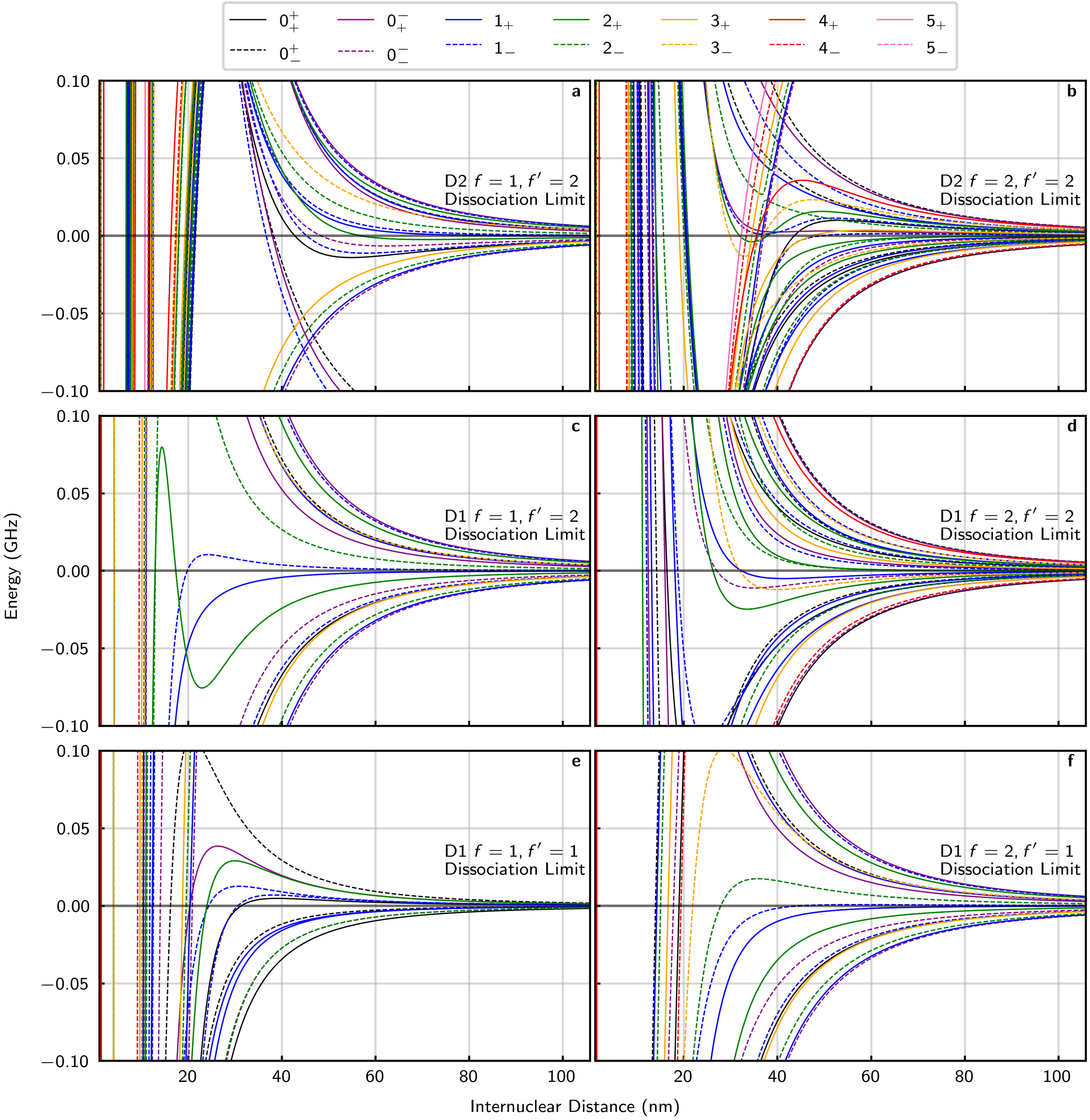

Figure 5.3: **Molecular Potentials with Hyperfine Interactions Zoomed-In.** Zoomed in views at the hyperfine dissociation limits of some of the potentials seen in Fig. 5.2(b,c,e,f). **(a)** The states which dissociate to the large separated atom D_2 $f = 1, f'' = 2$ manifold. **(b)** The states which dissociate to the large separated atom D_2 $f = 2, f'' = 2$ manifold. Near $R = 40$ nm, there are a number of avoided crossings with potentials that eventually dissociate to the higher energy $f = 2, f'' = 3$ manifold. **(c)** The states which dissociate to the separated atom D_1 $f = 1 f' = 2$ manifold. This set of states, combined with the states in (d), are where the enhanced loading technique generally works the best. **(d)** The states which dissociate to the separated atom D_1 $f = 2 f' = 2$ manifold. **(e)** The states which dissociate to the separated atom D_1 $f = 1 f' = 1$ manifold. This manifold in particular is lacking in good repulsive states. **(f)** The states which dissociate to the separated atom D_1 $f = 2 f' = 1$ manifold.

The maximum rotational kinetic energy scale of the collision is set by considering a collision between two atoms whose kinetic energy is just below twice the trap depth and is entirely rotational, which would be approximately 40 MHz. This energy scale is well below the HFS splitting of ^{87}Rb. As a result, even in this statistically improbable limit, the rotational kinetic energy should not mix states of good symmetry as described above very significantly.

Transitions between states with different rotational kinetic energy eigenvalues are limited by an angular momentum selection rule $\Delta\ell = \pm 1$. Therefore, the first effects one might see if including rotation become important when neighboring rotational states have differences in energy that are larger than the linewidth of the transition. Otherwise, the extra rotational states simply slightly broaden existing transitions. This occurs as atoms in optical tweezers are typically loaded after sub-doppler free-space cooling, they have relatively little kinetic energy and can only populate relatively low energy rotational kinetic energy states. For example, typical red-detuned polarization gradient cooling and Λ-enhanced gray molasses techniques make atoms reach free-space temperatures of approximately $10\,\mu$K or approximately $200\,$kHz. In the most extreme case of a glancing collision, this energy could be entirely rotational. Our analysis of the potentials without rotation indicate that collisions should generally happen at distances greater than $25\,$nm. At this distance and with these energies, the highest rotational state which might be reasonably populated would only have $\ell = 1$. At this distance the difference in energy between $\ell = 2$ and $\ell = 1$ states is $0.75\,$MHz, which is well below the ^{87}Rb D_1 transition linewidth of $\sim 6\,$MHz. Therefore in the worst case, the interaction between different rotational states would contribute only a small broadening of the normal transition, which is a small enough effect to neglect in our case. At larger distances, it is possible to populate higher rotational kinetic energy states, but the difference in energy between states drops still.

At the more extreme energy scale, two atoms that are very hot inside an optical tweezer might have a rotational kinetic energy as high as nearly twice the trap depth, or on the order of $40\,$MHz, at which point a similar calculation gives a maximal energy splitting of approximately 30 MHz, which is noticeably above the linewidth of the transition. This means that at this extreme some collisions which have somewhat significantly higher centrifugal repulsive barriers. However, since for these collisions all of the kinetic energy is rotational, little distance is traveled along the inter-nuclear axis, and so little kinetic energy, other than from photon recoil, should be gained from this type of collision.

5.9 Fine Structure and Rotation

Adding rotation to the problem complicates matters greatly. The original reference for this derivation is [143]. Notably, this resource is more general than my notes here and includes extra general quantum numbers to allow one to fully define the electronic configuration for more complicated atoms than alkali atoms. If you've made it this far, this is where the calculation gets much more difficult. Therefore I begin by omitting the HFS which will make the angular momentum algebra significantly easier. The rotational Hamiltonian here is

$$H_R = \frac{\hat{L}_R^2}{2m_\mu R^2} \tag{5.31}$$

where R is again the distance between atomic nuclei. The operator has standard eigenvalues $\hbar^2\ell(\ell+1)/2m_\mu R^2$, where ℓ is the rotational excitation quantum number. H_R doesn't commute with either H_{BO} or H_{FS}, so at this point we have three Hamiltonians in our main total Hamiltonian. Depending on R and the rotational state, any of these Hamiltonians can dominate, and so different quantum numbers are good, and different state bases are best to describe the states. The different cases of which terms are strongest are called Hund's cases in the literature, and there are five of them labeled (a)-(e). A description of Hund's cases is available in Table 5.2. Notably, Hund's cases don't consider the strength of the hyperfine interactions at all, so they will be limited to being useful in this section. H_{BO} is diagonal in case (a) and case (b) bases, H_{FS} is diagonal in the case (c) states, and H_R is diagonal in cases (d) and case (e). Therefore, since we have been working in the BO basis for all this work, the challenge of adding this to the Hamiltonian to the calculation amounts to finding the transformation matrices which transform states from case (e), where H_R is diagonal and easy to evaluate, to case (a), which should be the best basis to describe the states in our case.

With rotation included in the Hamiltonian, the case (a) states do not have good rotational angular momentum but they have good total angular momentum L_{JR} and it's **space-fixed** projection m_{JR}, and so should be written as $|L_{JR}m_{JR}\Lambda S\mathcal{P}\rangle$, where $\mathcal{P}$ is the space-fixed total parity eigenvalue, either of ±1. Notably, many references will commonly use the letter J for the total angular momentum including rotation in the FS case and $\hat{j} = \hat{j}_a + \hat{j}_b$ for the electronic angular momentum omitting rotation. This breaks the pattern in definitions I've established (and which other references mostly follow) however. In any case there is the potential for confusion. So for this thesis I follow my own preference and use the unique operator L_{JR} for the total angular momentum and $\hat{J} = \hat{j}_a + \hat{j}_b$ for the two-atom electronic angular momentum, maintaining the pattern that lower-case quantum numbers with subscripts are the individual atom angular momentum, while their capitalized counterparts are two-atom combined angular momentum. Since the projection of the rotational angular momentum along the internuclear axis is zero by construction, the projection of L_{JR} along the internuclear axis is Ω, the same as J. Refer to Table 5.1 for all angular momentum definitions.

States in case (e) are then described by quantum numbers $L_{JR}, m_{JR}, \ell, J, j_a$, and j_b, and they are related to the case (a) basis as

$$|L_{JR}m_{JR}(\ell J(j_a j_b))\rangle = \sum_{\Lambda S\Sigma} |L_{JR}m_{JR}\Lambda S\Sigma p\rangle\langle \ell J(j_a j_b)|\Lambda S\Sigma\mathcal{P}\rangle_{L_{JR}} \tag{5.32}$$

Where it should be understood that the matrix element $\langle \ell J(j_a j_b)|\Lambda S\Sigma p\rangle_{L_{JR}}$ between the eigenstates of the rotational Hamiltonian and the eigenstates of the BO Hamiltonian varies depending on the value of the total angular momentum L_{JR}. This equation can be thought of as the definition of this matrix element. Therefore the matrix elements we need to calculate are $\langle \ell J(j_a j_b)|\Lambda\sigma\Sigma\rangle$. How can one calculate this? The answer is to, in a somewhat orthogonal way, explicitly calculate the relationship between these states at large internuclear distance R, at which point the matrix element can be recovered. This calculation involves a good amount of non-trivial angular momentum algebra and very careful consideration of various phase factors which I will not attempt to reproduce here, and will instead only outline the approach. For more details and references I encourage the reader to study the original work [143].

I start by generally constructing the states $|L_{JR} m_{JR} \Lambda S \Sigma \mathcal{P}\rangle$, which include rotation through the total angular momentum quantum number L_{JR} and it's space-fixed projection m_{JR}, out of the non-rotating BO eigenstates $|\Lambda S \Sigma\rangle$. The rotational wavefunction can be added by making use of the Wigner D matrices which represent solutions to the rigid rotor problem in quantum mechanics and which are related to the spherical harmonic functions. Careful consideration of symmetrization and normalization, especially of the Wigner D matrices leads to the conclusion that this must be

$$\begin{aligned} &|L_{JR} m_{JR} \Lambda S \Sigma \mathcal{P}\rangle = \\ &\frac{1}{\sqrt{2-\delta_{\Lambda 0}\delta_{\Sigma 0}}}\sqrt{\frac{2L_{JR}+1}{8\pi^3}}\Big[D^{*L_{JR}}_{m_{JR}\Omega}(\alpha\beta\gamma)|\Lambda; S\Sigma\rangle \\ &\qquad + \mathcal{P}(-1)^{l_a+l_b+L_{JR}-S} D^{*L_{JR}}_{m_{JR}-\Omega}(\alpha\beta\gamma)|-\Lambda; S, -\Sigma\rangle\Big] \end{aligned} \tag{5.33}$$

This equation is general and should hold for all R, which is possible because of the hidden R dependence of the BO Eigensetates $|\Lambda S \Sigma\rangle$. Through a non-trivial amount of nuanced angular momentum algebra, one can expand this solution in the limit of large R to express it in terms of the case (e) states which have good j, ℓ, j_a, and j_b to get the following result:

$$\begin{aligned} |L_{JR} m_{JR} \Lambda S \Sigma \mathcal{P}\rangle \xrightarrow{R\to\infty} \sum_{J,\ell,j_a,j_b} |L_{JR} m_{JR}(\ell J(j_a j_b))\rangle \sqrt{\frac{2-\delta_{\Lambda,0}\delta_{\Sigma,0}}{2\pi}}(1-\mathcal{P}(-1)^{l_a+l_b+\ell})(-1)^{\ell-\Omega-L_{JR}} \\ \times C^{\ell 0}_{J,-\Omega L_{JR}\Omega}\langle J\Omega(j_a j_b)|L\Lambda; S\Sigma\rangle \end{aligned} \tag{5.34}$$

This can now be used to directly extract the transformation matrix element:

$$\begin{aligned}\langle \ell J(j_a j_b)|\Lambda S \Sigma \mathcal{P}\rangle_{L_{JR}} &= (-1)^{\ell-\Omega-L_{JR}} \frac{1+(-1)^{l_b+\ell+p}(1-\delta_{\Lambda,0}\delta_{\Sigma,0})}{\sqrt{2-\delta_{\Lambda,0}\delta_{\Sigma,0}}} \\ &\times C^{\ell 0}_{J,-\Omega L_{JR}\Omega}\langle J\Omega(j_a j_b)|L\Lambda; S\Sigma\rangle\end{aligned} \tag{5.35}$$

Now we can make use of the 9j relation discussed before (Eqn. 5.7), to quickly arrive at the result for the matrix element above:

$$\begin{aligned}\langle J\Omega(j_a j_b)|L\Lambda; S\Sigma\rangle &= \langle J\Omega(j_a j_b)|\sum_{J'} C^{J'\Omega LS}_{L\Lambda S\Sigma}|J'\Omega(LS)\rangle \\ &= C^{J\Omega LS}_{L\Lambda S\Sigma}\langle J\Omega(j_a j_b)|J\Omega(LS)\rangle \\ &= \sqrt{\breve{S}\breve{j}_a\breve{j}_b\breve{L}}\, C^{J\Omega LS}_{LS\Lambda\Sigma}\begin{Bmatrix} l_a & s_a & j_a \\ l_b & s_b & j_b \\ L & S & J\end{Bmatrix}\end{aligned} \tag{5.36}$$

With the recognition that $j_1 = l_a$, $j_2 = l_b$, $j_3 = s_a$, $j_4 = s_b$, $j_{12} = L$, $j_{34} = S$, $j_{13} = j_a$ and $j_{24} = j_b$.

This relation allows you to calculation transformation matrices to convert all the case (e) basis states to case (a) in order to evaluate the Hamiltonian for each value of ℓ and as a function of R. Specifically calculating $(\langle \ell J(j_a j_b)|\Lambda S\Sigma p\rangle_{L_{JR}})^{\dagger} H_R(R)\langle \ell J(j_a j_b)|\Lambda S\Sigma p\rangle_{L_{JR}}$ for a the relevant bases states for a given value of L_{JR}. With some herculean mastery of angular momentum algebra, a previous author has calculated analytical forms of Eqn. 5.35 and written them down in one reference [142]. These results are quite useful, although, we believe there is some mistake in this reference's equation 11, which gives a non-unitary transformation matrix which does not numerically match my results in numerically calculating the matrix element above.

For a given value of L_{JR}, states can have either positive or negative total parity. It turns out that the results of these calculations result in pairs of closely spaced rotational energy levels which have different parity, and so each state gets an additional label. States with parities $(-1)^{L_{JR}}$ are said to have "e" parity, and states with parities $-(-1)^{L_{JR}}$ are said to have "f" parity. For example, the state with $L_{JR} = 5$ and negative total parity is also of "e" parity and the state with positive total parity is of “f” parity. This scheme ensures that each state in the doublet has different such parity. The “e” and “f” labels are independent of the Hund’s case basis used. In other words, the matrix elements above do not mix states of different “e/f” parity. This parity label has historically fluctuated and been the source of confusion in the field, but was resolved in the 70’s. [144]. In the end, these results are used to calculate the potentials seen in Fig. 5.4. Similar analysis can be done for the hyperfine potentials discussed in the next section.

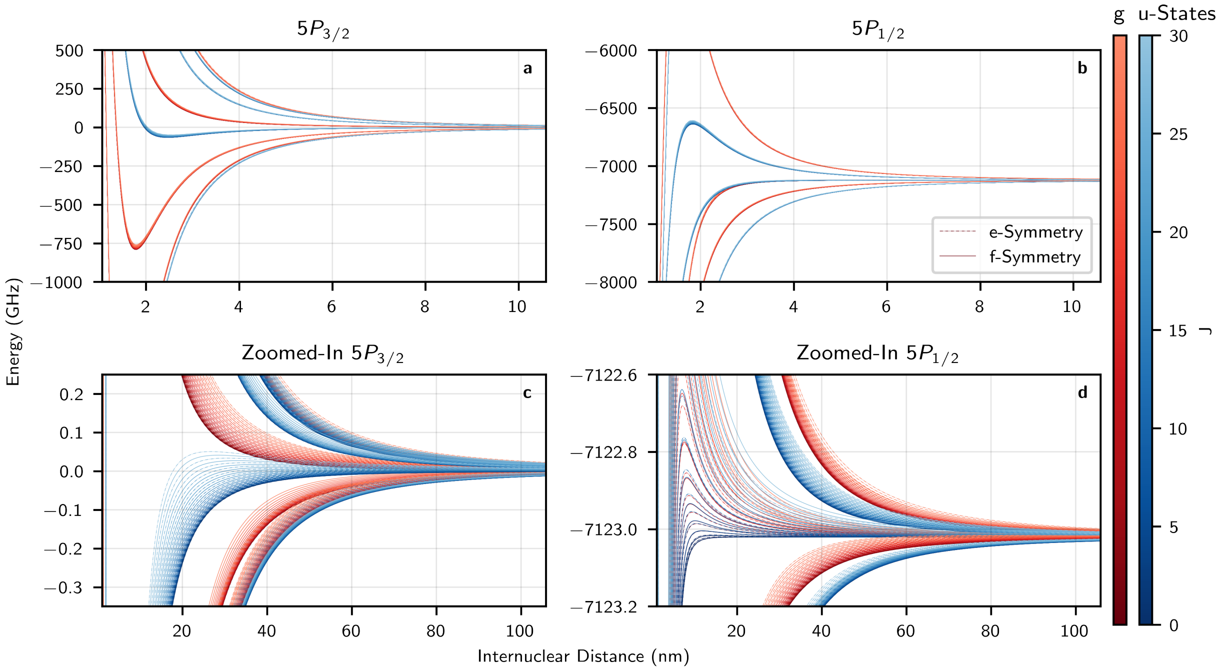

Figure 5.4: **Molecular Potentials with Rotation and Fine Structure.** Lines of various red colors represent states with different total angular momentum J and gerade symmetry. Lines of various blue colors represent states with different total angular momentum J and **ungerade** symmetry. **(a)** Large energy scale, short distance view of the $5P_{3/2}$ potential. **(b)** Large energy scale, short distance view of the $5P_{1/2}$ potential. **(c)** Lower energy scale, long distance view of the $5P_{3/2}$ potential. **(d)** Lower energy scale, long distance view of the $5P_{1/2}$ potential.

5.10 Hyperfine Structure With Rotation

This section is less well tested than the previous and should be viewed as notes on progress to the full calculation of potentials which include HFS and rotation simultaneously. These notes are partially aided based off of some unfinished notes which were received from Paul Julienne in the course of my studies [132]. The calculation should proceed similarly to the calculation above but with more angular momentum algebra to keep track of. With the inclusion of the hyperfine interactions, our total angular momentum is now A_F and it's space-fixed projection is m_{FR}. In this case with the HFS included, there are sparingly few resources to establish a common standard for the total angular momentum quantum numbers here, so there is less room for confusion, although some other resources may wish to define the total angular momentum as F and use $f = f_a + f_b$ for the total atomic angular momentum without rotation. But we will stick with L_{FR} and m_{FR}.

Working with case (a) is slightly more tricky because we want to have states of good total parity. Similarly to the case without rotation, we can start by adding rotational states to the BO states with HFS by using the Wigner D-matrices which gives terms like $\sqrt{\frac{2L_{FR}+1}{8\pi^2}} D^{*L_{FR}}_{m_{FR},\Phi}(\alpha\beta\gamma)|\Lambda S\Sigma I\mathcal{I}\rangle$. Here $D^{*L_{FR}}_{m_{FR},\Phi}(\alpha\beta\gamma)$ is the complex conjugate of the Wigner rotation matrix for angles α, β, and γ, which are arbitrary angles in the present context. In general these angles are unimportant and so will often be omitted from the matrix symbol. However, this is surprisingly not a state of good total parity, so instead we form a linear combination of these states with appropriate parity, and we get our case a basis:

$$\begin{aligned}|L_{FR} m_{FR} \Lambda S\Sigma I\mathcal{I}\mathcal{P}\rangle = &\frac{1}{\sqrt{2-\delta_{\Lambda 0}\delta_{\Sigma 0}\delta_{\mathcal{I}0}}}\sqrt{\frac{2L_{FR}+1}{8\pi^2}} \\ &\times \Bigg[D^{*L_{FR}}_{m_{FR},\Phi}(\alpha\beta\gamma)|\Lambda; S\Sigma; I\mathcal{I}\rangle \\ &+ p(-1)^{l_a+l_b+L_{FR}-I-S} D^{*L_{FR}}_{m_{FR},\Phi}(\alpha\beta\gamma)|-\Lambda; S, -\Sigma; I, -\mathcal{I}\rangle \Bigg]\end{aligned} \tag{5.37}$$

It's only at large R that the BO states gain good values for the quantum numbers l_a, l_b. As such, it's only as $R \to \infty$ that

$$\begin{aligned}|\Lambda; S\Sigma; I\mathcal{I}\rangle &= \sum_{\lambda_a,\lambda_b} |l_a\lambda_a\rangle|l_b\lambda_b\rangle|S\Sigma\rangle|I\mathcal{I}\rangle\langle l_a\lambda_a l_b\lambda_b|L\Lambda\rangle \\ |l_a\lambda_a\rangle|l_b\lambda_b\rangle|S\Sigma\rangle|I\mathcal{I}\rangle &= \sum_{F,f_a,f_b} |F\Phi(f_af_b)\rangle\langle F\Phi(f_af_b)|l_a\lambda_a l_b\lambda_b; S\Sigma; I\mathcal{I}\rangle \\ |F\Phi(f_af_b)\rangle &= \sum_{m_F} D^F_{m_F\Phi}|Fm_F(f_af_b)\rangle\end{aligned} \tag{5.38}$$

It should be possible to use these relations and some non-trivial angular momentum algebra to show that

$$\begin{aligned}|L_{FR}m_{FR}\Lambda; S\Sigma; I\mathcal{I}\mathcal{P}\rangle &\xRightarrow{R\to\infty} \sqrt{\frac{2-\delta_{\Lambda 0}\delta_{\Sigma 0}\delta_{\mathcal{I}0}}{2\pi}} \\ \times \sum_{F\ell f_a f_b} &|L_{FR}m_{FR}(\ell F(f_af_b))\rangle(1-\mathcal{P}(-1)^{l_a+l_b+\ell})(-1)^{\ell-\Phi-L_{FR}} \\ &\times C^{\ell 0}_{F,-\Phi L_{FR}\Phi}\langle F\Phi(f_af_b)|\lambda_a\lambda_b S\Sigma I\mathcal{I}\rangle\end{aligned} \tag{5.39}$$

Where now we have a much harder additional matrix element to calculate.

And this should give the result:

$$\begin{aligned}\langle F\ell(f_af_b)|\Lambda S\Sigma I\mathcal{I}\mathcal{P}\rangle_{L_{FR}} &= (-1)^{\ell-\Phi-L_{FR}}\frac{1+(-1)^{l_b+\ell+p}(1-\delta_{\Lambda 0}\delta_{\Sigma 0}\delta_{\mathcal{I}0})}{\sqrt{2-\delta_{\Lambda 0}\delta_{\Sigma 0}\delta_{\mathcal{I}0}}} \\ &C^{\ell 0}_{F,-\Phi L_{FR}\Phi}\langle F\Phi(f_af_b)|L\Lambda; S\Sigma; I\mathcal{I}\rangle\end{aligned} \tag{5.40}$$

There are 6 basic angular momentum and multiple ways to couple them to construct states of total angular momentum F. In the case here, there are two ways to construct the total electronic angular momentum J. We have $\hat{J} = \hat{l}_a + \hat{s}_a + \hat{l}_b + \hat{s}_b$, and we can first couple the two orbital angular momentums and spins to create states $|Jm_J(LS)\rangle$, or we can construct the individual electronic angular momentum first and create states $|Jm_J(j_aj_b)\rangle$. Similarly, we have four angular momentum j_a, j_b, i_a, and i_b to construct states of good F in two critical ways to create two bases: $|Fm_F(JI)\rangle$ or $|Fm_F(f_af_b)\rangle$. This is going to lead to two Wigner 9j symbols. And this is suggestive that we are looking to construct the matrix elements $\langle Fm_F(f_af_b)|Fm_F(JI)\rangle$ and $\langle Jm_J(j_aj_b)|Jm_J(LS)\rangle$ out of the given matrix element, both of which will reduce to Clebsch Gordon coefficients. With these patterns identified, it's just angular momentum algebra to get to the result. In the following I explicitly label $f_a(j_a i_a)$ and similar terms until the middle of the derivation to emphasize the cancellation with the j'_a terms in the sum. It is important to keep in mind thought that any time in these derivations f_a is a good quantum number, j_a (and l_a and s_a) and i_a are as well, and I just typically omit these because there is only one standard way to combine these angular momentum.

$$\begin{aligned}
&\langle F\Phi(f_a(j_a i_a)f_b(j_b i_b))|l_a\lambda_a l_b\lambda_b; S\Sigma; I\mathcal{I}\rangle \\
&= \langle F\Phi(f_a(j_a i_a)f_b(j_b i_b))|\left(\sum_L C^{L\Lambda}_{l_a\lambda_a,l_b\lambda_b}|L\Lambda\rangle\right)|S\Sigma; I\mathcal{I}\rangle \\
&= \sum_L C^{L\Lambda}_{l_a\lambda_a,l_b\lambda_b}\langle F\Phi(f_a(j_a i_a)f_b(j_b i_b))|\Big(\sum_J C^{J\Omega LS}_{L\Lambda S\Sigma}|J\Omega(LS)\rangle\Big)|I\mathcal{I}\rangle \\
&= \sum_{L,J} C^{L\Lambda}_{l_a\lambda_a,l_b\lambda_b}C^{J\Omega}_{L\Lambda S\Sigma}\langle F\Phi(f_a(j_a i_a)f_b(j_b i_b))|\left(\sum_{j'_a j'_b}|J\Omega j'_a j'_b\rangle\langle J\Omega j'_a j'_b|J\Omega(LS)\rangle\right)|I\mathcal{I}\rangle \\
&= \sum_{L,J} C^{L\Lambda}_{l_a\lambda_a,l_b\lambda_b}C^{J\Omega}_{L\Lambda S\Sigma}\langle F\Phi(f_a f_b)| \\
&\quad \times\Big(\sum_{F'} C^{F'\Phi JI}_{J\Omega I\mathcal{I}}|F'\Phi(JI)\rangle\Big)\langle J\Omega(j_a j_b)|J\Omega(LS)\rangle \qquad (5.41) \\
&= \sum_{L,J} C^{L\Lambda}_{l_a\lambda_a,l_b\lambda_b}C^{J\Omega}_{L\Lambda S\Sigma}C^{F\Phi JI}_{J\Omega I\mathcal{I}}\langle F\Phi(f_a f_b)|F\Phi(JI)\rangle\langle J\Omega(j_a j_b)|J\Omega(LS)\rangle \\
&= \sum_{L,J}\left(C^{L\Lambda l_a l_b}_{l_a\lambda_a,l_b\lambda_b}C^{J\Omega LS}_{L\Lambda S\Sigma}C^{F\Phi}_{J\Omega I\mathcal{I}}\right)\sqrt{\breve{j}_a\breve{j}_b\breve{f}_a\breve{f}_b\breve{L}\breve{S}\breve{j}\breve{I}}\begin{Bmatrix} l_a & s_a & j_a \\ l_b & s_b & j_b \\ L & S & J\end{Bmatrix}\begin{Bmatrix} j_a & i_a & f_a \\ j_b & i_b & f_b \\ J & I & F\end{Bmatrix} \\
&= \sum_J\left(C^{J\Omega 1S}_{1\Lambda S\Sigma}C^{F\Phi JI}_{J\Omega I\mathcal{I}}\right)\sqrt{3\breve{j}_a\breve{j}_b\breve{f}_a\breve{f}_b\breve{S}\breve{J}\breve{I}}\begin{Bmatrix} 0 & s_a & j_a \\ 1 & s_b & j_b \\ 1 & S & J\end{Bmatrix}\begin{Bmatrix} j_a & i_a & f_a \\ j_b & i_b & f_b \\ J & I & F\end{Bmatrix}
\end{aligned}$$

In the last step I substitute $L = 1, l_a = 0, l_b = 1$ as this is always true for alkali metals in S+P potentials. I also remove the sum and Clebsch-Gordon coefficient and sum, as there is always exactly one non-zero Clebsch-Gordon coefficient of value 1 in this sum. Where in second-to-last I use the Wigner 9j relations (Eqn. 5.7) with the appropriate substitutions. If this is difficult to follow, consider reviewing the fine structure calculation or the notation section. Now we can really appreciate the breve. It is useful to realize that a number of sums in this derivation, the F', j'_a, and j'_b sums, immediately reduce to single values because of the matrix left hand side of the inner product will select out the appropriate numbers. The Clebsch-Gordon coefficient with only orbital angular momentum is typically 1.

5.11 Future Work

We believe that there are many avenues for future work in this area. Among the extensions to these calculations, the primary remaining addition is the inclusion of rotation into the potentials which have HFS. However, other additional corrections such as relativistic retardation effects have been significant in other contexts [145], and may be interesting to explore here as well.

There are many additional properties of the potentials which are of interest. These include the transition line strengths, excitation rates, state lifetimes, transition selection rules, and other properties of the states relevant for loading processes [146]. Many more radical extensions of this work are also possible, such as the studying of three-body potentials and collisions, or studying different species with different level structures in this context.

These potentials could be used to model and study loading processes in more advanced ways. Previous experiments with single atoms in optical tweezers have attempted to characterize and model the nature of related collisions using a variety of methods, but without the insight that these potentials provide. Similar methods could be used to experimentally validate some of these calculations [47, 128].

Table 5.1: **Angular Momentum Definitions and Other Notation.**

Description	Angular Momentum Operator $\hat{Z}$	$\hat{Z}^2$ Eigenvalues $(\hbar^2 z(z+1))$	Body-Fixed $\hat{Z}_z$ Eigenvalues $(\hbar m_z)$	Space-Fixed $\hat{Z}_z$ Eigenvalues $(\hbar m_z)$
Single Electron Orbital A.M.	$\hat{l}_\alpha$	l_α	λ_α	m_{l_α}
Total Electron Orbital A.M.	$\hat{L} = \hat{l}_a + \hat{l}_b$	L	$\Lambda = \lambda_a + \lambda_b$	$m_L = m_{l_a} + m_{l_b}$
Single Electron Spin	$\hat{s}_\alpha$	s_α	σ_α	m_{s_α}
Total Electron Spin	$\hat{S} = \hat{s}_a + \hat{s}_b$	S	$\Sigma = \sigma_a + \sigma_b$	$m_S = m_{s_a} + m_{s_b}$
Single Electron Total A.M.	$\hat{j}_\alpha = \hat{l}_\alpha + \hat{s}_\alpha$	j_α	$\omega_\alpha = \lambda_a + \sigma_a$	$m_{j_\alpha} = m_{l_\alpha} + m_{s_\alpha}$
Total Electron A.M.	$\hat{J} = \hat{L} + \hat{S}$	J	$\Omega = \Lambda + \Sigma$	$m_J = m_L + m_S$
Total A.M. Except Nuclear Spin	$\hat{L}_{JR} = \hat{L} + \hat{S} + \hat{L}_R$	L_{JR}	The same Ω	$m_{JR} = m_L + m_S + \mu$
Nuclear Rotational A.M.	$\hat{L}_R = \hat{L}_{JR} - \hat{L} - \hat{S}$	ℓ	0 (Always)	$\mu = m_{JR} - m_L - m_S$
Single Nuclear Spin	$\hat{i}_\alpha$	i_α	ι_α	m_{i_α}
Total Nuclear Spin	$\hat{I} = \hat{i}_a + \hat{i}_b$	I	$\mathcal{I} = \iota_a + \iota_b$	$m_I = m_{i_a} + m_{i_b}$
Single Atom Total A.M.	$\hat{f}_\alpha = \hat{j}_\alpha + \hat{i}_\alpha$	f_α	$\phi_\alpha = \omega_\alpha + \iota_\alpha$	$m_{f_\alpha} = m_{j_\alpha} + m_{i_\alpha}$
Total Non-Rotational A.M.	$\hat{F} = \hat{J} + \hat{I}$	F	$\Phi = \Omega + \mathcal{I}$	$m_F = m_J + m_I$
Total A.M.	$\hat{L}_{FR} = \hat{J} + \hat{I} + \hat{L}_R$	L_{FR}	The same Φ	$m_{FR} = m_J + m_I + \mu$

Hund's Case	Energy Hierarchy
(a)	$\lvert E_{BO}\rvert \gg \lvert E_{FS}\rvert \gg E_R$
(b)	$\lvert E_{BO}\rvert \gg E_R \gg \lvert E_{FS}\rvert$
(c)	$\lvert E_{FS}\rvert \gg \lvert E_{BO}\rvert \gg E_R$
(d)	$E_R \gg \lvert E_{BO}\rvert \gg \lvert E_{FS}\rvert$
(e)	$\lvert E_{FS}\rvert \gg E_R \gg \lvert E_{BO}\rvert$

Table 5.2: **Hund's Case Energy Hierarchies.** The various Hund's cases and their energy hierarchies. $|E_{BO}|$ denotes the magnitude of the electrostatic energy or the BO energy, $|H_{FS}|$ denotes the magnitude of the FS energy, and E_R, which is strictly positive, denotes the magnitude of the rotational energy.

Chapter 6

Time-of-Flight Quantum Tomography of Single Atom Motion

Time of flight is an intuitive way to determine the velocity of particles and lies at the heart of many capabilities ranging from mass spectrometry to fluid flow measurements. Here we show time-of-flight imaging can realize tomography of a quantum state of motion of a single trapped atom. Tomography of motion requires studying the phase space spanned by both position and momentum. By combining time-of-flight imaging with coherent evolution of the atom in an optical tweezer trap, we are able to access arbitrary quadratures in phase space without relying on coupling to a spin degree of freedom. To create non-classical motional states, we harness quantum tunneling in the versatile potential landscape of optical tweezers, and our tomography both demonstrates Wigner function negativity and assesses coherence of non-stationary states. Our demonstrated tomography concept has wide applicability to a range of particles and will enable characterization of non-classical states of more complex systems or massive dielectric particles [147].

The creation and full reconstruction of quantum states featuring genuine non-classical behavior has played a key role in the development of quantum systems. Such reconstructions are perhaps most familiar in quantum optics, where preparing and measuring modes of the electromagnetic field in non-classical states were striking demonstrations of the quantum nature of light. In these experiments, state characterization has been accomplished both with homodyne tomography [148, 149, 150, 151] and by coupling photons to a spin degree of freedom in cavity or circuit quantum electrodynamics (QED) [152, 153]. The associated quasiprobability distributions that are obtained, such as the Wigner function, are useful tools in analyzing non-classical behavior. While quasi-classical coherent states have strictly positive Wigner functions, other states, such as excited Fock states and Schrödinger cat states, can exhibit regions of negative phase-space density that have no classical analog.

For particles with mass, the observation of non-classical states of motion is equally intriguing. Early experiments with trapped ions created non-classical states using trap displacements and Raman sideband transitions, the spin-phonon analog to cavity QED. They verified the generation of squeezed states, Fock states, and cat states among others [154], and have continued to explore a rich space of tomography methods [155]. Meanwhile, the control of quantum motion of objects has expanded greatly in recent years, for instance with the ability to couple artificial spins to mechanical solid-state acoustical excitations [156, 157]. Another example is particle levitation, where one can achieve environmentally-isolated masses whose wavefunction can be expanded over large scales for fundamental studies with massive particles [158, 159, 160]. It is now possible to cool the center-of-mass motion of a dielectric particle to its quantum ground state [53, 161, 162], and it has been proposed that quantum state creation and characterization for these masses can be explored using nonlinear potential landscapes and time-of-flight tomography [163, 164]. But to date directly measuring rotated quadratures in position and momentum [165], the natural analogy to optical homodyne tomography, has not been harnessed to characterize a non-classical state of a single trapped particle.

In this work, we demonstrate tomography of a single neutral atom prepared in non-classical motional states using time-of-flight imaging (Fig. 6.1). Time-of-flight samples a particle's momentum distribution (Fig. 6.1a), and has been used in optical tweezers to measure thermal single atoms [166] and to probe spin correlations in few-fermion systems [167]. Time-of-flight imaging and detection has also been used to great effect in neutral atomic gases and optical lattices [168, 169, 170, 171, 172], and has enabled momentum distribution measurements of atomic ensembles prepared in squeezed, Fock, and superposition states [173], and tomography of the dynamics of a Bose-Einstein condensate [174]. In our work, using detection with single atom sensitivity, and measurements at multiple quadrature angles, we carry out full tomography and reveal

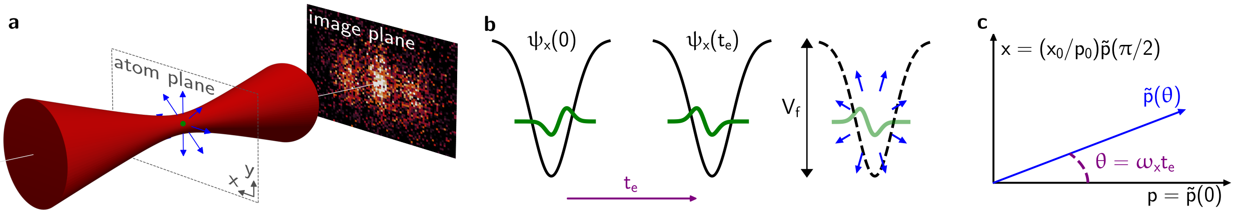

Figure 6.1: Tomography sequence and notation. **(a)** Many time-of-flight images of a single atom released from the optical tweezer are averaged to measure the momentum distribution of a quantum state of motion. **(b)** An initial state (green) is prepared in an optical tweezer. The state evolves over a time t_e. The tweezer is turned off from a depth of V_f, and the atom expands in free space (blue arrows) for a fixed flight time t_f. **(c)** The distribution measured after a given evolution time t_e in the trap, $\tilde{p}(\theta) = \tilde{p}(\omega_x t_e)$, is a generalized quadrature measurement of the initial state. At specific t_e, this generalized quadrature can be equivalent to the momentum quadrature $p = \tilde{p}(0)$ or the position quadrature $x = (x_0/p_0)\tilde{p}(\pi/2)$.

negative valued Wigner functions with a single particle [163].

As illustrated in Fig. 6.1, to obtain a time-of-flight image we suddenly turn off the optical tweezer and allow the atom to fly in free space for a fixed time t_f. We then average many such images to determine the momentum distribution at the time of release. We extract arbitrary quadrature distributions by combining time-of-flight imaging with in-trap harmonic evolution for a time t_e (Fig. 6.1b,c). We start with a state $\psi_x(t_e = 0)$ that we want to characterize, and measuring this initial state via time of flight gives the momentum quadrature $\tilde{p}(t_e = 0) = p$. If we allow the atom with mass m to evolve in an ideal harmonic trap, the in-trap momentum after a time t_e is the rotated quadrature $\tilde{p}(\theta) = p\cos\theta + (p_0/x_0)x\sin\theta$ (Fig. 6.1c), where $\theta = \omega_x t_e$, and $x_0 = \sqrt{\hbar/(2m\omega_x)}$ and $p_0 = \sqrt{m\hbar\omega_x/2}$ are the characteristic length and momentum of the harmonic oscillator with angular frequency ω_x. By varying the evolution time t_e we can extract an ensemble of quadrature distributions $\tilde{p}(\theta)$ for $\theta \in [0, 2\pi]$, analogous to what is done in optical homodyne tomography. The quadratures can be used to reconstruct the complete quantum state of the particle or equivalently the Wigner function $W(x, p)$.

In our experiments we test our protocol with multiple motional states, such as Fock states and displaced Fock states. To create the near-ground state of a single neutral ^{87}Rb atom, we use Raman sideband cooling [175]. To then create non-classical motional states, we use versatile control of quantum tunneling in the optical tweezer [58]. This capability does not rely upon internal states and spin-motion coupling as in standard trapped ion settings [154, 176], and hence, can be extended to polarizable particles with no controlled internal degrees of freedom. With large mass dielectric particles, while quantum tunneling is not experimentally feasible, it has been proposed that other non-harmonic potentials created by optical tweezers can enable quantum state synthesis [177, 178].

Our experiments start by stochastically loading single ^{87}Rb atoms into optical tweezer traps using grey optical molasses and ascertaining the presence or absence of an atom through an initial in-trap fluorescence image. We then use optical molasses cooling followed by three-dimensional Raman sideband cooling in a trap of depth 1.0 mK to prepare the atom close to the three-dimensional motional ground state $|n_x, n_y, n_z\rangle = |0, 0, 0\rangle$ (Sec. 6.1) [175]. The trap is then adiabatically ramped down to a depth of $0.33\,\mu\mathrm{K}$ where remaining thermal population is allowed to escape to further purify the initial state.

In the first set of experiments, we measure the momentum distribution of motional states at $t_e = 0$ (Fig. 6.2). After preparing the state of interest, we adiabatically ramp the trap to a final depth $V_f/k_B = 2.4\,\mu\mathrm{K}$ and then abruptly turn off the trap (Sec. 6.1). We then wait a flight time t_f before applying resonant light for $\tau = 10\,\mu\mathrm{s}$ and collecting fluorescence through the high numerical aperture (NA) lens that creates the optical tweezers on an electron-multiplying CCD (EMCCD) camera. We repeat this procedure to realize multiple instances of single atom momentum measurements, and collect enough data to create an averaged momentum distribution that is observable above the camera noise. Experimental runs where an atom is not detected in the initial in-trap fluorescence image are used to characterize our imaging background, which is then subtracted from our captured momentum distribution (Sec. 6.2.3).

We first characterize the expansion dynamics of an atom prepared close to the ground state of the optical tweezer with angular trap frequencies $\omega_{x,y,z}$ (Fig. 6.2a,d). The initial ground-state root mean square (RMS) size $\sigma_{x,y}$ in position space is estimated as $x_0 = 86\,\mathrm{nm}$, which is well below the resolution of our imaging system (Fig. 6.1a). At an expansion time of $t_f = 0.5\,\mathrm{ms}$, the atomic probability distribution has expanded to an RMS size of $2.4(1)\,\mu\mathrm{m}$ in the atom plane, which is resolved by our imaging system (Fig. 6.2d). By studying the expansion as a function of flight time t_f, we can ascertain that the expansion's kinetic energy observed in the radial directions of $(k_B \times 0.256(16)\,\mu\mathrm{K})/2$ is partly driven by the expected zero-point kinetic energy of the harmonic oscillator, $E_{\mathrm{zp}}/2 = \hbar\omega_{x,y}/4 = (k_B \times 0.188(1)\,\mu\mathrm{K})/2$ (Sec. 6.3.2). The difference in energy is due to the finite temperature of the atoms, which can also be seen in Raman spectroscopy (Sec. 6.3.1).

Starting with a ground-state atom, we create $n_x = 1$ or $n_x = 2$ motional Fock states using one-dimensional tunneling in a double well. The tweezer is moved to $0.88\,\mu\mathrm{m}$ from a second empty optical tweezer on the right, and with both tweezers near a depth of $1.8\,\mu\mathrm{K}$ we bring the ground state of the left tweezer nearly energetically resonant with higher-n_x states of the right tweezer. Then, with an adiabatic sweep of the relative tweezer depths, the atom is transferred into the target excited state of the right tweezer (Fig. 6.2b,c) (Sec. 6.1.4) [58]. The two tweezers are then slowly separated and the intensity of the left tweezer is ramped to zero, releasing any atom that did not successfully transfer to avoid polluting the final image (Sec. 6.2.4). We abruptly turn the remaining right tweezer off from 2.4 µK and proceed with the same imaging procedure as for the $n_x = 0$ state. The resulting $n_x = 1$ and $n_x = 2$ momentum distributions in Fig. 6.2e,f show characteristic fringing that is expected of the excited motional states.

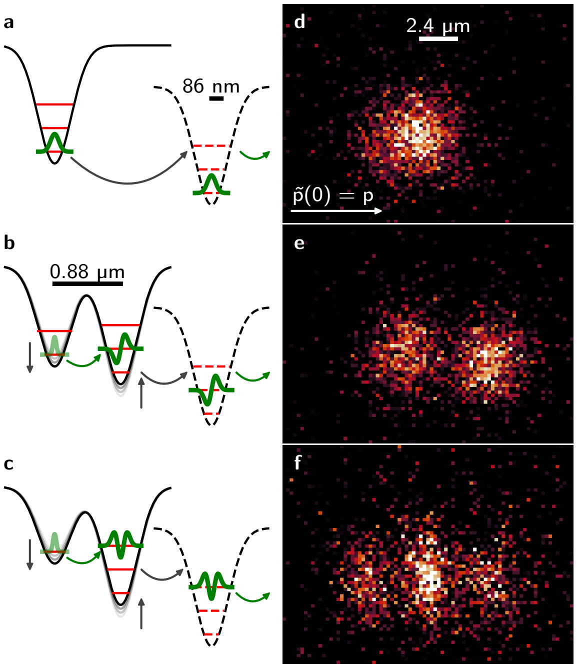

Figure 6.2: **Single-atom Fock state preparation and imaging.** **(a),(b),(c)** Illustration of motional state preparation of $n \in \{0, 1, 2\}$ states, respectively. **(d),(e),(f)** Time-of-flight momentum distributions at $t_e = 0$ and for $t_f = 0.5$ ms of $n_x = (0, 1, 2)$ states for which (64008, 48309, 58899) images were averaged, respectively.

We now proceed to the full tomographic characterization of motional states. In these experiments, we study multiple quadrature distributions by waiting a variable amount of evolution time t_e before releasing the atom and imaging the result. We can visualize the quadrature data as time-sequence waterfall plots (Fig. 6.3a,d,g), which are derived from our raw distributions by deconvolving with the imaging point spread function (PSF) and integrating out the vertical axis (Sec. 6.2.4). We study states with a goal of testing the capacity of time-of-flight tomography to

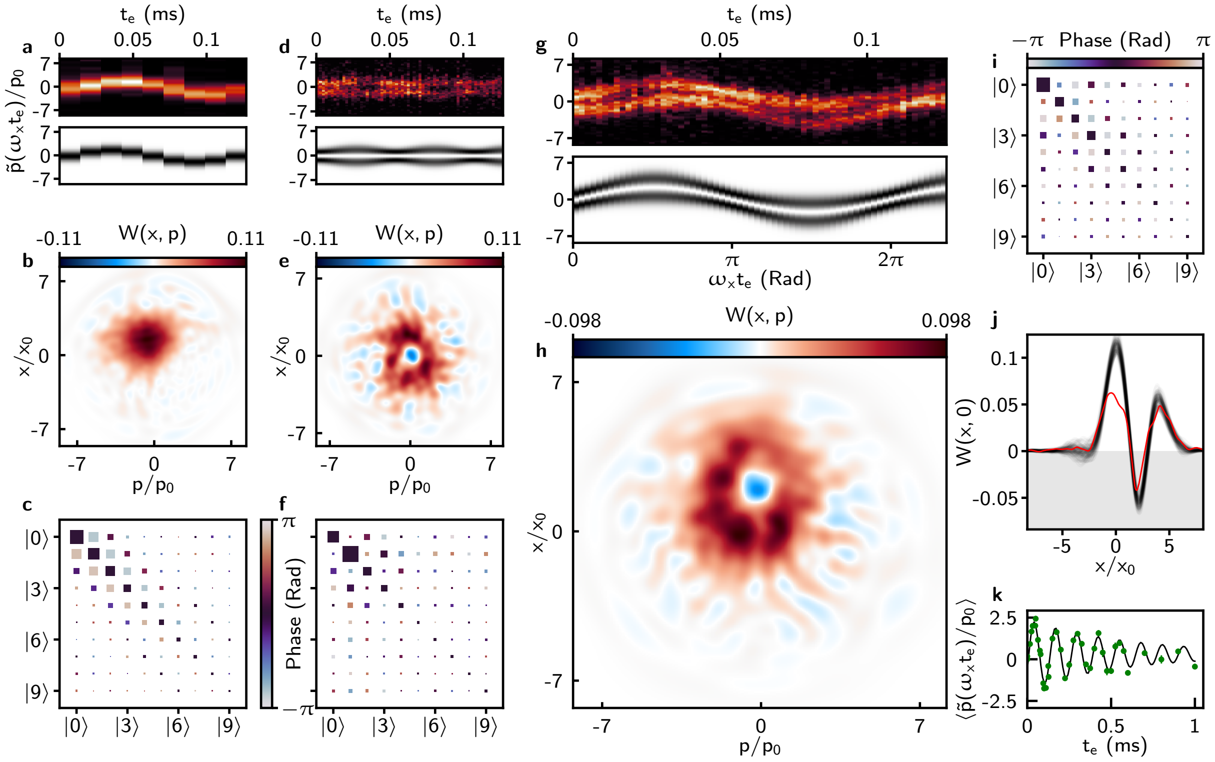

Figure 6.3: **Motional quantum state tomography via time-of-flight imaging and maximum likelihood estimation**. Measured quadrature data, Wigner function, and density matrix Hinton plot for the displaced $n_x = n_y = 0$ state **(a,b,c)**; $n_x = 1$ state **(d,e,f)** and displaced $n_x = 1$ state **(g,h,i)** both with a slight squeezing operator also applied. **Quadrature data:** Waterfall plots (a,d,g). Each vertical slice corresponds to a raw quadrature distribution, such as in Fig. 6.2, after deconvolving with the imaging PSF and integration along the vertical axis. The measured data (upper waterfall plot) is compared to the expectation for ideal preparation and harmonic time evolution based upon our protocol (lower waterfall plot). **Wigner functions:** Wigner functions (b,e,h) show classical positive values as red and non-classical negative values as blue. We normalize the Wigner function such that the ideal negativity of a pure $n_x = 1$ state is $-1/\pi$. **Density matrices:** Hinton plots (c,f,i) for density matrices as reconstructed via MLE. The area of each square is proportional to the magnitude of the corresponding element's complex value; the color of the square represents the element's phase. **(j)** $p = 0$ slice of reconstructed Wigner functions from (h) (red). Equivalent slices as reconstructed through a bootstrapping method (black) that characterize the statistical uncertainty of our reconstruction algorithm. **(k)** Evolution of the measured center of the coherent state (green circles) and damped sinusoidal fit (black line), which is used to characterize the trap frequency and anharmonicity.

identify non-classicality and phase preservation, as well as subtle non-stationary features. First, we create a coherent state by starting with an $n_x = 0$ state in the $V_f/k_B = 2.4\,\mu\mathrm{K}$ trap and abruptly displacing the optical tweezer by 180 nm. We find the state oscillates back and forth in the trap as expected (Fig. 6.3a). Next, we produce an $n_x = 1$ Fock state using the same protocol as the data presented in Fig. 6.1b. In addition, after the tunneling and optical tweezer separation, the depth is suddenly doubled, resulting in application of a squeezing operation. The atom is then released from a trap of $V_f/k_B = 3.6\,\mu\mathrm{K}$. We observe that the state is mostly stationary, as expected, with the addition of a slight breathing from the squeezing induced by the depth jump (Fig. 6.3d). Lastly, we combine multiple techniques by starting with an $n_x = 1$ state, applying the sudden doubling of the trap depth, and in addition displacing the optical tweezer by 140 nm. As shown in Fig. 6.3g, we are able to observe the expected oscillation dynamics of the state in the trap.

To reconstruct the quantum state from the quadrature data, we choose to use maximum likelihood estimation (MLE) [179] (Sec. 6.4.2). An appropriately designed MLE algorithm takes the quadrature data and returns the density matrix that is most likely to reproduce this data [180]. We implement an iterative MLE protocol based on the standard optical homodyne tomography literature [181], and from the density matrix, the Wigner function is directly recovered (Fig. 6.3).

The results of applying the MLE algorithm to the quadrature data are then presented in Fig. 6.3b,c,e,f,h,i. The coherent state displays significant off-diagonal coherences but, as expected, a positive Wigner function (Fig. 6.3b,c). The non-Gaussian state preparation associated with Fig. 6.3d,g results in the density matrices and Wigner functions with negative values displayed in Fig. 6.3e,h,f,i. The value and statistical error on the density matrix and Wigner function negativity is estimated by a bootstrapping technique [181], in which we randomly sample predicted quadrature and noise distributions based on the MLE result and our camera noise characterization respectively. We then extract the density matrices of these data sets to create a statistical ensemble of density matrices and Wigner functions (Sec. 6.5). The nearly-stationary $n_x = 1$ state displays a dominant $n_x = 1$ component and the Wigner minimum is found to be $-0.060(6)$ (Fig. 6.3e). Adding a displacement demonstrates non-trivial off-diagonal coherences and a negative Wigner function value at the displaced center of $-0.064(6)$ (Fig. 6.3h,j).

A full assessment of the reconstructed wavefunction must also consider systematic errors (Sec. 6.5). Trap anharmonicity, for example, will result in measured quadratures that do not simply follow from the rotated quadratures of the ideal protocol. We determine the impact of anharmonicity by theoretically assessing the tomography protocol based on a model using measured trap parameters. We estimate our trap anharmonicity by studying the coherent state oscillations of Fig. 6.3a over a longer time (Fig. 6.3k). The center of the Gaussian oscillates at 7.84(5) kHz, and decays with a time constant of 0.63(14) ms. A model of the trap containing an anharmonic term is fitted to match the observed damping. For a displaced $n_x = 1$ state in this model, we compare the reconstructed states obtained from MLE after evolution in a trap with and without our modelled anharmonic terms. We observe only a small infidelity of $< 5\%$ between the resulting reconstructed states, and the Wigner function minimum for anharmonic evolution is smaller in magnitude by < 0.01 compared to harmonic evolution, and remains negative (Sec. 6.5.3). In the future, the large dynamic range and control afforded by optical traps can be used to control the harmonicity. Specifically, a shallow double-well or other anharmonic traps could be used for state creation, and the tomography could be carried out after ramping to a much deeper and less anharmonic trap.

We have demonstrated quantum tomography of non-classical single atom motional states. By using time-of-flight imaging we have measured negative-valued Wigner functions with non-trivial phase-space structure. This work lays the foundation for tomography and characterization of massive levitated particles without exploitable spin structure [160, 177, 164]. Further, time-of-flight imaging of single atoms will enable study of high-n motional superposition states [182], highly squeezed states, and interference [183] of complex delocalized states.

Acknowledgements: We thank Tobias Thiele, Steven Pampel, and Ting-Wei Hsu for valuable insights and technical assistance, and Konrad Lehnert and Adam Kaufman for input on the manuscript. We acknowledge funding from NSF Grant PHYS 1734006, ONR Grant N00014-17-1-2245 and Grant N00014-21-1-2594, NSF QLCI Award OMA 2016244, and the U.S. Dept. of Energy, Office of Science, National Quantum Information Science Research Centers, Quantum Systems Ac-

celerator, and the Baur-SPIE Endowed Professor at JILA. W. J. D acknowledges support from an NSF Graduate Fellowship.

6.1 Optical tweezers

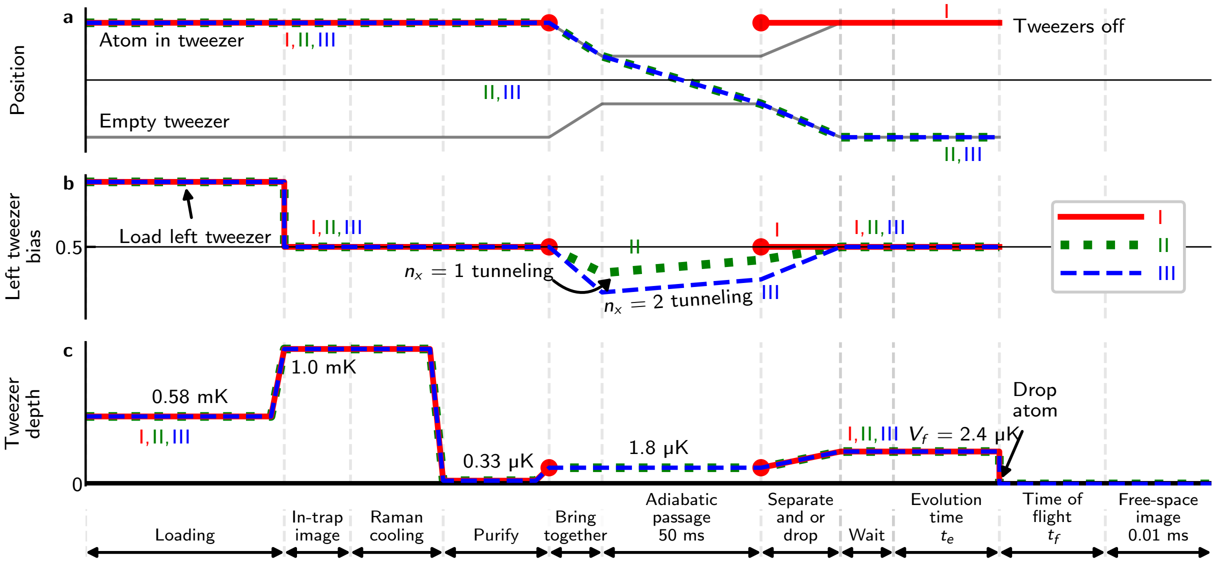

Figure 6.4: **Schematic timing diagram for Fock-state momentum distribution experiment (Fig. 6.2)** Not-to-scale experiment diagrams, showing **(a)** the position of the atoms and tweezers, **(b)** the bias of the tweezers, and **(c)** the depth of the atom-holding tweezer. Stationary Fock-state momentum distributions in which we prepared $n_x = 0, 1, 2$ states are labeled I, II, and III respectively. Round markers indicate adiabatic passage into an excited state is not used in experiment I that works with the $n_x = 0$.

6.1.1 Tweezer generation and control via acousto-optic deflectors

Tweezer generation: The optical tweezers are generated by sending light at a wavelength of 850 nm through two orthogonal acousto-optic deflectors (AODs) that are driven simultaneously with multiple RF tones to create multiple deflections. In the case of this experiment, the horizontal AOD is used to generate the two deflections used for tunneling, in order to avoid complications arising from gravity.

Depth and bias control: The vertical AOD is used to direct extra laser power far away

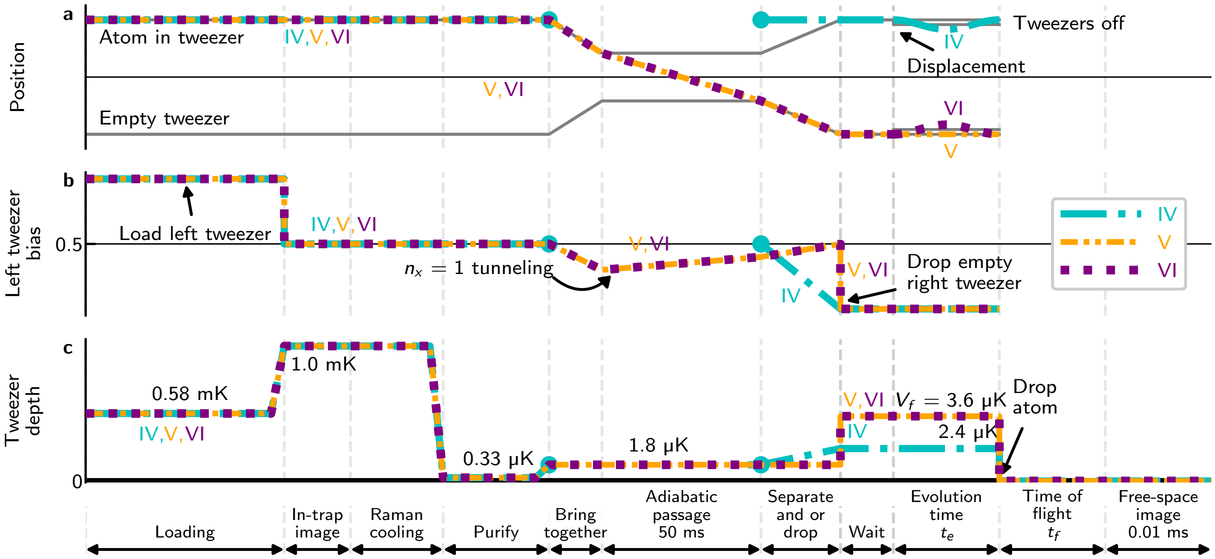

Figure 6.5: **Schematic timing diagram for tomography experiment (Fig. 6.3)** Not-to-scale experiment diagrams, showing **(a)** the position of the atoms and tweezers, **(b)** the bias of the tweezers, and **(c)** the depth of the atom-holding tweezer. Displaced coherent state data shown in Fig. 6.3a-c is labeled IV. Non-displaced $n_x = 1$ data shown in Fig. 6.3d-f is labeled V. Displaced $n_x = 1$ data shown in Fig. 6.3g-j is labeled VI. Round markers indicate adiabatic passage into an excited state is not used in experiment I that works with the $n_x = 0$.

from the main tweezers that hold atoms, which allows us to reduce the depth of the main tweezers by many orders of magnitude even given the limited dynamic range of our intensity servo. The relative depths of the traps are modified by dynamically adjusting the amount of RF power in each tone driving the horizontal AOD.

Tweezer position and movement: The tweezers are moved by changing the frequencies of the RF tones that drive the AODs. The speed of this movement is then limited by the size of the laser beam inside the AOD crystal and the time it takes the acoustic wavefront to cross this distance ($\sim 100\,\mathrm{ns}$). This is very fast compared to the tweezers' radial trap frequencies. However, there is $10\,\mu\mathrm{s}$ of electronic jitter in the time between the trigger to change the RF frequency and when the frequency jumps. This could be easily improved in future experiments, but is the likely explanation of small phase offsets noticeable in the center-of-mass oscillation data (Fig. 6.6).

6.1.2 Tweezer loading

During the initial loading stage, $V/k_B = 0.58\,\mathrm{mK}$. The loading procedure is stochastic, and the ΛGM loading technique we use is capable of up to ∼90% loading efficiency [184]. However, because interleaving background images without atoms provides useful information, we use sub-optimal loading (50% to 80% efficiency) (Fig. 6.4 and Fig. 6.5).

6.1.3 Trap depth and frequency calibrations

Trap depth calibration: We calibrate our trap depth V by measuring the light shift of the trap on the D_2 ^{87}Rb $F = 2 \rightarrow F' = 3$ transition at relatively high depths ($\sim 0.1\,\mathrm{mK}$ to $1\,\mathrm{mK}$). We extrapolate this calibration to low depths where the shift is smaller than the linewidth of the transition and therefore difficult to measure directly.

Trap frequency calibration methods: We can measure trap frequencies $\omega_{x,y,z}$ in deep traps through Raman sideband spectroscopy. We can then estimate the trap frequencies at smaller depths according to $\omega_{x,y,z} \propto \sqrt{V}$.

Independently, displacing a state in a harmonic oscillator ideally causes the state's center-of-mass momentum to oscillate at the trap frequency. These oscillations can then be measured in order to independently determine the trap frequency at the small depths used for motional state preparation and tomography (Fig. 6.6). The oscillations can be analyzed either by calculating $\langle \tilde{p}(t_e) \rangle$ from the deconvolved quadrature data (Fig. 6.3a,d,g), or they can be analyzed by fitting the quadrature data and tracking the location of the fit. Specifically for the displaced $n_x = 0$ state, which is approximately Gaussian, the fits more reliably characterize the state as the fit is less susceptible to far-off-axis noise.

Comparing frequency calibrations: The $n_x = 0$ state was released from a depth of $V_f = 2.4\,\mu\mathrm{K}$. Extrapolating the Raman sideband spectroscopy trap frequency calibrations to this depth predicts $\omega_{x,y}/2\pi = 6.8\,\mathrm{kHz}$ and $\omega_z/2\pi = 1.4\,\mathrm{kHz}$. We measure via the center-of-mass oscillations of the displaced $n_x = 0$ state $7.84(5)\,\mathrm{kHz}$ (Fig. 6.6).

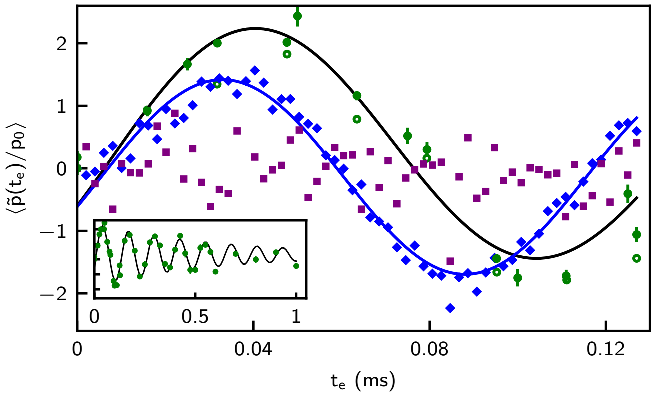

Figure 6.6: **Center of mass oscillations of data from Fig. 6.3.** Displaced $n_x = 0$ centers of Gaussian fits (green circles), and for comparison $\langle \tilde{p} \rangle$ (open green circles) [in a 2.4 µK trap]. Non-displaced $n_x = 1$ $\langle \tilde{p} \rangle$ (purple squares), and displaced $n_x = 1$ $\langle \tilde{p} \rangle$ (blue diamonds) [in a 3.6 µK trap]. The $n_x = 0$ ($n_x = 1$) is fit with a decaying sinusoid to find an $n_x = 0$ ($n_x = 1$) oscillation frequency of 7.84(5) kHz (9.05(11) kHz) (black and blue curves). Inset: Re-print of Fig. 6.3k for reference, which displays the same fitted centers of the $n_x = 0$ data (green circles) and their fit (black curve) over a longer time.

The $n_x = 1$ displaced and non-displaced states were released from a larger depth of 3.6 µK, where we measure via the center-of-mass oscillations 9.05(11) kHz for $n_x = 1$ (Fig. 6.6). Extrapolating the measured $n_x = 0$ trap frequency to the larger depth predicts 9.60(6) kHz. The difference between the value 9.05(11) kHz and 9.60(6) kHz is most likely due anharmonicity in these relatively shallow traps. In Sec. 6.5.3, we discuss a theoretical model for our trap that accounts for these observations.

6.1.4 Excited Fock state preparation via tunneling

Tunneling parameters and calibrations: In order to complete the adiabatic ground-to-excited state transfer (Fig. 6.2b,c), we must find and characterize the appropriate tunneling resonance and adiabatic transfer process. Tunneling is always done at a depth of $V = 1.8$ µK and with the tweezers spaced at a set Gaussian function spacing of 0.88 µm. Assuming the tweezers are Gaussian, the spacing between the double-well minima is expected to be 0.78 µm based upon this setting. For only the characterization of the resonances, we load atoms into both tweezers individually in order to measure both the intended transfer from ground to excited state and the unintended reverse transfer from excited state to ground state, which is a result of imperfect ground-state preparation.

We calibrate the relative tunneling depth (ΔV) by comparing the width of a ground-to-ground tunneling resonance to its oscillation frequency. This is done at shallower depths where the ground-to-ground tunneling resonance is measurable. At the relatively deep depths used for ground-to-excited-state tunneling, the $n_x = 0 \to n_x = 0$ tunnel coupling is too weak to be easily measured. We calculate where we expect it to be located based on the splitting between the $n_x = 1$ and $n_x = 2$ resonances and the assumption that the trap is harmonic, and set this location as $\Delta V = 0$.

$n_x = 0 \to n_x = 1$ characterization: We characterize the $n_x = 0 \to n_x = 1$ resonant tunneling transfer efficiency as a function of ΔV. We fit the transfer efficiency with a Gaussian function and find that the resonance occurs at $\Delta V = 294.5(2)$ nK and has a RMS size of 3.6(3) nK

(Fig. 6.7a). Ramping the relative depths across a width of 69.3 nK centered on this resonance over 50 ms achieves adiabatic rapid passage to the excited state at an efficiency of $92.4^{+1.9}_{-2}\%$. Meanwhile, we find transfer in the reverse direction, $n_x = 1 \rightarrow n_x = 0$, to be $11^{+3}_{-2}\%$, reflecting that there is a small population in excited states of the tweezer, which is capable of transferring the reverse direction. This is consistent with our expectations from characterization of our single-atom temperatures via other methods where we estimate 90% radial ground-state fraction (Sec. 6.3.1).

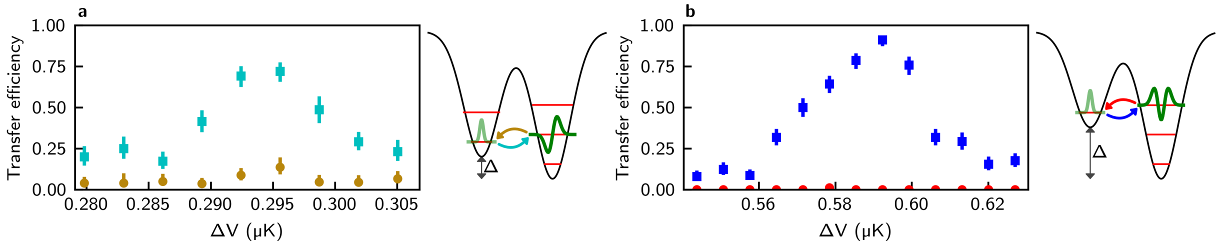

Figure 6.7: **Excited state tunneling resonances.** **(a)** The $n_x = 1$ tunneling resonance. Probability for an atom to tunnel from the ground state to $n_x = 1$ (teal squares) and from $n_x = 1$ to the ground state (gold circles). **(b)** The $n_x = 2$ tunneling resonance. The probability for an atom to tunnel from the ground state to $n_x = 2$ (blue squares) and from $n_x = 2$ to the ground state (red circles). Due to the ground-state cooling there are nearly no atoms in the excited state of the second tweezer to transfer backwards.

$n_x = 0 \rightarrow n_x = 2$ **characterization:** We similarly find an $n_x = 0 \rightarrow n_x = 2$ tunneling resonance located at $\Delta V = 589.0(11)$ nK which has a RMS size of 12.1(13) nK (Fig. 6.7b). Ramping the relative depths across a width of 111 nK centered on this resonance over 50 ms achieves adiabatic rapid passage to the excited state at an efficiency of $86.0^{+2}_{-3}\%$. We find transfer in the reverse direction, $n_x = 2 \rightarrow n_x = 0$, to be $3.2^{+1.7}_{-1.1}\%$, which is significantly smaller than the reverse transfer measured on the $n_x = 0 \rightarrow n_x = 1$ resonance. This reflects that there is very little population in $n_x = 2$ that is capable of transferring the wrong direction, as is expected after Raman sideband cooling.

Parameter	Value
Vertical shift speed	2 MHz
Horizontal shift speed	1 MHz
EM gain setting	×300
Frame transfer mode	Off
Pixel size	16 µm
Pixel binning	1x1
Camera temperature	−60 °C
Ideal imaging NA	0.55
Time-of-flight imaging time	10 µs
RPGC imaging time	5 ms

Table 6.1: **Camera and imaging settings.** (upper section) Camera settings directly programmed or reported by the manufacturer . Here, we report the vertical and horizontal shift speed as they are programmed. However, our camera is mounted sideways (Fig. 6.9). (lower section) Imaging parameters.

6.2 Imaging methods

6.2.1 Imaging setup

The camera used is an Andor IXON-EM+ back-illuminated electron-multiplying CCD (EMCCD) camera, model number DU-897E-C00-#BV-9GT. Camera settings for the experiment are listed in Table 6.1. The imaging light at 780 nm is collected through the same high-NA objective lens used to create our tweezer array, split from the optical tweezer light using a dichroic mirror, and focused using a 1 m focal-length achromatic doublet.

6.2.2 In-tweezer RPGC imaging

RPGC imaging configuration: Red-detuned polarization gradient cooling (RPGC) and associated light scattering is used to determine if an atom is loaded at the start of the experiment. Time-of-flight images are post-selected based the presence of an atom in the RPGC image. Some time-of-flight images that record cosmic ray events are additionally removed in post-selection. Time-of-flight images where atoms are not loaded are used for background analysis. The RPGC cooling is in a balanced, σ^+-σ^- configuration with zeroed background magnetic field. During the imaging, we alternate trap light and imaging light at a 2 MHz flashing rate [77, 185]. This eliminates light shifts and anti-trapping effects during the scattering of the imaging light to create more uniform images.

RPGC image point spread function: One measure of the point spread function (PSF) of our imaging system is the average of in-trap RPGC images of single atoms (Sec. 6.2.4). This averaged image represents the effect of the lens NA, aberrations, and the finite spatial extent of the atom in the trap during imaging. We note that this PSF may vary spatially within the field of view of the imaging system, but we utilize the central point as a representative value. The measured PSF (Fig. 6.8) is roughly an astigmatic Gaussian with a long asymmetric tail. We subtract the averaged image's background and fit the result with a 2D Gaussian to extract effective RMS PSF sizes of 0.445(2) µm (horizontal) and 0.328(2) µm (vertical) (Table 6.2). This result is the PSF used for deconvolution in the tomography analysis. Considerations of systematic error based on this choice are discussed in Sec. 6.5.

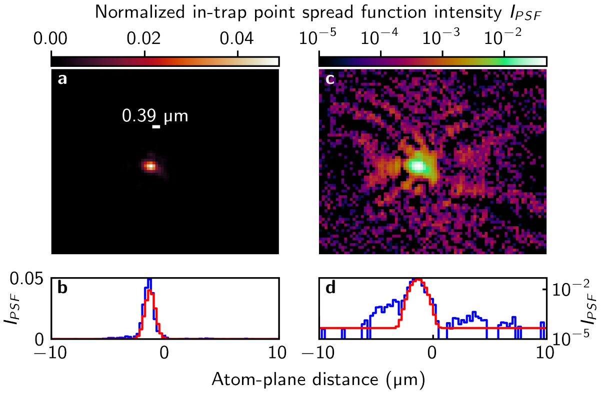

Figure 6.8: **Imaging system point spread function**. Averaged image intensity (color bars) is normalized so that the integration of the averaged image is 1. The image shown is the average of 131,000 RPGC images with a single atom present. **(a)** The PSF on a linear color scale. **(b)** A slice of the PSF and a Gaussian fit to the PSF displayed on a linear y-axis. **(c)** The PSF displayed on a logarithmic color scale, emphasizing the observed long tail and structure due to aberrations. **(d)** A slice of the PSF and Gaussian fit to the PSF displayed on a logarithmic y-axis.

6.2.3 Time-of-flight imaging characterization

Time-of-flight imaging configuration: The time-of-flight imaging is near-resonant and operates with an intensity $I \gg I_{\mathrm{sat}}$. The light is applied in a power-balanced σ_+, σ_- polarization configuration on the D_2 $f = 2$ to $f' = 3$ ^{87}Rb transition with zero background magnetic field.

Collected photon number: In a 10 µs image, as we nearly saturate the atomic transition, we expect to scatter 180 photons from a single atom. Based on the final quadrature distributions and characterizations of our camera system's count-to-photon conversion ratio at our EM gain setting (0.0124 photons per count), we estimate that we collect $\sim 5 - 10$ photons, depending on which data set is analyzed, suggesting an overall collection efficiency of 3%-6%.

Time-of-flight imaging blur considerations:

In addition to the imaging resolution PSF discussed above, in time of flight there are additional blurring effects [166, 186], and in this section we estimate these effects theoretically (Table 6.2).

For $V_f/k_B = 2.4\,\mu\mathrm{K}$, the confinement of the atom prior to release, combined with the measured atom temperature, we predict an initial atomic probability distribution RMS size of 100 nm. During the $\tau = 10\,\mu\mathrm{s}$ imaging time, atoms move due to their initial velocity a RMS distance of 57 nm. Atoms additionally undergo random-walk motion due to the scattering of the imaging photons. We estimate during τ the atom moves an additional RMS distance of 0.83 nm [166].

The released atomic wavefunction expands in 3D before being imaged onto the 2D image plane of our camera. The extent of the atom probability distribution in the z direction combined with a finite depth of focus is another potential blurring effect. We apply geometric optics and the expected impact of diffraction to an impulse response of the form $\delta x, y \times \exp(-z^2/(2\sigma_z^2))$, where σ_z here is the predicted z-size of the atomic wavefunction in our experiments after 0.5 ms of flight time. Diffraction alone would result in a PSF size of $\sigma_x = 300\,\mathrm{nm}$, and our calculation indicates that the DOF increases this to $\sigma_x = 320\,\mathrm{nm}$, which is 110 nm as a value added in quadrature.

First 10 µs **time-of-flight distribution measurement:** A useful experimental compar-

In-trap measurement	
Measured PSF σ_x	445(2) nm
Measured PSF σ_y	328(2) nm
Expectations	
Expected diffraction limit σ	300 nm
In-trap thermal distribution $\sigma_T(0)$	100 nm

Atomic flight measurement	
Measured PSF first 10 µs σ_x	461(5) nm
Measured PSF first 10 µs σ_y	366(4) nm
Atomic flight calculations	
DOF effect σ_{DOF}	110 nm
Thermal displacement during τ, σ_τ	57 nm
Random walk during τ, σ_{recoil}	0.83 nm

Table 6.2: **Factors contributing to imaging blur.** The upper table reflects in-trap measurements and the expected diffraction limit calculated using the NA of the ideal tweezer lens. The lower table reflects blurring from effects unique to the time-of-flight imaging and that can be sensitive to the length of a single image τ.

ison to the theoretical estimate of time-of-flight blur is the size of a time-of-flight distribution of a near ground state atom in its first 10 µs of flight, the smallest time-of-flight distribution possible without shortening the imaging time (Fig. 6.10a). This distribution is affected by the photon-scattering random walk during a single image and some of the thermal displacement effects, although not DOF effects. Note, however, that it is a noisier PSF estimate than the in-trap RPGC based PSF estimate (Sec. 6.2) due to the significantly shorter single image time. We find this time-of-flight distribution has Gaussian RMS size of 0.461(5) µm and 0.366(4) µm in the horizontal and vertical directions respectively, which is only slightly larger than the in-trap measurement and is similarly astigmatic, indicating that the dominant source of blur is the imaging optics (Table 6.2). Error based on our ability to account all blurring effects is discussed in Sec. 6.5.

Clock-induced charge noise: We are limited by our camera's so-called clock induced charge (CIC) [186]. These are events in which a pixel on the camera gains a "clock-induced" charge during the process by which photoelectrons are shifted into gain and readout registers. The CIC is amplified the same as any charge, making it indistinguishable from the photoelectrons we wish to measure. The number of such charges scales with the number of pixels in a single image. As such, there is a tradeoff between improved imaging resolution and camera noise. CIC is reduced by shifting electrons across the camera sensor and gain registers at the maximum rate. Even at the fastest shift speed of 0.3 µs per shift, Andor reports that CIC occurs at a rate of 1.8×10^{-3} events/pixel. Due to technical issues our Andor camera is only currently capable of operating at 0.5 µs per shift, which will increase CIC.

Background characterization: An undesirable effect of averaging together many images is a sensitivity to background patterns on the camera, including "hot" pixels that have consistently higher counts, a small amount of background light, patterns in the camera's sensitivity, large profiles in counts which are a result of the camera's cleaning and shifting processes, and CIC (Fig. 6.9). Most of the spatial variation in these noise sources is only horizontal, depending on the proximity of a column of pixels to the camera's readout sensor. Some of these sources vary over time. To combat these issues, backgrounds subtracted from our data are taken from the same experimental sequence as the data of interest, and are therefore temporally interleaved with the desired data. Most of these sources, such as the overall profile left by the cleaning process, are large compared to the averaged imaging signal, but very consistent.

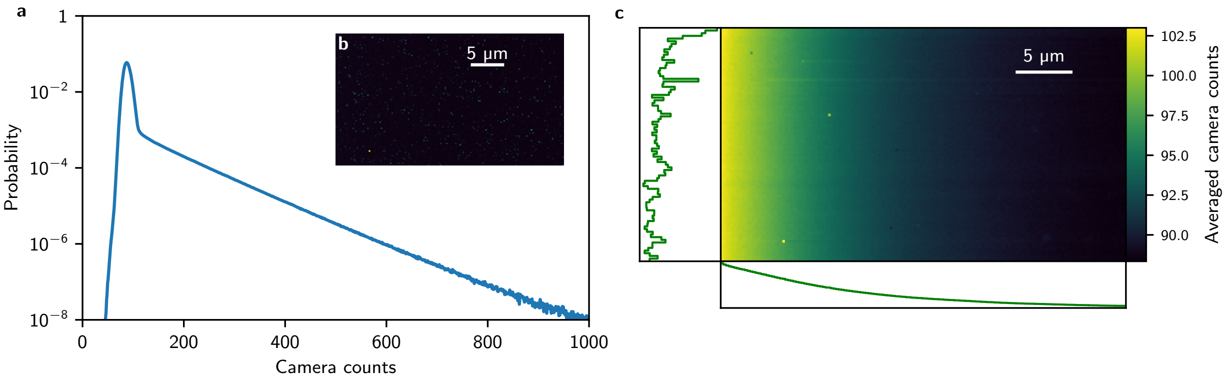

Figure 6.9: **Background and noise analysis.** **(a)** The measured probability of observing a given count value in a single background image averaged over all columns in the images, which characterizes our camera noise. **(b)** Inset: a representative, single, background image. High points in the image are primarily due to CIC. **(c)** An averaged background, the average of many single background images. The CIC has mostly averaged out, and a non-negligible background profile has appeared, along with several hot spots. Vertical and horizontal integrations of the background are also displayed, emphasizing that most of the profile is in the horizontal direction (direction of Andor vertical shift, see Table 6.1), increasing toward the readout register on the left.

Gaussian camera noise characterization: After subtracting the background from an averaged image but before further post-processing, there remains noise in the averaged image which is visible, for example, near the edges of the images in Fig. 6.2, where we expect negligible real signal. The noise on a single pixel approximately samples a Gaussian distribution and is primarily a result of camera CIC, so we refer to this as Gaussian camera noise. Our analysis takes into account potential spatial dependence of the noise across the camera.

We characterize this noise by first carefully measuring, from a very large data set of background images, the single-image count-probability distribution for every column of pixels (Fig. 6.9a). If we analyze this noise probability distribution, we find an average CIC rate of 7.0×10^{-2} events/pix, which is larger than ideal rates, largely due to our slower shift speed (Table 6.3) [186]. With these column-wise-measured count-probability distributions, we can simulate an ideal uncorrelated background image by sampling from the measured single-image count-probability distributions. We can then create an averaged background by creating an arbitrary number N of sampled single background images and averaging them together. We finally simulate many averaged backgrounds in order to reconstruct the probability distribution of a count value in an averaged background for every column of pixels. The resulting probability distribution approximately follows a Gaussian function with a standard deviation σ_{noise}, which decreases as N increases. We simulate σ_{noise} as a function of N, and fit the result with a function of the form $\sigma_{\text{noise}} = A/\sqrt{N}$. The resulting values of A vary slightly by column, as expected, with a mean value averaged over all columns of $A = 26.5$ counts and a standard deviation among the columns of 1.4.

In practice, we find that the observed noise in our tomography data is larger than this sampling analysis would predict, as determined by analyzing the edges of background-subtracted quadrature distributions. Specifically, we observe RMS noise $(1.6, 1.05, 1.16)$ times larger for the $n_x = 0$ displaced, $n_x = 1$ non-displaced, $n_x = 1$ displaced states, respectively, than the predicted noise from images with no atoms discussed above. The discrepancy is likely due to a combination of effects, such as differences in the background between different data sets and small correlations in the background data which average out in the larger background data set used for the above analysis. Non-trivial correlations exist in the background between data sets which are taken in close temporal proximity to each other, suggesting that some of the background signal may be due to fluctuating weak light signals, for example coming from light elsewhere in the apparatus. Some signal and noise may also come from atom-scattered photons as a result of our PSF having a long tail (Fig. 6.8). To be consistent our observations, we always use the observed approximately Gaussian camera RMS noise from the tomography images when bootstrapping datasets. We discuss error based on the amount of Gaussian camera noise in Sec. 6.5.

Magnification: We first measure the magnification of our imaging system using gravity in an atom-drop experiment. We prepare an atom in a tweezer, release it, and then take a picture a variable amount of time later to reconstruct the gravitationally assisted descent of the atom's center-of-mass position. We fit the signal with a Gaussian and plot the center as a function of

Specified camera noise	
CIC specified rate (ideal)	1.8×10^{-3} events/pix
Readout noise	$< 1e^{-}$
Dark current	$1.5 \times 10^{-4}\ e^{-}/(\mathrm{pix} \cdot \mathrm{sec})$

Measured noise characteristics	
CIC measured rate	7.0×10^{-2} events/pix
Measured readout noise σ	5.4 counts
EM gain signal γ	73.1 counts
Count offset	88.4 counts

Table 6.3: Noise sources in our images. Note that we expect our CIC rate to be larger than the specified value both due to our inability to run the camera at its fastest shift speed and because our measured value may be contaminated by a small amount of scattered light.

flight time and fit to $y(t_f) = y_0 + (1/2)at_f^2$ to extract the acceleration a of the magnified signal on the camera. The magnification is then $a/(9.8\,\mathrm{m/s^2})$, which we find to be ×64(1). This is the value used for calculations throughout the text.

Alternatively, we can measure the magnification based on measuring the $n_x = 1$ Fock state. The distinctly non-Gaussian nature of the momentum distribution is a useful calibration because the fringe pattern is measurable in the image plane and independently predictable in the atom plane given m, ω_x, and t_f. In contrast to the Gaussian $n_x = n_y = 0$ state, it is discernible from thermal population, which manifests as spatially-Gaussian-distributed signal with an RMS size dependent on the population's temperature. Specifically, we know how large the atom-plane σ_x should be given the functional form of the $n_x = 1$ state (Eq. 6.3,6.4,6.5), and we know from analyzing our momentum distributions (Sec. 6.4.1) how large the image-plane σ_x is. Taking the ratio of these two sizes gives us a magnification of ×66, which is consistent with our previous measurement.

6.2.4 Time-of-flight image analysis

Imaging signal loss: In some cases, whether due to background collisions or thermal excitations, atoms that are imaged in the first RPGC image of the experiment are lost from the optical traps before the time-of-flight imaging procedure. In the case of optical homodyne tomography, where one typically measures the occupation of an optical mode, the loss of a photon registers as a measurement of the $n = 0$ state. In our case, the loss of an atom does not result in the measurement of an atom in the $n = 0$ state; rather, it simply results in a reduction of the signal to noise of the experiment, so no additional analysis is necessary to account for this.

Richardson-Lucy deconvolution: The point spread function (PSF) of our imaging system is non-zero in size and astigmatic, resulting in blurring of the measured quadrature distribution. In order to compensate for these effects, we deconvolve our measured quadrature with an estimate of our PSF (Sec. 6.2). While convolving two-dimensional imaging data is trivial, deconvolution is difficult numerically, being is very sensitive to any imaging noise.

We use the Richardson-Lucy deconvolution algorithm as implemented in the scikit-image python package. This iterative algorithm consists of iterating the relation

$$D^{(k+1)} = D^{(k)} \times \Big(\frac{I}{D^{(k)} \circledast P} \circledast P^{*} \Big), \tag{6.1}$$

where $D^{(k)}$ is the quadrature distribution after k iterations of the algorithm, I is the original distribution, P is the PSF, P^{*} is the PSF flipped along all axes, and $\circledast$ is the convolution operator. Multiplication and division of all terms is done element-wise. $D^{(0)}$ is initialized as an array uniformly filled with 1. This algorithm iteratively approaches the quadruatre distribution that, when convolved with our measured PSF, maximizes the likelihood of reproducing the measured quadruatre distribution, subject to Poissonian noise in our photon signal. This iterative method is similar to one that we use for density matrix reconstruction (Sec. 6.4.2).

In the equation above, a crucial intermediary step involves division, which in the presence of sufficient noise can produce issues related to the division by small numbers issues and floating point arithmetic. Therefore, the algorithm implements a filter step, whereby if an element in the term $I^{(k)} \circledast P$ is smaller than the filter value ζ_0, the division result is floored to zero. While this retains the spirit of the algorithm, it also introduces added complexity into choosing the number of iterations to perform. As such, given the PSF there are two free parameters in the deconvolution algorithm: the number of iterations of the algorithm and the filter value ζ_0. We discuss how we minimize error due to this in Sec. 6.5.

6.3 Single-atom temperature characterization

6.3.1 Raman sideband spectra

A well-established method of characterizing the temperature of a single atom in a harmonic trap is Raman sideband spectroscopy that evaluates the imbalance between the red and blue Raman sidebands [175]. We do Raman sideband cooling at a trap depth of 1 µK where we measure a radial trap frequency of 139(4) kHz and an axial trap frequency of 28(6) kHz. Our cooling is capable of producing 3D ground-state fractions greater than 90%. We estimate that over the course of several weeks of data taking required for this experiment $\bar{n}_x = 0.10(4)$ in the radial dimension based on Raman sideband spectroscopy. This corresponds to a temperature of $(k_B T/2)/(E_{\text{zp}}/2) = 0.83(7)$, where $E_{\text{zp}} = \hbar\omega_x/2$ is the zero point energy. Our Raman sideband spectroscopy addresses both the x and y-dimensions so we do not isolate the x-axis temperature. However, expansion momentum distributions indicate that there is no significant difference between radial axes (Sec. 6.3.2). The Raman spectroscopy temperature is consistent with our observation of $11^{+3}_{-2}\%$ reverse transfer during g-e adiabatic tunneling transfer (Sec. 6.1.4). In the axial dimension, which we are relatively insensitive to, we measure $\bar{n}_z = 0.08(10)$.

6.3.2 Ballistic expansion

When the trap is shut off the atom's wavefunction will expand according to the standard ballistic expansion formula

$$\sigma_x(t) = \sqrt{\frac{2E_{\text{KE}}}{m} t_f^2 + \sigma_x(0)^2}, \tag{6.2}$$

for a given expansion kinetic energy E_{KE}, which is the observable we directly measure via time-of-flight imaging. At high temperatures, $E_{\text{KE}} \to k_B T/2$. However, as $T \to 0$, the expansion energy diverges from the thermal energy as E_{KE} is asymptotically dominated by the kinetic part of the harmonic-oscillator ground-state zero-point energy $E_{\text{zp}}/2 = \hbar\omega_x/4$.

To measure this expansion kinetic energy, we conduct a similar experiment as that of Fig. 6.2, but we vary the expansion time t_f before imaging (Fig. 6.10a). We fit the averaged momentum distributions with a 2D Gaussian function, and then fit the Gaussian RMS values as a function of expansion time with Eq. 6.2 in order to extract an expansion energy from this data.

The experimentally measured results show a ballistic expansion kinetic energy of $E_{\text{KE}} = (k_B \times 0.256(16)\,\mu\text{K})/2$, which is close to the theoretical minimum at these trap parameters of $(k_B \times 0.188(1)\,\mu\text{K})/2$ (Fig. 6.10). It makes no statistically significant difference whether we use $\sigma_x, \sigma_y, (\sigma_x + \sigma_y)/2$, or if we deconvolve the time-of-flight distributions with the in-trap PSF first with reasonable deconvolution parameters, therefore we quote the temperature obtained from analyzing the mean σ of the non-deconvolved data $\sigma_{\text{fit}} = (\sigma_x + \sigma_y)/2$. This corresponds to a temperature of $0.205(12)\,\mu\text{K}$ (Fig. 6.10c), which is significantly different than the ballistic expansion energy. The temperature determined from ballistic expansion corresponds to a normalized energy of $(k_BT/2)/(E_{\text{zp}}/2) = 1.08^{+11}_{-10}$, which is similar to the value measured via Raman spectroscopy of $(k_BT/2)/(E_{\text{zp}}/2) = 0.83(7)$ (Sec. 6.3.1). The slight discrepancy may suggest that the trap depth ramps that occurs between Raman cooling and the release of the atom for ballistic imaging are not perfectly adiabatic, or it may arise from fluctuations in the Raman cooling efficiency during the long experiments required to measure the atoms in free-space.

6.4 Quantum state tomography and related characterizations

6.4.1 Single Fock-state momentum distribution analysis

In general, the momentum space wavefunction is related to the position space wavefunction via a Fourier transform. The momentum space distribution of the $n_x = 0, n_x = 1$, and $n_x = 2$ states with ground-state RMS momentums $p_{0,x} = \sqrt{m\hbar\omega_x/2}$ and $p_{0,y} = \sqrt{m\hbar\omega_y/2}$ are

$$|\phi_0(p_x, p_y)|^2 = \frac{1}{2\pi p_{0,x} p_{0,y}} \exp\Big(- \Big(\frac{p_x^2}{2p_{0,x}^2} + \frac{p_y^2}{2p_{0,y}^2}\Big)\Big), \tag{6.3}$$

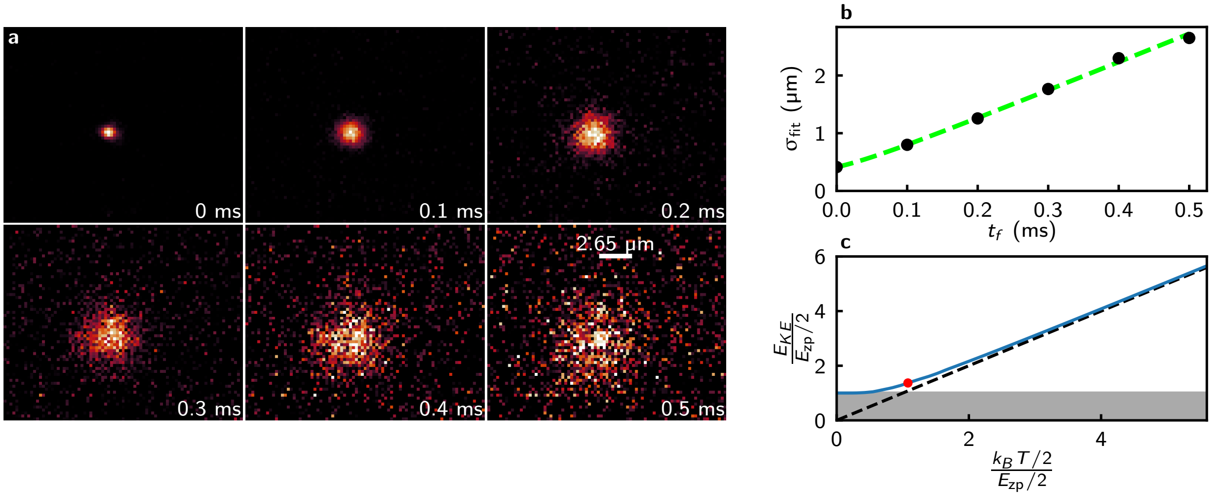

Figure 6.10: **Ground state expansion.** **(a)** The averaged time-of-flight distributions used in the temperature measurement, labeled by the starting time of the 10 μs time-of-flight image. Color scales for different distributions are set individually. **(b)** The average RMS size $\sigma_{\text{fit}} = (\sigma_x + \sigma_y)/2$ of the 2D fits of the data in part (a) (black circles) and their ballistic expansion fit (green line) versus expansion time t_f. Error bars are too small to be visible. **(c)** Relation between the measurable expansion kinetic energy E_{KE} and the underlying thermal kinetic energy $k_B T/2$ (blue line), a slope-1 reference (black line) and our measured data point (red point) which is significantly offset from the slope-1 reference, indicating that the zero-point energy is significant in this expansion.

$$|\phi_1(p_x,p_y)|^2 = \frac{1}{2\pi p_{0,x}^3 p_{0,y}} p_x^2 \exp\Big(-\Big(\frac{p_x^2}{2p_{0,x}^2}+\frac{p_y^2}{2p_{0,y}^2}\Big)\Big), \tag{6.4}$$

$$|\phi_2(p_x,p_y)|^2 = \frac{1}{4\pi p_{0,x} p_{0,y}} \Big(\frac{p_x^2}{p_{0,x}^2}-1\Big)^2 \exp\Big(-\Big(\frac{p_x^2}{2p_{0,x}^2}+\frac{p_y^2}{2p_{0,y}^2}\Big)\Big). \tag{6.5}$$

As a baseline estimate of the stationary state, we can fit the raw momentum distributions from Fig. 6.2d-f with a variable-weighted sum of the above momentum-space distributions convolved with our imaging PSF to estimate the populations in the different states we prepare. We scale the RMS x and y sizes of the above $n_x = 0$ ($n_x = 1$ and $n_x = 2$) states based on our displacement-based trap-frequency measurement of the $n_x = 0$ ($n_x = 1$) states, t_f, and the independently measured imaging magnification of ×64(1). It is important to fix the RMS size for characterization of the ground-state, as a ground-state Gaussian of one trap frequency can be easily confused with a thermal state with a smaller trap frequency. The excited state momentum distributions, which do not suffer from this issue, can be used as independent calibrations of the magnification system (Sec. 6.2.4), but for this analysis we fix the size of these functions as well. This analysis is a useful preliminary diagnostic of our state preparation and imaging system. The $n_x = 0$ state was measured to have $n_x = (0,1,2)$ populations of $(0.93(3), 0.07(2), 0.00(2))$ which is consistent with our expectations based on Raman sideband spectroscopy (Sec. 6.3.1), free-space expansion (Sec. 6.3.2), and excited state preparation (Sec. 6.1.4). The $n_x = 1$ state was measured to have diagonal populations of $(0.260(10), 0.651(14), 0.089(15))$, and the $n_x = 2$ state had diagonal populations of $(0.395(14), 0.125(18), 0.480(16))$. Deviations of these excited state results from the ideals of $(0,1,0)$ and $(0,0,1)$ likely result from a combination of imperfect state preparation (Sec. 6.1.4) and blurring effects in the imaging which are not accounted for by the PSF deconvolution (Sec. 6.2). Most such blurring effects that reduce the fringe contrast naturally manifest as population in lower states, so these numbers can be reasonably understood as lower-bound estimates on our Fock state preparation procedure. These considerations are treated in more detail in the context of the full tomography in Sec. 6.5.

6.4.2 Maximum likelihood estimation algorithm

We now turn to analysis of the full tomographic quadrature data of Fig. 6.3.

Quadrature data: The data in Fig. 6.3a,d,g for displaced $n_x = 0$, non-displaced $n_x = 1$, and displaced $n_x = 1$ states consist of data sets of 9, 64, and 64 quadrature measurements respectively. Each quadrature measurement is the average of a variable number of pictures. The median numbers of pictures averaged for these individual quadrature measurements were 10852, 6191, and 11320 pictures for the data in Fig. 6.3a,d,g. The non-displaced $n_x = 1$ data was taken with notably fewer pictures than the other data sets.

We note that N quadrature measurements are needed to distinguish phase oscillations in the quadrature distributions differing in angular frequency by $N\omega_x$, assuming the quadrature measurements are equally spaced by phase angle $2\pi/N$. Hence, N such measurements are needed to reconstruct a density matrix occupying Fock states up to $n_x = N/2$ [179]. However, even in the case where we have occupation of states with $n_x \geq N/2$, we expect to accurately capture the density matrix up to the $N/2$ off-diagonal. Given the expected form of the density matrix, considering independent measures of the atom temperature and the size of the trap displacements, we estimate the number of quadrature measurements used is sufficient for capturing all non-trivial elements of the density matrix within error bounds.

MLE algorithm: Maximum likelihood estimation (MLE) is a common statistical technique for estimating the free parameters of a model based on how likely they are to reproduce a given data set. In the case of quantum tomography, we can take the quantum state as a model for producing measured observables, where the free parameters are typically the complex-valued matrix elements of the density matrix in some basis. MLE will then return the density matrix most likely to result in the observed data. This approach is attractive as we may a priori impose physical assumptions about our state, as opposed to other methods like the inverse Radon transform that may predict nonphysical states [181].

To determine the density matrix, we utilize an iterative MLE algorithm based off of the discussion in Ref. [181], which we briefly review here. Suppose we have a set of projective measurement outcomes, $\{(\tilde{p}_j, \theta_j)\}$, with shorthand $\tilde{p} = \tilde{p}(\theta)$, labelled by index j and occurring with frequency f_j in our data set. Here, $\tilde{p}_j$ is the result of a measurement of $\tilde{p}(\theta_j) = p\cos\theta_j + m\omega_x x \sin\theta_j$, corresponding to the quadrature distribution at phase angle θ_j. For any given pair $(\tilde{p}, \theta)$, we may form the projection operator $\Pi\left(\tilde{p}, \theta\right) = |\tilde{p}, \theta\rangle\langle\tilde{p}, \theta|$ so that the probability of obtaining such a measurement in the state ρ is given by

$$P\left(\tilde{p}, \theta\right) = \mathrm{Tr}\left(\rho\,\Pi\left(\tilde{p}, \theta\right)\right). \tag{6.6}$$

The problem of MLE then corresponds to finding the quantum state ρ that maximizes the likelihood of obtaining the data set $\{(\tilde{p}_j, \theta_j)\}$,

$$\mathcal{L}\left(\rho\right) = \prod_j P\left(\tilde{p}_j, \theta_j\right)^{f_j}, \tag{6.7}$$

while also subjecting the resulting state to various physical constraints. Namely, ρ must be a trace-normalized, Hermitian, positive semi-definite matrix in a convenient, physically-motivated basis of our choosing.

An iterative algorithm to maximize Eq. (6.7) is motivated by the observation that, for the state ρ_0 maximizing $\mathcal{L}$, we must have $f_j \propto P\left(\tilde{p}_j, \theta_j\right)$ in the large sample limit. Introducing the operator

$$R\left(\hat{\rho}\right) = \sum_j \frac{f_j}{P\left(\tilde{p}_j, \theta_j\right)} \Pi\left(\tilde{p}_j, \theta_j\right), \tag{6.8}$$

and noting that $\sum_j \Pi\left(\tilde{p}_j, \theta_j\right) \propto I$ for identify matrix I, this translates to the condition

$$\rho_0 \propto R\left(\rho_0\right)\rho_0 R\left(\rho_0\right). \tag{6.9}$$

We may then leverage this to form the basis of an iterative algorithm,

$$\rho^{(k+1)} \propto R\left(\rho^{(k)}\right)\rho^{(k)} R\left(\rho^{(k)}\right), \tag{6.10}$$

where we start with the initial trial state $\rho^{(0)} \propto J$, where J is a matrix of ones in our truncated Fock basis, which has a nonzero probability for each possible outcome. We iterate this procedure until the error, as defined via $T\left(\rho^{(k)}, \rho^{(k+1)}\right)$ for trace distance $T\left(\rho, \rho'\right) = \frac{1}{2}\mathrm{Tr}(\sqrt{(\rho - \rho')^2})$ is less than 10^{-4} or 500 iterations have been completed.

In practice, it is necessary to choose an appropriate reduced basis in which to restrict the set of possible states. For our purposes, we restrict ourselves to motional Fock states with occupation $n \leq n_{\max}$ for a maximum occupation $n_{\max} = 25$. The projection operators can then be defined via

$$\begin{aligned} \Pi_{mn}\left(\tilde{p}, \theta\right) &= \langle m|\Pi\left(\tilde{p}, \theta\right)|n\rangle \\ &= \langle m|\tilde{p}, \theta\rangle\langle\tilde{p}, \theta|n\rangle \end{aligned} \tag{6.11}$$

with the standard harmonic oscillator matrix element

$$\langle n|\tilde{p}, \theta\rangle = ie^{-in\theta}\Big(\frac{1}{2\pi p_0^2}\Big)^{1/4}\frac{H_n\left(\tilde{p}/p_0\sqrt{2}\right)}{\sqrt{2^n n!}}e^{-(\tilde{p}/p_0)^2/4} \tag{6.12}$$

for Hermite polynomials H_n.

After reconstructing the density matrix, the state's Wigner function may be obtained via

$$W(x,p) = \frac{1}{\pi}\sum_{m,n=0}^{n_{\max}}\rho_{mn}(-1)^k e^{-i\phi(m-n)}e^{-|\alpha|^2/2}\sqrt{\frac{k!}{(k+\Delta)!}}|\alpha|^{\Delta}L_k^{\Delta}(|\alpha|^2) \tag{6.13}$$

for $\alpha = x/x_0 + ip/p_0$, $\phi = \arg(\alpha)$, $k = \min(m,n)$, and $\Delta = |m-n|$, where L_k^{Δ} are the generalized Laguerre polynomials.

6.4.3 Alternative tomography methods

There are many alternatives to our use of maximum likelihood estimation. We explored several in order to better understand and support our state preparation and tomography. Each method has different drawbacks, making different assumptions about our states. We discuss several alternative methods below for thoroughness.

Inverse Abel transform. It is possible to derive the Wigner function based on a single time-of-flight image based on the assumption that the state's Wigner function should be radially symmetric [187], such that the quadrature distribution is time-invariant. These assumptions should hold for Fock states and phase-randomized states.

The Wigner functions of harmonic oscillator eigenstates are radially symmetric, meaning that $W(x, p_x) \rightarrow W(\tilde{p})$. In particular,

$$W_{n_x=0}(x, p_x) = \frac{1}{2\pi x_0 p_0} \exp(-\frac{x^2}{2x_0^2} - \frac{p_x^2}{2p_0^2}) \tag{6.14}$$

$$W_{n_x=1}(x, p_x) = \frac{1}{\pi}\Big(\frac{2p^2}{\hbar^2} + \frac{2x^2}{\sigma_x^2} - 1\Big) \exp\Big(-\frac{\sigma_x^2 p^2}{\hbar^2} - \frac{x^2}{\sigma_x^2}\Big) \tag{6.15}$$

The prepared states displayed in Fig. 6.2 should be primarily of fock state character. To the extent that they are not pure Fock states, it is reasonable to suspect that they are an incoherent or phase-randomized mixture of Fock states, as this infidelity would likely be driven by thermal population, laser intensity and bias noise issues, and other issues which we do not coherently control. Such incoherent or phase-randomized states would have Wigner functions which would be radially symmetric. It has been shown and demonstrated that for radially symmetric Wigner functions, the Wigner function is related to it's quadrature distribution via the inverse Abel transform [187, 150]:

$$W(\tilde{p}) = -\frac{1}{2\pi}\left[\int_{-\tilde{p}}^{-\infty} + \int_{\tilde{p}}^{\infty}\right] \frac{\Phi'(\tilde{p})}{\sqrt{r^2 + \tilde{p}^2}}[dr] \tag{6.16}$$

We use this result to reconstruct the approximate Wigner function of our single atom states based on the assumptions discussed above. Specifically, we integrate the deconvolved profiles of the raw data in Fig. 6.2 vertically, average the quadruatre distribution between the positive and negative values of $\tilde{p}$, and numerically evaluate the above integral to obtain the Wigner function (Fig. 6.11).

Inverse Radon transform. Another alternative method for the construction of a states Wigner function is the use of the inverse Radon transform [188], which is given by the following relation:

$$\begin{aligned} W(x, p) = \frac{1}{4\pi^2} \int_{-\infty}^{\infty} [d\tilde{p}] \int_{-\infty}^{\infty} [d\eta] \int_{0}^{\pi} [d\theta] \Phi(\tilde{p}, \theta) \\ \times |\eta| \exp(i\eta(\tilde{p} - x\cos(\theta) - p\sin(\theta))) \end{aligned}$$

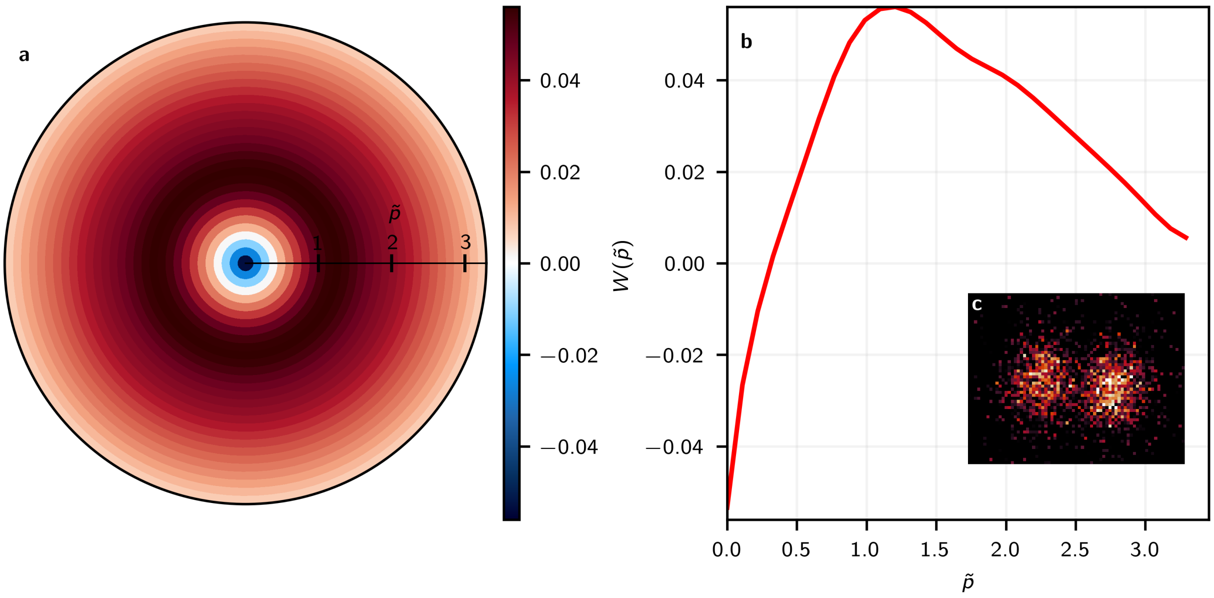

Figure 6.11: **Inverse Abel Transform Wigner Function a** The Wigner function the $n = 1$ state data from Fig. 6.2 as reconstructed through the inverse Abel transform. Here, the one-dimensional result of the transform is symmetrically wrapped around the origin in order to compare to other estimation of the Wigner function. **b** The raw one-dimensional Wigner function used to create part a of this figure. To obtain this result, we assume our data in Fig. 6.2 are stationary. **c** The raw image reprinted from Fig. 6.2 which this Wigner function is derived from.

Where $\Phi(\tilde{p},\theta)$ is the measured quadrature distribution. The inverse Radon transform is widely used in the field of medical topographical imaging. Both the inverse Radon transform and maximum likelihood estimation make assumptions about the underlying system. For the integral transform such assumptions are necessary to evaluate the divergent kernel in the above relation, and in MLE one must pick a finite basis with which to use in the algorithm. Maximum likelihood estimation is widely preferred in quantum state tomography, however, because it is easier to enforce reasonable physical assumptions about the state in this method than with the integral transform. In particular, the inverse Radon transform can result in obviously non-physical states which have non-Hermitian density matrices which have non-unity trace and negative diagonal values. When we evaluate it for our tomography data presented in Fig. 6.3, it suggests, as an explanation for camera noise in our data, non-trivial populations in unreasonably highly excited states. However, it can still be illustrative to view the results of the inverse Radon transform, as it still consistently reconstructs the main features of the data, including a strongly negative and displaced center for our displaced $n_x = 1$ atom data. Therefore, we include the result of taking the inverse Radon transform of our deconvolved quadrature data in Fig. 6.12.

Pattern function overlap. Another method for reconstructing the density matrix is the use of the so-called "pattern functions". These can be used to reconstruct a density matrix directly from the measured quadrature distributions without the use of maximum likelihood estimation. The pattern functions $\tilde{f}_{k,\ell}(f_{\tilde{p}})$ are not unique, but one convenient form is given by [189]:

$$\tilde{f}_{k,\ell}(f_{\tilde{p}}) = \tilde{f}_{\ell,k}(f_{\tilde{p}}) = \pi(-i)^{\ell-k}\sqrt{\frac{2^k k!}{2^\ell \ell!}}|f_{\tilde{p}}|f_{\tilde{p}}^{\ell-k} \tag{6.17}$$

$$\times \exp(-f_{\tilde{p}}^2/4)L_k^{\ell-k}(f_{\tilde{p}}^2/2) \tag{6.18}$$

These can be used to construct a density matrix via the following relation:

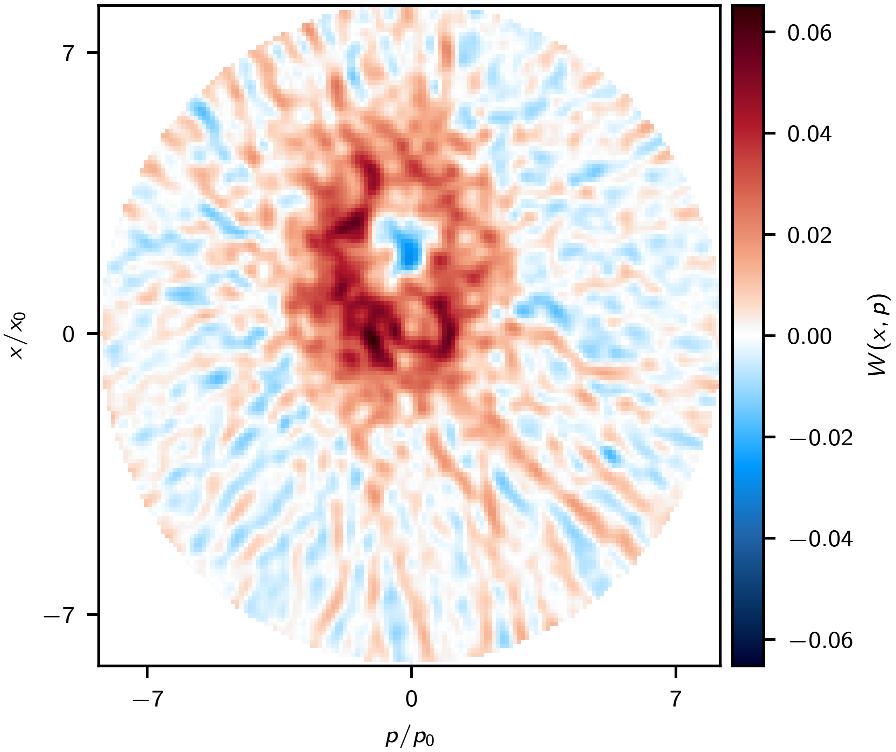

Figure 6.12: **Inverse Radon transform Wigner function.** The measured Wigner function of a displaced $n_x = 1$ state. The inverse Radon transform is more sensitive in many ways to camera noise than the maximum likelihood estimation is, although both methods result in a Wigner function with the same primary features.

$$\rho_{k,\ell} = \frac{1}{4\pi^2}\int_{-\infty}^{+\infty}[df_x]\int_0^{2\pi}[d\theta]\tilde{w}(f_{\tilde{p}},\theta) \tag{6.19}$$

$$\times \exp(i(k-\ell)\theta)\tilde{f}_{k,l}(-f_{\tilde{p}}) \tag{6.20}$$

Where $\tilde{w}(f_{\tilde{p}},\theta)$ is the 1-dimensional Fourier-transform of the quadrature data $w(x,\theta)$, and $f_{\tilde{p}}$ is the spatial frequency coordinate, and $L_m^n(z)$ is the generalized Laguerre polynomial.

The main downside to this method is that like the inverse-Radon transform, when applied to noisy data, this method produces unphysical density matrices with negative diagonal elements. Normalization and comparison to other methods when these effects are significant are not trivial. Error from this method can be estimated with a similar bootstrapping routine.

6.5 Error estimation

6.5.1 Estimating statistical error through bootstrapping

To present the Wigner functions distributions in Fig. 6.3 we apply MLE directly to the observed quadrature data. When this is done, we obtain Wigner function maximum negativities of -0.052 (-0.043) for the non-displaced (displaced) $n_x = 1$ states discussed in Fig. 6.3. However, this calculation does not naturally lend itself to estimation of the error on these values or on the density matrices.

The calculation of confidence intervals for the results of the MLE algorithm is a non-trivial task. We take the bootstrapping approach outlined in Ref. [181]. We begin by calculating the expected quadrature distributions as a function of θ and $\tilde{p}$ for the non-bootstrapped MLE density matrix, which is obtained from our measured quadrature data. For every value of θ, we then simulate projective measurements of $\tilde{p}$ by sampling from these expected quadrature distributions, and use this to generate an ensemble of bootstrapped images.

Separately, based on our Gaussian camera noise analysis, we reconstruct noise that is added to each bootstrapped quadrature distribution. Specifically, we use Gaussian-distributed noise with a

State	$P(n_x = 0)$	$P(n_x = 1)$	$P(n_x = 2)$	$P(n_x = 3)$	$P(n_x > 3)$	$P(n_x > 9)$	**Min** W	**Max** W	Purity
Least-Squares Single Image Fit									
Stat. $n_x = 0$	0.93(3)	0.07(2)	0.00(2)	X	X	X	X	X	X
Stat. $n_x = 1$	0.260(10)	0.651(14)	0.089(15)	X	X	X	X	X	X
Stat. $n_x = 2$	0.395(14)	0.125(18)	0.480(16)	X	X	X	X	X	X
Maximum Likelihood									
Disp. $n_x = 0$	0.338(14)	0.214(15)	0.148(9)	0.095(10)	0.205(16)	0.067(12)	-0.001(4)	0.110(11)	0.361(15)
Sq. $n_x = 1$	0.227(8)	0.477(9)	0.092(8)	0.039(5)	0.166(7)	0.102(5)	-0.060(6)	0.113(6)	0.351(7)
Sq. Disp. $n_x = 1$	0.455(7)	0.133(8)	0.113(6)	0.116(7)	0.184(7)	0.038(3)	-0.064(6)	0.133(6)	0.443(9)
Aggressively Deconvolved Maximum Likelihood									
Disp. $n_x = 0$	0.336(10)	0.259(15)	0.184(12)	0.104(9)	0.117(12)	0.034(8)	-0.002(5)	0.141(13)	0.470(16)
Sq. $n_x = 1$	0.324(7)	0.514(7)	0.024(3)	0.029(3)	0.109(5)	0.081(5)	-0.070(5)	0.136(5)	0.448(6)
Sq. Disp $n_x = 1$	0.642(6)	0.080(3)	0.077(3)	0.082(3)	0.119(4)	0.021(2)	-0.124(4)	0.231(3)	0.749(8)
Ideal States									
Stat. $n_x = 0$	1	0	0	0	0	0	0	0.318	1
Stat. $n_x = 1$	0	1	0	0	0	0	−0.318	0.142	1
Sq. $n_x = 1$	0	0.958	0	0.041	0.001	0	−0.318	0.142	1
Stat. $n_x = 2$	0	0	1	0	0	0	−0.132	0.318	1
Disp. $n_x = 0$	0.327	0.366	0.204	0.0759	0.027	0	0	0.318	1
Sq. Disp. $n_x = 1$	0.417	0.012	0.135	0.175	0.262	0.001	−0.318	0.142	1

Table 6.4: **State populations predicted through different types of analysis**. **Least-Squares Single Image Fit**: The fraction of each of the stationary (stat.) $n_x = 0$, $n_x = 1$, and $n_x = 2$ states. Results come from fitting the data with a sum of the three relevant quantum states which have been convolved with the fitted PSF of our imaging system. The standard deviation of the $n_x = 0$ ($n_x = 1$ and $n_x = 2$) fit is fixed by our measurement of the displaced oscillation period of the $n_x = 0$ ($n_x = 1$) state. All errors are least squared errors from the fitting routine, notable as most other errors reported come from MLE bootstrapping simulations. **Maximum Likelihood:** The results of the full maximum likelihood analysis and bootstrapping to our various displaced (disp.) and squeezed (sq.) quadrature measurements, as used in Fig. 6.3. Notably, only the on-diagonal values and uncertainties are reported, while off-diagonal coherences contribute significantly to the Wigner function negativity. **Aggressively Deconvolved Maximum Likelihood:** The results of setting the deconvolution filter value to $\zeta_0 = 1.9$ counts in all analysis. Filtering aggressively will reduce the effects of noise, as is evidenced by the reduced fraction of each state with $n > 10$, which we attribute to noise. However, aggressively filtering may overestimate the negativity of the Wigner function.

standard deviation consistent with what we observe in the tomography quadrature data (Sec. 6.2.3). Note, for the highly-averaged statistics of our experiment, the quadrature distributions are well-sampled, and the projection noise is small compared to the Gaussian camera noise.

At this point, we have an ensemble of bootstrapped quadrature distributions, which we can run through our deconvolution algorithm and MLE, as done for our raw experimental data. This yields an ensemble of density matrices, whose variation reflects the Gaussian camera noise in the quadrature data.

The diagonal density matrix elements derived from the direct MLE and the bootstrapped ensemble are displayed in Fig. 6.13a,b,c. While off-diagonal components are also important for the state inference, this picture provides a simple method to compare different techniques and expectations. From this comparison we can see the bootstrapped ensemble results in slightly less population in higher n_x states. From these density matrices we calculate the Wigner negativities, as presented in the main text. The minimum value of the Wigner function for the nearly-stationary $n_x = 1$ state is found to be $-0.060(6)$ and the displaced $n_x = 1$ state of $-0.064(6)$ Recall, for the direct MLE analysis we obtain Wigner function maximum negativities of -0.052 (-0.043) for the non-displaced (displaced) $n_x = 1$ states discussed in Fig. 6.3. While all analyses clearly point to negative Wigner values, we note the difference between the non-bootstrapped and bootstrapped analyses is likely indicative of subtle effects such as non-ideal noise and the non-invertibility of our numerical deconvolution routine (Sec. 6.2.3).

Lastly, we note that our reconstructed Wigner function for the displaced and non-displaced $n_x = 1$ states are qualitatively similar despite having independent noise patterns (Fig. 6.3d,g), which indicates the robustness of the MLE reconstruction protocol.

6.5.2 Noise and imaging systematic effects

Systematic error due to variable Gaussian noise: We can simulate the systematic effect of varying amounts of Gaussian noise on our MLE state reconstruction by again using our bootstrapping procedure. For this simulation, we construct mixed states with only diagonal ele-

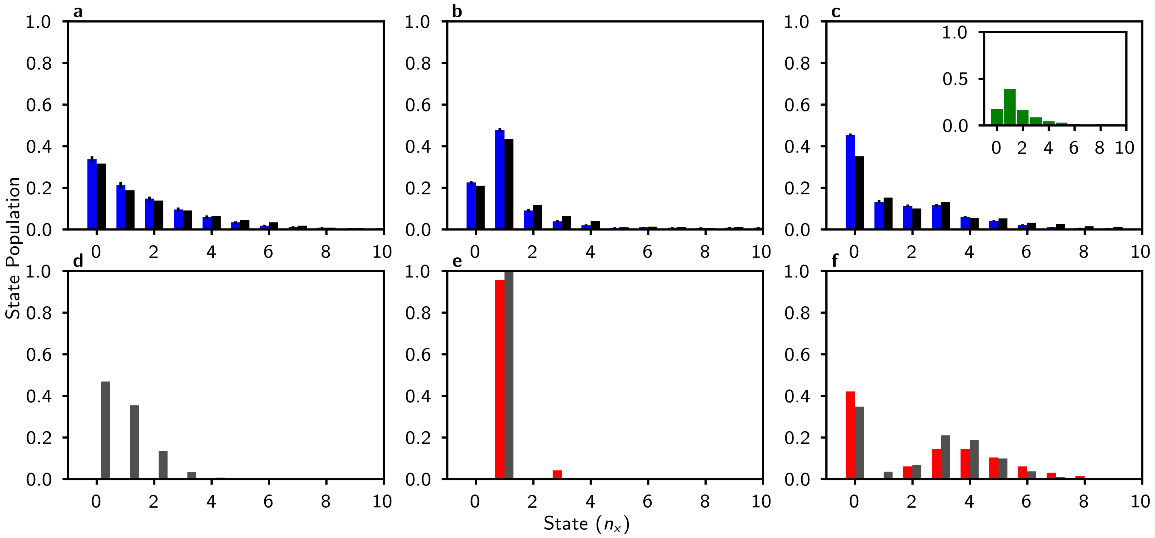

Figure 6.13: **State populations visualization via diagonal populations** (top row) Populations of harmonic oscillator states measured in our tomography as calculated through the error bootstrapping (blue bars) or the direct MLE result (black bars) for **(a)** the displaced $n_x = 0$ state, **(b)** the non-displaced $n_x = 1$ state, and **(c)** the displaced $n_x = 1$ state. **(c)** inset: populations of the experimentally displaced $n_x = 1$ data set after being displaced back to the origin. (bottom row) For comparison, we display the populations of theoretically ideal states, which do not include experimental imperfections in state preparation, with (red bars) and without (grey bars) the applied squeezing operator for **(d)** the displaced $n_x = 0$ state, **(f)** the non-displaced $n_x = 1$ state, and **(e)** the displaced $n_x = 1$ state.

ments based on the least squares fits of the heavily averaged momentum distributions in Fig. 6.2, as this data has the least relative noise. By adding variable amounts of Gaussian noise to this initial state and conducting MLE on the result, we find that increasing amounts of Gaussian noise biases the reconstruction to overestimate the population in higher-n states, and underestimates the true negativity of the Wigner function (Fig. 6.14).

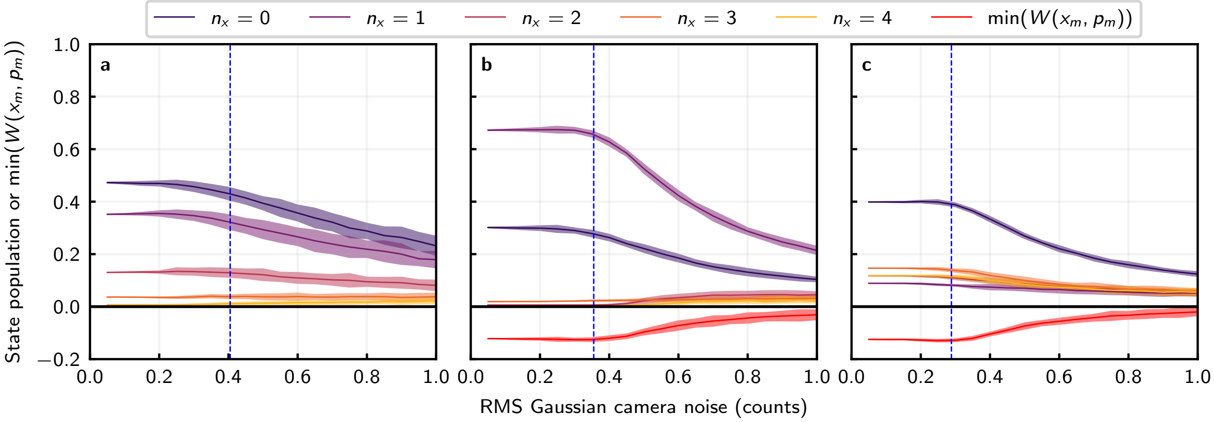

Figure 6.14: **Simulating the effects of Gaussian noise on maximum likelihood estimation (a)** Simulation of noise on a numerically displaced $n_x = 0$ state with undisplaced diagonal $n_x = (0, 1, 2)$ populations of $(0.93(3), 0.07(2), 0.00(2))$ and no off-diagonal populations, the values suggested by least squares fitting of the highly-averaged momentum distributions in Fig. 6.2, for demonstration. Shown are the mean values (solid lines) of populations $n_x = 0$ through $n_x = 4$, averaged over 50 simulations at each RMS noise value. 95% of the single-simulation observed values fall within the color bands to demonstrate variation of these parameters between simulations. **(b)** Simulation of noise on an undisplaced but numerically squeezed $n_x = 1$ state with undisplaced and unsqueezed $n_x = (0, 1, 2)$ populations of $(0.260(10), 0.651(14), 0.089(15))$ picked similarly from the least squares fitting routine for demonstration. Additionally shown are the mean Wigner values at the location of the true minimum (x_m, p_m) (red line), and 95% of single-simulation Wigner function values at this location lie within the red color band. **(c)** Similar to (b) with the same initial populations, but for a displaced $n_x = 1$ state. A key reference point is the measured Gaussian camera noise, as measured in our real quadrature data in Fig. 6.3 for each state (blue dotted lines).

Point-spread function and blurring effects: As discussed in Sec. 6.2, in order to accurately reconstruct our state, we must take into account aberrations and blurring effects in the time-of-flight images. Ideally, one could measure and characterize all such effects to reconstruct the true point-spread function, which can then be used to deconvolve the measured quadrature distribution. Because characterizing all blur is challenging for certain types of effects, we use a conservative value in our analysis, namely the in-trap size measured with RPGC, which is our smallest PSF estimate (Sec. 6.2). A less conservative estimate is the larger time-of-flight distribution of the atoms immediately after being released.

We verify that using larger PSF functions for deconvolution in the analysis of displaced and non-displaced $n_x = 1$ Fock state data (Fig. 6.3d-j), up to a factor of 1.5 larger in both dimensions, results in uniformly more negative Wigner functions. For example, using the first-10 µs time-of-flight distribution (Table 6.2), which also has slightly less astigmatism, has a negligible impact on our Wigner negativity — the reconstructed non-displaced $n_x = 1$ Wigner function would have a minimum value from the non-bootstrapped MLE analysis of -0.055 (instead of -0.052).

Other deconvolution parameters: In general, we expect the optimal deconvolution parameters to depend on the nature of the state being reproduced and the amount of noise present. To choose suitable values for our analysis, we perform bootstrapping similar to that done for statistical error estimation, except that we allow the deconvolution parameters in the bootstrapped ensemble to vary from the direct MLE reconstruction parameters. We then compare the resulting bootstrapped density matrix to the direct MLE result to find optimal parameters that reproduce the non-bootstrapped density matrix with the highest possible fidelity, where the fidelity is defined as

$$\mathcal{F} = \left(\mathrm{Tr}\left(\sqrt{\sqrt{\rho_1}\rho_2\sqrt{\rho_1}}\right)\right)^2. \tag{6.21}$$

Let ζ_0 and ζ_b denote the deconvolution filter values for our direct MLE and boostrapped density matrices, respectively. We choose ζ_0 such that the boostrapped density matrix with filter value ζ_b yields the highest fidelity when $\zeta_b = \zeta_0$. For the displaced $n_x = 1$ data set, we find that a filter value of $\zeta_b = 0.69$ counts and between 2 and 10 iterations of the deconvolution algorithm reliably reproduces the density matrix for a wide range of ζ_0. We thus choose to use this value, $\zeta_0 = 0.69$, in our main analysis. To minimize additional artifacting, we also apply only 2 iterations of the deconvolution algorithm, for which our bootstrapping routine reproduces the non-bootstrapped density matrix with a fidelity of 0.934(2).

We apply a similar analysis to find that the highest-fidelity parameters for the displaced $n_x = 0$ analysis also corresponds to a filter value of $\zeta_0 = 0.69$, and that the best for the non-displaced $n_x = 1$ is $\zeta_0 = 1.03$, both similarly with 2 iterations of the algorithm. The non-displaced $n_x = 1$ requires slightly larger filtering to compensate for having slightly increased noise due fewer points in this data set.

Noise and imaging analysis summary:

In conclusion, noise and imaging blur processes can influence the MLE algorithm when carrying out tomography using imperfect camera imaging. We have shown through a survey of systematic effects that their impact is either small or they result in our state reconstruction being a conservative underestimate of parameters such as the magnitude of the Wigner function negativity and state preparation fidelity.

6.5.3 Trap anharmonicity

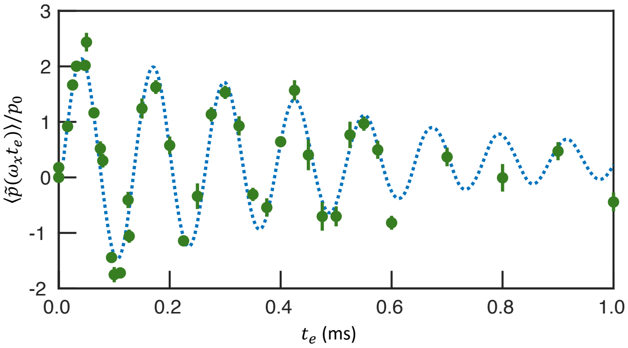

Figure 6.15: Best-fit dynamics for $\langle\tilde{p}(\omega_x t_e)\rangle/p_0$ generated by Eq. (6.22) for an initial displaced ground state (blue, dotted), compared to experimental results from Fig. 6.6 for an initial displaced $n_x = 0$ state (green).

Characterizing trap anharmonicity To analyze the effect of trap anharmonicity on state reconstruction, we consider the dynamics of a single atom in a one-dimensional anharmonic oscillator, which serves as a phenomenological model for the experimental optical tweezer potential.

Specifically, we consider dynamics generated by the Hamiltonian

$$\begin{aligned} H =&\frac{p^2}{2m} + \frac{m\omega_x^2 x^2}{2} + \Lambda x^4 \\ =&\hbar\omega_x \left[(p x_0/\hbar)^2 + \frac{1}{4}(x/x_0)^2 + \lambda (x/x_0)^4 \right], \end{aligned} \tag{6.22}$$

which describes an atom of mass m in a harmonic trap with frequency ω_x, plus an additional quartic term of characteristic strength Λ. In the second line, we have rewritten this potential in terms of the harmonic length $x_0 = \sqrt{\hbar/(2m\omega_x)}$, and defined the dimensionless parameter $\lambda = \Lambda x_0^4/(\hbar\omega_x)$ as the relative strength of the anharmonic correction.

We can obtain estimates of ω_x and λ by comparing the predictions of our phenomenological model with experimental observations. Specifically, we compare experimental data for the long-time center-of-mass dynamics of an initially-displaced $n_x = 0$ state (see Fig. 6.2k) to the average momentum $\langle \tilde{p}(\omega_x t_e) \rangle$ obtained from Eq. (6.22) for an initially-displaced $n_x = 0$ state. In the case that $\lambda < 0$, we add a minimal sextic term $\hbar\omega_x (2\lambda^2/3)(x/x_0)^6$ that ensures our potential remains stable and retains only a single local minimum, and thus induces only local deformations of our ground state; this term plays a negligible role in the resulting dynamics for the considered parameters.

Treating ω_x, λ, and the initial state displacement x_i as free parameters, we perform a least-squares fit of $\langle \tilde{p}(\omega_x t_e) \rangle$ to the experimental center-of-mass oscillations. We obtain best-fit values of $\lambda = -0.0037(4)$, $\omega_x = 2\pi \times 8.50(5)\,\mathrm{kHz}$ (corresponding to $x_0 = 83\,\mathrm{nm}$) and $x_i = 166(5)\,\mathrm{nm}$. As shown in Fig. 6.15, we observe that the fitted model robustly captures the observed damping. As a crude estimate of the relative significance of the harmonic and quartic potential terms in the Hamiltonian when considering the dynamics of this displaced state, we can compare their expected values at $t_e = 0$. By approximating moments by their harmonic values, we find $4|\lambda|\langle (x/x_0)^4 \rangle / \langle (x/x_0)^2 \rangle \approx 0.13$. While this indicates that the harmonic term remains dominant for displacements of this size, the anharmonic term is not so small as to be easily discounted without further analysis. Separately, we note the the best-fit estimate for the trap frequency in this model ($8.50(5)\,\mathrm{kHz}$, with $x_0 = 83\,\mathrm{nm}$) is comparable to the observed oscillation frequency in the experiment, $7.84(5)\,\mathrm{kHz}$ with $x_0 = 86\,\mathrm{nm}$.

The deviation between these values is consistent with the negative λ in our model, which generally leads to a slower observed oscillation frequency for a displaced $n_x = 0$ state than what is expected for the corresponding ideal harmonic oscillator.

Maximum likelihood estimation in an anharmonic potential We now examine how anharmonicity affects state reconstruction, utilizing the Hamiltonian in Eq. (6.22) as a model for the tweezer potential. Following the protocol in the main text, we spatially displace an initial state ρ_i by a fixed amount x_i, which in the Schrödinger picture can be described by acting the displacement operator $D(x_i) = e^{-ipx_i/\hbar}$ on the initial state. We then evolve for a time t_e, described by the unitary operator $U\left(t\right) = e^{-it_e H/\hbar}$. The resulting dynamical state is expressed as,

$$\rho\left(t_e\right) = U\left(t_e\right) D(x_i)\rho_i D^{\dagger}(x_i)U^{\dagger}\left(t_e\right), \tag{6.23}$$

from which we extract the time-evolved momentum distribution $P\left(p, t_e\right) = \mathrm{Tr}\left(\rho\left(t_e\right)|p\rangle\langle p|\right)$ for momentum eigenstate $|p\rangle$. This distribution is used as the input for the iterative MLE algorithm (Sec. 6.4.2).

To make connections with the experiment, we would like to analyze the effect of an anharmonic trap on reconstruction of a displaced $n_x = 1$ state. Because the prepared state contains contributions from other Fock states, we assume the initial state ρ_i can be well modelled by an incoherent mixture of the low-energy eigenstates of the Hamiltonian,

$$\rho_i = P_0|0\rangle\langle 0| + P_1|1\rangle\langle 1| + P_2|2\rangle\langle 2|. \tag{6.24}$$

Here, P_{n_x} denotes the probability of staring in the eigenstate $|n_x\rangle$; we denote this state by the triplet $\mathbf{P} = (P_0, P_1, P_2)$. By choosing P_{n_x} that generally resembles the makeup of the state in the experiment we are able to analyze the effects of initial mixed states in both the dynamics and ensuing state reconstruction, and demonstrate robustness of MLE tomography over a range of possible initial states.

As the state reconstruction data for the displaced $n_x = 1$ state, featured in Fig. 6.3g-k, is obtained using a deeper trap depth and smaller displacement than that used in our initial analysis of the anharmonic oscillator model Eq. (6.22) for the $n_x = 0$ center-of-mass oscillations, we modify the previously obtained best-fit parameters by an appropriate scaling. Assuming that H is linear in the trap depth V, we have that $\lambda \sim 1/\sqrt{V}$ and $\omega_x \sim \sqrt{V}$. Hence we can rescale based on the relative ratios of both the depth and displacement.

In Fig. 6.16a, we plot the fidelity of our reconstructed state, ρ_{MLE}, to the actual underlying state, $\rho(0) = D(x_i)\rho_i D^\dagger(x_i)$, for a variety of compositions $\mathbf{P}$. In the figure, we indicate $\mathbf{P}$ that produces a state before displacement with a similar spatial extent in the trap as the $n_x = 1$ states in Fig. 6.3e, h. This point, indicated by the purple star, corresponds to $\mathbf{P} = (0.28, 0.57, 0.15)$, and corresponds to estimates obtained in Fig. 6.13 for the diagonal composition of the state prepared in the trap.

Within our model and for the indicated state, we find that the reduction in the fidelity owing to anharmonic effects does not exceed 5%. However, for higher populations of the $n_x = 2$ state, a larger reduction in fidelity is expected from anharmonicity, and a deeper trap or smaller displacement would be needed to reduce the effect of anharmonicity and faithfully characterize such states. Moreover, we find that the diagonal elements of the density matrix indicated by the purple star remain very similar (Fig. 6.16b).

While the fidelity provides some measure of similarity between our states, of specific interest is the robustness of the nonclassical nature of the prepared states, which may be identified through the Wigner negativity $\gamma \leq 0$, where $\gamma = \min_{x,p} W(x,p)$. Therefore, we also plot the difference in negativity between $\rho(0)$ and ρ_{MLE} in Fig. 6.16c. Over the entire range of $\mathbf{P}$ considered, the difference in obtained negativity never exceeds 0.06, and for the indicated estimates of our $n_x = 1$ initial state composition, for which $\gamma \approx -0.04$, the corresponding MLE state remains negative with a difference in negativity of < 0.01.

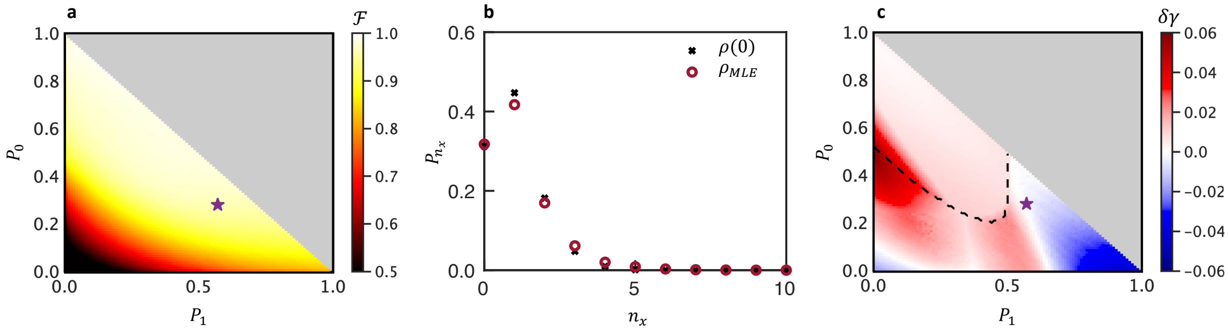

Figure 6.16: **(a)** Fidelity $\mathcal{F}$ (Eq. (6.21)) between the state $\rho\,(0)$ and the reconstructed state ρ_{MLE} for initial states ρ_i characterized by a range of $\mathbf{P} = (P_{n=0}, P_{n=1}, P_{n=2})$, after evolution with our anharmonic model Eq. (6.22). **(b)** Comparison of the diagonal elements for $n_x \leq 10$ of $\rho(0)$ and ρ_{MLE} after a displacement back to the origin, corresponding to $\mathbf{P} = (0.28, 0.57, 0.15)$ (purple star in **a**). This point corresponds to a state with similar spatial extent as the $n_x = 1$ state shown in Fig. 6.3e, h. Here, n_x labels the Fock states of the oscillator in Eq. (6.22). **(c)** For each $\mathbf{P}$, we then compute the Wigner negativity, $\gamma = \min_{x,p} W(x,p)$, for our initial state $\rho(0)$, as well as the Wigner negativity γ_{MLE} of the reconstructed state. We plot the difference $\delta\gamma = \gamma - \gamma_{\text{MLE}}$; positive regions indicate parameters for which ρ_{MLE} estimates more nonclassicality than the underlying state, whereas negative regions indicate parameters for which ρ_{MLE} is an upper bound on this negativity. The dashed black dashed line separates nonclassical states with $\gamma < 0$ from those with $\gamma = 0$.

Bibliography

[1] A. L. Schawlow and C. H. Townes, Infrared and Optical Masers, *Physical Review* **112**, 1940 (1958).

[2] T. H. Maiman, Stimulated Optical Radiation in Ruby, *Nature* **187**, 493 (1960).

[3] A. Ashkin, Acceleration and Trapping of Particles by Radiation Pressure, *Physical Review Letters* **24**, 156 (1970).

[4] T. W. Hänsch and A. L. Schawlow, Cooling of gases by laser radiation, *Optics Communications* **13**, 68 (1975).

[5] D. Wineland and H. Dehmelt, Proposed $1014\delta\nu/\nu$ laser fluorescence spectroscopy on Tl+ mono-ion oscillator III (side band cooling), *Bull. Am. Phys. Soc* **20**, 637 (1975).

[6] D. J. Wineland, R. E. Drullinger, and F. L. Walls, Radiation-Pressure Cooling of Bound Resonant Absorbers, *Physical Review Letters* **40**, 1639 (1978).

[7] E. L. Raab, M. Prentiss, A. Cable, S. Chu, and D. E. Pritchard, Trapping of Neutral Sodium Atoms with Radiation Pressure, *Physical Review Letters* **59**, 2631 (1987).

[8] Z. Hu and H. J. Kimble, Observation of a single atom in a magneto-optical trap, *Optics Letters* **19**, 1888 (1994).

[9] W. D. Phillips, Nobel Lecture: Laser cooling and trapping of neutral atoms, *Rev. Mod. Phys.* **70**, 721 (1998).

[10] A. Ashkin, History of optical trapping and manipulation of small-neutral particle, atoms, and molecules, *IEEE Journal of Selected Topics in Quantum Electronics* **6**, 841 (2000).

[11] C. N. Cohen-Tannoudji, Nobel Lecture: Manipulating atoms with photons, *Reviews of Modern Physics* **70**, 707 (1998).

[12] S. Chu, Nobel Lecture: The manipulation of neutral particles, *Reviews of Modern Physics* **70**, 685 (1998).

[13] M. H. Anderson, J. R. Ensher, M. R. Matthews, C. E. Wieman, and E. A. Cornell, Observation of Bose-Einstein condensation in a dilute atomic vapor, *Science* **269**, 198 (1995).

[14] K. B. Davis, M. O. Mewes, M. R. Andrews, N. J. V. Druten, D. S. Durfee, D. M. Kurn, and W. Ketterle, Bose-Einstein Condensation in a Gas of Sodium Atoms, *Phys. Rev. Lett.* **75**, 3969 (1995).

[15] B. DeMarco and D. S. Jin, Onset of Fermi Degeneracy in a Trapped Atomic Gas, *Science* **285**, 1703 (1999).

[16] S. Jochim, M. Bartenstein, A. Altmeyer, G. Hendl, S. Riedl, C. Chin, J. Hecker Denschlag, and R. Grimm, Bose-Einstein Condensation of Molecules, *Science* **302**, 2101 (2003).

[17] M. Greiner, C. A. Regal, and D. S. Jin, Emergence of a molecular Bose–Einstein condensate from a Fermi gas, *Nature* **426**, 537 (2003).

[18] M. Lu, N. Q. Burdick, S. H. Youn, and B. L. Lev, Strongly Dipolar Bose-Einstein Condensate of Dysprosium, *Physical Review Letters* **107**, 190401 (2011).

[19] L. Chomaz *et al.*, Long-Lived and Transient Supersolid Behaviors in Dipolar Quantum Gases, *Physical Review X* **9**, 021012 (2019).

[20] L. De Marco, G. Valtolina, K. Matsuda, W. G. Tobias, J. P. Covey, and J. Ye, A degenerate Fermi gas of polar molecules, *Science* **363**, 853 (2019).

[21] M. Greiner, O. Mandel, T. Esslinger, T. W. Hänsch, and I. Bloch, Quantum phase transition from a superfluid to a Mott insulator in a gas of ultracold atoms, *nature* **415**, 39 (2002).

[22] W. S. Bakr, J. I. Gillen, A. Peng, S. Fölling, and M. Greiner, A quantum gas microscope for detecting single atoms in a Hubbard-regime optical lattice, *Nature* **462**, 74 (2009).

[23] C. Weitenberg, M. Endres, J. F. Sherson, M. Cheneau, P. S. s, T. Fukuhara, I. Bloch, and S. Kuhr, Single-spin addressing in an atomic Mott insulator, *Nature (London)* **471**, 319 (2011).

[24] R. Yamamoto, J. Kobayashi, T. Kuno, K. Kato, and Y. Takahashi, An ytterbium quantum gas microscope with narrow-line laser cooling, **18**, 023016 (2016).

[25] E. Haller, J. Hudson, A. Kelly, D. A. Cotta, B. Peaudecerf, G. D. Bruce, and S. Kuhr, Single-atom imaging of fermions in a quantum-gas microscope, *Nature Physics* **11**, 738 (2015).

[26] L. W. Cheuk, M. A. Nichols, M. Okan, T. Gersdorf, V. V. Ramasesh, W. S. Bakr, T. Lompe, and M. W. Zwierlein, Quantum-Gas Microscope for Fermionic Atoms, *Physical Review Letters* **114**, 193001 (2015).

[27] H. Ott, Single atom detection in ultracold quantum gases: a review of current progress, *Reports on Progress in Physics* **79**, 054401 (2016), publisher: IOP Publishing.

[28] N. Schlosser, G. Reymond, I. Protsenko, and P. Grangier, Sub-poissonian loading of single atoms in a microscopic dipole trap, *Nature (London)* **411**, 1024 (2001).

[29] N. Schlosser, G. Reymond, and P. Grangier, Collisional Blockade in Microscopic Optical Dipole Traps, *Phys. Rev. Lett.* **89**, 023005 (2002).

[30] J. Beugnon *et al.*, Two-dimensional Transport and Transfer of a Single Atomic Qubit in Optical Tweezers, *Nat. Phys.* **3**, 696 (2007).

[31] C. Tuchendler, A. M. Lance, A. Browaeys, Y. R. P. Sortais, and P. Grangier, Energy distribution and cooling of a single atom in an optical tweezer, *Physical Review A* **78**, 033425 (2008).

[32] D. D. Yavuz, P. B. Kulatunga, E. Urban, T. A. Johnson, N. Proite, T. Henage, T. G. Walker, and M. Saffman, Fast Ground State Manipulation of Neutral Atoms in Microscopic Optical Traps, *Phys. Rev. Lett.* **96**, 063001 (2006).

[33] M. Saffman and T. G. Walker, Analysis of a quantum logic device based on dipole-dipole interactions of optically trapped Rydberg atoms, *Physical Review A* **72**, 022347 (2005).

[34] T. Johnson, E. Urban, T. Henage, L. Isenhower, D. Yavuz, T. Walker, and M. Saffman, Rabi Oscillations between Ground and Rydberg States with Dipole-Dipole Atomic Interactions, *Phys. Rev. Lett.* **100**, 113003 (2008).

[35] T. Wilk, A. Gaëtan, C. Evellin, J. Wolters, Y. Miroshnychenko, P. Grangier, and A. Browaeys, Entanglement of Two Individual Neutral Atoms Using Rydberg Blockade, *Phys. Rev. Lett.* **104**, 010502 (2010).

[36] L. Isenhower, E. Urban, X. L. Zhang, A. T. Gill, T. Henage, T. A. Johnson, T. G. Walker, and M. Saffman, Demonstration of a Neutral Atom Controlled-NOT Quantum Gate, *Phys. Rev. Lett.* **104**, 010503 (2010).

[37] F. Serwane, G. Zürn, T. Lompe, T. B. Ottenstein, A. N. Wenz, and S. Jochim, Deterministic Preparation of a Tunable Few-Fermion System, *Science* **332**, 336 (2011).

[38] L. W. Cheuk, L. Anderegg, B. L. Augenbraun, Y. Bao, S. Burchesky, W. Ketterle, and J. M. Doyle, Λ-Enhanced Imaging of Molecules in an Optical Trap, *Physical Review Letters* **121**, 083201 (2018).

[39] L. Anderegg, L. W. Cheuk, Y. Bao, S. Burchesky, W. Ketterle, K.-K. Ni, and J. M. Doyle, An optical tweezer array of ultracold molecules, *Science* **365**, 1156 (2019).

[40] M. A. Norcia, A. W. Young, W. J. Eckner, E. Oelker, J. Ye, and A. M. Kaufman, Seconds-scale coherence on an optical clock transition in a tweezer array, *Science* **366**, 93 (2019).

[41] I. S. Madjarov, J. P. Covey, A. L. Shaw, J. Choi, A. Kale, A. Cooper, H. Pichler, V. Schkolnik, J. R. Williams, and M. Endres, High-fidelity entanglement and detection of alkaline-earth Rydberg atoms, *Nature Physics* **16**, 857 (2020).

[42] B. M. Spar, E. Guardado-Sanchez, S. Chi, Z. Z. Yan, and W. S. Bakr, A Fermi-Hubbard Optical Tweezer Array, *arXiv:2110.15398 [cond-mat, physics:physics]* (2021), arXiv: 2110.15398.

[43] A. Bergschneider, V. M. Klinkhamer, J. H. Becher, R. Klemt, L. Palm, G. Zürn, S. Jochim, and P. M. Preiss, Experimental characterization of two-particle entanglement through position and momentum correlations, *Nature Physics* **15**, 640 (2019).

[44] Y. Lu, C. M. Holland, and L. W. Cheuk, Molecular Laser-Cooling in a Dynamically Tunable Repulsive Optical Trap, *arXiv:2109.04589 [cond-mat, physics:physics]* (2021), arXiv: 2109.04589.

[45] K. Barnes *et al.*, Assembly and coherent control of a register of nuclear spin qubits, *arXiv:2108.04790 [physics, physics:quant-ph]* (2021), arXiv: 2108.04790.

[46] A. M. Kaufman and K.-K. Ni, Quantum science with optical tweezer arrays of ultracold atoms and molecules, *Nature Physics* 1 (2021).

[47] A. Fuhrmanek, R. Bourgain, Y. R. P. Sortais, and A. Browaeys, Light-assisted collisions between a few cold atoms in a microscopic dipole trap, *Phys. Rev. A* **85**, 062708 (2012).

[48] T. Grünzweig, A. Hilliard, M. McGovern, and M. F. Andersen, Near-deterministic preparation of a single atom in an optical microtrap, *Nat. Phys.* **6**, 951 (2010).

[49] M. McGovern, A. J. Hilliard, T. Grünzweig, and M. F. Andersen, Counting atoms in a deep optical microtrap, *Opt. Lett.* **36**, 1041 (2011).

[50] J. D. Thompson, T. G. Tiecke, A. S. Zibrov, V. Vuletic, and M. D. Lukin, Coherence and Raman sideband cooling of a single atom in an optical tweezer, *Phys. Rev. Lett.* **110**, 133001 (2013).

[51] A. M. Kaufman, B. J. Lester, C. M. Reynolds, M. L. Wall, M. Foss-Feig, K. R. A. Hazzard, A. M. Rey, and C. A. Regal, Two-particle quantum interference in tunnel-coupled optical tweezers, *Science* **345**, 306 (2014).

[52] S. Murmann, A. Bergschneider, V. M. Klinkhamer, G. Zürn, T. Lompe, and S. Jochim, Two Fermions in a Double Well: Exploring a Fundamental Building Block of the Hubbard Model, *Phys. Rev. Lett.* **114**, 080402 (2015).

[53] U. Delić, M. Reisenbauer, K. Dare, D. Grass, V. Vuletić, N. Kiesel, and M. Aspelmeyer, Cooling of a levitated nanoparticle to the motional quantum ground state, *Science* **367**, 892 (2020).

[54] F. Tebbenjohanns, M. L. Mattana, M. Rossi, M. Frimmer, and L. Novotny, Quantum control of a nanoparticle optically levitated in cryogenic free space, *Nature* **595**, 378 (2021).

[55] E. Munro, A. Asenjo-Garcia, Y. Lin, L. C. Kwek, C. A. Regal, and D. E. Chang, Population mixing due to dipole-dipole interactions in a one-dimensional array of multilevel atoms, *Physical Review A* **98**, 033815 (2018).

[56] J. Rui, D. Wei, A. Rubio-Abadal, S. Hollerith, J. Zeiher, D. M. Stamper-Kurn, C. Gross, and I. Bloch, A subradiant optical mirror formed by a single structured atomic layer, *Nature* **583**, 369 (2020).

[57] A. M. Kaufman, M. E. Tai, A. Lukin, M. Rispoli, R. Schittko, P. M. Preiss, and M. Greiner, Quantum thermalization through entanglement in an isolated many-body system, *Science* **353**, 794 (2016).

[58] A. M. Kaufman, B. J. Lester, M. Foss-Feig, M. L. Wall, A. M. Rey, and C. A. Regal, Entangling two transportable neutral atoms via local spin exchange, *Nature* **527**, 208 (2015).

[59] M. Bonneau, W. J. Munro, K. Nemoto, and J. Schmiedmayer, Characterizing twin-particle entanglement in double-well potentials, *Physical Review A* **98**, 033608 (2018).

[60] C. Yannouleas and U. Landman, Anyon optics with time-of-flight two-particle interference of double-well-trapped interacting ultracold atoms, *Physical Review A* **100**, 013605 (2019).

[61] O. Romero-Isart, M. L. Juan, R. Quidant, and J. I. Cirac, Toward Quantum Superposition of Living Organisms, *New J. Phys.* **12**, 033015 (2010).

[62] O. Romero-Isart, A. C. Pflanzer, F. Blaser, R. Kaltenbaek, N. Kiesel, M. Aspelmeyer, and J. I. Cirac, Large Quantum Superpositions and Interference of Massive Nanometer-Sized Objects, *Phys. Rev. Lett.* **107**, 020405 (2011).

[63] M. Brown, T. Thiele, C. Kiehl, T.-W. Hsu, and C. Regal, Gray-Molasses Optical-Tweezer Loading: Controlling Collisions for Scaling Atom-Array Assembly, *Physical Review X* **9**, 011057 (2019).

[64] A. Kaufman, Laser cooling atoms to indistinguishability: Atomic Hong-Ou-Mandel interference and entanglement through spin exchange, Ph.D. thesis, 2015.

[65] B. J. Lester, Atom-by-atom control and readout for studying spin-motional dynamics and entanglement in neutral atom arrays, Ph.D. thesis, 2016.

[66] D. A. Steck, Rubidium 87 D Line Data, 2021, available online at http://steck.us/alkalidata (revision 2.2.2, 9 July 2021).

[67] M. Egorov, B. Opanchuk, P. Drummond, B. V. Hall, P. Hannaford, and A. I. Sidorov, Measurement of s-wave scattering lengths in a two-component Bose-Einstein condensate, *Physical Review A* **87**, 053614 (2013).

[68] E. D. Black, An introduction to Pound-Drever-Hall laser frequency stabilization, *American Journal of Physics* **69**, 79 (2001).

[69] G. C. Bjorklund, Frequency-modulation spectroscopy: a new method for measuring weak absorptions and dispersions, *Optics Letters* **5**, 15 (1980).

[70] J. Bechhoefer, Feedback for physicists: A tutorial essay on control, *Reviews of Modern Physics* **77**, 783 (2005).

[71] D. J. McCarron, S. A. King, and S. L. Cornish, Modulation transfer spectroscopy in atomic rubidium, *Measurement Science and Technology* **19**, 105601 (2008).

[72] P. C. Miles and R. S. Barlow, A fast mechanical shutter for spectroscopic applications, *Measurement Science and Technology* **11**, 392 (2000).

[73] G. H. Zhang, B. Braverman, A. Kawasaki, and V. Vuletić, Note: Fast compact laser shutter using a direct current motor and three-dimensional printing, *Review of Scientific Instruments* **86**, 126105 (2015).

[74] P. Zupancic, P. M. Preiss, R. Ma, A. Lukin, M. E. Tai, M. Rispoli, R. Islam, and M. Greiner, Ultra-precise holographic beam shaping for microscopic quantum control, *Opt. Express* **24**, 13881 (2016).

[75] M. Reicherter, T. Haist, E. U. Wagemann, and H. J. Tiziani, Optical particle trapping with computer-generated holograms written on a liquid-crystal display, *Optics Letters* **24**, 608 (1999).

[76] D. Ohl de Mello, D. Schäffner, J. Werkmann, T. Preuschoff, L. Kohfahl, M. Schlosser, and G. Birkl, Defect-Free Assembly of 2D Clusters of More Than 100 Single-Atom Quantum Systems, *Physical Review Letters* **122**, 203601 (2019).

[77] N. R. Hutzler, L. R. Liu, Y. Yu, and K.-K. Ni, Eliminating light shifts for single atom trapping, *New Journal of Physics* **19**, 023007 (2017).

[78] A. M. Kaufman, B. J. Lester, C. M. Reynolds, M. L. Wall, M. Foss-Feig, K. R. A. Hazzard, A. M. Rey, and C. A. Regal, Hong-Ou-Mandel atom interferometry in tunnel-coupled optical tweezers, *Science* **345**, 6194 (2013).

[79] T.-W. Hsu, W. Zhu, T. Thiele, M. O. Brown, S. B. Papp, A. Agrawal, and C. A. Regal, Single atom trapping in a metasurface lens optical tweezer, *arXiv:2110.11559 [physics, physics:quant-ph]* (2021), arXiv: 2110.11559.

[80] D. R. Leibrandt and J. Heidecker, An open source digital servo for atomic, molecular, and optical physics experiments, *Review of Scientific Instruments* **86**, 123115 (2015).

[81] A. M. Kaufman, M. C. Tichy, F. Mintert, A. M. Rey, and C. A. Regal, in *Advances In Atomic, Molecular, and Optical Physics*, edited by E. Arimondo, L. F. DiMauro, and S. F. Yelin (Academic Press, ADDRESS, 2018), Vol. 67, pp. 377–427.

[82] R. Lopes, A. Imanaliev, A. Aspect, M. Cheneau, D. Boiron, and C. I. Westbrook, Atomic Hong-Ou-Mandel experiment, *Nature (London)* **520**, 66 (2015).

[83] M. L. Wall, K. R. A. Hazzard, and A. M. Rey, Effective many-body parameters for atoms in nonseparable Gaussian optical potentials, *Phys. Rev. A* **92**, 013610 (2015).

[84] M. Endres, H. Bernien, A. Keesling, H. Levine, E. R. Anschuetz, A. Krajenbrink, C. Senko, V. Vuletic, M. Greiner, and M. D. Lukin, Atom-by-atom assembly of defect-free one-dimensional cold atom arrays, *Science* **354**, 1024 (2016).

[85] D. Barredo, S. de Léséleuc, V. Lienhard, T. Lahaye, and A. Browaeys, An atom-by-atom assembler of defect-free arbitrary two-dimensional atomic arrays, *Science* **354**, 1021 (2016).

[86] D. Barredo, V. Lienhard, S. de Léséleuc, T. Lahaye, and A. Browaeys, Synthetic three-dimensional atomic structures assembled atom by atom, *Nature* **561**, 79 (2018).

[87] A. Kumar, T.-Y. Wu, F. Giraldo, and D. S. Weiss, Sorting ultracold atoms in a three-dimensional optical lattice in a realization of Maxwell's demon, *Nature* **561**, 83 (2018).

[88] W. Lee, H. Kim, and J. Ahn, Three-dimensional rearrangement of single atoms using actively controlled optical microtraps, *Optics Express* **24**, 9816 (2016).

[89] H. Kim, W. Lee, H.-g. Lee, H. Jo, Y. Song, and J. Ahn, In situ single-atom array synthesis using dynamic holographic optical tweezers, *Nature Communications* **7**, 13317 (2016).

[90] H. Kim, M. Kim, W. Lee, and J. Ahn, Gerchberg-Saxton algorithm for fast and efficient atom rearrangement in optical tweezer traps, *Optics Express* **27**, 2184 (2019).

[91] W. Lee, H. Kim, and J. Ahn, Defect-free atomic array formation using the Hungarian matching algorithm, *Physical Review A* **95**, 053424 (2017).

[92] C. Sheng, J. Hou, X. He, P. Xu, K. Wang, J. Zhuang, X. Li, M. Liu, J. Wang, and M. Zhan, Efficient preparation of two-dimensional defect-free atom arrays with near-fewest sorting-atom moves, *Physical Review Research* **3**, 023008 (2021).

[93] B. J. Lester, N. Luick, A. M. Kaufman, C. M. Reynolds, and C. A. Regal, Rapid Production of Uniformly Filled Arrays of Neutral Atoms, *Phys. Rev. Lett.* **115**, 073003 (2015).

[94] J. F. Sherson, C. Weitenberg, M. Endres, M. Cheneau, I. Bloch, and S. Kuhr, Single-atom-resolved fluorescence imaging of an atomic Mott insulator, *Nature (London)* **467**, 68 (2010).

[95] D. S. Weiss, J. Vala, A. V. Thapliyal, S. Myrgren, U. Vazirani, and K. B. Whaley, Another Way to Approach Zero Entropy for a Finite System of Atoms, *Phys. Rev. A* **70**, 040302(R) (2004).

[96] Y. Miroshnychenko, W. Alt, I. Dotsenko, L. Förster, M. Khudaverdyan, D. Meschede, D. Schrader, and A. Rauschenbeutel, Quantum engineering: An atom-sorting machine, *Nature (London)* **442**, 151 (2006).

[97] D. Barredo, S. de Léséleuc, V. Lienhard, T. Lahaye, and A. Browaeys, An atom-by-atom assembler of defect-free arbitrary two-dimensional atomic arrays, *Science* **354**, 1021 (2016).

[98] H. Bernien *et al.*, Probing many-body dynamics on a 51-atom quantum simulator, *Nature* **551**, 579 (2017).

[99] M. Marcuzzi, J. Minář, D. Barredo, S. de Léséleuc, H. Labuhn, T. Lahaye, A. Browaeys, E. Levi, and I. Lesanovsky, Facilitation Dynamics and Localization Phenomena in Rydberg Lattice Gases with Position Disorder, *Phys. Rev. Lett.* **118**, 063606 (2017).

[100] A. T. Grier, I. Ferrier-Barbut, B. S. Rem, M. Delehaye, L. Khaykovich, F. Chevy, and C. Salomon, Λ-enhanced sub-Doppler cooling of lithium atoms in D_1 gray molasses, *Phys. Rev. A* **87**, 063411 (2013).

[101] D. R. Fernandes, F. Sievers, N. Kretzschmar, S. Wu, C. Salomon, and F. Chevy, Sub-Doppler laser cooling of fermionic 40 K atoms in three-dimensional gray optical molasses, *Europhys. Lett.* **100**, 63001 (2012).

[102] A. V. Carpentier, Y. H. Fung, P. Sompet, A. J. Hilliard, T. G. Walker, and M. F. Andersen, Preparation of a single atom in an optical microtrap, *Laser Phys. Lett.* **10**, 125501 (2013).

[103] Y. H. Fung and M. F. Andersen, Efficient collisional blockade loading of a single atom into a tight microtrap, *New J. Phys.* **17**, 073011 (2015).

[104] A. Aspect, E. Arimondo, R. Kaiser, N. Vansteenkiste, and C. Cohen-Tannoudji, Laser Cooling below the One-Photon Recoil Energy by Velocity-Selective Coherent Population Trapping, *Phys. Rev. Lett.* **61**, 826 (1988).

[105] M. S. Shahriar, P. R. Hemmer, M. G. Prentiss, P. Marte, J. Mervis, D. P. Katz, N. P. Bigelow, and T. Cai, Continuous polarization-gradient precooling-assisted velocity-selective coherent population trapping, *Phys. Rev. A* **48**, R4035 (1993).

[106] G. Grynberg and J.-Y. Courtois, Proposal for a Magneto-Optical Lattice for Trapping Atoms in Nearly-Dark States, *Europhys. Lett.* **27**, 41 (1994).

[107] T. Esslinger, F. Sander, A. Hemmerich, T. W. Hänsch, H. Ritsch, and M. Weidemüller, Purely optical dark lattice, *Opt. Lett.* **21**, 991 (1996).

[108] D. J. McCarron, E. B. Norrgard, M. H. Steinecker, and D. DeMille, Improved magneto-optical trapping of a diatomic molecule, *New J. Phys.* **17**, 035014 (2015).

[109] J. A. Devlin and M. R. Tarbutt, Three-dimensional Doppler, polarization-gradient, and magneto-optical forces for atoms and molecules with dark states, *New J. Phys.* **18**, 123017 (2016).

[110] L. W. Cheuk, L. Anderegg, B. L. Augenbraun, Y. Bao, S. Burchesky, W. Ketterle, and J. M. Doyle, Λ-enhanced imaging of molecules in an optical trap, *Phys. Rev. Lett.* **121**, 083201 (2018).

[111] J. Lim, J. R. Almond, M. A. Trigatzis, J. A. Devlin, N. J. Fitch, B. E. Sauer, M. R. Tarbutt, and E. A. Hinds, Laser Cooled YbF Molecules for Measuring the Electron's Electric Dipole Moment, *Phys. Rev. Lett.* **120**, 123201 (2018).

[112] L. Anderegg, B. L. Augenbraun, Y. Bao, S. Burchesky, L. W. Cheuk, W. Ketterle, and J. M. Doyle, Laser cooling of optically trapped molecules, *Nat. Phys.* **14**, 890 (2018).

[113] S. Rosi, A. Burchianti, S. Conclave, D. S. Naik, G. Roati, C. Fort, and F. Minardi, Λ-enhanced grey molasses on the D_2 transition of Rubidium-87 atoms, *Sci. Rep.* **8**, 1301 (2018).

[114] G. D. Bruce, E. Haller, B. Peaudecerf, D. A. Cotta, M. Andia, S. Wu, M. Y. H. Johnson, B. W. Lovett, and S. Kuhr, Sub-Doppler laser cooling of 40 K with Raman gray molasses on the D_2 line, *J. Phys. B* **50**, 095002 (2017).

[115] F. L. Kien, P. Schneeweiss, and A. Rauschenbeutel, Dynamical polarizability of atoms in arbitrary light fields: general theory and application to cesium, *Eur. Phys. J. D* **67**, 92 (2013).

[116] L. D. Brown, T. T. Cai, and A. DasGupta, Interval Estimation for a Binomial Proportion, *Stat. Sci.* **16**, 101 (2001).

[117] J. P. Covey, I. S. Madjarov, A. Cooper, and M. Endres, 2000-times repeated imaging of strontium atoms in clock-magic tweezer arrays, *arXiv:1811.06014* (2018).

[118] J. Weiner, V. S. Bagnato, S. Zilio, and P. S. Julienne, Experiments and theory in cold and ultracold collisions, *Rev. Mod. Phys.* **71**, 1 (1999).

[119] L. R. Liu, J. D. Hood, Y. Yu, J. T. Zhang, N. R. Hutzler, T. Rosenband, and K.-K. Ni, Building one molecule from a reservoir of two atoms, *Science* **360**, 900 (2018).

[120] K. M. Jones, E. Tiesinga, P. D. Lett, and P. S. Julienne, Ultracold photoassociation spectroscopy: Long-range molecules and atomic scattering, *Reviews of Modern Physics* **78**, 483 (2006).

[121] J. L. Bohn and P. S. Julienne, Semianalytic theory of laser-assisted resonant cold collisions, *Physical Review A* **60**, 414 (1999).

[122] C. Chin, R. Grimm, P. Julienne, and E. Tiesinga, Feshbach resonances in ultracold gases, *Reviews of Modern Physics* **82**, 1225 (2010).

[123] S. Weber, C. Tresp, H. Menke, A. Urvoy, O. Firstenberg, H. P. Büchler, and S. Hofferberth, Calculation of Rydberg interaction potentials, *Journal of Physics B: Atomic, Molecular and Optical Physics* **50**, 133001 (2017).

[124] F. H. Mies, Molecular Theory of Atomic Collisions: Fine-Structure Transitions, *Physical Review A* **7**, 942 (1973).

[125] M. Kemmann, I. Mistrik, S. Nussmann, H. Helm, C. J. Williams, and P. S. Julienne, Near-threshold photoassociation of ^{87}Rb$_2$, *Physical Review A* **69**, 022715 (2004).

[126] C. J. Williams, E. Tiesinga, and P. S. Julienne, Hyperfine structure of the Na2 0g- long-range molecular state, *Physical Review A* **53**, R1939 (1996).

[127] M. Egorov, B. Opanchuk, P. Drummond, B. V. Hall, P. Hannaford, and A. I. Sidorov, Measurement of s-wave scattering lengths in a two-component Bose-Einstein condensate, *Physical Review A* **87**, 053614 (2013).

[128] P. Sompet, A. V. Carpentier, Y. H. Fung, M. McGovern, and M. F. Andersen, Dynamics of two atoms undergoing light-assisted collisions in an optical microtrap, *Phys. Rev. A* **88**, 051401(R) (2013).

[129] K.-A. Suominen, K. Burnett, P. S. Julienne, M. Walhout, U. Sterr, C. Orzel, M. Hoogerland, and S. L. Rolston, Ultracold collisions and optical shielding in metastable xenon, *Physical Review A* **53**, 1678 (1996).

[130] K.-A. Suominen, M. J. Holland, K. Burnett, and P. Julienne, Optical shielding of cold collisions, *Physical Review A* **51**, 1446 (1995).

[131] S. C. Zilio, L. Marcassa, S. Muniz, R. Horowicz, V. Bagnato, R. Napolitano, J. Weiner, and P. S. Julienne, Polarization Dependence of Optical Suppression in Photoassociative Ionization Collisions in a Sodium Magneto-optic Trap, *Physical Review Letters* **76**, 2033 (1996).

[132] P. S. Julienne, 2020, private communication.

[133] H. Lefebvre-Brion and R. W. Field, *Perturbations in the Spectra of Diatomic Molecules*, 1 ed. (Academic Press, 24-28 Oval Road, London NW1 7DX, 1986), Vol. 1.

[134] J. T. Hougen and G. G. Wiersma, *The Calculation of Rotational Energy Levels and Rotational Line Intensities in Diatomic Molecules*, *Monograph (NIST MN)* (National Institute of Standards and Technology, Gaithersburg, MD, [online], 2001).

[135] A. R. Edmonds, *Angular Momentum in Quantum Mechanics*, 3rd printing ed. (Princeton University Press, New Jersey, 1960).

[136] D. A. Varshalovich, A. N. Moskalev, and V. K. Khersonskii, *Quantum Theory of Angular Momentum* (World Scientific Publishing Co. Pte. Ltd., Singapore, 1988).

[137] E. U. Condon and G. H. Shortley, *The Theory of Atomic Spectra* (The Syndics of the Cambridge University Press, London, 1970).

[138] S. Magnier, P. Millié, O. Dulieu, and F. Masnou-Seeuws, Potential curves for the ground and excited states of the Na2 molecule up to the (3s+5p) dissociation limit: Results of two different effective potential calculations, *The Journal of Chemical Physics* **98**, 7113 (1993).

[139] M. Marinescu and A. Dalgarno, Dispersion forces and long-range electronic transition dipole moments of alkali-metal dimer excited states, *Physical Review A* **52**, 311 (1995).

[140] M. Movre and G. Pichler, Resonance interaction and self-broadening of alkali resonance lines. I. Adiabatic potential curves, *Journal of Physics B: Atomic and Molecular Physics* **10**, 2631 (1977).

[141] W. C. Stwalley, Y.-H. Uang, and G. Pichler, Pure Long-Range Molecules, *Physical Review Letters* **41**, 1164 (1978).

[142] T. Bergeman, P. S. Julienne, C. J. Williams, E. Tiesinga, M. R. Manaa, H. Wang, P. L. Gould, and W. C. Stwalley, Predissociations in 0u+ and 1g states of K2, *The Journal of Chemical Physics* **117**, 7491 (2002).

[143] S. J. Singer, K. F. Freed, and Y. B. Band, Theory of diatomic molecule photodissociation: Electronic angular momentum influence on fragment and fluorescence cross sections, *The Journal of Chemical Physics* **79**, 6060 (1983).

[144] J. M. Brown, J. T. Hougen, K. P. Huber, J. W. C. Johns, I. Kopp, H. Lefebvre-Brion, A. J. Merer, D. A. Ramsay, J. Rostas, and R. N. Zare, The labeling of parity doublet levels in linear molecules, *Journal of Molecular Spectroscopy* **55**, 500 (1975).

[145] K. M. Jones, P. S. Julienne, P. D. Lett, W. D. Phillips, E. Tiesinga, and C. J. Williams, Measurement of the atomic Na(3P) lifetime and of retardation in the interaction between two atoms bound in a molecule, *EPL (Europhysics Letters)* **35**, 85 (1996).

[146] C. Zener and R. H. Fowler, Non-adiabatic crossing of energy levels, *Proceedings of the Royal Society of London. Series A, Containing Papers of a Mathematical and Physical Character* **137**, 696 (1932).

[147] M. O. Brown, S. R. Muleady, W. J. Dworschack, R. J. Lewis-Swan, A. M. Rey, O. Romero-Isart, and C. A. Regal, Time-of-Flight Quantum Tomography of Single Atom Motion, *arXiv:2203.03053 [quant-ph]* (2022), arXiv: 2203.03053.

[148] K. Vogel and H. Risken, Determination of quasiprobability distributions in terms of probability distributions for the rotated quadrature phase, *Physical Review A* **40**, 2847 (1989).

[149] D. T. Smithey, M. Beck, M. G. Raymer, and A. Faridani, Measurement of the Wigner distribution and the density matrix of a light mode using optical homodyne tomography: Application to squeezed states and the vacuum, *Physical Review Letters* **70**, 1244 (1993).

[150] A. I. Lvovsky, H. Hansen, T. Aichele, O. Benson, J. Mlynek, and S. Schiller, Quantum State Reconstruction of the Single-Photon Fock State, *Phys. Rev. Lett.* **87**, 050402 (2001).

[151] C. Gross, H. Strobel, E. Nicklas, T. Zibold, N. Bar-Gill, G. Kurizki, and M. Oberthaler, Atomic homodyne detection of continuous-variable entangled twin-atom states, *Nature* **480**, 219 (2011).

[152] S. Deleglise, I. Dotsenko, C. Sayrin, J. Bernu, M. Brune, J.-M. Raimond, and S. Haroche, Reconstruction of non-classical cavity field states with snapshots of their decoherence, *Nature* **455**, 510 (2008).

[153] M. Hofheinz *et al.*, Synthesizing arbitrary quantum states in a superconducting resonator, *Nature* **459**, 546 (2009).

[154] D. Leibfried, D. M. Meekhof, B. E. King, C. Monroe, W. M. Itano, and D. J. Wineland, Experimental Determination of the Motional Quantum State of a Trapped Atom, *Physical Review Letters* **77**, 4281 (1996).

[155] C. Flühmann and J. P. Home, Direct characteristic-function tomography of quantum states of the trapped-ion motional oscillator, *Physical Review Letters* **125**, 043602 (2020).

[156] A. D. O'Connell *et al.*, Quantum ground state and single-phonon control of a mechanical resonator, *Nature* **464**, 697 (2010).

[157] Y. Chu, P. Kharel, T. Yoon, L. Frunzio, P. T. Rakich, and R. J. Schoelkopf, Creation and control of multi-phonon Fock states in a bulk acoustic-wave resonator, *Nature* **563**, 666 (2018).

[158] D. E. Chang, C. Regal, S. Papp, D. Wilson, J. Ye, O. Painter, H. J. Kimble, and P. Zoller, Cavity opto-mechanics using an optically levitated nanosphere, *Proceedings of the National Academy of Sciences* **107**, 1005 (2010).

[159] O. Romero-Isart, M. L. Juan, R. Quidant, and J. I. Cirac, Toward Quantum Superposition of Living Organisms, *New J. Phys.* **12**, 033015 (2010).

[160] C. Gonzalez-Ballestero, M. Aspelmeyer, L. Novotny, R. Quidant, and O. Romero-Isart, Levitodynamics: Levitation and control of microscopic objects in vacuum, *Science* **374**, eabg3027 (2021).

[161] F. Tebbenjohanns, M. L. Mattana, M. Rossi, M. Frimmer, and L. Novotny, Quantum control of a nanoparticle optically levitated in cryogenic free space, *Nature* **595**, 378 (2021).

[162] L. Magrini, P. Rosenzweig, C. Bach, A. Deutschmann-Olek, S. G. Hofer, S. Hong, N. Kiesel, A. Kugi, and M. Aspelmeyer, Real-time optimal quantum control of mechanical motion at room temperature, *Nature* **595**, 373 (2021).

[163] O. Romero-Isart, A. C. Pflanzer, M. L. Juan, R. Quidant, N. Kiesel, M. Aspelmeyer, and J. I. Cirac, Optically levitating dielectrics in the quantum regime: Theory and protocols, *Physical Review A* **83**, 013803 (2011).

[164] M. Vanner, J. Hofer, G. Cole, and M. Aspelmeyer, Cooling-by-measurement and mechanical state tomography via pulsed optomechanics, *Nature communications* **4**, 1 (2013).

[165] T. Dunn, I. Walmsley, and S. Mukamel, Experimental determination of the quantum-mechanical state of a molecular vibrational mode using fluorescence tomography, *Physical review letters* **74**, 884 (1995).

[166] A. Fuhrmanek, A. M. Lance, C. Tuchendler, P. Grangier, Y. R. P. Sortais, and A. Browaeys, Imaging a single atom in a time-of-flight experiment, *New Journal of Physics* **12**, 053028 (2010).

[167] A. Bergschneider, V. M. Klinkhamer, J. H. Becher, R. Klemt, L. Palm, G. Zürn, S. Jochim, and P. M. Preiss, Experimental characterization of two-particle entanglement through position and momentum correlations, *Nature Physics* **15**, 640 (2019).

[168] C. Kurtsiefer, T. Pfau, and J. Mlynek, Measurement of the Wigner function of an ensemble of helium atoms, *Nature* **386**, 150 (1997).

[169] M. Greiner, O. Mandel, T. Esslinger, T. W. Hänsch, and I. Bloch, Quantum phase transition from a superfluid to a Mott insulator in a gas of ultracold atoms, *Nature* **415**, 39 (2002).

[170] M. Schellekens, R. Hoppeler, A. Perrin, J. V. Gomes, D. Boiron, A. Aspect, and C. I. Westbrook, Hanbury Brown Twiss effect for ultracold quantum gases, *Science* **310**, 648 (2005).

[171] I. Bloch, J. Dalibard, and W. Zwerger, Many-body physics with ultracold gases, *Rev. Mod. Phys.* **80**, 885 (2008).

[172] R. Bücker, J. Grond, S. Manz, T. Berrada, T. Betz, C. Koller, U. Hohenester, T. Schumm, A. Perrin, and J. Schmiedmayer, Twin-atom beams, *Nature Physics* **7**, 608 (2011).

[173] M. Morinaga, I. Bouchoule, J.-C. Karam, and C. Salomon, Manipulation of motional quantum states of neutral atoms, *Physical review letters* **83**, 4037 (1999).

[174] R. Bücker, T. Berrada, S. Van Frank, J.-F. Schaff, T. Schumm, J. Schmiedmayer, G. Jäger, J. Grond, and U. Hohenester, Vibrational state inversion of a Bose–Einstein condensate: optimal control and state tomography, *Journal of Physics B: Atomic, Molecular and Optical Physics* **46**, 104012 (2013).

[175] A. M. Kaufman, B. J. Lester, and C. A. Regal, Cooling a Single Atom in an Optical Tweezer to Its Quantum Ground State, *Phys. Rev. X* **2**, 041014 (2012).

[176] D. Kienzler, H.-Y. Lo, B. Keitch, L. de Clercq, F. Leupold, F. Lindenfelser, M. Marinelli, V. Negnevitsky, and J. P. Home, Quantum harmonic oscillator state synthesis by reservoir engineering, *Science* **347**, 53 (2015).

[177] T. Weiss and O. Romero-Isart, Quantum motional state tomography with nonquadratic potentials and neural networks, *Physical Review Research* **1**, 033157 (2019).

[178] M. A. Ciampini, T. Wenzl, M. Konopik, G. Thalhammer, M. Aspelmeyer, E. Lutz, and N. Kiesel, Experimental nonequilibrium memory erasure beyond Landauer's bound, *arXiv preprint arXiv:2107.04429* (2021).

[179] U. Leonhardt, *Measuring the Quantum State of Light*, No. 22 in *Cambridge Studies in Modern Optics*, 1st ed. (Cambridge University Press, UK, 1997).

[180] K. Banaszek, G. M. D'Ariano, M. G. A. Paris, and M. F. Sacchi, Maximum-likelihood estimation of the density matrix, *Physical Review A* **61**, 010304 (1999).

[181] A. I. Lvovsky, Iterative maximum-likelihood reconstruction in quantum homodyne tomography, *Journal of Optics B: Quantum and Semiclassical Optics* **6**, S556 (2004).

[182] K. C. McCormick, J. Keller, S. C. Burd, D. J. Wineland, A. C. Wilson, and D. Leibfried, Quantum-enhanced sensing of a single-ion mechanical oscillator, *Nature* **572**, 86 (2019).

[183] L. P. Parazzoli, A. M. Hankin, and G. W. Biedermann, Observation of free-space single-atom matter wave interference, *Physical review letters* **109**, 230401 (2012).

[184] M. Brown, T. Thiele, C. Kiehl, T.-W. Hsu, and C. Regal, Gray-Molasses Optical-Tweezer Loading: Controlling Collisions for Scaling Atom-Array Assembly, *Physical Review X* **9**, 011057 (2019).

[185] B. J. Lester, Y. Lin, M. O. Brown, A. M. Kaufman, R. J. Ball, E. Knill, A. M. Rey, and C. A. Regal, Measurement-Based Entanglement of Noninteracting Bosonic Atoms, *Phys. Rev. Lett.* **120**, 193602 (2018).

[186] A. Bergschneider, V. M. Klinkhamer, J. H. Becher, R. Klemt, G. Zürn, P. M. Preiss, and S. Jochim, Spin-resolved single-atom imaging of Li 6 in free space, *Physical Review A* **97**, 063613 (2018).

[187] U. Leonhardt and I. Jex, Wigner functions and quadrature distributions for quantum-oscillator states with random phase, *Physical Review A* **49**, R1555 (1994).

[188] A. Wünsche, Radon transform and pattern functions in quantum tomography, *Journal of Modern Optics* **44**, 2293 (1997).

[189] T. Richter, Realistic pattern functions for optical homodyne tomography and determination of specific expectation values, *Physical Review A* **61**, 063819 (2000).